



TECHNISCHE
UNIVERSITÄT
WIEN
Vienna University of Technology

DISSERTATION

Precise Point Positioning (PPP) - an alternative technique for ground based GNSS troposphere monitoring

carried out in order to obtain the academic degree
"doctor of the technical sciences" under the supervision of

a.o.Univ.-Prof. Dipl.-Ing. Dr.techn. Robert Weber

presented at the Vienna University of Technology
Faculty of Mathematics and Geoinformation

by

Dipl.-Ing. Ana Karabatić
Matriculation number: 0627427
Jägerstraße 5–6
1200 Vienna

Vienna, February 2011

Supervisors

a.o.Univ.-Prof. Dipl.-Ing. Dr.techn. Robert Weber
Institute of Geodesy and Geophysics
Vienna Technical University
Gusshausstrasse 27-29, 1040 Vienna, Austria

Dipl.-Ing. Dr.Sc. Tomislav Bašić
Faculty of Geodesy
University of Zagreb
Kačićeva 26, 10000 Zagreb, Croatia

*If you compare yourself with others,
you may become vain or bitter,
for always there will be greater and lesser persons than yourself.
Enjoy your achievements as well as your plans.
Keep interested in your own career, however humble;
it is a real possession in the changing fortunes of time.*

Max Ehrmann, 1920s

Acknowledgments

There are many people to be acknowledged here. But, there are some very special ones without whom this words would have never been written. Most of all I'd like to thank my mentor, Prof.Dr. Robert Weber. Besides an enormous knowledge, and never ending spirit to know even more, he has so much kindness for other people, unconditionally and unprejudiced. He is always ready to give advices, inputs, critics, and most importantly small shots of motivation in the moments when everything seems worthless. I am so lucky to have been your student! Next, I would like to thank my second supervisor, Prof.Dr. Tomislav Bašić, who was my bridge to the world of science. Thank you for your guidance during my faculty days and your help in entering this overwhelming world of research.

I want to thank my family: Roland, my parents and my brother. You are puzzles of my life. Nothing would be worth without you. I love you endlessly.

Many thanks to all my colleagues at HG. Thank you for your help during my years at the Institute, either by an advice, joint work or just a kind word or a smile. A special thank goes to Prof.Dr. Harald Schuh for allowing me to be a part of this wonderful group.

Ana

Abstract

Electromagnetic signals emitted by the Global Navigation Satellite System (GNSS) satellites are time delayed when passing through the atmosphere. Based on this signal delay, e.g. the humidity distribution within the troposphere can be determined. It has already been shown that the delivery of the Zenith Wet Delays (ZWD) derived from a network solution with hourly resolution and an accuracy of 1 mm in precipitable water is achievable. In the case of very large networks along with an increased number of observations and computational demands, an alternative processing technique has to be applied — Precise Point Positioning (PPP). PPP is a technique that uses un-differenced single- or dual-frequency pseudorange and carrier phase observations of a single receiver along with precise orbit and clocks products to achieve a cm-level positioning precision. The advantage of this zero difference technique is that no regional correlations will be introduced as well as no reference station data is explicitly required for data processing. On the other hand hardware biases (both from the satellite and the receiver), which cancel when forming double-difference observations in a network approach remain, and have to be accounted for carefully. Furthermore, the necessary correction models have to be made available close to real-time by organizations like IGS or by regional reference station providers.

In this thesis it is shown how the atmospheric precipitable water content derived from GNSS data can be assimilated within an operational meteorological now-casting system and how PPP results compare to the network solution. Passing weather fronts can be analyzed much better by considering the information provided by GNSS derived tropospheric wet delays because this data is directly influenced by changes in humidity in the free atmosphere, whereas the data at the meteorological ground stations react to these changes with a considerable time delay. This allows to forecast, e.g. heavy rainfall potentially causing local floodings more reliable and to narrow down the affected region. It is to be expected that the accuracy of the PPP ZWD estimates is worse due to several effects (satellite clock errors, biases, no ambiguity resolution), but independence from the reference station data will significantly shorten the latency of the results (few min), and provide the regional/national weather service to enhance the prognosis in the numerical forecast model.

Nomenclature

Abbreviations

AC	Analysis Center
ANTEX	Antenna Exchange Format
A-S	Anti-Spoofing
TDB	Barycentric Dynamic Time
BIPM	Bureau International des Poids et Mesures (International Bureau of Weights and Measures)
BOC	Binary Offset Carrier
BPE	Bernese Processing Engine
BSW	Bernese Software
C/A	Coarse/Acquisition
CDMA	Code Division Multiple Access
CODE	Center for Orbit Determination in Europe
CS	Commercial Service
DCB	Differential Code Bias
DD	Double-Difference
DoD	Department of Defense
DOP	Dilution of Precision
DOY	Day Of Year

EC	European Commission
ECMWF	European Center for Medium-Range Weather Forecast
EGNOS	European Geostationary Navigation Overlay System
E-GVAP	EUMETNET EIG GNSS water VApour Programme
EM	Electromagnetic
ERP	Earth Rotation Parameters
ESA	European Space Agency
ESOC	European Space Operations Center
EU	European Union
EUREF	EUropean REference network
FDMA	Frequency Division Multiple Access
FOC	Full Operational Capability
GDOP	Geometry Dilution of Precision
GFZ	GeoForschungZentrum
GLONASS	GLObal'naya NAVigatsionnaya Sputnikovaya Sistema
GMF	Global Mapping Function
GNSS	Global Navigation Satellite System
GOP	Geodetic Observatory Pecny
GPS	Global Positioning System
GPST	GPS Time
GPT	Global Pressure and Temperature model
GST	Galileo System Time
GTRF	Galileo Terrestrial Reference Frame
IAG	International Association of Geodesy

IERS	International Earth Rotation and Reference System Service
IGEX	International GLONASS Experiment
IGRM	International Geomagnetic Reference Model
IGS	International GNSS Service
IMF	Isobaric Mapping Function
INCA	Integrated Now-casting through Comprehensive Analysis
IOV	In-Orbit Validation
IRI	International Reference Ionosphere
ITRF	International Terrestrial Reference Frame
IWV	Integrated Water Vapor
JPL	Jet Propulsion Laboratory
JPO	Joint Program Office
LC	Linear Combination
MIT	Massachusetts Institute of Technology
NASA	National Aeronautics and Space Administration
NMF	Niell Mapping Function
NOAA	National Oceanic and Atmospheric Administration
NRCan	Natural Resources Canada
NWM	Numerical Weather Model
NWP	Numerical Weather Prediction
OS	Open Service
PCF	Processing Control File
PDOP	Position Dilution of Precision
PE-90 (PZ-90)	Parameters of the Earth 1990 (Parametry Zemli 1990)

PPP	Precise Point Positioning
PPS	Precise Positioning Service
PRN	Pseudo Random Noise
PRS	Public Regulated Service
PW	Precipitable Water
RHCP	Right Hand Circularly Polarized
RINEX	Receiver INdependent EXchange format
RTK	Real-Time Kinematic
SA	Selective Availability
SI	Système International d'unités (International System of Units)
SIO	Scripps Institution of Oceanography
SNR	Signal-to-Noise Ratio
SoL	Safety-of-Life service
SP3	Standard Product v.3
SPP	Single Point Positioning
SPS	Standard Positioning Service
STEC	Slant Total Electron Content
TAI	Temps Atomique International (International Atomic Time)
TDOP	Time Dilution of Precision
TDT	Terrestrial Dynamic Time
TEC	Total Electron Content
TECU	Total Electron Content Unit
TID	Traveling Ionospheric Disturbances
TT	Terrestrial Time

TT&C	Telemetry, Tracking and Control
USNO	United States Naval Observatory
UT1	Universal Time 1
UTC	Universal Time, Coordinated
VDOP	Vertical Dilution of Precision
VLBI	Very Long Baseline Interferometry
VMF	Vienna Mapping Function
VTEC	Vertical Total Electron Content
WGS-84	World Geodetic System 1984
ZHD	Zenith Hydrostatic Delay
ZTD	Zenith Total Delay
ZWD	Zenith Wet Delay

Constants

c	speed of light in vacuum ($299792.458 \text{ km s}^{-1}$), source: http://www.bipm.org/en/si/
G	gravitational constant ($6.67259 \cdot 10^{-11} \text{ m}^3\text{kg}^{-1}\text{s}^{-2}$), source: http://ssd.jpl.nasa.gov/?constants
m_d	molar mass of dry air ($28.9644 \pm 0.0014 \text{ g/mol}$) source: Böhm [2008]
M_E	mass of Earth ($5.9736 \cdot 10^{24} \text{ kg}$), source: http://nssdc.gsfc.nasa.gov/planetary/factsheet/earthfact.html
m_w	molar mass of water vapor (18.01528 g/mol) source: Böhm [2008]
R	universal gas constant ($8.314345 \pm 0.00007 \text{ Pa}\cdot\text{m}^3/\text{K}\cdot\text{mol}$) source: Böhm [2008]

Contents

List of Figures	xvii
List of Tables	xxi
1 Introduction	1
2 Global Navigation Satellite System	5
2.1 Principles of satellite-based positioning	5
2.2 Time systems	6
2.3 Components of GNSS	8
2.3.1 GPS	9
2.3.2 GLONASS	13
2.3.3 Galileo	15
2.4 GNSS modernization on user level	18
3 Concept of Precise Point Positioning	19
3.1 Observation equations	20
3.2 Precise Point Positioning correction model	22
3.2.1 Relativistic effects	22
3.2.2 Satellite antenna phase center offset and variation	25
3.2.3 Receiver antenna phase center pattern	26
3.2.4 Phase wind-up correction	27
3.2.5 System biases	28
3.2.6 Multipath	30
3.2.7 Site displacement effects	30
3.3 Observation adjustment	34
3.4 PPP services	37
3.4.1 International GNSS Service (IGS)	37

3.4.2	PPP processing and analysis services	39
3.5	Current state of Precise Point Positioning	40
4	Signal propagation in the atmosphere	43
4.1	Ionospheric delay	44
4.2	Tropospheric delay	49
4.2.1	Refractivity of the troposphere	52
4.2.2	Modeling and estimation of tropospheric path delay	53
4.2.3	Zenith delays	56
4.2.3.1	Zenith hydrostatic delay	56
4.2.3.2	Zenith wet delay	59
4.2.4	Slant delays	60
4.2.4.1	Mapping functions	61
4.2.4.2	Gradient modeling	64
5	GNSS Meteorology	67
5.1	Project GNSSMET	67
5.2	Station network	69
5.3	Estimation of the zenith wet delay	70
5.4	Choice of orbits	74
5.5	Precipitable water	76
5.6	Validation and assimilation	77
6	Troposphere monitoring using PPP	85
6.1	Observation data	86
6.2	Processing strategy	87
6.3	Parameter estimation	88
6.4	Estimation of zenith wet delay by PPP	89
6.5	Validation of the ZWD estimates	99
6.5.1	PPP versus double-difference solution	99
6.5.2	Comparison of results with IGS solution	102
6.5.3	Meteorological data	104
6.6	Solution parameters	107
6.6.1	Satellite orbits	107
6.6.2	Satellite clock corrections	109
6.6.3	Observation selection	109
6.6.4	Setup of troposphere criteria	111

6.7	Impact on station coordinates	114
6.8	Summary	115
7	Future improvements	117
7.1	Geometry effects	117
7.2	New linear combinations	119
7.3	Water vapor tomography	121
8	Conclusions	125
8.1	Summary	125
8.2	Outlook	127
	Appendix A	129
	Appendix B	135
	Appendix C	207
	Bibliography	252

List of Figures

2.1	Satellite-based positioning	5
2.2	Relationships between time scales	8
3.1	Satellite antenna phase center offset and variation	25
3.2	Satellite antenna pattern for GPS and GLONASS satellites	26
3.3	IGS tracking network	38
4.1	Mean electron content over last 15 years	44
4.2	Ionospheric single-layer model	47
4.3	Global ionosphere maps	48
4.4	Density of dry and wet air	50
4.5	Variation of temperature through the layers of the atmosphere	51
4.6	Geometric bending effect	53
4.7	Pressure differences between GPT and the models by Berg and Hopfield	58
4.8	Azimuthal asymmetry	65
5.1	KELSAT network	69
5.2	TAWES network	71
5.3	Comparison of ZWD estimates based on a priori ZHD from standard atmosphere and a priori ZHD from real meteorological data	72
5.4	Scheme of the GNSSMET processing work-flow	73
5.5	Estimated ZWDs for all network stations	74
5.6	Weighted RMS of IGU combined orbits compared to IGR orbits	75
5.7	Comparison of ZWD estimates calculated using IGS rapid (IGR) and IGS ultra-rapid (IGU) orbits for station Bleiburg	75
5.8	Weather front passing the area of Carinthia	77
5.9	Comparison of PWs derived from the INCA model, radiosonde observa- tions and GNSS analysis	78

5.10	Humidity profiles over Graz	80
5.11	Comparison of PW from INCA, GNSS and radiosonde data	81
5.12	PW over the KELSAT area	82
6.1	Map of sites used for this PPP study	86
6.2	ZWD time series of all stations on March 27th, 2010	90
6.3	Formal errors of ZWD estimates of all stations on March 27th, 2010	91
6.4	ZWD for station Graz and nearby stations on March 27th, 2010	92
6.5	ZWD for station GRAZ and the nearby station GRAR (March 27–April 16, 2010)	93
6.6	ZWD and formal errors of ZWD for station GRAR (March 27–April 16, 2010)	93
6.7	ZWD and formal errors of ZWD for station KOLM (March 27–March 29, 2010)	94
6.8	Sky plots for stations KOLM and SONN	95
6.9	ZWD time series of all stations on June 15th, 2010	96
6.10	Formal errors of ZWD estimates of all stations for June 15th, 2010	97
6.11	ZWD estimates and their formal errors of ZWD for station GRAR (June 13–25, 2010)	98
6.12	ZWD estimates for four stations on different station heights (June 13–15, 2010)	98
6.13	Comparison of ZWD estimates derived from PPP and double-difference solution for station GRAR (March 27–April 16, 2010)	99
6.14	Difference of ZWD from PPP and double-difference solution for station GRAR (March 27–April 16, 2010)	100
6.15	Comparison of formal errors of ZWD estimates from PPP and double-difference (relative) solution for station GRAR (March 27–April 16, 2010)	101
6.16	Comparison of PPP ZTDs provided by IGS and estimated within this thesis for station Graz	102
6.17	Standard deviation of the IGS PPP ZTD and PPP ZTD estimates	103
6.18	Difference between the IGS PPP ZTD and PPP ZTD time series (station Graz)	104
6.19	Meteo records of temperature and precipitation for station Graz in April 2010	104
6.20	ZWD for IGS station GRAZ (March 27–April 16, 2010)	105

6.21	ZWD time series of IGS station GRAZ and several nearby stations (April 5–11, 2010 (DOY 95–101))	105
6.22	ZWD of IGS station GRAZ and nearby stations (June 13–26, 2010 (DOY 164–177))	106
6.23	Meteo records of temperature and precipitation for station Graz in June 2010	106
6.24	Weighted RMS of the individual AC orbit solutions with respect to the IGS final product (April 15, 2009 – July 4, 2010)	108
6.25	PPP ZWD for station GRAR using IGS final orbits and CODE final orbits	108
6.26	PPP ZWD estimates and respective formal errors for station GRAR using 15-minute and 30-second satellite clock corrections	109
6.27	Hourly PPP ZWD estimates and respective formal errors for station GRAR using 30-second and 15-second data rate	110
6.28	PPP ZWD estimates and respective formal errors for station GRAR with higher temporal resolution	111
6.29	ZWD estimates and respective formal errors for station GRAR with different constraints	112
6.30	ZWD estimates and respective formal errors for station ROET with different constraints	113
6.31	ZWD estimates and respective formal errors for station KOLM with different constraints	113
6.32	Station GRAR: station displacement in the north-, east- and up-component for March 27th, 2010	114
6.33	ZWD estimates for station GRAR on March 27th, 2010	115
7.1	The number of visible satellites and GDOP for station KOLM in the case of GPS-only (left) and simulated GPS+Galileo scenario	118
7.2	Comparison of GPS-only and GPS+GLONASS derived ZWD estimates and respective formal errors for the station Kolm-Saigurn	119
7.3	Tomography model	122
7.4	Simulated raytraced tomography model using GPS-only and GPS+Galileo observations	123
7.5	The impact of additional GNSS observations and network extension on tomography results	124
A.1	Example of Bernese SW input panel	134

B.1	ZWD of all stations on March 27th, 2010	136
B.2	Formal errors of ZWD estimates of all stations on March 27th, 2010 . .	137
B.3	ZWD of all stations on March 28th, 2010	138
B.4	Formal errors of ZWD estimates of all stations on March 28th, 2010 . .	139
B.5	ZWD of all stations on March 29th, 2010	140
B.6	Formal errors of ZWD estimates of all stations on March 29th, 2010 . .	141
B.7	ZWD of all stations on March 30th, 2010	142
B.8	Formal errors of ZWD estimates of all stations on March 30th, 2010 . .	143
B.9	ZWD of all stations on March 31th, 2010	144
B.10	Formal errors of ZWD estimates of all stations on March 31th, 2010 . .	145
B.11	ZWD of all stations for April 1st, 2010	146
B.12	Formal errors of ZWD estimates of all stations on April 1st, 2010	147
B.13	ZWD of all stations on April 2nd, 2010	148
B.14	Formal errors of ZWD estimates of all stations on April 2nd, 2010 . . .	149
B.15	ZWD of all stations on April 3rd, 2010	150
B.16	Formal errors of ZWD estimates of all stations on April 3rd, 2010	151
B.17	ZWD of all stations on April 4th, 2010	152
B.18	Formal errors of ZWD estimates of all stations on April 4th, 2010	153
B.19	ZWD of all stations on April 5th, 2010	154
B.20	Formal errors of ZWD estimates of all stations on April 5th, 2010	155
B.21	ZWD of all stations on April 6th, 2010	156
B.22	Formal errors of ZWD estimates of all stations on April 6th, 2010	157
B.23	ZWD of all stations on April 7th, 2010	158
B.24	Formal errors of ZWD estimates of all stations on April 7th, 2010	159
B.25	ZWD of all stations on April 8th, 2010	160
B.26	Formal errors of ZWD estimates of all stations on April 8th, 2010	161
B.27	ZWD of all stations on April 9th, 2010	162
B.28	Formal errors of ZWD estimates of all stations on April 9th, 2010	163
B.29	ZWD of all stations on April 6th, 2010	164
B.30	Formal errors of ZWD estimates of all stations on April 10th, 2010 . . .	165
B.31	ZWD of all stations on April 11th, 2010	166
B.32	Formal errors of ZWD estimates of all stations on April 11th, 2010 . . .	167
B.33	ZWD of all stations on April 12th, 2010	168
B.34	Formal errors of ZWD estimates of all stations on April 12th, 2010 . . .	169
B.35	ZWD of all stations on April 13th, 2010	170
B.36	Formal errors of ZWD estimates of all stations on April 13th, 2010 . . .	171

B.37 ZWD of all stations on April 14th, 2010	172
B.38 Formal errors of ZWD estimates of all stations on April 14th, 2010 . . .	173
B.39 ZWD of all stations on April 15th, 2010	174
B.40 Formal errors of ZWD estimates of all stations on April 15th, 2010 . . .	175
B.41 ZWD of all stations on April 16th, 2010	176
B.42 Formal errors of ZWD estimates of all stations on April 16th, 2010 . . .	177
B.43 ZWD of all stations on June 13th, 2010	178
B.44 Formal errors of ZWD estimates of all stations on June 13th, 2010 . . .	179
B.45 ZWD of all stations on June 14th, 2010	180
B.46 Formal errors of ZWD estimates of all stations on June 14th, 2010 . . .	181
B.47 ZWD of all stations on June 15th, 2010	182
B.48 Formal errors of ZWD estimates of all stations on June 15th, 2010 . . .	183
B.49 ZWD of all stations on June 16th, 2010	184
B.50 Formal errors of ZWD estimates of all stations on June 16th, 2010 . . .	185
B.51 ZWD of all stations on June 17th, 2010	186
B.52 Formal errors of ZWD estimates of all stations on June 17th, 2010 . . .	187
B.53 ZWD of all stations on June 18th, 2010	188
B.54 Formal errors of ZWD estimates of all stations on June 18th, 2010 . . .	189
B.55 ZWD of all stations on June 19th, 2010	190
B.56 Formal errors of ZWD estimates of all stations on June 19th, 2010 . . .	191
B.57 ZWD of all stations on June 20th, 2010	192
B.58 Formal errors of ZWD estimates of all stations on June 20th, 2010 . . .	193
B.59 ZWD of all stations on June 21st, 2010	194
B.60 Formal errors of ZWD estimates of all stations on June 21st, 2010 . . .	195
B.61 ZWD of all stations on June 22nd, 2010	196
B.62 Formal errors of ZWD estimates of all stations on June 22nd, 2010 . . .	197
B.63 ZWD of all stations on June 23rd, 2010	198
B.64 Formal errors of ZWD estimates of all stations on June 23rd, 2010 . . .	199
B.65 ZWD of all stations on June 24th, 2010	200
B.66 Formal errors of ZWD estimates of all stations on June 24th, 2010 . . .	201
B.67 ZWD of all stations on June 25th, 2010	202
B.68 Formal errors of ZWD estimates of all stations on June 25th, 2010 . . .	203
B.69 ZWD of all stations on June 26th, 2010	204
B.70 Formal errors of ZWD estimates of all stations on June 26th, 2010 . . .	205

C.1	Comparison of PPP and double-difference solution for station GRAR (March 27–April 16, 2010)	208
C.2	Comparison of PPP and double-difference solution for station GRAR (June 13–26, 2010)	209
C.3	Comparison of PPP and double-difference solution for station GRAZ (March 27–April 16, 2010)	210
C.4	Comparison of PPP and double-difference solution for station GRAZ (June 13–26, 2010)	211
C.5	Comparison of PPP and double-difference solution for station KIBG (March 27–April 16, 2010)	212
C.6	Comparison of PPP and double-difference solution for station KIBG (June 13–26, 2010)	213
C.7	Comparison of PPP and double-difference solution for station KOLM (March 27–April 16, 2010)	214
C.8	Comparison of PPP and double-difference solution for station KOLM (June 13–26, 2010)	215
C.9	Comparison of PPP and double-difference solution for station KOET (March 27–April 16, 2010)	216
C.10	Comparison of PPP and double-difference solution for station KOET (June 13–26, 2010)	217
C.11	Comparison of PPP and double-difference solution for station LEOB (March 27–April 16, 2010)	218
C.12	Comparison of PPP and double-difference solution for station LEOB (June 13–26, 2010)	219
C.13	Comparison of PPP and double-difference solution for station LEIB (March 27–April 16, 2010)	220
C.14	Comparison of PPP and double-difference solution for station LEIB (June 13–26, 2010)	221
C.15	Comparison of PPP and double-difference solution for station MATR (March 27–April 16, 2010)	222
C.16	Comparison of PPP and double-difference solution for station MATR (June 13–26, 2010)	223
C.17	Comparison of PPP and double-difference solution for station NEUS (March 27–April 16, 2010)	224
C.18	Comparison of PPP and double-difference solution for station NEUS (June 13–26, 2010)	225

C.19 Comparison of PPP and double-difference solution for station OCHS (March 27–April 16, 2010)	226
C.20 Comparison of PPP and double-difference solution for station OCHS (June 13–26, 2010)	227
C.21 Comparison of PPP and double-difference solution for station ROET (March 27–April 16, 2010)	228
C.22 Comparison of PPP and double-difference solution for station ROET (June 13–26, 2010)	229
C.23 Comparison of PPP and double-difference solution for station SILL (March 27–April 16, 2010)	230
C.24 Comparison of PPP and double-difference solution for station SILL (June 13–26, 2010)	231
C.25 Comparison of PPP and double-difference solution for station SHLA (March 27–April 16, 2010)	232
C.26 Comparison of PPP and double-difference solution for station SHLA (June 13–26, 2010)	233
C.27 Comparison of PPP and double-difference solution for station SONN (March 27–April 16, 2010)	234
C.28 Comparison of PPP and double-difference solution for station SONN (June 13–26, 2010)	235
C.29 Comparison of PPP and double-difference solution for station TREI (March 27–April 16, 2010)	236
C.30 Comparison of PPP and double-difference solution for station TREI (June 13–26, 2010)	237
C.31 Comparison of PPP and double-difference solution for station WOBG (March 27–April 16, 2010)	238
C.32 Comparison of PPP and double-difference solution for station WOBG (June 13–26, 2010)	239
C.33 Comparison of PPP and double-difference solution for station WTZR (March 27–April 16, 2010)	240
C.34 Comparison of PPP and double-difference solution for station WTZR (June 13–26, 2010)	241
C.35 Comparison of PPP and double-difference solution for station ZIMM (March 27–April 16, 2010)	242
C.36 Comparison of PPP and double-difference solution for station ZIMM (June 13–26, 2010)	243

List of Tables

2.1	GPS signal modernization	11
2.2	GLONASS signal modernization	14
2.3	Galileo signals	17
3.1	GPS ephemerides data provided by IGS	39
4.1	Empirically determined values for refractivity constants	52
5.1	Bias and RMS between INCA and GNSS derived PWs and the ra- diosonde observation for the station Graz	78
6.1	Approximate geographic coordinates of network sites	87
6.2	Mean formal errors, and median and maximal differences of double- difference and PPP solution for all stations	100
6.3	A posteriori RMS of unit weight of double-difference and PPP solution for March 27–April 15, 2010	102
7.1	GPS linear combinations	120
7.2	Galileo linear combinations	121

Chapter 1

Introduction

Electromagnetic (EM) signals emitted by the Global Navigation Satellite System satellites are time delayed when passing through the atmosphere compared to the travel time they would need in the vacuum. The signal delay is a consequence of temporally and spatially distinctive and unpredictable atmospheric properties. This is the reason why the corresponding GNSS signal delay is also of random nature. With respect to GNSS signal propagation, the atmosphere is divided in a dispersive and a non-dispersive part, namely the ionosphere and the troposphere. Accordingly, ionospheric and tropospheric signal delays are defined. While the ionospheric delay can be eliminated almost completely either by the use of simultaneous observations on two or more frequencies, or by applying an ionospheric model, the tropospheric delay remains one of the major error sources in space geodesy.

The total tropospheric delay is interpreted as the signal delay between an observing station and the satellite caused by the neutral atmosphere and integrated over the whole ray path. To describe the tropospheric delay by a vertical delay model, it is usually integrated over a certain period of time and mapped from the line of sight to the zenith direction (zenith total delay, ZTD). The tropospheric delay of GNSS microwave signals is comprised of a hydrostatic component and a wet component. The zenith hydrostatic delay (ZHD) is usually modeled on the basis of temperature and pressure at the observing site which can be obtained either from a standard atmosphere model or from surface meteorological measurements. The zenith wet delay (ZWD) is then estimated as a difference between the observed zenith total delay and the zenith hydrostatic delay.

It is exactly the delay caused by the lower earth's atmosphere that is an important

additional data source for Numerical Weather Prediction (NWP). The symbiosis of two sciences, namely geodesy and meteorology, has been a trigger for a number of national and regional scientific projects in the area of GNSS meteorology over the past 20 years. Information about the tropospheric delay derived from ground-based GNSS systems for weather prognosis systems is of particular importance in areas with a rugged topography or in areas where insufficient meteorological instrumentation exists. GNSS derived tropospheric delays showed to be mapping the weather situation sometimes better than forecast systems, specially in periods of increased humidity (summer months) or in the case of rapidly passing weather fronts. This is because GNSS data is directly influenced by changes in humidity in the free atmosphere, whereas the data at the meteorological ground stations accounts for these changes with a considerable time delay.

On the other hand, accurate meteorological measurements of the air pressure are an important input for GNSS analysis, in particular for a very precise determination of the *a priori* hydrostatic part of the tropospheric delay which accounts for approx. 90% of total troposphere delay. *A priori* troposphere delays calculated by GNSS analysis software are usually based on a standard atmosphere model and do not account for local and seasonal pressure deviation. A correct modelling of the ZHD influences consecutively the ZWD estimates since they also cover contributions to the ZHD not captured by the *a priori* model. The difference in the remaining wet delay in the zenith direction can be up to several centimeters.

GNSS meteorology activities are traditionally based on a double-difference network approach where baselines between a known reference station and any other network station are built to assure a stable solution and eliminate the majority of error sources. The delivery of the tropospheric delay derived from a network solution with hourly resolution and accuracy of 5 mm in ZWD is shown to be achievable. Due to the demonstrated advantages for weather forecast provided by the assimilated GNSS delay information, many countries established an operational GNSS meteorology system. In Europe, for example, the project *EUMETNET EIG GNSS water vapour programme* (E-GVAP) started in 2004 with a goal to provide the GNSS derived tropospheric delay for an operational GNSS meteorology. In such a case we deal with very large networks along with an increased number of observations and computational demands. Hence an alternative processing technique such as Precise Point Positioning (PPP) has to be considered.

Precise Point Positioning is a positioning technique that uses un-differenced single- or dual-frequency pseudorange and carrier phase observations of a single receiver along with precise orbit and clock correction products to achieve a cm-level precision. The advantage of this zero-difference technique is that no regional correlations will be introduced as well as no reference station data is explicitly required for data processing. Independence of reference station data, i.e. the requirement of only one equipment set, makes this technique also cost effective compared to the classic relative technique. However, hardware biases (both from satellite and receiver), which cancel when forming observation differences in a relative positioning approach remain, and have to be accounted for carefully. Furthermore, the necessary models have to be made available by organizations like the International GNSS Service (IGS) or by regional reference station providers.

Understanding the used technology is a main prerequisite to fully exploit the possibilities of PPP. The most prominent currently active global navigation satellite systems, namely GPS and GLONASS, are presented in **Chapter 2**. Special emphasis is set on the modernization processes of the existing GNSS and advantages brought with the naissance of new global systems such as Galileo.

A detailed description of the Precise Point Positioning technique and the corresponding observation equations are the topic of **Chapter 3**. To achieve the ultimate accuracy level many error sources have to be accounted for. Each of the error sources influencing the desirable accuracy is thoroughly explained and a method to account for it or to eliminate it is presented. International services like IGS augment the GNSS by providing orbit and clock correction parameters, essential for any satellite positioning and navigation activities. In addition to aforementioned products, IGS provides earth rotation parameters, atmospheric parameters and observation data for more than 400 globally distributed sites. A short description of IGS and on-line processing services for PPP is given. The current state of PPP describing the accuracy, precision, availability, integrity and the convergence period is outlined at the end of this chapter.

Chapter 4 deals with delays caused by the earth's atmosphere. First, a short description of the ionospheric delay is given. Considering that a standard PPP model uses observations of at least two carrier frequencies, the impact of the ionosphere on signal propagation can be eliminated up to 99%. A similar procedure is not possible

in the case of the tropospheric delay. Therefore, this chapter describes in detail the properties of the troposphere and the techniques to account for it.

Assimilation of the GNSS derived tropospheric delays in a numerical weather model is presented in **Chapter 5**. This work is part of a project GNSSMET, a joint activity of Vienna Technical University, Institute of Geodesy and Geophysics and the Austrian Meteorological Agency, with the aim to provide near real-time estimation of tropospheric water vapour content from a ground-based GNSS network and to investigate its potential contribution to weather now-casting in Austria.

The achievable performance of the PPP technique in the area of troposphere monitoring is topic of **Chapter 6**. GNSS observations are gathered over several weeks at 18 sites in Austria and surrounding countries to examine the components influencing a tropospheric delay determination by means of a static zero-difference solution. The chapter is corroborated by a number of numerical results from a test network and accompanying illustrations.

Chapter 7 is dedicated to future improvements and possible applications of both the PPP technique and the troposphere monitoring. Some of the improvements are brought by modernization and novelties in GNSS, others by advances in positioning and tropospheric delay algorithms. The importance of the knowledge of GNSS derived tropospheric delay in the past several years has increased significantly, specially in the area of warning systems. An improved spatial and temporal resolution enabled by new signals will allow operating 3D- or 4D-tomography models.

The thesis ends with a summary of the presented work and concluding remarks (**Chapter 8**).

Chapter 2

Global Navigation Satellite System

2.1 Principles of satellite-based positioning

The launch of the first artificial satellite Sputnik in 1957 and the use of the Doppler shift as an observable represent the major breakthroughs for satellite-based positioning. Upon this early experiences and the knowledge of Kepler's laws, today's global navigation and positioning systems were developed. The three-dimensional position of a receiver is determined using principles of electromagnetic trilateration. Satellite-based

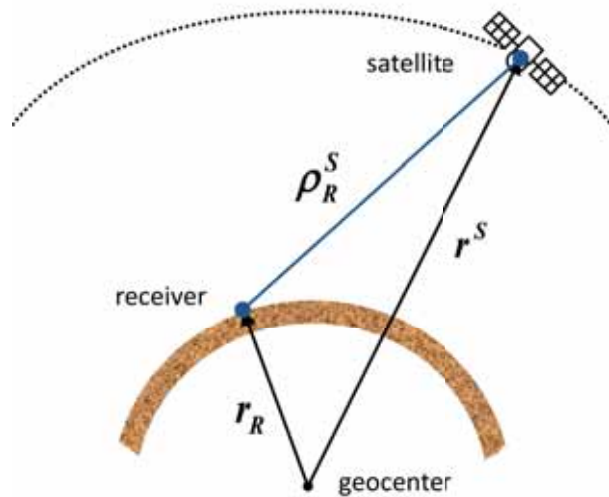


Figure 2.1: Satellite-based positioning

positioning relies on very accurate measurements of the period that a signal broadcasted by the satellite needs to reach the receiver on the ground, sea or in the air (or even space). The range ρ_R^S between satellite and receiver is calculated as follows

$$\rho_R^S = \|r^S - r_R\| = c \cdot \tau_R^S, \quad (2.1)$$

where r^S and r_R are the radius vectors from the geocenter to the satellite and the receiver, respectively (see Fig. 2.1), c is the speed of light and τ_R^S is the measured signal travel time. The signal travel time can be obtained either by code measurements, where a replica of the emitted code is generated at the receiver and compared to the received code, or by observing the phase of the carrier and comparing the received and receiver-generated signal. The time measurement is corrupted by satellite's and receiver's clock errors, hence we speak of *pseudoranges*. The satellite clock error, as well as the satellite position is transmitted within the broadcasted ephemerides, but receiver clock errors have to be calculated along with the receiver position. Therefore, observations from a minimum of four satellites are needed to successfully solve the observation equations. From Eq. (2.1) it becomes clear that the accuracy of the position of a single receiver will depend on the accuracy of the satellite position, accuracy of the pseudorange measurements and the geometry of the observed satellites.

2.2 Time systems

Precise determination of time is a prerequisite for a successful satellite-based positioning. Therefore, it is important to define the time systems (scales) used in satellite geodesy. Three basic groups of time systems, defined by specific periodic processes, are in use:

1. *Solar Time*, *Sidereal Time* and *Universal Time* UT, defined by the earth's rotation. They are used to relate earth- and space-fixed reference frames.
2. *Barycentric Dynamic Time* TDB and *Terrestrial Dynamic Time* TDT (or *Terrestrial Time* TT), derived from the planetary motions in the solar system. They are used to describe the motion of bodies in a gravitational field. Satellite's equation of motion are described in TDT.
3. *International Atomic Time* TAI, *Coordinated Universal Time* UTC and reference time in satellite-based positioning systems like *GPS Time*, derived from atomic oscillations.

The Universal Time (UT) is defined as the Greenwich hour angle of the mean Sun uniformly orbiting in the equatorial plane augmented by 12 hours. One mean solar day differs to a mean sidereal day by approx. 4 minutes. UT corrected by the effect of polar motion is denoted as UT1. The *International Atomic Time* (TAI, Temps Atomique International) was introduced as a strictly uniform time scale, where the unit of time was selected to equal the duration of the ephemeris second¹. The definition of the second of TAI is given by SI (International System of Units), and the time scale is maintained by the set of most accurate atomic clocks regulated by the International Bureau of Weights and Measures (BIPM). The epoch of TAI agrees with the epoch of UT1 on January 1, 1958. Because of the deceleration of the earth's rotation, the difference between the two time scales is increasing. For many applications the time scale providing the uniform time with the best possible adaptation to the earth rotation, hence the UT1, is needed. For that reason the UTC time scale was introduced with the SI second as the scale unit. The difference between UTC and UT1 is denoted as dUT1, and is reported by the IERS. When dUT1 becomes larger than 0.9 seconds a *leap second* is introduced. Therefore, UTC and TAI differ by an integer number of seconds:

$$\text{UTC} = \text{TAI} - n(1 \text{ s}). \quad (2.2)$$

From January 2009 onwards, the difference between UTC and TAI is 34 seconds.

Individual GNSS components (GPS, GLONASS, Galileo) maintain their own atomic time scales using different sets of atomic clocks. In the GNSS community the GPS Time (GPST) is usually the reference, even when observations from other satellite systems are captured. GPST was selected to coincide with UTC on January 5, 1980, thus it differs by an integer number to the UTC (today 15 s), and has a constant offset to TAI of 19 s:

$$\begin{aligned} \text{GPST} &= \text{TAI} - 19 \text{ s}, \\ \text{GPST} &= \text{UTC} - n(1 \text{ s}). \end{aligned} \quad (2.3)$$

Since TAI and GPST are two independently maintained time scales, there is a correction to the constant offset. The relation between GPST and UTC is included in time bulletins of the USNO and BIPM, as well as in the satellite message.

¹The ephemeris second is derived from the mean duration of the solar day between 1756 and 1895.

A graphic overview of the above described time scales is given in Fig. 2.2. The figure also includes the TDT (or TT), realized in practice by TAI with a constant offset of 32.184 s. Further details concerning the time scales and standards can be found in, e.g. Hofmann-Wellenhof *et al.* [2008], Xu [2003], Seeber [2003] or in IERS conventions (McCarthy & Petit [2004]).

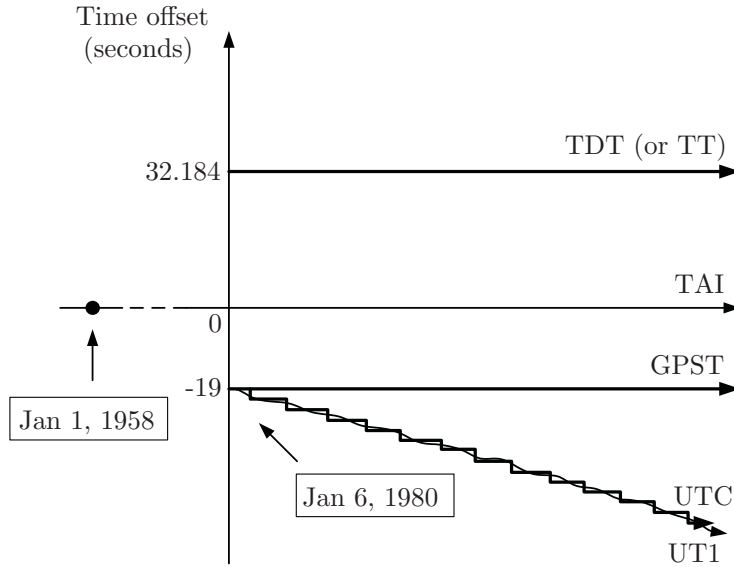


Figure 2.2: Relationships between time scales (*source: www.gmat.unsw.edu.au*)

2.3 Components of GNSS

Precise Point Positioning technique relies on the signal transmitted from one or multiple global navigation satellite systems such as the American GPS, the Russian GLONASS or the new-coming European system Galileo and the Chinese system Compass. It is now over 30 years since the first GPS satellite was launched. In the next years, when the four mentioned systems reach their full operational capability (FOC), it is expected to have over 100 GNSS satellites orbiting the earth and numerous signals available for different levels of services and applications. Moreover, the accompanying augmentation systems make the whole story even more overwhelming. Excessive descriptions and information about these systems have been given in numerous scientific books, articles and on-line services. Therefore in the following, solely a brief overview of GPS, GLONASS and Galileo, as well as GNSS modernization plans associated with each of them, is given.

GNSS modernization is driven by several circumstances: advances in technology, user requirements in performance, accuracy and applicability, market competition, to name a few. Modernized GNSS have two main goals: (1) improvements in performance, and (2) interoperability and compatibility between different satellite systems. It includes alteration in existing components such as GPS and GLONASS, as well as a dawn of new GNSS components like Galileo.

2.3.1 GPS

Overview

Initial activities in GPS development started already in 1973 by the Joint Program Office (JPO) directed by DoD with the goal to establish, develop, test, acquire and deploy a space-borne positioning system (Hofmann-Wellenhof *et al.* [2008]). An early definition of GPS is given by Wooden [1984]: *The Navstar Global Positioning System (GPS) is an all-weather, space-based navigation system under development by the Department of Defense (DoD) to satisfy the requirements for the military forces to accurately determine their position, velocity and time in a common reference system, anywhere on or near the earth on a continuous basis.* Originally designed to serve military purposes, the Navstar Global Positioning System (GPS) of the United States Department of Defense (DoD) became open for civil users in 1983, by a directive of US President Ronald Reagan.

The description of the GPS system is usually structured in three segments: a space, control and user segment. The space segment consists nominally of 24 operational satellites placed in six nearly circular orbits inclined by 55° with an altitude of about 20200 km above the earth and a revolution period of approx. 12 sidereal hours. In addition, several spare satellites are usually also operational. FOC of the system was declared in July 1995. With full constellation, the space segment provides four to eight simultaneously visible satellites above 15° on a global level. Lowering the elevation mask to 5° , 12 satellites can be simultaneously visible on occasion. Several types of satellites were developed until now: Block I, Block II, Block IIA, Block IIR, Block IIR-M, Block IIF. The Block IIR-M satellite type is part of space segment modernization program. The first satellite of this type was launched in March 2008. The first Block IIF satellite was launched in May 2010. The Block III satellite type is currently under studies and the first launch is expected in 2014.

The control segment of GPS includes a master control station, monitor stations

and ground antennas. The master control station is located in Colorado Springs, Colorado, USA and is responsible of satellite control and system operation. Five globally distributed monitor stations continuously measure pseudoranges to all visible satellites and forward data to the master control station for calculation of satellite orbit and clock parameters. Calculated ephemerides and clock informations are forwarded to ground antennas and uploaded to each GPS satellite three times per day to feed the navigation message.

There are two types of GPS users, namely military and civil users. The area of civilian application of GPS is vast and spreads over positioning, navigation, timing and controlling. Nevertheless, the main purpose of the system is determination of position and/or speed of a single user, on land, sea or air. The user type is also defined by the receiver properties, i.e. the type of signals the receiver is capable to observe. We can distinguish between single- or multi-frequency receivers, and their ability to receive pseudorange and/or carrier phase measurements. To further document these capabilities, basic information on the GPS satellite signal are required.

GPS satellite signal

The frequency standard of GPS signals is maintained by highly accurate atomic clocks with long-term frequency stability of a few parts of 10^{-13} to 10^{-14} per day. These clocks produce the fundamental frequency of 10.23 MHz. Two carrier waves L1 and L2 are generated by multiplying the fundamental frequency by 154 and 120, respectively. This yields the frequency of 1575.42 MHz and a wavelength of about 19 cm for carrier L1 and frequency of 1227.60 MHz and a wavelength of about 24 cm for carrier L2. The ranging codes and navigation messages are modulated onto the carriers. Different Pseudo Random Noise (PRN) codes are emitted from each GPS satellite revealing the code division multiple access (CDMA) principle. Three ranging codes are modulated on two carrier frequencies: a Coarse/Acquisition (C/A) code and a Precise (P1) code on carrier L1, and a Precise (P2) code on carrier L2. The C/A-code has an effective wavelength of approx. 300 m and defines the Standard Positioning Service (SPS), and the P-code with effective wavelength of approx. 30 m defines the Precise Positioning Service (PPS). Assuming a measurement resolution of 1% of the wavelength, this will lead to pseudorange uncertainties of 3 m for the C/A-code and 0.3 m for the P-code. For the carrier phase frequency the 1% resolution will result in 2 mm pseudorange uncertainties. Recent studies have shown that a precision of 0.1% of the chip length is possible.

The system depends on very accurate synchronization between codes of the same carrier frequency, the signals of two carrier frequencies and the synchronization of the signals from different satellites. An equipment group delay, the amount of time it takes the signal to travel from the frequency source to antenna phase center, is absorbed by the clock correction sent within the navigation message.

Several measures are undertaken to ensure the military advantages of the system. Two additional carrier frequencies L3=1381.05 MHz and L4=1379.913 MHz (Hofmann-Wellenhof *et al.* [2008]) are only used for military purposes. First field tests revealed that the accuracy of navigation was much better than predicted in the system design. Therefore two techniques are applied to restrict civilian use of the system. They are: Selective Availability (SA) and Anti-Spoofing (A-S). Selective Availability is achieved by two processes, namely the dithering of the satellite clock (δ -process) and manipulation of the orbital information (ϵ -process). The SA was turned off on May 2, 2000. Anti-Spoofing is accomplished by encrypting the precise code P by W-code, resulting in Y-code. This ensures access to the precise code only to military and other authorized users. The A-S is still active.

GPS modernization

The modernization of GPS covers all three system segments: space, ground and

Carrier	Factor ($\cdot f_0$)	Frequency [MHz]	Wavelength [cm]	PRN codes
L1	154	1575.42	19.0	C/A
				P
				M
				L1C
L2	120	1227.60	24.4	L2C
				P
				M
L5	115	1176.450	25.5	L5C
				L5I
				L5Q

Table 2.1: GPS signal modernization

user segment. However, special emphasis is given to the modernization of the signals (Tab. 2.1). With respect to the space segment, the modernization process started

already with the launch of the first Block IIR-M satellite which carries the new civil L2C-code modulated on the L2 frequency and the new military M-code on both L1 and L2. Today there are eight Block IIR-M satellites in space (one of those is in commissioning phase). FOC of L2C- and M-code satellites are expected in 2015. The addition of a new civil L5 carrier and a on-board inertial navigation system is the main highlight of the Block IIF satellites. The first satellite was launched in May 2010 and the FOC is not expected before 2019. The addition of a new L5 carrier opens a wide range of possible carrier phase combinations, and will especially be useful for ionosphere-free combination and ambiguity resolution. The next generation of GPS should rely on Block III satellites which also include new civil code on L1 carrier. Development and design of GPS III is still in process, and will include changes in the architecture of the whole system. Overall improvements are expected in the performance and life-span of the new satellite vehicles. Main improvements in ground segment should be in reducing the operational costs while enhancing the system performance. This will also include six new monitor stations and one alternative master control station. For the user segment, aside from advantages provided with new carriers and codes, the modernized system will provide an improved accuracy, availability, reliability and integrity.

GPS reference systems

GPS coordinates are defined in the terrestrial reference system WGS-84 (World Geodetic System 1984). The associated reference geocentric ellipsoid is represented by four parameters: semi-major axis a , flattening of the ellipsoid f , angular velocity of the earth ω_e and the earth's gravitational constant μ . There have been several realizations of the WGS-84 system. The current one, WGS-84 (G1150), is aligned to the current ITRF solution (i.e. ITRF2008) with insignificant systematic errors in the order of ± 1 cm. The time system is defined by GPS Time (see Sect. 2.2), which has a constant offset of 19 seconds to the international atomic time TAI and coincides with the UTC time scale on January 6, 1980. TAI and UTC time scales differ by an integer number of seconds, which is regularly reported by IERS. In 2010, the difference between UTC and GPS time equals 15 seconds.

2.3.2 GLONASS

Overview

The Russian satellite system GLONASS (GLObalnaya NAVigatsionnaya Sputnikovaya Sistema) is a sort of reply to the American GPS system. Similar to GPS, GLONASS is also established as a military system. This is the reason why no system information was available to the public until 1988, although the system development was initiated already in the 1970s. In 1995 the system was opened for civil use. FOC of 24 satellites was achieved in January 1996, but due to funding issues, the system reached a number of only six satellites in 2001. Today, 21 satellite (plus two spare) are operational.

The GLONASS space segment consists of nominally 21 (plus three spare) satellites placed in three circular orbital planes with an inclination of 64.8° and a revolution period of 11h 15min 44s. Satellites orbit at the altitude of 19100 km above the earth's surface. At least five satellites are simultaneously visible on 99% of the earth's surface if the full constellation is fulfilled. Currently, two types of satellites are in use, namely GLONASS and GLONASS-M, and the next generation is foreseen to be GLONASS-K and (still in design phase) GLONASS-KM satellite series. The ground segment is located in Russia or in former USSR countries. It consists of a System Control Center located in Krasnoznamensk Space Center, the center for GLONASS system time synchronization at Schelkovo, four TT&C (telemetry, tracking and control) stations and additional five tracking stations. To improve the accuracy of broadcasted GLONASS ephemeris and to improve the availability and integrity monitoring, the first station outside the Russian territory, the one on the Antarctica, is installed in 2010. Further ground segment modernization steps include the improvement of the overall performance of the system and further refinement of the GLONASS time and coordinate reference systems.

GLONASS satellite signal

Similar to GPS, GLONASS emits signals on two carrier frequencies on which the navigation message and two ranging codes are modulated: the standard-accuracy signal (C/A) on carrier G1¹ and the high-accuracy signal (P) on both carriers. However, GLONASS makes use of FDMA (Frequency Division Multiple Access) technology, which means that the satellites are identified according to their unique

¹To avoid confusion GPS signals will be denoted with “L”, GLONASS signals with “G” and Galileo signals with “E”.

carrier frequencies defined by

$$\begin{aligned} G1 &= 1602.0 + 0.5625k \text{ [MHz]}, \\ G2 &= 1246.0 + 0.4375k \text{ [MHz]}, \end{aligned}$$

where k indicates the frequency channel. FDMA design also implies that the PRN sequences are common to all satellites.

Only the standard-accuracy signal (C/A-code) is specified in the interface control document whereas the high-accuracy signal (P-code) is reserved for military purposes. P-code is unencrypted; however, it is subject of unannounced changes and its use is not recommended. C/A-code has a chip length of about 587 m and P-code about 59 m (Hofmann-Wellenhof *et al.* [2008]).

GLONASS modernization

The central highlight of the GLONASS system modernization is an addition of CDMA to FDMA technology. This will greatly improve the interoperability of GLONASS with other satellite systems and ease the troubles with ambiguity resolution. The new generation of GLONASS-K satellites should also include a signal on the third carrier¹ and addition of a second civil signal on G2 (Tab. 2.2). Overall improvements are expected in the space segment related to longer design lifetime, improved navigation message, improved clock stability and providing an integrity information (Hofmann-Wellenhof *et al.* [2008]). Nominal constellation is expected to be increased to 30 satellites, which requires improvements within the ground segment, too (Gibbons [2008]).

Carrier	Frequency [MHz]	Increment [MHz]	Wavelength [cm]	PRN codes
G1	1602.000	0.5625	18.7	C/A
				P
G2	1246.000	0.4375	24.1	C/A
				P
G3	1204.704	0.4230	24.9	C/A ₂
				P ₂

Table 2.2: GLONASS signal modernization

¹subject to change

GLONASS reference systems

The GLONASS terrestrial reference frame PE-90 (PZ-90) is defined by reference geocentric ellipsoid parameters and realized by 26 ground stations measured using different geodetic techniques. A comparison to ITRF solution carried out within the International GLONASS Experiment (IGEX-98) campaign in 2002 reveals significant differences, especially in the Z component. According to the Russian Federation government decree issued on June 20, 2007, the improved version of the national geocentric coordinate system PZ-90.02 has been applied to GLONASS. The transformation between PZ-90.02 and ITRF2000 contains only origin shifts along X, Y, Z by -36, +8, and +18 centimeters, respectively (Engelsberg *et al.* [2008]).

A set of hydrogen masers is used for GLONASS time maintenance. The GLONASS time scale is aligned with UTC time within 1 millisecond, hence includes the leap seconds; however, it contains a constant offset to UTC of 3 hours due to the Moscow time zone. A systematic time bias between GLONASS Time and UTC, originating from the keeping of the time scales by different clocks, is included in the navigation message.

2.3.3 Galileo

Overview

The European system Galileo is a joint initiative of the European Commission (EC) and the European Space Agency (ESA). Galileo is a civil navigation satellite system with the European Union responsible for legal and political issues and the ESA managing the technical part of the program.

First steps toward European activities in space navigation were taken in the 1980s, when ESA examined several possibilities and concepts. Finally, a two step approach was selected: first, an augmentation system to the existing GNSS was developed resulting in the geostationary navigation overlay system EGNOS, and second, the global navigation system for civil use will be deployed. Galileo is envisaged as an open, global system fully compatible with the existing GNSSs but independent of them, with high level of service reliability. The economic and social benefits of such a system were instantly recognized and included transportation, communication, energy, environment and many other sectors.

The Galileo program is divided in four phases: (1) the definition phase, (2) the development and in-orbit validation (IOV) phase, (3) the deployment phase, and (4) the operation phase. Currently the program is in phase 2, with two Galileo in-orbit validation elements (GIOVE) satellites in space to analyze the achievable performance and to secure the allocated frequency bands. Four more test satellites will be launched to validate the main components of the system before the deployment phase begins. A reduced FOC of Galileo, containing 18 satellites, is to be deployed by 2014. The deployment of the full constellation will be shifted by a couple of years.

Once in full operation phase, Galileo should offer nominally 27 (plus three spare) satellites in three orbital planes inclined by 56° and orbiting at 29600 km altitude above the earth, with a revolution period of 14h 4min 45sec. This satellite constellation guarantees six visible satellites at any time, anywhere on the earth, with an elevation mask of 10° . The Galileo satellites are the first GNSS satellites carrying the hydrogen maser clocks in space, offering up to now an unprecedented frequency stability. The space segment is supported by the ground infrastructure composed of two ground centers (in Germany and in Italy), five TT&C stations, nine C-band mission uplink station and 20–25 planned Galileo sensor stations distributed worldwide. The design of the system is service-oriented, and three basic categories can be listed:

- the global satellite-only service relying solely on Galileo signals. This category can be subdivided in: (1) open service (OS), (2) commercial service (CS), (3) safety-of-life service (SoL), and (4) public regulated service (PRS).
- Galileo + EGNOS service enhancing local performance and providing maximum integrity.
- Galileo in combination with other GNSS.

This concept defines additionally three Galileo segments: global, regional and local. Galileo will contribute to the international COSPAS-SARSAT cooperative system for humanitarian search and rescue activities. Each satellite will be equipped with a transponder transferring distress signal from users to the Rescue Coordination Center.

Galileo satellite signal

Galileo signals are based on the fundamental frequency of $f_0 = 10.23$ MHz. They cover in total five frequency bands: E1, E6, E5, E5a and E5b. A number of ranging codes and navigation messages are modulated onto these signals. Each Galileo satellite will broadcast ten different navigation signals making it possible for Galileo to offer open

(OS), safety-of-life (SoL), commercial (CS) and public regulated services (PRS)¹. A large variety of signals will allow improvements in GNSS algorithm and satisfy needs of a large spectrum of users. Galileo signal components, related PRN codes and navigation messages are listed in Table 2.3. It can be noticed that two Galileo signals, E1 and E5a, coincide with GPS signals, and E5b overlays with the future GLONASS carrier G3. This has been chosen on purpose to increase the interoperability with existing GNSS. To avoid interference of signals from different satellite systems, a different modulation scheme was chosen for Galileo. The implemented scheme is called BOC(1,1), meaning Binary Offset Carrier of rate (1,1). This kind of modulation allows GPS and Galileo signals to occupy the same frequency ranges while avoiding mutual interference, and enables the building of receiver hardware capable of receiving signals on the same frequency bands from different satellite system. Of exceptional importance will become the utilization of the new broadband AltBOC(E5) signal which promises a reduced noise level and an optimal resistance against the multipath.

Carrier	Factor ($\cdot f_0$)	Frequency [MHz]	Wavelength [cm]	PRN codes	Navigation message
E1	154	1575.420	19.0	E1A	PRS (G/NAV)
				E1B	OS/CS/SoL (I/NAV)
				E1C	
E6	125	1278.750	23.4	E6A	PRS (G/NAV)
				E6B	CS (C/NAV)
				E6C	
E5	116.5	1191.795	25.2		
E5a	115	1176.450	25.5	I	OS (F/NAV)
				Q	
E5b	118	1207.140	24.8	I	OS/CS/SoL (I/NAV)
				Q	

Table 2.3: Galileo signals (G/NAV - Governmental nav. message, F/NAV - Freely accessible nav. message, I/NAV - Integrity nav. message, C/NAV - Commercial nav. message)

Galileo reference systems

The coordinate frame of Galileo is defined as Galileo terrestrial reference frame (GTRF) and will be closely aligned with the ITRF solution ($< \pm 3$ cm). The time

¹http://www.esa.int/esaNA/SEM86CSMD6E_galileo_0.html

system is maintained by a set of atomic frequency standards with hydrogen maser clocks as master clocks. Similar to GPS, the Galileo system time (GST) will have a constant offset to the international atomic time (TAI). The offset of GST to TAI and UTC time will be broadcasted to the users via the navigation message.

2.4 GNSS modernization on user level

Multi-constellation availability promised with GNSS modernization requires alteration and modification of several user-related domains.

Particular care should be paid to providing reliable inter-system offsets, namely the inter-system time system offset and the inter-system coordinate system offset, along with respective biases and transformation parameters. The modernized navigation message from each of the global satellite systems should include a time offset and coordinate system transformation parameters to other systems. Also, the differential code- and phase-biases should be investigated in detail and provided by international organizations like the International GNSS Service (IGS).

An increased number of systems, signals and observations demands an alteration in the receiver architecture, both in hardware — number of channels, antenna type, signal-tracked, etc. — and in software — application of transformation parameters and delivery of coordinates in one system frame (probably GPS). Exchange data formats such as RINEX (Receiver INdependent EXchange format¹) or SP3 (Standard Product v.3²) should be adjusted to cover new signals. Along with new GNSS features, the existing GNSS analysis softwares should include the updated routines for processing the new signals.

¹<ftp://ftp.unibe.ch/aiub/rinex/rinex300.pdf>

²http://www.ngs.noaa.gov/orbits/sp3_docu.txt

Chapter 3

Concept of Precise Point Positioning

Precise Point Positioning (PPP) is a positioning technique that uses un-differenced single- or dual-frequency pseudorange and carrier phase observations of a single receiver along with the precise orbit and clock products to achieve a cm-level precision. The concept of PPP was first introduced in the 1970's by R.R. Anderle, and was characterized as a single station positioning with fixed precise orbit solutions and Doppler satellite observations (Kouba & Hèroux [2001]). Nevertheless, the relative positioning has dominated the field of GPS data processing until the late 1990's, when the Jet Propulsion Laboratory (NASA) showed that the achievable precision of PPP can be comparable to the one from relative positioning and implemented this new technique in their GIPSY/OASIS-II GPS processing software (Zumberge *et al.* [1997]). The PPP technique, however, should not be confused with the Single Point Positioning (SPP) technique. SPP uses the broadcasted instead of precise orbit and clock correction products, and only the pseudorange observations are used. Consequently, the achievable positioning accuracy for a static receiver provided by SPP is on the 1–10 m level, whereas PPP can give coordinates at the cm-level in accuracy with 24 hours of observations for a static receiver.

The beauty of this zero-difference technique is that no regional network correlations will be introduced as well as no reference station data is explicitly required for data processing. This allows to check the consistency of the introduced orbit, clock and atmosphere error models. Omitting the building of baselines significantly reduces the required processing time compared to the network (baseline) solution. On the

other hand, hardware biases, both from satellite and receiver, remain and have to be accounted for carefully and the necessary error models have to be made available by global or regional services.

3.1 Observation equations

The un-differenced observation equations for code $P_{R,i}^S$ and carrier phase $L_{R,i}^S$ measurements in metric units read

$$P_{R,i}^S = [\vec{r}_R(t_R) - \vec{r}^S(t_R - \tau_R^S)] + c\Delta t_R - c\Delta t^S, \quad (3.1)$$

$$L_{R,i}^S = [\vec{r}_R(t_R) - \vec{r}^S(t_R - \tau_R^S)] + c\Delta t_R - c\Delta t^S + \lambda_i N_{R,i}^S, \quad (3.2)$$

where \vec{r}_R is the station geocentric vector at the time¹ of signal reception t_R , \vec{r}^S is the geocentric vector to the satellite at the time of signal emission $t^S = t_R - \tau_R^S$ with τ_R^S being the signal travel time between satellite S and receiver R . i indicates the carrier frequency. The true geometric distance between satellite and receiver ρ_R^S , expressed in the square brackets as

$$\rho_R^S = [\vec{r}_R(t_R) - \vec{r}^S(t_R - \tau_R^S)], \quad (3.3)$$

adulterated with an offset caused by satellite and receiver clocks ($c\Delta t^S$ and $c\Delta t_R$, respectively) gives finally the observed pseudorange $P_{R,i}^S$. The carrier phase measurements $L_{R,i}^S$ have to additionally account for the ambiguity factor $\lambda_i N_{R,i}^S$, with λ_i being the wavelength of the respective carrier i and $N_{R,i}^S$ the number of full carrier cycles between satellite and receiver.

In addition to clock errors there are a number of additional corrections that need to be applied to pseudorange and carrier phase observations. To achieve the ultimate PPP accuracy a correction of error effects up to the mm-level is needed. Many of these error sources are safely neglected or differenced out in the relative processing mode. The error effects can be grouped in satellite specific corrections, receiver specific corrections, site specific effects and signal propagation errors. Considering this, the

¹In GNSS analysis, the time stamps (reception time, emission time) are always given in, or relative to the GPS time scale, even when observations from other satellite systems are used. This requires the conversion of the time of other systems to the GPS system time.

observation equations (3.1) and (3.2) will adopt the expanded form as follows

$$P_i = \rho + c\Delta t_R - c\Delta t^S + \Delta\rho_{iono,i} + \Delta\rho_{tropo} + \Delta\rho_{rel} + \Delta\rho_{mp,i} + c\beta_R + c\beta^S + \epsilon_{P,i}, \quad (3.4)$$

$$\begin{aligned} L_i = & \rho + c\Delta t_R - c\Delta t^S - \Delta\rho_{iono,i} + \Delta\rho_{tropo} + \Delta\rho_{rel} + \Delta\rho_{mp,i} + \lambda_i w + \Delta\rho_{pcv,i} \\ & + \lambda_i \alpha_{R,i} + \lambda_i \alpha_i^S + \lambda_i N_i + \epsilon_{L,i}, \end{aligned} \quad (3.5)$$

where

P_i and L_i stand for code and phase measurements, i noting the frequency,

ρ is a geometric distance between satellite and receiver,

$c\Delta t_R$ and $c\Delta t^S$ are receiver and satellite clock corrections multiplied with the speed of light c ,

$\Delta\rho_{iono,i}$ is a frequency dependent ionospheric delay,

$\Delta\rho_{tropo}$ is a range correction due to tropospheric refraction,

$\Delta\rho_{rel}$ is a range correction due to relativistic effects,

$\Delta\rho_{mp,i}$ is a frequency dependent delay due to multipath,

β_R and β^S are code biases for the receiver and the satellite,

$\lambda_i \alpha_{R,i}$ and $\lambda_i \alpha_i^S$ are phase biases for the receiver and the satellite, multiplied with the respective wavelength λ_i ,

w is a phase wind-up correction,

$\Delta\rho_{pcv,i}$ is a frequency dependent delay due to the phase center variation,

N_i is the ambiguity for the respective frequency i , and

$\epsilon_{P,i}$ and $\epsilon_{L,i}$ are the remaining un-modeled errors and white noise for the code and the phase measurements.

For Precise Point Positioning, the satellite's position is held fixed or tightly constrained, therefore no orbital error is assumed. However, the accuracy of the applied orbits limits the accuracy of PPP. Furthermore, the satellite clock corrections provided by, e.g. IGS are also introduced as known. Signal propagation errors will be explained in detail in Chapter 4, and are therefore omitted in the following section. The remaining effects listed in the Eqs. (3.4) and (3.5) are explained hereafter.

3.2 Precise Point Positioning correction model

3.2.1 Relativistic effects

The GNSS technology is based on very stable and accurate clocks on board the satellites and in the ground receivers¹. Their synchronization is of the utmost importance for a proper operation of the system. However, the time transfer between satellite and ground receiver is affected by relativistic effects. The GPS receiver time t (after applying the clock corrections) observed at the ground is obtained as

$$t = t^S - \Delta t_{rel}, \quad (3.6)$$

where t^S is the time on board the satellites either calculated from the coefficients included in the broadcast message, or given in the IGS clock solution files (Kouba [2004]). The relativistic correction of time Δt_{rel} is divided into a constant Δt_{con} and a periodic Δt_{per} correction, i.e.,

$$\Delta t_{rel} = \Delta t_{con} + \Delta t_{per}. \quad (3.7)$$

The constant relativistic components originates from two effects: the gravitational field affecting the satellites (General Relativity effect) and the speed of satellites causing a clock displacement (Special Relativity effect). These effects are causing a frequency shift from the nominal frequency $f_0 = 10.23$ MHz as indicated in the following expression:

$$\frac{\Delta f}{f_0} = \frac{f - f_0}{f_0} = \frac{v^2}{2c^2} + \frac{\Delta U}{c^2} = \frac{v^2}{2c^2} + \frac{GM_E}{c^2} \left(\frac{1}{r_S} - \frac{1}{r_E} \right). \quad (3.8)$$

Here, v represents the satellite clock velocity with respect to ground receiver clock, c is the speed of light in vacuum and ΔU is the difference between the gravitational potential of the satellite's orbit and the geoid. This potential difference can be rewritten using the gravitational constant G and the mass of the earth M_E multiplied by a term $(1/r_S - 1/r_E)$. r_S is the distance from the center of the earth to the satellite and r_E is the radius of the earth. For GPS satellites this will lead to

$$\frac{\Delta f}{f_0} = 446.47 \cdot 10^{-12}. \quad (3.9)$$

¹Satellite clocks are by a factor ≈ 1000 more stable than ground receiver clocks, except in the case of ground hydrogen maser clocks.

The integration of Eq. (3.9) over one day yields the clock correction value of 38.58 microseconds. The effect of General Relativity causes the faster run of the clocks as the altitude of the satellites increases. The value of this effect is approx. 45 microseconds per day. On the other hand, the effect of the Special Relativity indicates that the clocks moving with higher velocity run slower than the clocks with smaller relative velocity. This leads to values of approx. 7 microseconds per day. In order that the satellite-transmitted nominal frequency of 10.23 MHz is received at the ground, the satellite's clocks are adjusted lower in frequency of 10.22999999543 MHz. The effect of General and Special Relativity is in general not equal for all satellites as it accounts for slight rate changes of the clock with respect to the changes in the value of a semi-major axis a_0 .

The periodic correction in the Eq. (3.7) is caused by the eccentricity of the satellite's orbit and includes the effect of the orbital perturbation. The eccentricity of each satellite's orbit causes the periodic clock error effect Δt_{ecc} that varies with the satellite's position in its plane (Ashby [2003]). This effect has an amplitude of about 46 ns for the GPS satellites with maximum eccentricities of 0.02. The correction is derived as follows:

$$\Delta t_{ecc} = 2\vec{r} \cdot \vec{v}/c^2, \quad (3.10)$$

where \vec{r} and \vec{v} are the satellite's radius vector and the velocity vector, respectively. The Eq. (3.10) can also be written as

$$2\vec{r} \cdot \vec{v}/c^2 = \frac{2\sqrt{GM_E a}}{c^2} e \sin(E) = 4.4428 \cdot 10^{-10} e \sin(E(t)) \sqrt{a}, \quad (3.11)$$

e being the satellite eccentricity and E the eccentric anomaly. The second periodical component, caused by the orbital perturbation due to the oblateness term $J_2 = 1.083 \cdot 10^{-3}$. It can be written:

$$\delta \Delta t_{per} = -\frac{a_E^2}{2a^2 c^2} J_2 [3\sqrt{GM_E} a \sin^2(i) \sin(2\omega_0 + 2nt) - 7\frac{GM_E}{a} (1 - \frac{3}{2} \sin^2(i)) t], \quad (3.12)$$

where a_E and a are the semi-major axis of the "mean" earth and the satellite, respectively, i indicates the inclination of the satellite, ω_0 is the unperturbed argument of perigee and n is the mean angular velocity of satellite. t indicates the elapsed time. Earth's oblateness causes a periodic fractional frequency shift with a period of almost 6 hours and an amplitude of $\frac{\Delta f}{f_0} = 6.95 \cdot 10^{-15}$.

The Sagnac effect is another correction to be accounted for and it is caused by the earth's rotation during the signal's transmission time. The correction of the signal's travel time due to this effect can be written as

$$\delta t = \frac{\vec{v} \cdot (\vec{r}_R - \vec{r}_S)}{c^2}, \quad (3.13)$$

where \vec{v} represents the geocentric velocity vector of the receiver, and \vec{r}_R and \vec{r}_S are geocentric vectors of the receiver and the satellite, respectively. This effect can reach up to 30 m (Xu [2003]). The relativistic correction due to the eccentricity of the satellite's orbit and due to the Sagnac effect have to be taken into account within the receiver software.

There are several additional relativistic effects to be considered when aiming at cm-level accuracy. The signal propagation delay, also known as Shapiro delay, is caused by changes in the light's velocity when it is exposed to the earth's gravitational field. The Shapiro time delay as measured by clocks at rest on the earth's geoid can be expressed as follows

$$\delta t = \frac{2GM_E}{c^3} \ln \left[\frac{r^S + r_R + \rho}{r^S + r_R - \rho} \right], \quad (3.14)$$

with r^S and r_R being the distance from the earth's center to the satellite and receiver, respectively, and ρ being the geometric distance between satellite and the receiver. The effect can reach up to a few cm, and in double-difference approach it is differenced out. However, in case of PPP it should be taken into account.

The effect of General and Special Relativity, known as the "factory offset", is applied to satellite clocks prior to the satellite vehicle (SV) launch. The *proper time*, i.e. the time maintained by the atomic clocks on-board the SVs, used for the signal generation, has to be aligned to GPS Time (in case of GPS). This error (bias) originates in the time keeping by different set of clocks. The correction is known as the satellite clock correction, and it is broadcasted along with the satellite ephemeris. All the remaining relativistic corrections have to be applied later on by the receiver software or the GPS analysis software.

3.2.2 Satellite antenna phase center offset and variation

Satellite coordinates refer to the satellite's center of mass. On the other hand, the signal transmission and therefore the phase measurements are related to the satellite's antenna phase center, hence the offset to the satellite's center of mass and orientation of the offset vector have to be known.

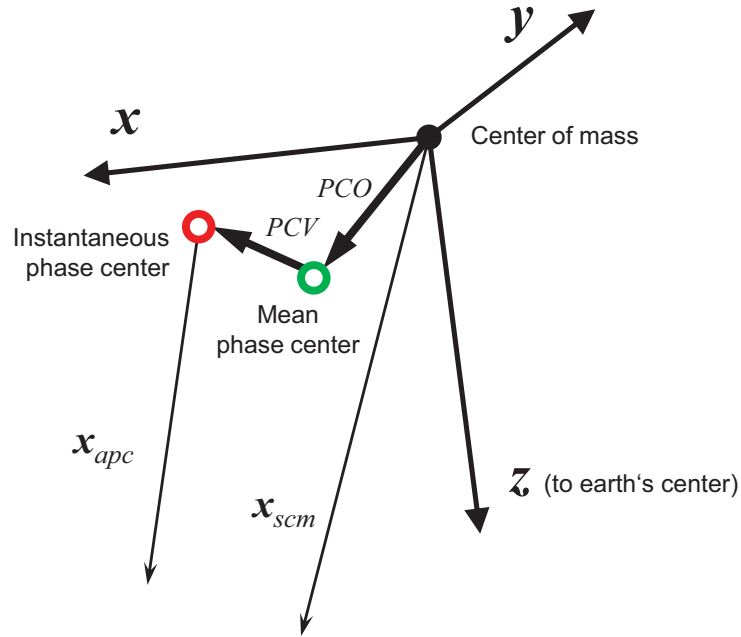


Figure 3.1: Satellite antenna phase center offset and variation

The satellite antenna phase center offset is described using a satellite-fixed coordinate system (Fig. 3.1). The origin of this system is the satellite's center of mass. The z -axis is pointing to the earth's center, the y -axis lays in the plane perpendicular to the vector pointing to the sun, and the x -axis is chosen to complete the right-handed coordinate system. Estimated z -offsets reach values between 0.5 m and 2.65 m for GPS satellites and between 1.80 m and 2.40 m for GLONASS satellites. The antenna phase center offset (PCO) has to be known for each satellite antenna type, and it is usually accounted for in the calculation using a publicly available satellite information file (e.g. ANTEX¹ file igs05.atx available at IGS ftp server²).

¹<ftp://igscb.jpl.nasa.gov/pub/station/general/antex13.txt>

²<ftp://igscb.jpl.nasa.gov/pub/station/general/igs05.atx>

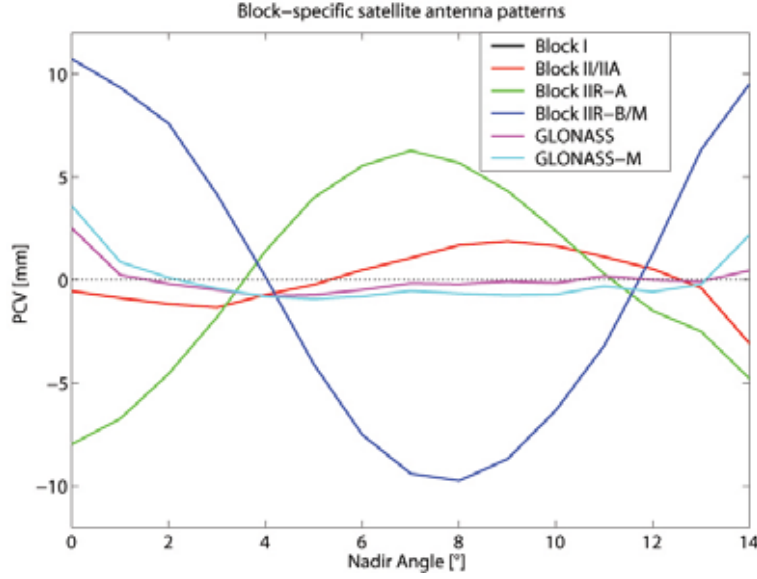


Figure 3.2: Satellite antenna pattern for GPS and GLONASS satellites (*source: Astronomical Institute, Bern*)

The position of the satellite's antenna phase center vector \vec{x}_{apc} with respect to the satellite's center of the mass vector \vec{x}_{scm} is given by

$$\vec{x}_{scm} = \vec{x}_{apc} + \overrightarrow{PCO} + \overrightarrow{PCV}. \quad (3.15)$$

Additionally to the PCO, each antenna type has a variable offset relative to the mean antenna reference point — phase center variation (PCV). The block-specific satellite patterns are shown in Fig. 3.2. GPS satellite antenna patterns show variations as functions of the nadir angle of the transmitted signal of up to 1 cm, which are not negligible for high precision positioning. GLONASS satellite antenna patterns show a much lower variation. All PCV values of satellite antennas for each frequency with respect to nadir angle are stored in the ANTEX formatted file available on the IGS ftp server.

3.2.3 Receiver antenna phase center pattern

As in the case of the satellite's antenna phase offset, the receiver's antenna reference marker and the receiver's antenna phase center are spaced. Additionally to this an-

tenna dependent offset, the correction for the antenna phase center variation accounts for a signal direction and the frequency dependence. Furthermore, radomes that are used for the GNSS receiver antennas influence the antenna phase center variations. These corrections are generally obtained through a calibration and are listed in a publicly available file. Until the GPS week 1400 (November 5th, 2006), the *relative* antenna phase center model (IGS_01) was used with respect to reference antenna AOAD/M.T. This model omitted the antenna radomes and the azimuthal dependence and only elevation dependent corrections were introduced. Since the GPS week 1400, the *absolute* antenna phase center model based on robot- or anechoic chamber-calibrated receiver's antenna phase center variations is used. This model considers the azimuthal dependence and in addition allows to account for the impact of different antenna radomes (Dach *et al.* [2007]). The term *absolute* indicates independence of a reference antenna. However, the azimuth and the zenith dependent PCV values are determined by differencing the measurements of the same satellite signal on two days where the first day's measurement is regarded as a "zero position", and on the second day the antenna was tilted and rotated (Hofmann-Wellenhof *et al.* [2008]). Differenced observation indicate that the term "absolute" in this case can be misleading.

3.2.4 Phase wind-up correction

The phase wind-up effect affects the carrier phase measurements due to the change in the relative orientation between the transmitting and the receiving antenna. The effect originates in the properties of the electromagnetic signal emitted from the satellites. The GNSS signals are right hand circularly polarized (RHCP) signals and therefore highly dependent on rotations of the antennas. In the case of static measurements, the effect is mainly due to the motions of the satellite. These motions are usually slow and small, except in the case of eclipse and noon season when the satellite undergoes rapid maneuvers. In the kinematic measurement mode, this effect is usually due to the motion of the receiver's antenna and its rotation around its bore sight axis (Le & Tiberius [2007]).

One clockwise rotation along the axis of sight between the satellite and the receiver (as seen from the satellite) in the sense of polarization of the signal causes an apparent increase of the distance. On the other hand a clockwise rotation in the receiver's body frame (latitude, longitude, height) causes an apparent decrease of the distance. The wind-up effect can reach up to one wavelength (about 20 cm). In the double-difference mode and with shorter distances (baselines up to few hundreds of kilometers), this

effect is usually canceled, as it is similar for both receiver antennas. For longer baselines and specially for PPP, this effect has to be modeled. Neglecting the wind-up and fixing orbits and clocks can lead to positioning errors on dm-level (Bisnath *et al.* [2007]).

The phase wind-up can be derived using formulas by Wu *et al.* [1993] as follows

$$\delta\phi = \text{sign}(\xi)\cos^{-1}(\vec{D}' \cdot \vec{D}/(|\vec{D}'||\vec{D}|)), \quad (3.16)$$

where $\xi = \vec{k} \cdot (\vec{D}' \times \vec{D})$. \vec{k} is the satellite-to-receiver unit vector and \vec{D}' , \vec{D} represent the effective dipole vectors of the satellite and the receiver, computed from the unit vectors of the satellite's (\vec{x}' \vec{y}' \vec{z}') and the receiver's (\vec{x} \vec{y} \vec{z}) body coordinate system. The expressions for the effective dipole vectors are

$$\begin{aligned} \vec{D}' &= \vec{x}' - \vec{k}(\vec{k} \cdot \vec{x}') - \vec{k} \times \vec{y}', \\ \vec{D} &= \vec{x} - \vec{k}(\vec{k} \cdot \vec{x}) - \vec{k} \times \vec{y}. \end{aligned} \quad (3.17)$$

3.2.5 System biases

GNSS observation data suffer from hardware biases originating both from the satellites as well as from the receivers. These biases can be sub-categorized as follows:

1. inter-frequency biases,
2. intra-frequency biases, and
3. inter-system biases.

Currently operational GNSS systems emit signals on at least two frequencies. The GNSS modernization promises an increase of the number of frequency bands for the current systems and introduces the new multi-frequency satellite systems. In cases of precise time transfer, precise point positioning, ionosphere mapping and other time-oriented application of GNSS, it is necessary to apply the corrections both for inter- and intra-system biases. In a positioning scenario, the receiver's biases are usually absorbed by the receiver clock correction parameter in the adjustment as long as only one type of observable is being used, thus only satellite's biases have to be taken into account (Leandro *et al.* [2007]).

The inter-frequency bias is an issue for ionospheric delays estimation when signals of at least two frequencies are used. Also single-frequency users who rely on the

IGS satellite clock and orbit products computed using the ionospheric-free $L3$ linear combination, have to account for these biases to allow for consistency in the time transfer. Intra-frequency biases are an issue if a network containing different receivers is processed, or in the single receiver scenario, if the particular intra-frequency combination is used in the satellite's clock computation (Leandro *et al.* [2007]).

The code observation data suffer from differential code biases (DCB). For the GPS system, these biases are given with respect to C1, P1 and P2 signals. Therefore, it is important for the user to be aware of the type of the signals captured by the used receivers. Note that the DCB values are not absolute; they are estimated based on a zero-mean condition using a globally distributed network of the stations, and are therefore shifted by an arbitrary offset B_0 .

There are two types of DCBs to be applied for GPS code observables: inter-frequency bias B_{P1-P2} and intra-frequency bias B_{P1-C1} . The first one is related to a group delay differential, τ_{GD} provided in the navigation message, by the following relation:

$$\tau_{GD} = -1.55B_{P1-P2} + B_0, \quad (3.18)$$

where B_0 is the aforementioned offset (Dach *et al.* [2007]). According to ICD-GPS-200C, precise and broadcasted clock products contain the ionosphere-free linear combination of B_{P1} and B_{P2} biases as follows

$$2.55B_{P1} - 1.55B_{P2} \quad (3.19)$$

Therefore, it is not necessary to apply this DCBs when using $L3$ linear combination and when the IGS clock products are held fixed or are constrained. However, the code observations still have to be corrected for the B_{P1-C1} DCBs. The DCB correction files are published regularly and available for download from e.g. the CODE analysis center ftp server¹.

Instrumental biases are also present in the phase observations. In the case of Precise Point Positioning these will map into the ambiguity parameter. Un-differenced hardware biases, as they are often referred to, are the main reason why it is impossible

¹<ftp://ftp.unibe.ch/aiub/CODE/>

to fix the integer number of the ambiguities (see Sec. 3.3).

Combination of observations from two or more satellite systems brings up additional biases to be accounted for such as an inter-system time system offset and an inter-system coordinate system offset. The time offset of GLONASS (and future Galileo) with respect to GPS is known or determined via observations, and can be applied in the receiver software. These issues are crucial for the successful integration of data from hybrid navigation systems.

3.2.6 Multipath

The multipath effect occurs when the signal arrives at the receiver's antenna from more than one path via reflection, diffraction, scattering or combinations of these. In spite of the amazing developments in the performance of GNSS positioning, multipath is still referred to as one of the last large sources of un-modeled errors in the GNSS analysis. This primarily originates in the nature of the multipath: the phenomena is of site-specific nature, caused by the unique environment of each GNSS site; it is dynamic in the temporal and the spatial sense, and therefore cannot be differenced out. It affects both the code and phase measurements, and moreover it is frequency and elevation dependent. The multipath effect on pseudorange measurements of P-code can sum up to a few meters, although the theoretical maximum is about 15 meters (by inference, 150 meters for the C/A-code). On the carrier phase observations the multipath error reaches a maximum of about 5 cm (Langley [1998]). There is no absolute way to eliminate or predict multipath, however possible mitigating measures are careful selection of the antenna location, special design of the antennas (choke ring, micro-strip), receiver design to recognize and eliminate the effect of non-line-of-sight signals, filter techniques, etc.. Recent studies try to investigate how the analysis of the SNR (signal-to-noise ratio) values can be used to map the multipath environment surrounding the antenna (Bilich & Larson [2007]).

3.2.7 Site displacement effects

The vector of the Cartesian coordinates of a receiver $\vec{X}_R^T = [X_R \ Y_R \ Z_R]$ determined by PPP, is referenced to the coordinate system of the applied orbits and the epoch of the observation. To obtain the coordinates of a single station consistent with the current ITRF solution, site displacement effects have to be calculated. According to the

IERS conventions (McCarthy & Pétit [2004]), the ITRF solution is based on a tide-free reference system and therefore any tidal effects have to be taken into account (removed). The elastic earth responds to several external forces causing site displacement. The resulting effects can reach up to several decimeters and have to be modeled in order to achieve the ultimate accuracies. The vector of receiver coordinates consistent with the current realization of the ITRF includes the corrections for solid earth tides $\delta\vec{X}_{SET}$, rotational deformation due to polar motion $\delta\vec{X}_{PM}$ and ocean loading $\delta\vec{X}_{OL}$ as follows

$$\vec{X}_{R,ITRF} = \vec{X}_R + \delta\vec{X}_{SET} + \delta\vec{X}_{PM} + \delta\vec{X}_{OL}. \quad (3.20)$$

The equations explained below are overtaken from the IERS conventions 2003. For more details refer to (McCarthy & Pétit [2004]).

Solid Earth Tides

The solid earth tides effect occurs due to permanent, periodic (semi-diurnal and diurnal) and long-periodic movements of a station originating mainly from the gravitational forces of the moon and the sun. The resulting site displacement can be represented by a spherical harmonic expansion scaled by the Love and Shida numbers (radial and transverse components). According to McCarthy & Pétit [2004], the site displacement vector of the station due to the tides is calculated in two steps. In the first step we consider degree 2 and degree 3 tides. In the second step we introduce the frequency dependence of the Love and Shida numbers. The displacement vector due to degree 2 tides in Cartesian coordinates $\Delta\vec{r}^T = [\Delta x \ \Delta y \ \Delta z]$ is given by

$$\Delta\vec{r} = \sum_{j=2}^3 \frac{GM_j R_e^4}{GM_{\oplus} R_j^3} \{h_2 \hat{r} \left(\frac{3}{2} (\hat{R}_j \cdot \hat{r})^2 - \frac{1}{2} \right) + 3l_2 (\hat{R}_j \cdot \hat{r}) [\hat{R}_j - (\hat{R}_j \cdot \hat{r}) \hat{r}]\}, \quad (3.21)$$

where GM_j and GM_{\oplus} are the gravitational parameters of the moon ($j = 2$) or the sun ($j = 3$) and the earth, respectively, \hat{R}_j and R_j are unit vectors from the geocenter to the moon or the sun and the magnitude of that vector, R_e is the earth's equatorial radius, \hat{r} and r are unit vectors from the geocenter to the station and the magnitude of that vector, and h_2 and l_2 are nominal degree 2 Love and Shida numbers. As seen from the Eq. (3.21), the total displacement is the sum of the displacement induced by the moon and displacement induced by the sun. The nominal values for the Love and Shida numbers 0.6078 and 0.0847, respectively, have to be corrected for the latitude

dependence given by Eq. (3.22):

$$\begin{aligned} h_2 &= 0.6078 - 0.0006[(3 \sin^2 \phi - 1)/2], \\ l_2 &= 0.0847 + 0.0002[(3 \sin^2 \phi - 1)/2]. \end{aligned} \quad (3.22)$$

The displacement due to the degree 3 tides is given by

$$\Delta \vec{r} = \sum_{j=2}^3 \frac{GM_j R_e^5}{GM_{\oplus} R_j^4} \left\{ h_3 \hat{r} \left(\frac{5}{2} (\hat{R}_j \cdot \hat{r})^3 - \frac{3}{2} (\hat{R}_j \cdot \hat{r}) \right) + l_3 \left(\frac{15}{2} (\hat{R}_j \cdot \hat{r})^2 - \frac{3}{2} \right) [\hat{R}_j - (\hat{R}_j \cdot \hat{r}) \hat{r}] \right\}. \quad (3.23)$$

Here we consider only the moon's contribution ($j = 2$) since the effect of the sun is negligible. In practice, only the radial displacement due to degree 3 is considered (up to 1.7 mm) where the transverse displacement does not exceed 0.2 mm.

The tidal displacement model (Eq. (3.21)) includes a time-independent part. The radial component r and the transverse component t (in meters) of this permanent deformation are given by

$$\begin{aligned} r &= [-0.1206 + 0.0001 P_2(\sin \phi)] P_2(\sin \phi), \\ t &= [-0.0252 - 0.0001 P_2(\sin \phi)] (\sin \phi). \end{aligned} \quad (3.24)$$

Here P_2 equals $(3 \sin^2 \phi - 1)/2$. Adding these corrections to the tide-free positions (ITRF) results in a “mean tide” position. Neglecting of the radial component of the permanent tide effect leads to errors of up to -12 cm at the poles and about 6 cm at the equator.

Loading

Temporal variations in the geographic distribution of the atmospheric and the hydrological masses load and deform the earth (van Dam & Wahr [1998]). The site displacement due to the ocean loading tides is of one order of magnitude smaller than the solid earth tide effect (up to several cm in the vertical component) and is more localized (coast lines). Nevertheless, even if the station is far from the coast line, for cm-level precision this effect has to be included. The ocean loading is induced by the temporal variation of the ocean mass distribution and it is dominated by diurnal and semi-diurnal periods. By convention it does not include a permanent part. The loading displacement vector

Δc can be expressed in simplified form as

$$\Delta c = \sum_j f_j A_{cj} \cos(\omega_j t + \lambda_j + u_j - \Phi_{cj}), \quad (3.25)$$

where f_j and u_j depend solely on the longitude of the lunar node (McCarthy & Pétit [2004]). Angular velocity is given by ω_j , and λ_j denotes the astronomical argument at time $t = 0$ h TT corresponding to the tidal wave component j represented by 11 tidal waves (the semi-diurnal waves M_2 , S_2 , K_2 and N_2 , the diurnal waves O_1 , K_1 , P_1 and Q_1 and the long-period waves M_f , M_m and M_{sa}). The calculation of the station specific amplitude A_{cj} and the phase Φ_{cj} depends on the applied ocean tide model (e.g. FES2004). Changes of the sea surface height and the density in the water column causes additionally a non-tidal ocean loading resulting in changes in the ocean bottom pressure. These changes lead to vertical site displacement of up to several mm for the coast line stations. Unlike for tidal loading of the ocean mass, there is no conventional model that can be applied for the non-tidal influence. However, the un-modeled ocean loading will cause errors of the estimated zenith wet delay or clock corrections (Vey *et al.* [2002]).

Site displacement caused by variations in the continental water storage (ground water, soil moisture, snow, ice, etc.) at annual periods are also non-negligible and can reach up to 30 mm in the vertical component (Schuh *et al.* [2003]). However, the IERS conventions currently provide no standard procedure for handling of this surface loading effects.

Variations in the atmosphere pressure with respect to the reference pressure causes the respond of the earth in the sense of an additional site displacement. This effect is strongest in the mid-latitudes where the largest weather variations occur, i.e. the largest pressure variations, and can reach up to 25 mm in the vertical component (van Dam *et al.* [1994], Petrov & Boy [2004]). Similar to the ocean loading, we can distinguish between tidal and non-tidal atmospheric loading effects. However, unlike for ocean tide loading, non-tidal atmospheric loading shows much larger influence than the tidal part. Two thermally induced tidal signals are dominant in the atmospheric loading, namely S_1 (every 24 hours) which can reach amplitudes of 0.8 mm, and S_2 (every 12 hours) with amplitudes up to 1.5 mm in equatorial regions. The non-tidal atmospheric loading displacement is dominated by typical periods of two weeks and is associated with the passing synoptic scale pressure system. The IERS has published a recommendation for handling of the atmosphere pressure loading in the space geodetic

technique applications within the latest convention document (P  tit & Luzum [2010]).

The vertical component is dominant in cases of all loading-induced site displacement. The horizontal component is usually about 1/10 to 1/3 of the vertical displacement.

Rotational deformation due to polar motion

The changes of the earth's spin axis with respect to the earth's crust — polar motion — causes periodical deformations which can reach up to several cm. The approximate corrections of the latitude, the longitude and the height component expressed in millimeters is given as

$$\begin{aligned}\Delta\phi &= -9 \cos 2\phi [(X_p - \bar{X}_p) \cos \lambda - (Y_p - \bar{Y}_p) \sin \lambda], \\ \Delta\lambda &= 9 \sin \phi [(X_p - \bar{X}_p) \sin \lambda + (Y_p - \bar{Y}_p) \cos \lambda], \\ \Delta h &= -32 \sin 2\phi [(X_p - \bar{X}_p) \cos \lambda - (Y_p - \bar{Y}_p) \sin \lambda],\end{aligned}\tag{3.26}$$

with $(X_p - \bar{X}_p)$ and $(Y_p - \bar{Y}_p)$ denoting the pole variation from the mean pole (\bar{X}_p, \bar{Y}_p) .

3.3 Observation adjustment

Let us consider that the observations are not affected by multipath and that the corrections and the models for relativistic effects, phase center variations, phase wind-up effect and system biases are applied. Assuming a dual-frequency receiver we are able to build the code and the phase ionospheric-free observation equations as follows

$$P_{if} = \rho + c\Delta t_R - c\Delta t^S + \Delta\rho_{tropo} + \gamma_{P,if},\tag{3.27}$$

$$L_{if} = \rho + c\Delta t_R - c\Delta t^S + \Delta\rho_{tropo} + b_{if} + \gamma_{L,if},\tag{3.28}$$

where

$$P_{if} = \frac{f_1^2 P_1 - f_2^2 P_2}{f_1^2 - f_2^2} \quad \text{and} \quad L_{if} = \frac{f_1^2 L_1 - f_2^2 L_2}{f_1^2 - f_2^2}.\tag{3.29}$$

In the above equations, f_1 and f_2 denote the frequencies of any two carriers. $\gamma_{P,if}$ and $\gamma_{L,if}$ denote the remaining un-modeled biases for code and phase ionospheric-free

observations. It is important to note here that the observation biases $\epsilon_{P,i}$ and $\epsilon_{L,i}$ in Eqs. (3.4) and (3.5) are not the same for the two frequencies. The ionospheric-free linear combination increases the measurement noise by about 3 times with respect to the L1 observations. Nowadays, the most common ionospheric-free linear combination is between the GPS L1 and the L2¹ carriers.

Eq. (3.28) also contains the ambiguity factor b_i . The full number of cycles from the satellite to the receiver, the so-called ambiguity number N , is due to the phase hardware biases α_R and α^S (Eq. (3.5)) not an integer number anymore, i.e.,

$$b_i = N_i + \alpha_{R,i} + \alpha_i^S. \quad (3.30)$$

When applying the ionospheric-free linear combination, this factor is additionally multiplied by the same factors as in the Eq. (3.29), contributing to the real nature of this number,

$$b_{if} = \frac{f_1^2 \lambda_1 b_1 - f_2^2 \lambda_2 b_2}{f_1^2 - f_2^2} = 2.546 \lambda_1 b_1 - 1.546 \lambda_2 b_2. \quad (3.31)$$

The ambiguity factor b_i can be differenced out using the double-difference observations. Forming the triple-difference observation the initial ambiguity N_i is eliminated. In the PPP approach the ambiguity resolution remains one of the limiting factors for the achievable accuracy.

The computation of receiver coordinates and troposphere parameters is based on a linearization of the function of geometric distance between satellite and receiver:

$$\rho_R^S \equiv f(X_R, Y_R, Z_R), \quad (3.32)$$

and applying the adjustment algorithm. The linearized observation equations in the Gauss-Markov model are given as

$$l = Ax + v, \quad (3.33)$$

where

¹In this case, L1 and L2 denote the GPS carriers. Previously, the same notation has been used for the phase observations in metric units.

3.3 Observation adjustment

l [$n \times 1$] is the vector of observations, n being a number of observations,
 x [$u \times 1$] is the vector of unknowns,
 A [$n \times u$] is a design matrix, u being the number of unknowns, and
 v [$n \times 1$] is the residuals vector with the expectation defined as $E[v] = 0$.

The dispersion matrix of the observations is defined as

$$D[l] = \Sigma_{ll} = \sigma_0^2 Q_{ll}, \quad (3.34)$$

with Σ_{ll} being the covariance matrix of observation, σ_0^2 the a priori variance of unit weight (usually set to 1) and Q_{ll} the cofactor matrix commonly calculated as an inverse of the weight matrix P ($P = Q_{ll}^{-1}$). The adjustment strategy is based on minimizing the sum of squares of the residuals, i.e.,

$$v^T P v = (l - Ax)^T P (l - Ax) = \text{minimum}. \quad (3.35)$$

The estimated vector of unknowns \hat{x} reads

$$\hat{x} = (A^T P A)^{-1} A^T P l = N^{-1} n, \quad (3.36)$$

where N is the normal equation matrix and n is the measurement vector. The cofactor matrix of the estimated parameter vector $Q_{\hat{x}\hat{x}}$ follows from the covariance propagation law and is defined as

$$Q_{\hat{x}\hat{x}} = (N^{-1} A^T P) Q_{ll} (N^{-1} A^T P)^T = N^{-1}. \quad (3.37)$$

The *a posteriori* variance of unit weight reads

$$\hat{\sigma}_0^2 = \frac{\hat{v}^T P \hat{v}}{n - u}, \quad (3.38)$$

with $n - u$ defining the degree of freedom. The vector of estimated residuals \hat{v} is calculated from the vector of estimated parameters \hat{x} as

$$\hat{v} = l - A\hat{x}. \quad (3.39)$$

The covariance matrix of the estimated parameters is finally defined as

$$\Sigma_{\hat{x}\hat{x}} = \hat{\sigma}_0^2 Q_{\hat{x}\hat{x}}. \quad (3.40)$$

The algorithm described above is based on the principal assumption of Gaussian normally distributed observation noise and uncertainty, hence any bias or outlier must be removed prior to the least-squares adjustment procedure.

As previously mentioned, the vector of estimated station coordinates $\vec{X}_{R,ITRF}$ is related to the coordinate system of the applied orbits, which are always consistent with the current realization of the ITRF, and the epoch of the observation data. The coordinates of the receiver in any desired epoch can be obtained by adding the ITRF velocity vector \vec{v} multiplied by the difference of the time between the starting and desired epoch to the above calculated coordinate vector $\vec{X}_{R,ITRF}$.

3.4 PPP services

3.4.1 International GNSS Service (IGS)

The International GNSS Service, formerly International GPS Service (<http://igsceb.jpl.nasa.gov/>) was established as a service of the International Association of Geodesy (IAG) in 1994 to provide GNSS data and products free of charge to all interested users. It is a voluntary, non-commercial organization with more than 200 contributing institutions, more than a dozen regional and operational data centers, four global data centers, eleven analysis centers and a number of associate or regional analysis centers. The Central Bureau of the service is located at the Jet Propulsion Laboratory, which maintains the Central Bureau Information System (CBIS) and ensures access to IGS products and information. An international Governing Board oversees all aspects of the IGS.

The mission of IGS is outlined in the organization's 2002–2007 Strategic Plan: *The International GPS Service is committed to providing the highest quality data and products as the standard for global navigation satellite systems (GNSS) in support of earth science research, multidisciplinary applications, and education. These activities aim to advance scientific understanding of the earth system components and their interactions, as well as to facilitate other applications benefiting society.*

The IGS analyzes and combines the solution of eleven analysis centers, namely Center for Orbit Determination in Europe, AIUB, Switzerland (CODE), European Space Operations Center, ESA, Germany (ESOC), GeoForschungsZentrum, Germany (GFZ),

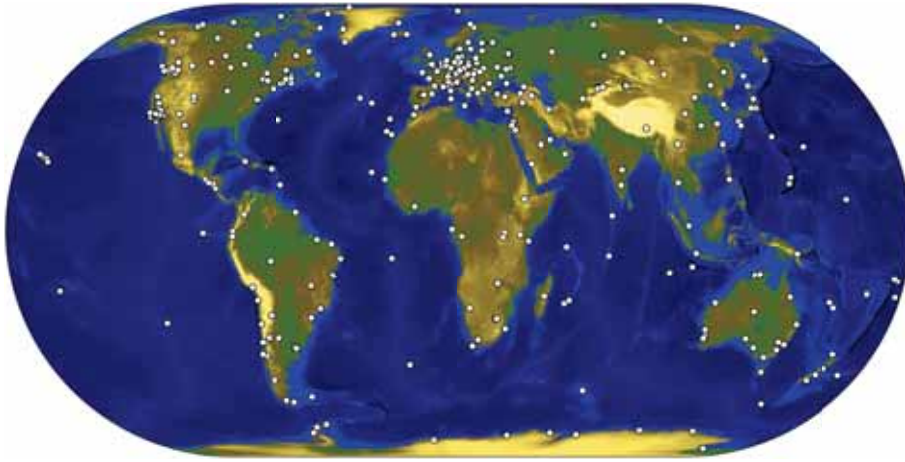


Figure 3.3: IGS tracking network (*source: <http://igs.cb.jpl.nasa.gov/>*)

Jet Propulsion Laboratory, USA (JPL), National Oceanic and Atmospheric Administration/NGS, USA (NOAA), Natural Resources Canada, Canada (NRCan), Scripps Institution of Oceanography, USA (SIO), U.S. Naval Observatory, USA (USNO), Massachusetts Institute of Technology, USA (MIT) and Geodetic Observatory Pecny, Czech Republic (GOP-RIGTC). Along with the observation data from more than 350 continuously operating GPS/GNSS stations (see Fig. 3.3), the following products are provided:

- GPS satellite ephemeris,
- GLONASS satellite ephemeris,
- Earth rotation parameters,
- IGS tracking station coordinates and velocities,
- GPS satellite and IGS tracking station clock information,
- Zenith tropospheric path delay estimates,
- Global ionospheric maps.

Table 3.1 lists the GPS ephemerides and clock products available from IGS, with their accuracy and availability. GLONASS final ephemerides are provided similar to GPS final orbits, about 12–18 days after, but with a slightly decreased accuracy of 5 cm.

IGS continues to develop and increase the quality of provided data and products. It incorporates the leading-edge expertise and resources to deliver world-standard quality GNSS data and products to all users globally (Dow *et al.* [2009]). Further development aims particularly to integrate new GNSS components and accordingly investigate

GPS Ephemerides		Accuracy	Latency	Updates	Sample Int.
Broadcast	Orbits	~ 100 cm	realtime		Daily
	Sat. Clocks	~ 5 ns			
IGS Ultra rapid (predicted half)	Orbits	~ 5 cm	realtime	4 times/day	15 min
	Sat. Clocks	~ 3 ns			
IGS Ultra rapid (observed half)	Orbits	~ 3 cm	3 hours	4 times/day	15 min
	Sat. Clocks	~ 150 ps			
IGS Rapid	Orbits	~ 2.5 cm	17 hours	Daily	15 min
	Sat. Clocks	~ 75 ps			5 min
IGS Final	Orbits	~ 2.5 cm	~ 13 days	Weekly	15 min
	Sat. Clocks	~ 75 ps			5 min & 30 s

Table 3.1: GPS ephemerides data provided by IGS

and extend the IGS standards (equipment, calibration, formats, delivery methods, etc.).

3.4.2 PPP processing and analysis services

In addition to satellite products provided by services like IGS, or any of IGS analysis centers, there is a number of PPP services for processing the global GNSS observations. Several software products implementing a PPP processing strategy have been developed recently by government agencies, universities, industries and individuals. Some of those processing services are available on-line for free use, and are listed below:

- **CSRS-PPP** (http://www.geod.nrcan.gc.ca/online_data_e.php), developed by Natural Resources Canada,
- **GPS Analysis and Positioning Software (GAPS)** (<http://gaps.gge.unb.ca/>), developed by University of New Brunswick, Canada,
- **Automatic Precise Positioning Service (APPS)** (<http://apps.gdgps.net/>), formerly *Auto-GIPSY*, developed by Jet Propulsion Laboratory (JPL), USA,
- **magicGNSS** (<http://magicgnss.gmv.com/ppp>), developed by the company GMV,

- **AUSPOS** (<http://www.ga.gov.au/geodesy/sgc/wwwgps/>), developed by Geoscience Australia,
- **Scripps Coordinate Update Tool (SCOUT)** (<http://csrc.ucsd.edu/cgi-bin/SCOUT.cgi>), developed by the Scripps Orbit and Permanent Array Center (SOPAC), Scripps Institution of Oceanography (SIO), University of California,
- **Online Positioning User Service (OPUS)** (<http://www.ngs.noaa.gov/OPUS/>), developed by NOAA.

On-line PPP softwares make use of precise IGS orbit and clock correction products to provide a static (and kinematic) coordinate solution for the submitted observation data. The single- or dual-frequency data are usually required in RINEX format. The processable data rate and option for processing combined GNSS (GPS+GLONASS) data varies from software to software. For individual specification, please check the previously indicated web-site links.

The web-site <http://gge.unb.ca/Resources/PPP/index.htm> provides the links to some of on-line PPP services and also allows the submission of the observation data at one place to be processed with several PPP softwares. This way, the individual, independent results can be obtained within 10–15 minutes and the performance of different implementation strategies can be compared.

3.5 Current state of Precise Point Positioning

The procedure described above represents what is currently understood as a standard Precise Point Positioning technique. Usually, dual-frequency receivers are used and the ionospheric-free linear combination is applied to eliminate the first order ionospheric delay. The corrections for the satellite clocks, satellite and receiver related biases and the relativistic corrections are applied. Relying on the precise orbit data, station position, receiver clock corrections and troposphere parameters are to be estimated (Eqs. (3.27) and (3.28)). Residual parameters such as multipath or receiver noise are either ignored or handled via stochastic methods (Bisnath & Gao [2008]).

According to Bisnath & Gao [2008], the standard metrics to describe the performance of PPP are:

1. accuracy,
2. precision,

3. convergence period,
4. availability, and
5. integrity.

Since corrections up to mm-level are applied within the PPP procedure, and the biases are typically on cm-level, there is a negligible difference between the precision and the accuracy metrics. PPP is able to provide results on cm-level in a static mode and dm-level in a kinematic mode, both in real-time and post-processing. The limiting factor in real-time scenarios is clearly the availability of the precise orbit and clock products.

The convergence period, i.e. the time required for coordinates to converge to the optimal solution, is typically about a couple of hours under standard conditions (no signal interruption, sufficient number of satellites) until the cm-level is reached. Decimeter level is obtained after approx. 30 minutes. There are many parameters to determine the convergence time, and therefore many opportunities for improvement. Among the limiting factors here, we can list the un-solved ambiguities (float solution) and quality and availability of the orbit and satellite clock products. The announced GNSS modernization will improve the convergence time with regard to an improved geometry and increased amount of observations, and possibly new linear combinations to reduce the observation noise.

Independence of reference station observations or regional or local correction data is a main advantage of PPP technique. Regarding integrity, aside of information about the level of biases introduced with different products and models, the post-fit solution residuals should be analyzed to check for possible outliers and problems. Additionally, the results could be compared to some reference double-differenced solution. A more straightforward approach is an implementation of the RAIM (Receiver Anonymous Integrity Monitoring) screening, providing the users with more confidence in the results.

Chapter 4

Signal propagation in the atmosphere

Global navigation satellite systems make use of signals of the electromagnetic spectrum which experience delays during their transmission from the satellite to the receiver. In space geodesy the properties of the propagation media play an important role in the way these delays are handled. Usually, the propagation delay $\Delta\rho$ is defined as an integral of the refractive index n of the media along the ray path s between the satellite S and the receiver R , i.e.,

$$\Delta\rho = \int_S^R (n - 1)ds. \quad (4.1)$$

The refractive index n is defined as the ratio of the propagation velocity of the signal in a respective medium v and the propagation velocity of the signal in the vacuum c .

Roughly speaking, the atmosphere is a set of concentric shells with different physical and chemical properties which can be divided in various ways depending on the context of interest. With respect to GNSS signal propagation, the atmosphere is divided in a dispersive and a non-dispersive part, namely the ionosphere and the troposphere. In both cases, delays have to be properly handled either by direct measurements and/or by an appropriate model, or considered within the adjustment procedure.

4.1 Ionospheric delay

The ionosphere is defined as a part of the atmosphere where sufficient free electrons and ions exist to affect the propagation of radio waves (Davis [1990]). It extends through the upper part of the earth's atmosphere between approx. 70–1000 km; however the peak electron and ion density is concentrated in the so-called F region beginning at about 150 km above the earth. Free electrons affect the speed, polarization and direction of the electromagnetic wave. The largest influence is on the speed of the microwave, therefore the ionosphere primarily affects the reception time of the signal and subsequently the measured range.

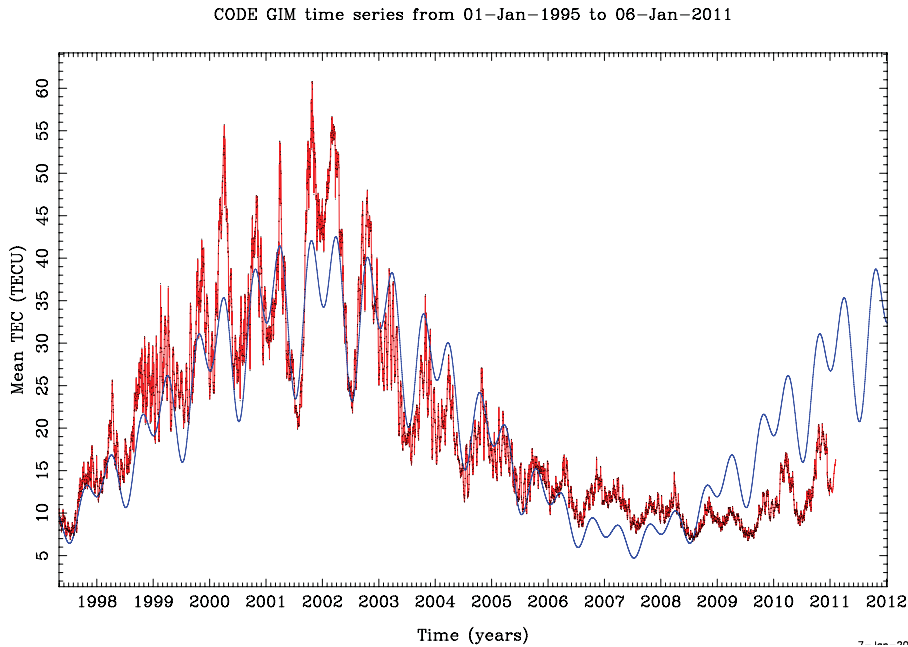


Figure 4.1: Mean electron content over last 15 years (*source: CODE analysis center*)

Several factors influence the number and distribution of free electrons. Solar radiation and the earth's magnetic field among those play the key roles. The ionization process (breaking of electrons from atoms and molecules) is caused by the solar ultra-violet radiation and therefore the amount of produced free electrons depends on the solar activity and density of ionized gas. It is therefore clear that the ionospheric path delay is a function of time of day, season and the elevation of the satellite. On the other hand, the earth's magnetic field affects the distribution of the free electrons and

adds a latitude dependence property. Also, in the region of the geomagnetic equator, the solar flux is, or close to, vertical which causes the highest electron production. Hence, the maximum ionospheric delay will occur in the region of about 10° – 15° north and south of the geomagnetic equator, in the period of maximum solar activity. Fig. 4.1 illustrates the evolution of the mean electron content (expressed in total electron content units TECU) over the last 15 years clearly showing a solar activity maximum around the year 2002 and solar activity minimum at the end of 2008. The red line represents the daily mean TEC values based on a least-squares collocation and the blue line represents the prediction for the next years based on a 7-parameter trend function (Schäfer *et al.* [1998]). The next solar maximum is expected in May 2013, indicating a 11-year period of solar activity. Nevertheless, aside from this long-term trend occasional irregularities such as ionospheric scintillation, traveling ionospheric disturbances (TIDs) and other can occur on short temporal and spatial scales, and can significantly affect the propagation delay.

The refractive index for the carrier phase n_L can be expressed by the Appleton expression (Davis [1990]) expanded into a second order Taylor approximation up to term f^{-4} for signals with frequencies used by GNSS systems. With the introduction of main physical constants and parameters of the SI system, we can write

$$n_L = 1 - \frac{40.309N_e}{f^2} - \frac{1.1284 \cdot 10^{12}N_e B \cos \theta}{f^3} - \frac{812.42N_e^2}{f^4} - \frac{1.5793 \cdot 10^{22}N_e B^2(1 + \cos^2 \theta)}{f^4}, \quad (4.2)$$

where N_e is the number of free electrons, B is the module of the magnetic field and θ is the angle between the vector of magnetic field \vec{B} and the propagation direction of the electromagnetic wave. Inserting Eq. (4.2) into Eq. (4.1), the ionospheric phase delay in metric units reads

$$\Delta\rho_{iono,L} = -\frac{s_1}{f^2} - \frac{s_2}{f^3} - \frac{s_3}{f^4}, \quad (4.3)$$

with coefficients s_1 , s_2 and s_3 defined as follows

$$s_1 = 40.309 \int_S^R N_e ds, \quad (4.4)$$

$$s_2 = 1.1284 \cdot 10^{12} \int_S^R N_e B \cos \theta ds, \quad (4.5)$$

$$s_3 = 812.42 \int_S^R N_e^2 ds + 1.5793 \cdot 10^{22} \int_S^R N_e B^2(1 + \cos^2 \theta) ds. \quad (4.6)$$

The effect of the ionosphere on code pseudorange measurements can be computed using the well known relationship between phase and code refractive indices, n_L and n_P respectively (Davis [1990]) as shown in the following equation

$$n_P = n_L + f \frac{dn_L}{df}. \quad (4.7)$$

Introducing the relation for the phase delay (Eq. (4.3)), the code ionospheric delay reads

$$\Delta\rho_{iono,P} = \frac{s_1}{f^2} + 2\frac{s_2}{f^3} + 3\frac{s_3}{f^4}. \quad (4.8)$$

Note that the ionospheric delay of the code measurements in Eq. (4.8) has an opposite sign then in the case of the phase measurements (Eq. (4.3)), indicating the phase advance and the code delay due to the ionosphere.

From the above equations it is clear that the propagation delay of GNSS signals depends on the signal frequency. The ionosphere is therefore often referred to as a dispersive media. This property is of great importance as it serves as the most effective way to account for ionospheric delay. Combining simultaneous observations on k frequencies and using Eqs. (4.3) and (4.8) we are able to eliminate the effect of the ionosphere up to order $k - 1$ (P  tit & Luzum [2010]). For observations on two GPS frequencies L1 and L2 we are able to build an *ionospheric-free linear combination L3* as follows

$$L3 = \frac{f_1^2 L1 - f_2^2 L2}{f_1^2 - f_2^2}, \quad (4.9)$$

providing us with observations free of first order ionospheric delay represented by s_1/f^2 . In Eq. (4.9) f_1 and f_2 indicate the frequencies of two carriers and L1 and L2 indicate either code or phase observation equations (Eqs. (3.4) and (3.5)) at both frequencies. This linear combination satisfies in most cases the aimed accuracy since the first order ionospheric delay captures about 99.9% of the total ionospheric delay. However, it does not include the influence of the geomagnetic field (Eq. (4.5)) and the bending effect of the ray (Eq. (4.6)). The second order ionospheric delay can reach values from a couple of millimeters to a few centimeters (Brunner & Gu [1991]), and for high accuracy performance it has to be taken into account. Correcting for the second order ionospheric effect is possible when using three frequencies, which will be the case e.g. for GPS with new L5 signals, or for new satellite systems like Galileo. The elimination requires consistent products such as satellite orbits and clock corrections.

These products are currently based on the $L3$ linear combination and do not account for higher order effects of the ionosphere. Applying those products when eliminating the second order ionosphere may lead to the inconsistency biases. It should be noted here that linear combinations of signals, while cancelling the ionospheric effects, significantly increase the measurement noise. Therefore, it might be the better option to explicitly model the second order ionospheric delay.

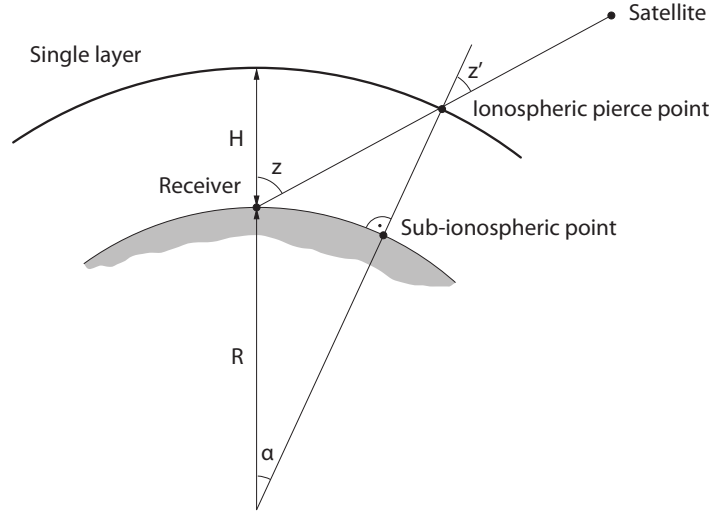


Figure 4.2: Ionospheric single-layer model (Dach *et al.* [2007])

With solely two frequencies available in operational GNSS, the second order ionosphere effect has to be explicitly calculated from Eq. (4.5) applying a model of the geomagnetic field such as the International Geomagnetic Reference Model (IGRM)¹ and information about the electron content along the ray path. Usually the electron content along the ray path is denoted as *Total Electron Content* (TEC),

$$\text{TEC} = \int_S^R N_e ds, \quad (4.10)$$

which corresponds to the integral on the right side of Eq. (4.4). This integral contains the total number of free electrons included in a cylinder with 1 m^2 diameter along the ray path s from the satellite S to the receiver R . There are several ways to obtain the TEC value. The most common one is a “single-layer” model, where the total electron

¹<http://www.ngdc.noaa.gov/IAGA/vmod/igrf.html>

content of the ionosphere is assumed to be concentrated in one layer, usually set to a height H of about 400 km (see Fig. 4.2). An alternative approach is to perform the multi-layer ionospheric tomography (Hernández-Pajares *et al.* [2000]), or ray tracing through the ionosphere density model (e.g. International Reference Ionosphere IRI¹).

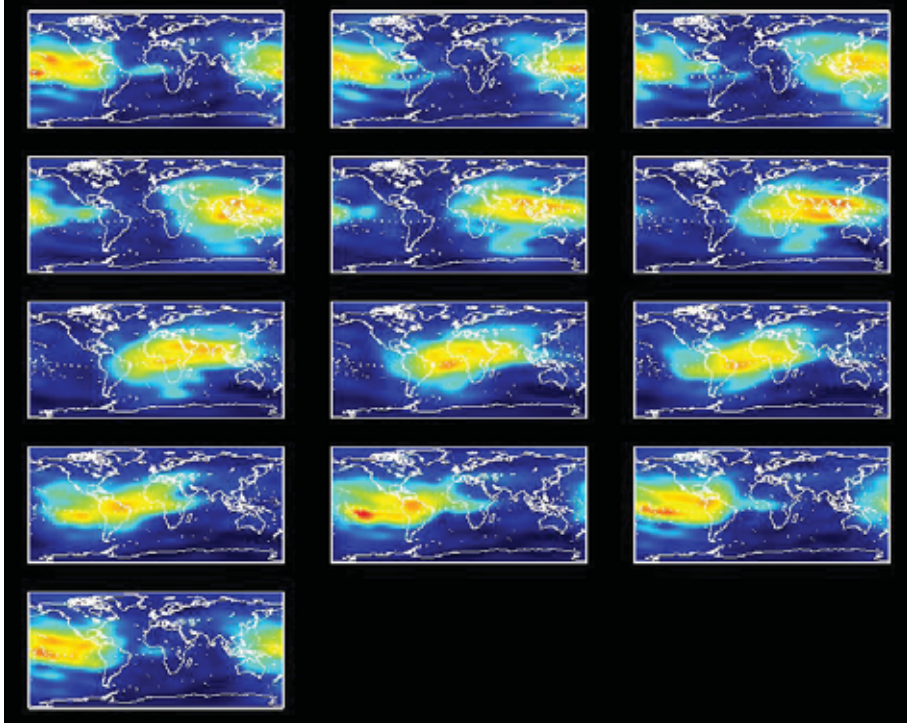


Figure 4.3: Global ionosphere maps for April 23, 2010 (*source: CODE analysis center*)

Information about the total electron content is of great importance for users with single-frequency receivers since no $L3$ combination can be applied. In this case, an external source of TEC must be available. TEC information is normally provided as *Vertical Total Electron Content* (VTEC) and has to be mapped to a certain satellite elevation angle in order to obtain the *Slant Total Electron Content* (STEC). This is performed using the ionospheric *mapping function*,

$$\text{STEC} = \text{VTEC} \cdot \cos z', \quad (4.11)$$

where z' is the zenith angle of the satellite at the ionosphere pierce point (see Fig. 4.2).

¹<http://modelweb.gsfc.nasa.gov/ionos/iri.html>

Here, the spherical layer model is applied with a fixed effective ionospheric height H . In Eq. (4.11) $\cos z'$ is a function of the mean radius of the earth R and the satellite's zenith angle z , i.e.,

$$\cos z' = \sqrt{1 - \frac{R^2 \sin^2 z}{(R + H)^2}}. \quad (4.12)$$

In summary, the TEC information can be obtained from: (1) global VTEC maps, provided by CODE or other IGS analysis centers (see Fig. (4.3)), (2) a predicted model such as the NeQuick model or simple Klobuchar model, (3) regional VTEC models, (4) empirical standard models such as IRI (International Reference Ionosphere), etc..

For the calculations presented in Chapter 6, the two GPS frequencies L1 and L2 were available, hence it was possible to build the $L3$ ionosphere-free linear combination. The effect of the second order ionospheric delay was ignored.

4.2 Tropospheric delay

The troposphere is the nethermost layer of the earth's atmosphere reaching up to more than 20 km at the equator and is lowest at the poles, reaching the altitudes of 7 km or more. It contains approx. 75% of the total atmosphere mass and 99% of the water vapor. The troposphere is comprised of a *dry* part containing nitrogen (78%), oxygen (20%) and a remaining 1% of other gases and a *wet* part, namely water vapor (about 1% of air gases). The troposphere ends with the tropopause layer followed by the stratosphere. The distribution of air gases within the troposphere is essentially uniform with the exception of water vapor. Water vapor shows high temporal and spatial variability and therefore it is impossible to predict or model it accurately. On the other hand, the amount of water vapor decreases as the altitude increases and it is almost entirely located below 10 km. Fig. 4.4 (note the axes scales) shows the distribution of dry and wet air densities for the station Albany at a latitude of 42.8°, obtained from the radiosonde profile on January 1st, 1992 at 0 UT.

Unlike the ionosphere, the troposphere is absent of charged particles. For electromagnetic waves in the radio-frequency spectrum (up to 15 GHz), the troposphere is a non-dispersive medium (Seeber [2003]). Troposphere refraction is thus identical for all GNSS carriers, and influences equally phase and code measurements. The refractive index is slightly larger than 1 and decreases with height as the air density decreases.

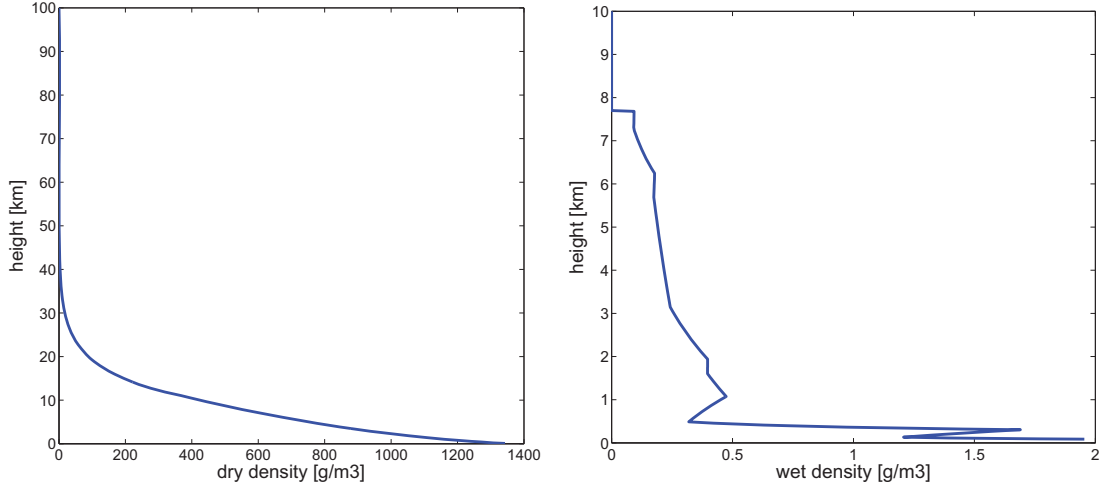


Figure 4.4: Density of *dry* (left) and *wet* (right) air

The air density, and accordingly signal refraction, depend on basic physical parameters of the troposphere: air pressure, temperature and humidity.

Air Pressure

The pressure is defined as force per area unit. Air masses suppress the earth's surface due to gravitational forces. At the mean sea level, pressure is about 1013.25 hPa, and equals to pressure of 1 kg per square centimeter of surface area. Due to gravity and decrease of air density (see Fig. 4.4), the air pressure decreases exponentially as the height above the surface increases. At the height of the tropopause it equals to values between 300 hPa at the poles and 70 hPa at the equator. In the stratosphere the air pressure is about 1 hPa.

Temperature

As can be seen in Fig. 4.5 the temperature has a more complex profile than the air pressure. In the tropospheric region it decreases with increasing altitude at a rate of about -5 to -7 Kelvin/km. The reason for this is a larger heat absorption from the sun-heated earth. This trend is disturbed in case of the so-called inversion layer within the first hundred meters. Here colder air may be located below warmer layers. In the tropopause layer, the temperature stays more or less constant and begins to increase in the stratosphere layer.

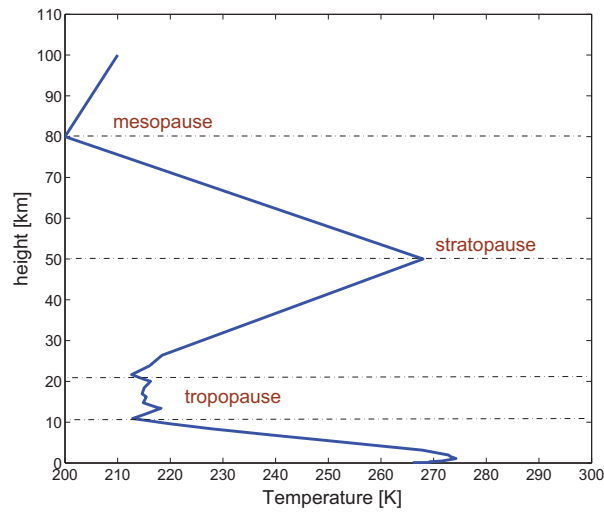


Figure 4.5: Variation of temperature through the layers of the atmosphere

Humidity

Humidity is defined as the amount of water vapor in the air. Its temporal and spatial (horizontal and vertical) distribution is highly inhomogeneous, variable and unpredictable. It is influenced by current weather conditions, season and location. Nevertheless, there are some regularities: it is almost entirely concentrated within the first 10 km above surface, it is higher and more variable in summer months and increases with decrease in latitude (see Sec. 6.4). The amount of water vapor cannot exceed a certain value depending on temperature conditions. If this temperature is reached, the air is saturated¹ with water vapor. There are several measures to characterize the amount of water vapor:

- *water vapor pressure* - expressed in hPa or mbar,
- *absolute humidity* - the amount of water vapor in the air expressed in g/m^3 ,
- *specific humidity* - the ratio of density of water vapor to density of wet air,
- *relative humidity* - the ratio of vapor pressure to saturation vapor pressure expressed in %,
- *mixing ratio* - the ratio of density of water vapor to dry air,

¹The saturation is the condition in which the partial pressure of any fluid constituent (water in the atmospheric air) is equal to its maximum possible partial pressure under the existing environmental conditions, such that any increase in the amount of that constituent will initiate within it a change to a more condensed state. Evaporation ceases under such conditions. Source: <http://nsidc.org/arcticmet/glossary/saturation.html>

- *dew point* - the temperature at which enough water vapor is in the air in order that saturation occurs.

4.2.1 Refractivity of the troposphere

The relation between physical parameters of the atmosphere and the *refractivity* N is given as

$$N = k_1 \frac{p_d}{T} Z_d^{-1} + [k_2 \frac{e}{T} + k_3 \frac{e}{T^2}] Z_w^{-1}, \quad (4.13)$$

where k_1 , k_2 and k_3 are empirically determined coefficients and Z_d and Z_w are compressibility factors for dry air and water vapor, respectively (Thayer [1974]). Partial pressure of dry air and water vapor is denoted as p_d and e , respectively, and T refers to temperature. The compressibility factors Z_d and Z_w are corrections to account for the deviation of atmospheric constituents from an ideal gas. For an ideal gas, aforementioned factors equal 1. For typical atmospheric conditions in the atmosphere, the compressibility factors deviate less than 10^{-3} (Langley [1998]). Owens [1967] gives expressions for compressibility factors with an accuracy of a few ppm. The values for the refractivity constants k_1 , k_2 and k_3 are usually taken from Smith & Weintraub [1953], Thayer [1974] or Bevis *et al.* [1994] and are summarized in Tab. 4.1.

	k_1 [K/hPa]	k_2 [K/hPa]	k_3 [K ² /hPa]
Smith & Weintraub [1953]	77.61±0.01	72±9	$(3.75 \pm 0.03) \cdot 10^5$
Thayer [1974]	77.6±0.014	64.8±0.08	$(3.776 \pm 0.004) \cdot 10^5$
Bevis <i>et al.</i> [1994]	77.6±0.05	70.4±2.2	$(3.739 \pm 0.0012) \cdot 10^5$

Table 4.1: Empirically determined values for refractivity constants

In Eq. (4.13) the first term is the refractivity caused by the induced dipole moment of the dry constituents of the atmosphere, the second term is the induced dipole moment of water vapor, and the third term shows the effect of the permanent dipole of the water vapor molecules (Davis *et al.* [1985]). The refractivity N and refractive index n are linked by the following expression

$$N = 10^6(n - 1). \quad (4.14)$$

4.2.2 Modeling and estimation of tropospheric path delay

Following Eq. (4.1), we define the tropospheric path delay between the satellite S and the receiver R along the path s as

$$\Delta\rho_{tropo} = \int_S^R (n_{trop} - 1)ds + [B - G]. \quad (4.15)$$

The term $[B - G]$ accounts for *geometric bending effect*¹ (Fig. 4.6). Assuming a horizontally stratified atmosphere the path length B and G are identical for the observation in the zenith direction. The difference between geometric and bended path increases up to ≈ 10 cm at an elevation of 5° . The bending effect is normally captured within the hydrostatic mapping function (Böhm [2008]).

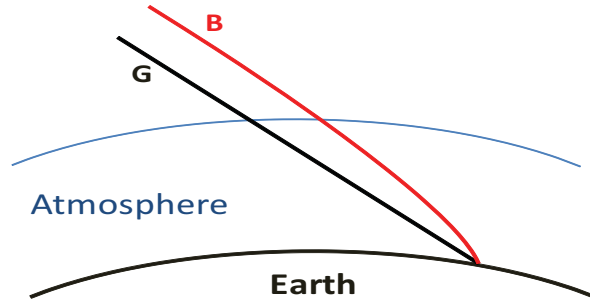


Figure 4.6: Geometric bending effect

Following Eqs. (4.14) and (4.15), and separating the refractivities for dry (N_d) and wet (N_w) air, we can write

$$\Delta\rho_{tropo} = 10^{-6} \left[\int_S^R N_d ds + \int_S^R N_w ds \right]. \quad (4.16)$$

By applying the refractivity terms for dry and wet air from Eq. (4.13) we get

$$\Delta\rho_{tropo} = 10^{-6} \left[\int_S^R k_1 \frac{p_d}{T} Z_d^{-1} ds + \int_S^R \left[k_2 \frac{e}{T} + k_3 \frac{e}{T^2} \right] Z_w^{-1} ds \right]. \quad (4.17)$$

The value for partial pressures of dry air p_d and water vapor e showing up in Eq. (4.17)

¹According to Fermat's principle, the EM waves take the path of shortest travel time. Due to refractivity of different layers of the atmosphere, the path of the shortest travel time does not correspond to geometrical path, so the path bending occurs.

are not easy to obtain since their mixing ratio is highly variable and needs to be obtained with sufficient accuracy. However, if we assume the hydrostatic equilibrium where total pressure p equals the sum of the pressure of the dry air p_d and water vapor pressure e , i.e.,

$$p = p_d + e, \quad (4.18)$$

we can apply the ideal gas law for dry air and water vapor

$$p_d = \rho_d \frac{R}{m_d} T Z_d \quad \text{and} \quad e = \rho_w \frac{R}{m_w} T Z_w. \quad (4.19)$$

ρ_d and ρ_w ¹ are densities of dry air and water vapor with molar masses m_d and m_w , respectively, and R stands for the universal gas constant. Values for R , m_d and m_w are given as (Davis *et al.* [1985])

$$R = 8.314345 \pm 0.00007 \text{ Pa}\cdot\text{m}^3/\text{K}\cdot\text{mol},$$

$$m_d = 28.9644 \pm 0.0014 \text{ g/mol},$$

$$m_w = 18.01528 \text{ g/mol}.$$

Inserting Eqs. (4.19) into Eq. (4.13), we can write

$$N = k_1 \frac{R}{m_d} \rho + \left[k_2 - k_1 \frac{m_w}{m_d} \right] \frac{e}{T} Z_w^{-1} + k_3 \frac{e}{T^2} Z_w^{-1}, \quad (4.20)$$

with ρ as the total density and a new constant factor k'_2 defined as

$$k'_2 = k_2 - k_1 \frac{m_w}{m_d} = 22.1 \pm 2.2 \text{ K/hPa}. \quad (4.21)$$

Finally, the tropospheric path delay can be expressed as

$$\Delta\rho_{tropo} = 10^{-6} \left[\int_S^R \left(k_1 \frac{R}{m_d} \rho \right) ds + \int_S^R \left(k'_2 \frac{e}{T} Z_w^{-1} \right) ds + \int_S^R \left(k_3 \frac{e}{T^2} Z_w^{-1} \right) ds \right]. \quad (4.22)$$

Eqs. (4.20) and (4.22) strictly separate the hydrostatic (first term) and a non-hydrostatic part (second and third term), and are clearly favorable since hydrostatic delay now depends solely on the total density and not on the mixing ratio of wet and dry parts. Note that the path delay is also influenced by dry air above troposphere,

¹Please note that the letter ρ is here used for densities. It is not to be confused with $\Delta\rho_{tropo}$ designating the tropospheric delay.

however the term *tropospheric delay* captures the influence of the entire neutral (non-dispersive) atmosphere.

Eq. (4.22) can be solved either by knowledge of the actual tropospheric parameters or by an approximation using an appropriate model. Following the first approach, refractivity profiles with sufficient horizontal and vertical resolution derived by e.g. ray tracing through a numerical weather model or radiosonde measurements have to be available. If this is not the case, the second approach must be applied. In space geodetic techniques, the *a priori* hydrostatic delay in zenith direction can be calculated rather accurately from a simplified surface pressure model and the remaining delay is estimated along with other parameters. This approach is adopted for test calculations presented in Ch. 6, since no meteorological data is available for the selected set of stations. The total delay in the line of sight is derived as the sum of the hydrostatic and wet delay in zenith direction multiplied by respective mapping functions, and a gradient correction as follows (McCarthy & Pétit [2004])

$$\Delta\rho_{tropo} = \Delta\rho_h^z \cdot m_h(\epsilon) + \Delta\rho_w^z \cdot m_w(\epsilon) + m_g(\epsilon)[G_N \cos \alpha + G_E \sin \alpha], \quad (4.23)$$

where $\Delta\rho_h^z$ and $\Delta\rho_w^z$ are the hydrostatic and wet zenith delays, respectively, with associated hydrostatic and wet mapping functions $m_h(\epsilon)$ and $m_w(\epsilon)$. ϵ is the elevation angle of the satellite. The term $m_g(\epsilon)[G_N \cos \alpha + G_E \sin \alpha]$ is called tropospheric gradient correction and allows to account for the azimuthal dependence of the tropospheric path delay. In Eq. (4.23) $m_g(\epsilon)$ stands for the gradient mapping function with respect to the elevation angle ϵ , G_N and G_E denote the horizontal delay gradients in the north and east direction, respectively, and α is the azimuth angle of the received signal measured east from north. Gradient modeling is needed to correct for the effect of the atmospheric bulge¹ and effects due to changing weather conditions.

Hereafter, the derivation of the hydrostatic and wet zenith delay models, accompanying mapping functions and gradient correction models will be explained.

¹The troposphere thickness is not uniform; it reaches higher altitudes at the equator and it narrows towards the poles.

4.2.3 Zenith delays

4.2.3.1 Zenith hydrostatic delay

Based on Eq. (4.22), we define the path delay due to hydrostatic refractivity as

$$\Delta\rho_h = 10^{-6} \int_S^R (k_1 \frac{R}{m_d} \rho) ds. \quad (4.24)$$

Applying the condition of satisfied hydrostatic equilibrium (Davis *et al.* [1985]) ,

$$\frac{dp}{dz} = -\rho(z)g(z), \quad (4.25)$$

we define its vertical profile. Here, $g(z)$ is the acceleration due to gravity along the vertical coordinate z . Integration of the equation Eq. (4.25) from the antenna a to infinity leads to

$$\int_a^\infty \rho(z)dz = \int_a^\infty -\frac{dp}{g(z)}dz = \frac{p_0}{g_{eff}}, \quad (4.26)$$

where p_0 is the pressure at the antenna and g_{eff} is the effective (mean) gravity, representing gravity acceleration at the center of mass of the vertical column of the atmosphere above the site. The zenith hydrostatic delay $\Delta\rho_h^z$ (ZHD) is now defined as

$$\Delta\rho_h^z = 10^{-6} k_1 \frac{R}{m_d} \frac{p_0}{g_{eff}}. \quad (4.27)$$

Based on Eqs. (4.25) and (4.26) we define the effective gravity g_{eff} as follows

$$g_{eff} = \frac{\int_a^\infty \rho(z)g(z)dz}{\int_a^\infty \rho(z)dz}. \quad (4.28)$$

Modeling of ZHD is therefore straightforward, and models can only differ due to the choice of the refractivity constant and due to the modeling of height and latitude dependence of the gravity term (Mendes [1999]).

According to Saastamoinen [1972] the g_{eff} can be approximated by

$$g_{eff} = 9.7840(1 - 0.00266 \cos(2\phi) - 0.28 \cdot 10^{-6}h), \quad (4.29)$$

with ϕ denoting the latitude of the station and h the height of the antenna above the geoid. Denoting the expression in parenthesis in Eq. (4.29) as $f(\phi, h)$, and applying the

values for the constants k_1 , R and m_d , Saastamoinen [1972] ends up with an expression for ZHD (in meters) as

$$\Delta\rho_h^z = 0.0022768 \frac{p_0 [\text{hPa}]}{f(\phi, h)}, \quad (4.30)$$

and claims the combined uncertainty of constants (k_1 , R and m_d) to be $5 \cdot 10^{-7}$ m.

Saastamoinen's formula (Eq. (4.30)), in a slightly modified, more precise form given by Davis *et al.* [1985] provides the hydrostatic zenith delay with accuracies better than 1 mm under the conditions of hydrostatic equilibrium (Niell [1996]). Because of a simple implementation and a requirement of only station latitude and height and surface pressure information, Saastamoinen's model is by far more used than any other model. Moreover, it is used to derive the *a priori* zenith hydrostatic delay in calculations presented in the next chapters.

If surface meteorological observations and the numerical weather model data are not available, the analytical model is adopted as a source for *a priori* meteorological information. Here only height dependence of pressure p , temperature T and humidity f above the sea surface is assumed (Berg [1948]),

$$\begin{aligned} p &= p_0 [1 - 2.26 \cdot 10^{-5} (h - h_0)]^{5.5225} \quad [\text{hPa}], \\ T &= T_0 - 0.0065 (h - h_0) \quad [^\circ\text{C}], \\ f &= f_0 \cdot \exp[-6.396 \cdot 10^{-4} (h - h_0)] \quad [\%], \end{aligned} \quad (4.31)$$

with corresponding values for pressure, temperature and humidity at the sea surface level:

$$\begin{aligned} p_0 &= 1013.25 \text{ hPa}, \\ T_0 &= 18^\circ\text{C}, \\ f_0 &= 50\%. \end{aligned}$$

Another, more experienced analytical model is the UNB3m latitude and height dependent prediction model (Leandro [2009]). A step forward is the derivation of a global model for pressure and temperature denoted as GPT by Böhm *et al.* [2007]. The pressure and temperature values are based on 3 years (September 1999 to August 2002) of global $15^\circ \times 15^\circ$ grids of monthly mean atmosphere profiles from ECMWF. This model, based on spherical harmonics expansion up to degree and order 9, includes annual variation of parameters and agrees with mean pressure values. Therefore no systematic

station height errors are introduced. Major pressure anomalies have been found over the Antarctic area when comparing GPT and the standard atmosphere approach (Berg [1948]) or pressure extrapolation used by Hopfield [1969] which also assumes a sea level pressure of 1013.25 hPa. Differences between GPT and standard atmosphere model pressure values are shown in Fig. 4.7. Precise pressure measurements are of utmost importance in calculation of *a priori* zenith hydrostatic delay. It has been shown (Davis *et al.* [1985], Hopfield [1969], Saastamoinen [1972]) that refractivity constants can be determined with high accuracy, however in order to reach a ZHD accuracy of 0.1 mm, pressure has to be measured with an accuracy of 0.05 hPa. In Sec. 5.3 it is shown how the errors in pressure value can influence the estimated ZWD.

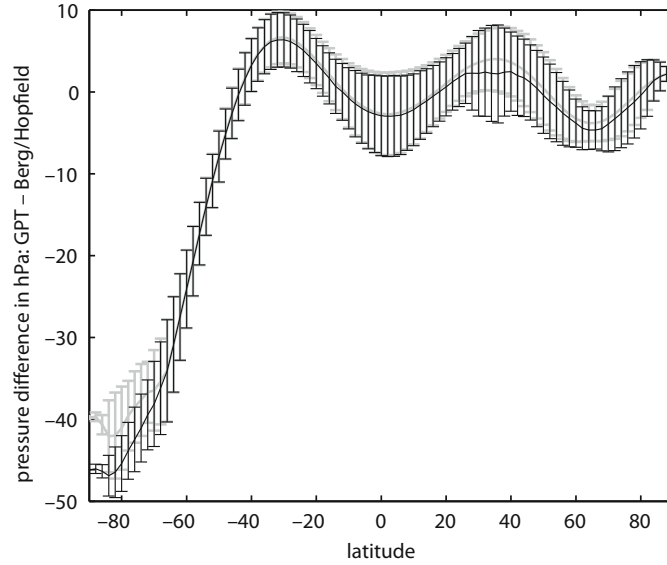


Figure 4.7: Pressure differences between GPT and the models by Berg (grey color bars) and Hopfield (black error bars) (*source: Böhm et al. [2007]*)

The hydrostatic path delay is in fact responsible for approx. 90% of the total tropospheric delay and in typical meteorological conditions it can be about 2.3 m at sea level in zenith direction. For an elevation angle of 5° the hydrostatic delay increases by a factor of 10. A model based on hydrostatic equilibrium as the one developed by Saastamoinen [1972] can be distorted in case of wind disturbances with a typical error of about 0.01% of the path delay (0.2 mm). These errors can even reach values of 20 mm if severe weather conditions occur (Davis *et al.* [1985]).

4.2.3.2 Zenith wet delay

The derivation of a model to account for the zenith wet delay (ZWD) is shown to be far more challenging than the one for the hydrostatic delay. This is due to high variability and unpredictability of the amount of water vapor, as it has been mentioned before. This is also a reason why numerous models have been developed over the past few decades while preserving either Saastamoinen's or Hopfield's model or their slight modification to determine the hydrostatic delay. The zenith wet delay varies between a few mm at the poles and about 40 cm above the equatorial regions. In order to keep millimeter accuracy in GNSS positioning, the ZWD is nowadays estimated as an additional parameter along with station coordinates during least squares adjustment. Nevertheless, some models are listed below and can be used as an initial value.

Saastamoinen [1972] proposes the calculation of the zenith wet delay $\Delta\rho_w^z$ based on ideal gas laws using a simple relation

$$\Delta\rho_w^z = 0.0022768(1255 + 0.05T)\frac{e}{T}, \quad (4.32)$$

where e is the water vapor pressure and T is the temperature. Similar to the hydrostatic delay, Hopfield [1969] proposes an expression for ZWD as follows,

$$\Delta\rho_w^z = \frac{10^{-6}}{5} N_w^{trop}(0) h_w, \quad (4.33)$$

with $N_w^{trop}(0)$ the refractivity of wet air at the surface (hence (0)) and a mean value $h_w = 11000$ m for the height of the troposphere up to which the water vapor exists. Ifadis [1986] proposes to model the zenith wet delay as a function of surface pressure, partial water vapor pressure and temperature. Mendes & Langley [1998] derived a linear relation between ZWD and partial water vapor pressure. Some other models are being described by Mendes [1999]. An approximate relation between water vapor pressure and density reads

$$\Delta\rho_w^z \approx \frac{0.217e}{T}. \quad (4.34)$$

Assuming an isothermal atmosphere with exponential decrease of water vapor pressure e , and assuming that water vapor exists until a height of 2 km, we get an approximation for the wet delay as a function of water vapor pressure at the earth's surface e_0

$$\Delta\rho_w^z \approx 748 \frac{e_0}{T^2}. \quad (4.35)$$

An even simpler way is a rule of thumb that suggests that the wet zenith delay in cm equals the water vapor pressure in hPa at the earth's surface. In any case, information of water vapor pressure and/or temperature at the surface has to be known. If no surface meteorological observation is available, we can use the simple model of the standard atmosphere described above in Eq. (4.31) where e can be calculated as a function of the humidity f , i.e.,

$$e = \frac{f}{100} \exp(-37.2465 + 0.213166T - 0.000256908T^2). \quad (4.36)$$

4.2.4 Slant delays

The line-of-sight component of hydrostatic and non-hydrostatic (wet) tropospheric delays can be obtained by scaling the zenith delays with geometric factors, widely known as *mapping functions*, to account for elevation angle dependence of the delay as shown in Eq. (4.23). Hydrostatic and wet mapping function, $m_h(\epsilon)$ and $m_w(\epsilon)$ respectively, provide the ratio of slant delay to the delay in zenith direction. For the first approximation, when evenly stratified atmosphere and no earth curvature is assumed, we can write

$$\Delta\rho_{tropo} = \Delta\rho_{tropo}^z \frac{1}{\sin \epsilon}, \quad (4.37)$$

where $\Delta\rho_{tropo}$ is the tropospheric slant delay, $\Delta\rho_{tropo}^z$ is the tropospheric zenith delay and ϵ is the elevation angle of the observation. The mapping function value approaches the $1/\sin \epsilon$ value as the thickness of the troposphere gets smaller (Niell [1996]). It has been shown that the hydrostatic zenith delays can be calculated with accuracies better than 1 mm (Saastamoinen [1972], Davis *et al.* [1985]), but the limiting factors in accurate tropospheric delay determination were deficiencies in mapping functions and negligence of the azimuthal asymmetry. Importance of mapping function accuracy and introduction of gradients increases as the elevation angles of the observations decrease. Observations at low elevation angle are critical to achieve a better satellite geometry, increase the amount of observations and de-correlate the estimates of troposphere delays and station heights. Accordingly, many different approaches in troposphere modeling were embraced and will be explained in the following sections. However, common to all of the approaches is the assumption of a hydrostatic equilibrium.

4.2.4.1 Mapping functions

Early mapping functions were based on the “cosecant” model (Saastamoinen [1972], Baby *et al.* [1988]) and were used to map the observations to an elevation angles above 10° . These mapping functions did not account for the curvature of the earth and consequently caused errors of more than 0.1 m at an elevation angle of 10° . A number of mapping functions were developed based on a quartic model introduced by Hopfield [1969]. A comprehensive description of those is given e.g. in Mendes [1999]. A significant contribution to the research was made by Marini [1972] who introduced the mapping function for horizontally stratified atmosphere based on a continued fraction form as shown by

$$m(\epsilon) = \frac{1}{\sin \epsilon + \frac{a}{\sin \epsilon + \frac{b}{\sin \epsilon + \frac{c}{\sin \epsilon + \dots}}}}, \quad (4.38)$$

with constant terms a , b , c , etc. Verification of the model with four sinus terms in expansion was carried out using the standard atmosphere model, but not real weather data. However, Marini found the agreement to be better than 0.3% down to elevations of 1° . A comparison with radiosonde data revealed the increase of standard deviation of range corrections from 20 mm in zenith to almost 200 mm at 10° elevation (Niell [1996]). The applied Marini concept was first presented in analysis of VLBI observations in Marini & Murray [1973], where the Saastamoinen model for zenith path delay and continued fractions with two constant terms were utilized. Based on the Marini model further mapping functions were introduced aiming at increased accuracy while lowering the elevation angle. Among those are: Chao [1974], Davis *et al.* [1985], Ifadis [1986], Herring [1992], Niell [1996].

Chao developed mapping functions that were applied for delay determination at stations where tracking antennas of the Mariner Mars 1971 spacecraft were installed. He applied continued fractions with two terms a and b , different for the hydrostatic and the wet mapping function, based on 2 year radiosonde data nearby the station antennas, and replaced the denominator of the a term in Eq. (4.38) with $\tan \epsilon$ to satisfy the unity of mapping function in the zenith direction. Davis *et al.* [1985] developed a mapping function, designated CfA2.2, applicable to the elevation of 5° by extending the Chao’s mapping function with an additional constant c , and using only sine functions of elevation (a tangent term led to errors of 1–2 mm for elevation angles between 20° and 60°). This mapping function shows differences to the radiosonde

(model) profiles at 5° to be less than 10 mm compared to ≈ 230 mm obtained by Chao's mapping function. The terms a and b were developed as linear function of total pressure, water vapor pressure, temperature, height dependent temperature gradients and height of the troposphere obtained by ray tracing through an idealized atmosphere model. Ifadis [1986] developed the global and climate dependent hydrostatic and wet mapping functions down to an elevation angle of 2° based on radiosonde data of 49 stations in the northern hemisphere and one in the southern.

The mapping function introduced by Herring [1992] (MTT mapping function) has a slightly different continued fraction form, i.e.

$$m(\epsilon) = \frac{1 + \frac{a}{1 + \frac{b}{1 + c}}}{\sin \epsilon + \frac{\frac{b}{\sin \epsilon + c}}{\sin \epsilon + c}}, \quad (4.39)$$

and this form remained in use to the present day. The MTT mapping function is based on radiosonde data from various sites in the US and requires only temperature, latitude and height of the station as input parameters. The coefficients are determined by least squares fittings for the hydrostatic and the wet component, for latitudes between 27° and 65° and station heights from 0 to 1600 meters. Both the MTT and Ifadis mapping function have a drawback in dependency of surface temperature. Changes that may occur in lower layers do not represent the conditions in the upper atmosphere and if the appropriate compensation is not included this will result in an erroneous hydrostatic mapping function.

The New Mapping Function, now called the Niell Mapping Function NMF was introduced in 1996 by Niell [1996], and was based on a continued fraction form shown in Eq. (4.39). The derivation of the a and b terms requires knowledge of only day of year (DOY) and station latitude and height. Thus, no meteorological data is needed. Additionally, a height correction term is introduced. For the wet mapping function only the station latitude is needed. A rather simple implementation and significantly reduced bias are the reasons that this mapping function is until recently the most frequently used one in analysis of space geodetic observations. The terms a , b and c were derived from profiles of US Standard Atmosphere for the northern hemisphere, stored for the months January and July, to the elevation of 3° . The inversion of seasons was used for the southern hemisphere by adding

half a year to the phase of the southern latitudes. However, this simple inversion of seasons introduces systematic biases to observations taken in the southern hemisphere. Meanwhile, Lanyi [1984] developed a total mapping function using an analytical approach for elevations down to 6° . The tropospheric delay is expanded up to the third order of refractivity, where second and third order capture the bending effect. The coefficient parametrization is based on knowledge of surface temperature, height of the tropopause, height of the isothermal surface layer and the temperature lapse rate.

In the last 10 years several mapping functions based on numerical weather models (NWM) were developed. The Isobaric Mapping Function IMF was introduced by Niell [2001] who used global NWM with 6-hour resolution to derive new coefficients of the continued fraction form shown in Eq. (4.39). Based on the dependence of the hydrostatic mapping function on atmospheric thickness, Niell investigated a possible empirical relation of coefficients with the geopotential height of constant pressure levels (isobaric surfaces) and found that a level of 200 hPa gives the best agreement. The derivation of a wet mapping function was based on coarse ray tracing through NWM at 3.3° . IMF requires as input the station latitude and height, as well as the height of the 200 hPa pressure level and the ratio of the wet path delay along a straight line at 3.3° elevation angle and its zenith delay. Böhm & Schuh [2004] applied a rigorous ray tracing approach for both hydrostatic and wet mapping functions at 3.3° . The Vienna Mapping Function VMF, as it is called, was developed using direct ray tracing through the ECMWF weather model, without intermediate step like IMF. The coefficient a was determined from the ray trace data, while the coefficients b and c were determined empirically as functions of the station latitude and DOY, and are symmetric w.r.t. the equator. However, the condition of symmetry of b and c showed some discrepancies in the Antarctic and equatorial regions up to 4 mm in the mean station height. In order to solve these flaws, the Vienna Mapping Function 1 VMF1 was developed with new b and c coefficients (Böhm *et al.* [2006a]). Comparison of VMF1 and NMF with radiosonde data reveals an improvement of station height precision from ± 1 cm for NMF to ± 3 mm for VMF1. The coefficients a , b and c of site-dependent VMF1 with 6-hour resolution for selected sites can be downloaded from the web-page <http://ggosatm.hg.tuwien.ac.at/DELAY/>. The global gridded VMF1 can be applied to calculate coefficients for any given location with agreement of 1 and 2 mm in the horizontal and vertical position component, respectively, when compared with site-specific VMF1 (Kouba [2008]). Also, the *a priori* hydrostatic zenith delays as well as predicted coefficients for the following day (0, 6, 12, 18 UT) are available for download. The VMF1 is till today the most accurate tropospheric mapping function,

however the main drawback is a rather complicated implementation in the software packages (coefficients update) compared to other mapping functions (e.g. NMF). For this reason Böhm *et al.* [2006b] developed a Global Mapping Functions GMF, based on spherical harmonics expansion up to degree and order 9, which is consistent with VMF1 but simple to implement. Consistency in this case refers to the longer (annual) variations. However, GMF like NMF is not able to capture weather changes with shorter signals and extreme, station dependent weather events.

In practice, there is always a trade-off between the minimum elevation angle of observations and accuracy of the mapping functions. Since the zenith hydrostatic delay is obtainable with decent accuracy and the high precision of wet delay is assured by a proper estimation procedure, any error in the mapping function will directly propagate to the vertical component of the position estimates. It has been shown by e.g. Niell [1991] and MacMillan & Ma [1994] that the error of the estimated vertical component is about one third of the error in mapping function when the elevation angle is set to $\approx 5^\circ$. If VMF1 is not implemented, and no surface meteorological data for the observing station is available, it is advisable to apply GMF together with the global pressure and temperature model GPT developed by Böhm *et al.* [2007]. This approach was adapted for ZWD calculation in Ch. 6.

4.2.4.2 Gradient modeling

The effect of azimuthal asymmetry of the neutral atmosphere around the GNSS station is captured by gradient determination as shown in Eq. (4.23). The importance of gradient modeling has been well documented in various papers, e.g. MacMillan [1995], Chen & Herring [1997], Meindl *et al.* [2004]. North and east gradients, G_N and G_E , which describe the azimuth dependence of the neutral atmosphere in the north-south and east-west component, respectively, are mapped with the gradient mapping function $m_g(\epsilon)$ to the elevation angle of the observation. As it has been mentioned before, the thickness (height) of the atmosphere is not equal, but increases from polar to the equatorial regions. For an observer at mid-latitudes, the path toward the equator will be longer, specially if the observations are at low elevations (see Fig. 4.8). Moreover, the signal travels through more humid equatorial regions. Modeled gradients also account for the impact of the local troposphere but additionally could capture some systematic and multipath effects. Therefore it is not always beneficial in sense of improved accuracy if the *a priori* gradients are applied.

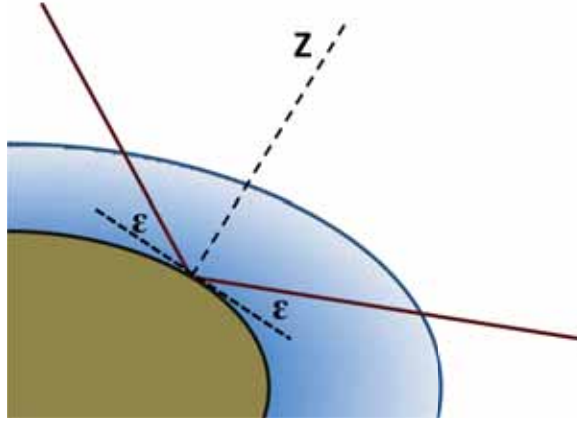


Figure 4.8: Azimuthal asymmetry

There are several approaches how to model the gradients. Generally, the linear horizontal gradients (LHG) are derived. This concept assumes that the gradients of refractivity at height h and azimuth α are valid at any horizontal distance around the site vertical. In GNSS analyses, the north and the east gradients G_N and G_E , respectively, are estimated along with the station coordinates and wet zenith delay. Gradients are then mapped to the elevation angle of observation ϵ using the gradient mapping function m_g . In most cases, the simple mapping model given by MacMillan [1995] is used, i.e.,

$$m_g(\epsilon) = m_h(\epsilon) \cot(\epsilon), \quad (4.40)$$

where $m_h(\epsilon)$ is a hydrostatic mapping function. In principle, it is not important which of the approaches for gradient modeling is used, except if a combination on the normal equation level is performed. Scaled to the elevation angle of e.g. 3° , gradient parameters correspond to a path delay of up to 50 cm. Gradient estimation contributes mainly to the improvement of position estimation in the horizontal component, and less in the vertical component.

Chapter 5

GNSS Meteorology

The wet component of the tropospheric delay is of special interest to meteorology as an additional data source for Numerical Weather Prediction (NWP). Several regional projects were initiated in Europe and abroad to derive the zenith wet delay from ground based GNSS observation data. The first continuous GPS network for meteorology was the NOAA GPS-IPW Network led by NOAA's Forecast System Laboratory in the USA in the 1990s (Wolfe & Gutman [2000]). Soon many regional and national projects with similar scope were started, e.g. COST Action 716¹, E-GVAP² and WAVEFRONT in Europe, BALTEX in Baltic Sea, MAGIC in Mediterranean, and others. While the accuracy of water vapor estimates based on microwave data is proven to be comparable to radiosonde and radiometer data, their timeliness is a major concern. To contribute to operational numerical weather prediction the water vapor content has to be made available within 45–60 minutes. This requirement is hard to fulfill taking into account delays in data transfer, the large amount of observation data to be processed and last but not least the accompanying requirements on real-time orbit accuracy.

5.1 Project GNSSMET

The importance of high resolution meteorological analysis of the atmosphere increased over the past years. A detailed analysis of the humidity field is an important precondition for a better monitoring of local and regional extreme precipitation events and for forecasts with improved spatial resolution. For this reason, the Austrian Meteorological Agency (ZAMG) is operating the spatial and temporal

¹<http://www.oso.chalmers.se/~kge/cost716.html/>

²<http://egvap.dmi.dk/>

high resolution INCA system (Integrated Now-casting through Comprehensive Analysis) since begin of 2005. The INCA analysis and now-casting system has been developed primarily as a mean of providing improved numerical forecast products in the now-casting range (up to +4 h) and very short range (up to about +12 h) and for application in mountain areas, hence special consideration is given to the treatment of orographic effects (Haiden *et al.* [2007]¹). For the three-dimensional INCA analyses of temperature, humidity, and wind, NWP forecast fields provide the "first guess" on which corrections based on observations from more than 200 ground meteorological sensor stations are superimposed. For the purpose of the "first guess" the output of the limited area model ALADIN is used which runs operationally at ZAMG since 1999. The surface sensor observations, together with radar and satellite data, topography data and forecast models represent the data-base of the INCA system. Updated analyses and now-casts are generated at 1-hour intervals. The operational availability of the now-cast is approximately 20 minutes after measurement time.

Errors in this analysis occur mainly in the areas of rapidly changing and hard to predict weather conditions or rugged topography with extremely varying altitudes such as the alpine area of Austria. Furthermore, considering a very sparse radiosonde network like in Austria, the humidity information from GNSS analysis becomes absolutely valuable. For that reason the project GNSSMET (Karabatić *et al.* [2010], Weber *et al.* [2008b]) was initiated with the aim to investigate potential improvements of weather forecasts by assimilating GNSS derived wet delays into a high resolution meteorological now-cast system such as the INCA system in Austria. Main requirements of the project were to provide GNSS based measurements of the integral tropospheric water vapor content with a temporal resolution of 1 hour and a temporal delay of less than 1 hour to assimilate these estimates into the INCA system. Additional requirement is an accuracy of better than 1mm of the precipitable water (PW) estimates.

The project GNSSMET started in September 2006 and the first phase ended in February 2008. The project was conducted by three collaborating partners: Vienna Technical University (TU WIEN), Austrian Meteorological Agency (ZAMG) and Carinthia power supplier (KELAG). Funding was provided by the Austrian Research Promotion Agency (FFG). The second phase of the project focused on the expansion of the network over the whole Austrian territory and the application of Precise Point Positioning technique for the zenith wet delay estimation.

¹http://www.zamg.ac.at/fix/INCA_system.doc

5.2 Station network



Figure 5.1: KELSAT network located in Austrian alpine region Carinthia (Kärnten) extended with IGS/EUREF stations Graz, Wettzell and Zimmerwald

The Austrian territory is covered by a dense network of GNSS reference stations with a mean station distance of 50 km. These stations were primarily established for providing nationwide geodetic network RTK services. For project GNSSMET, GNSS measurements taken from a subset of 8 GPS/GLONASS stations located in predominately high alpine area were utilized to set up a routine to process the zenith wet delays and to investigate further potential assimilation procedures. The station network KELSAT (Fig. 5.1) is located in Carinthia (Kärnten), Austrian alpine area, which is well known for rapidly changing and hard to predict weather conditions. During data processing this network was further tied to surrounding stations of the IGS and the EUREF network (Wettzell, Graz, Zimmerwald). Station Sonnblick is the second highest meteorological station in Europe and aside of meteorological sensors it is equipped with sensors for glaciology, climatology, chemistry, geology and other related sciences. Additionally, observations from the nearby GNSS station Kolm-Sigurn have been processed. This station, also equipped with pressure and temperature sensors, is located at the foot of the mountain Sonnblick and has a vertical distance to the top of about 1500 meters. This station constellation is adequate to monitor local rapid water vapor changes with an extremely high time resolution with regard to vertical profiles. Observation data were collected by the local power supplier KELAG and sent to their central office. An automated data transfer was set up between the KELAG central office and the Technical University of Vienna to deliver hourly GNSS observation data

with a time delay of a couple of minutes. However, hourly observation data from the IGS/EUREF stations Wettzell, Graz and Zimmerwald were delivered with a time delay of about 30 minutes resulting in significant latency of processing initialization.

5.3 Estimation of the zenith wet delay

The calculation of tropospheric parameters and station coordinates for the first phase of the project was based on a double-differencing approach (Dach *et al.* [2007], Hofmann-Wellenhof *et al.* [2008]). This approach requires simultaneous observations at two stations. Considering this, differencing the original observations allows to eliminate or reduce some biases such as satellite and receiver clock errors. Baselines between reference stations Graz, Wettzell and Zimmerwald and each of the KELSAT network stations were formed. The *a priori* coordinates of reference stations are tightly constrained to their ITRF2000 coordinates as provided by IERS. Remaining parameters to be estimated are therefore coordinates of the KELSAT stations and troposphere parameters (ZWD). To catch the temporal development of humidity and to restrict physically not-meaningful jumps of this parameter the most recent 12 hours of observations were stacked and processed using the Bernese software v5.0. Processing is started automatically at every full hour and 40 minutes, ensuring enough time for delivery of both KELSAT network and reference station data. For parameter estimation the ionospheric-free narrow lane linear combination was used. Further characteristics of the solution are a horizon mask of 5 degrees and the Saastamoinen model to calculate the *a priori* ZHD based simply on the station height and the standard atmosphere, and therefore not including any temporal variations of air pressure. The calculated *a priori* ZHD are introduced in the estimation process as knowns and ZWDs are estimated with a time resolution of 1 hour. The individual ray delays are mapped from the relevant elevation angle to the zenith by the inverse Wet Niell mapping function.

To separate more precisely the hydrostatic part from the non-hydrostatic contribution the exact pressure and temperature at the GNSS sensor stations has to be known or carefully extrapolated from nearby located meteorological sensor stations. Currently the ZAMG operates a network of automated stations at ~ 250 sites all over Austria for monitoring meteorological parameters (TAWES network, Fig. 5.2). Temperature, air pressure and humidity are measured at these stations with a temporal resolution of 10 minutes. The provided data allows us to feed in a parallel processing step the Saastamoinen model with surface data and to re-calculate the hydrostatic part (ZHD_{new}).



Figure 5.2: TAWES network

Fig. 5.3 displays the actual impact of the introduced real meteo-observations for station Klagenfurt. The full black line displays the ZWD estimated with respect to the hydrostatic delay calculated from a height-dependent standard atmosphere model (Dach *et al.* [2007]), and the full-crossed green line represents the ZWDs after correction of ZHD calculated from real pressure and temperature values extrapolated from the nearest TAWES station to the GNSS station by means of the following expression:

$$P_{GNSS} = P_{TAWES} \left(\frac{T_{TAWES} - \gamma(h_{GNSS} - h_{TAWES})}{T_{TAWES}} \right)^{\frac{g}{R\gamma}}. \quad (5.1)$$

The pressure at the GNSS station P_{GNSS} is extrapolated from the pressure measured at the TAWES station P_{TAWES} . T_{TAWES} denotes the temperature at the TAWES station, and h_{GNSS} and h_{TAWES} are the orthometric GNSS and TAWES station heights. The parameter γ represents the temperature gradient. The gravitational parameter g is calculated by a slight modification of Eq. (4.29) provided by (Hitsch [2004]) as follows

$$g(h, \phi) = 9.8063(1 - 10^{-7}h)(1 - 0.0026373 \cos(2\phi) + 5.9 \cdot 10^{-6} \cos^2(2\phi)), \quad (5.2)$$

and is dependent on the station height h and the latitude ϕ . At stations Klagenfurt, Koetschach and Sonnblick a TAWES sensor is installed next to the GNSS antenna. For other stations, the pressure and temperature data are extrapolated from the nearest

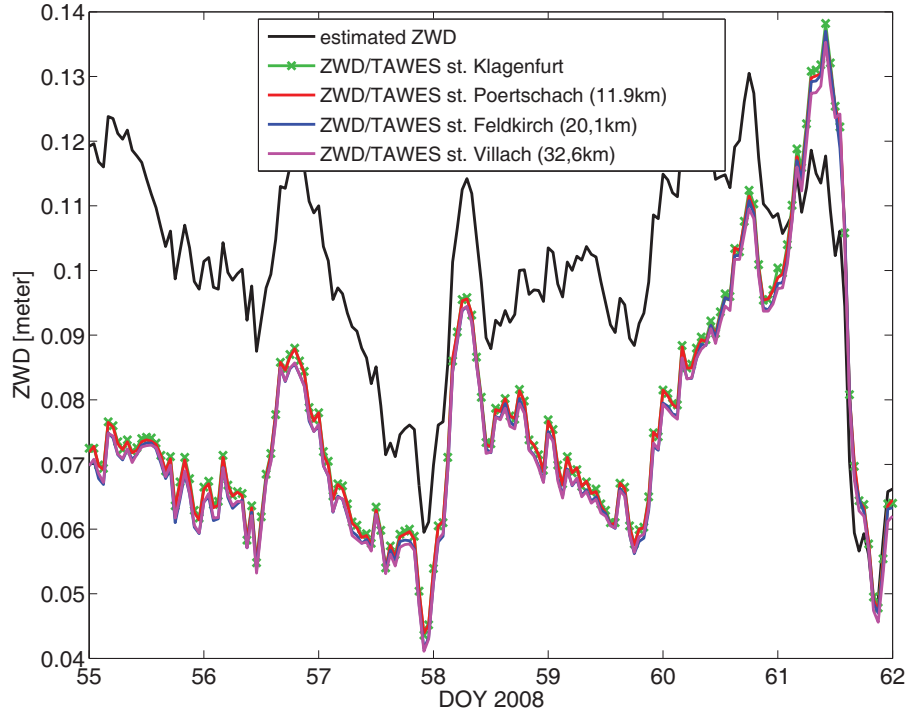


Figure 5.3: Comparison of ZWD estimates based on a priori ZHD from standard atmosphere and a priori ZHD from real meteorological data

TAWES station by means of the above described procedure. For comparison Fig. 5.3 also displays corrected ZWDs where pressure and temperature were extrapolated from TAWES station data observed at distances of 11.9 km, 20.1 km and 32.6 km. It can be noticed that pressure and temperature extrapolation over 20 km is possible within the desired accuracy (less than 1 mm ZWD). Recalculated ZWDs are delivered to ZAMG with a delay of about 45–50 minutes after the last recorded GNSS observation with a formal error of better than ± 1 mm. The formal error, resulting from the least-squares adjustment, is usually too optimistic in GPS parameter estimation due to the high correlation of subsequent observations. Under the assumption of accurate orbit information, a reliable estimated accuracy of these parameters is about ± 5 mm. More adequate to be used within the INCA system is the precipitable water which can be obtained from ZWD by multiplication with a factor of roughly 0.16 (see Sec. 5.5). This leaves us in the best case with an accuracy in PW of about ± 1 mm. Fig. 5.4 visualizes the described processing strategy.

Fig. 5.5 presents results of hourly data processing of the time span from February

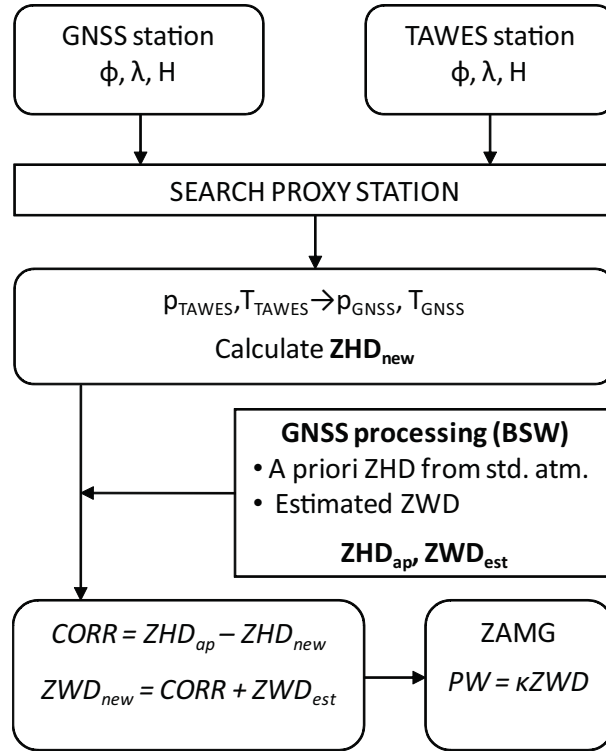


Figure 5.4: Scheme of the GNSSMET processing work-flow

24 to March 1, 2008. It can be clearly distinguished between two bulks of time series; the upper bulk shows ZWDs for stations at about 500–700 m elevation. The time series behave similar but slightly shifted due to moving atmospheric events over the area of the network (exception is the reference station Wettzell (WTZR) situated in south Germany). The lower bulk shows ZWDs for the stations Kolm-Saigurn and Sonnblick situated at heights of about 1600 m and 3100 m, respectively. For station Kolm-Saigurn a quite noisy behavior due to local obstructions can be noticed. The station Kolm-Saigurn is located in a very steep valley, surrounded with high mountains, and therefore obtains a significantly lower amount of observations. Due to increased formal errors of the ZWD at the station Kolm-Saigurn and due to errors in the *a priori model* for ZHD, ZWD time series show sometimes unrealistic negative values (e.g. DOY 55 or 59).

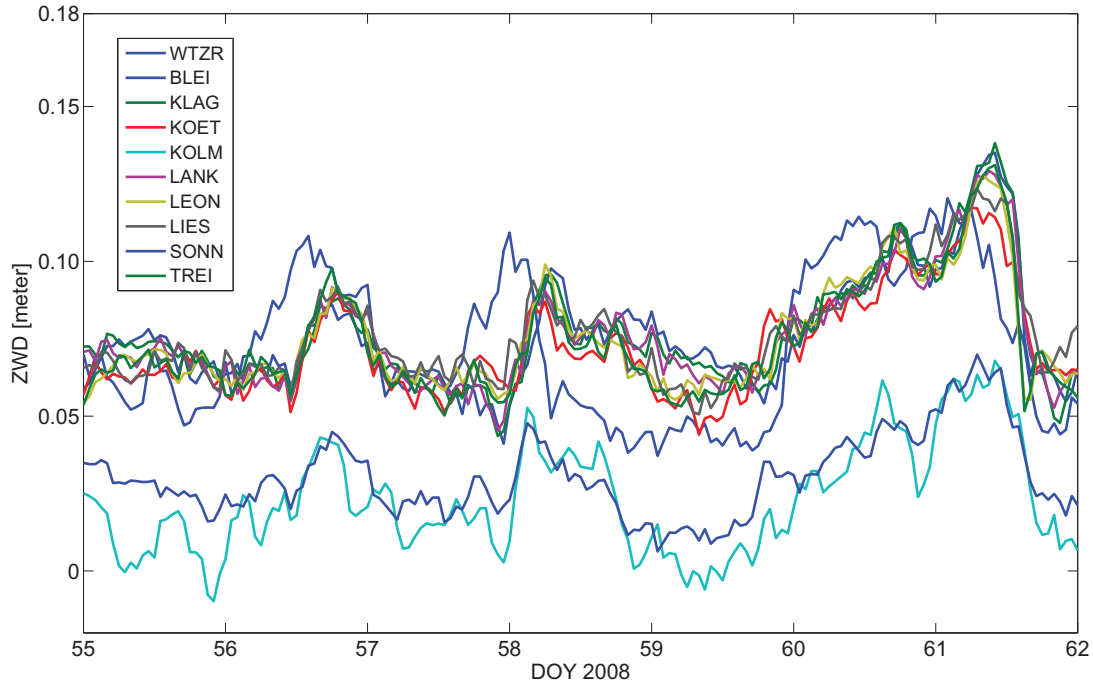


Figure 5.5: Estimated ZWDs for all network stations

5.4 Choice of orbits

To fulfill the requirement of delivering the PW estimates in less than one hour, the IGS ultra rapid orbit predictions (IGU) have to be applied. These orbits are delivered 4 times per day with an average accuracy at the few cm level. Fig. 5.6 shows the Weighted RMS (WRMS) of the IGS combined orbit predictions (IGU orbits) with respect to the post-processed IGS rapid products (IGR orbits) over 70 GPS weeks (July 27, 2008 – December 5, 2009). While the predicted part of the IGU orbits is rated to be worse only by a factor 2 compared to the rapid orbits, the problem are occasionally occurring outliers which may harm significantly the PW estimation. For that reason the ZWD is reprocessed with a delay of about a week using the IGR products as an verification of the near real-time solution and to obtain a high precision time series to support e.g. climate studies.

Fig. 5.7 displays as an example time series of hourly ZWD estimates covering a 36 hours span in April 2008 calculated once close to real time utilizing IGU orbit predictions and secondly as re-processed series using IGR orbit products. Depending on geometry and the number of satellites in view of the observing site the differences

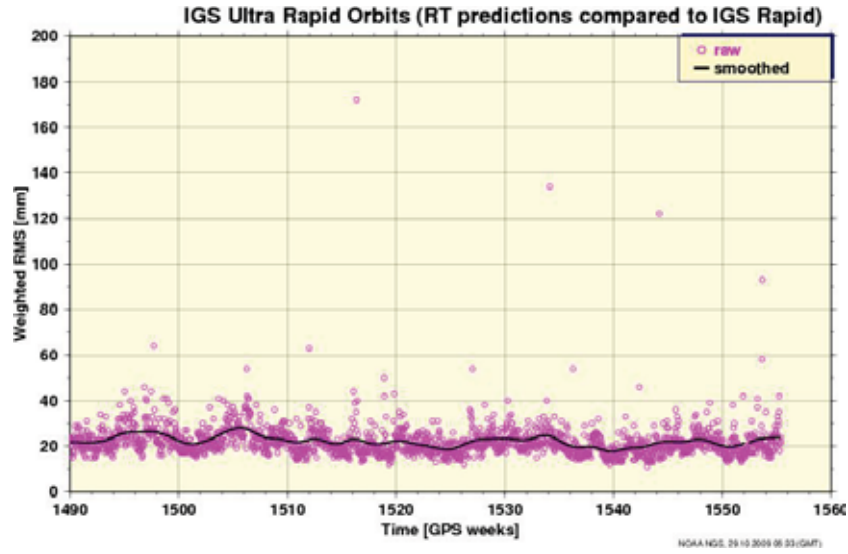


Figure 5.6: Weighted RMS of IGU (ultra-rapid) combined orbits compared to IGR (rapid) orbits (*courtesy of NOAA/NGS*)

are usually up to a few mm in ZWD but in the case of a mis-modeled satellite they may reach up to 2 cm. As a result of all available re-processed series it can be concluded that using the ultra-rapid orbits increases the formal errors of the ZWD estimates by approx. 50% (from ~ 1 – 1.5 mm) compared to the IGR solution. However, the re-processing based on 24-hour orbit information also infers physically not meaningful jumps of the ZWD estimates at the day boundaries accompanied by increased formal errors.

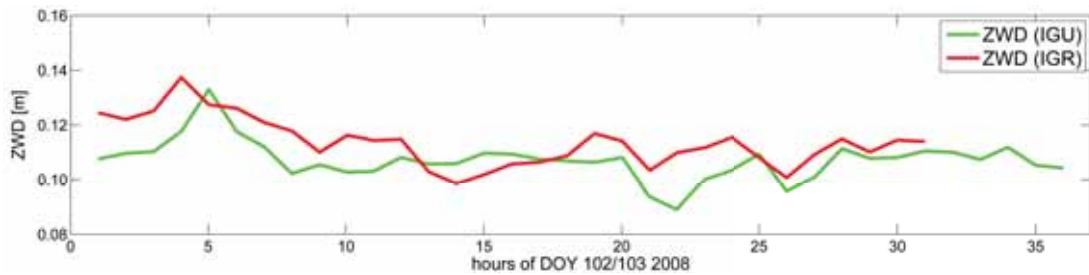


Figure 5.7: Comparison of ZWD estimates calculated using IGS rapid (IGR) and IGS ultra-rapid (IGU) orbits for station Bleiburg

5.5 Precipitable water

A more adequate value than ZWD to be used within the meteorological system is *precipitable water* (PW). The PW value corresponds to the height of the equivalent water column. It can be obtained using the following expression

$$PW = \frac{IWV}{\rho_{w,fl}}, \quad (5.3)$$

where IWV stands for *integrated water vapor* in the zenith direction and $\rho_{w,fl}$ is the density of liquid water. IWV is calculated as follows

$$IWV = \Delta\rho_w^z \cdot \Pi, \quad (5.4)$$

where $\Delta\rho_w^z$ is zenith wet delay and Π is defined using the equation of wet tropospheric delay (Eq. (4.22)), i.e.,

$$\Delta\rho_w = 10^{-6} \left[k'_2 + \frac{k_3}{T} \right] \int_s \frac{e}{T} Z_w^{-1} ds. \quad (5.5)$$

Applying the ideal gas laws (Eq. (4.19)), Eq. 5.5 can be reformulated as

$$\Delta\rho_w = 10^{-6} \left[k'_2 + \frac{k_3}{T} \right] \frac{R}{m_w} \int_s \rho_w ds. \quad (5.6)$$

The factor Π is now defined as follows

$$\Pi = \frac{10^6 m_w}{\left[k'_2 + \frac{k_3}{T} \right] R} \quad (5.7)$$

Precipitable water can also be expressed using a dimensionless quantity κ , i.e.,

$$PW = \kappa \Delta\rho_w^z \quad (5.8)$$

with κ defined as

$$\kappa = \frac{\Pi}{\rho_{w,fl}}. \quad (5.9)$$

The precipitable water is roughly 0.16 of ZWD. This value can vary with respect to station latitude and season. If the accuracy of ZWD estimates obtained within the GNSSMET project is ± 5 mm, this leaves us with an accuracy in PW of about ± 1 mm.

5.6 Validation and assimilation

A first inspection of the GNSS PW values confirms that special weather events like passing weather fronts can be easily detected in the data. Furthermore these PWs match the regional time delay of the front approaching at individual stations more reasonably than the INCA model.

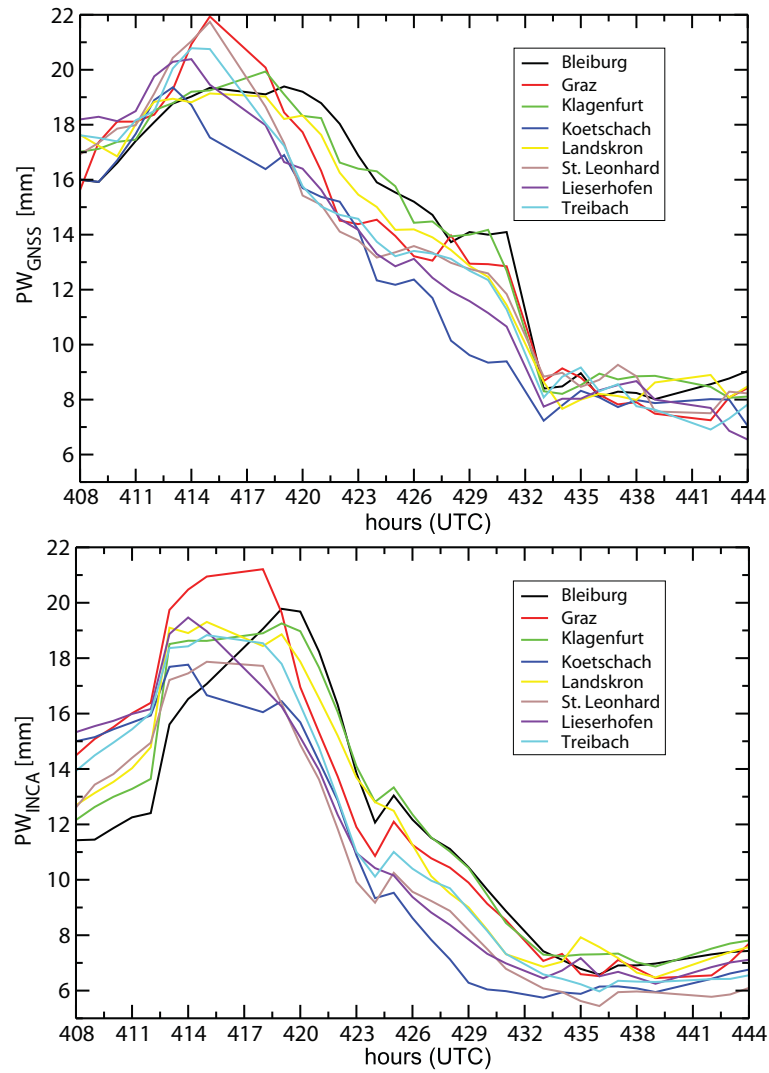


Figure 5.8: Weather front passing the area of Carinthia evident in the GNSS PWs time series (upper panel) and predicted by the INCA model (lower panel) for period October 18–19, 2007.

Fig. 5.8 displays a weather front passing the area of the KELSAT network as seen by the GNSS PWs (upper panel) and by the INCA model (lower panel) for the period October 18–19, 2007. Both methods indicate that the weather front affects the stations in the same sequence but the forecast model shows a steeper decrease of the humidity. In comparison with radiosonde (RASO) and surface (TAWES) observations gained at the nearby station Graz, the GNSS PWs match quite well the humidity content of the lower atmosphere (Fig. 5.9).

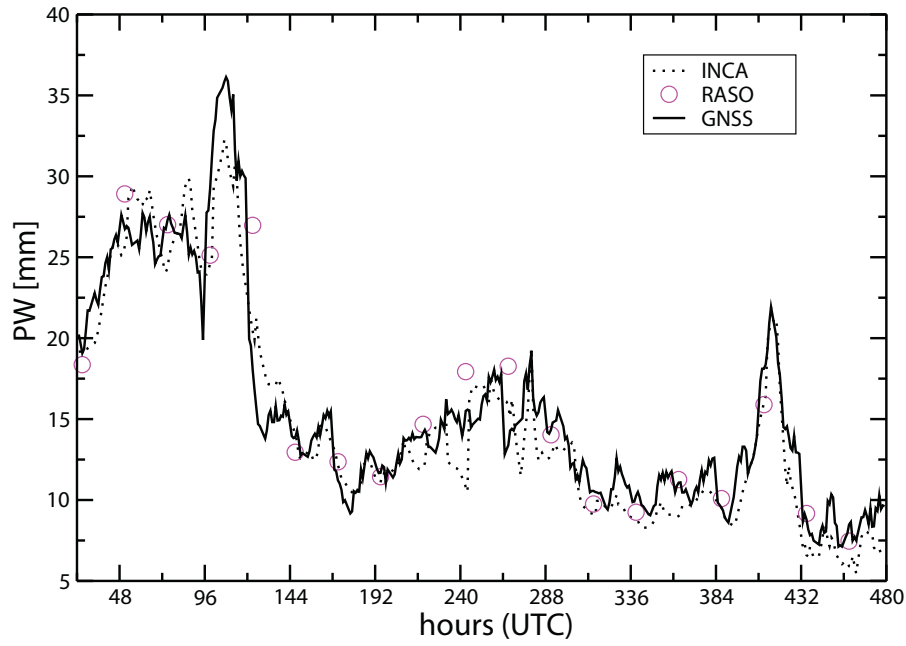


Figure 5.9: Comparison of PWs derived from the INCA model, radiosonde observations (RASO) and GNSS analysis (GNSS) for station Graz in period October 2–20, 2007

	RMS	BIAS
PW^{INCA}	1.95	-1.74
PW^{GNSS}	1.73	-0.51

Table 5.1: Bias and RMS between INCA and GNSS derived PWs and the radiosonde observation for the station Graz (in mm)

Table 5.1 shows the statistical comparison of INCA and GNSS derived PWs with

radiosonde observations gained at the station Graz. An increased bias of the INCA PWs implies some systematic errors. The accuracy of the PW estimates derived from the INCA system is difficult to estimate, and varies widely depending on the weather situation. Several possible error sources contribute to the total uncertainty. In addition to the actual measurement errors of the radiosonde data, there are errors due to imperfections in the NWP forecast of the temporal evolution of PW between radiosonde ascents (typically 12 or 24 hours). These are corrected by INCA only in the lowest 2–3 km layers of the atmosphere, depending on the maximum elevation of mountain stations in an area. In these lower layers, however, there is the problem that corrections derived from surface stations may not always improve the estimation of column water content. By comparing INCA PW with GPS-derived PW it is found that under conditions of strong insolation and low wind speed the near-surface humidity was not sufficiently representing the conditions in the free atmosphere to justify the station-based corrections in INCA.

When comparing the obtained results, it is usually assumed that the radiosonde values are the reference. However, it has to be considered that these measurements are also afflicted with sensor biases. There are several papers discussing the radiosonde biases, e.g. Niell *et al.* [2001], Wang & Zhang [2008], Haimberger *et al.* [2008]. In their comparative study of PW estimation based on different techniques, Niell *et al.* [2001] analyzed measurement errors of the widely used Vaisala radiosonde. They found that errors in relative humidity (on the order of 5%) and temperature (on the order of 0.5 K) are the main sources of error in the radiosonde measurements of PW. They found negative biases in the temperature and humidity measurements which could only partially be explained. In the case of humidity, a bias of about -5% appeared to be due to contamination by the packing material.

The approach developed at ZAMG to assimilate GNSS estimates is based on the subsequently described algorithm. To obtain the integrated value of PW at each point of the model grid the PWs from the INCA system are multiplied with the f_{ij} coefficients for each grid point i, j :

$$PW_{ij} = f_{ij} PW_{ij}^{INCA}. \quad (5.10)$$

To calculate the coefficients f_{ij} at each grid point, the following function has been

applied:

$$f_{ij} = \sum_{k=1}^N w_{ij}^k f_k(\theta, \phi) \quad (5.11)$$

The coefficients are weighted with respect to distance r of the GNSS station k to the

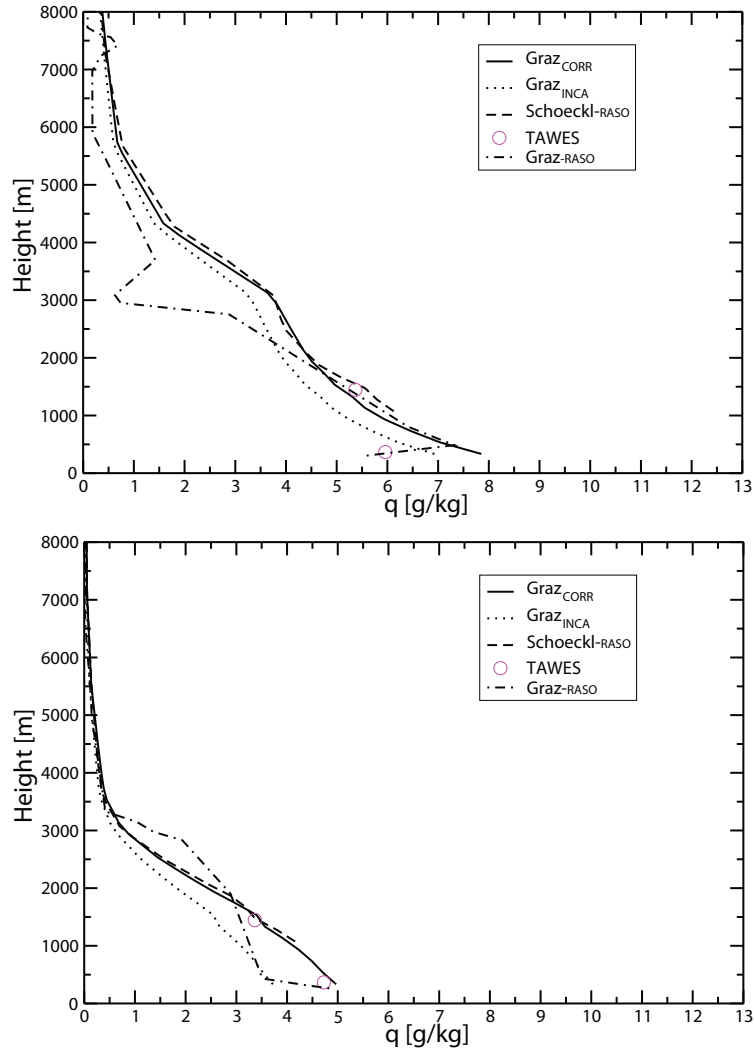


Figure 5.10: Humidity profiles over Graz for October 18th 2007 at 3 UTC (upper panel) and October 19th 2007 at 3 UTC (lower panel)

grid point using the following weighting function:

$$w_{ij}^k = \begin{cases} \frac{\frac{1}{r_k^2}}{\sum_l \frac{1}{r_l^2}} & \text{when } r_k \leq 100 \text{ km;} \\ 0 & \text{when } r_k > 100 \text{ km.} \end{cases} \quad (5.12)$$

r_l represents the distance of all relevant stations, i.e. the ones within 100 km (denoted with l). The multipliers f_k for each of the GNSS stations are calculated using the following expression:

$$f_k(\theta, \phi) = \frac{PW^{GNSS}}{PW^{INCA}}, \quad (5.13)$$

where PW^{GNSS} represents precipitable water derived from GNSS observations and PW^{INCA} represents precipitable water derived from the INCA system, and θ and ϕ are geographic longitude and latitude of station k , respectively.

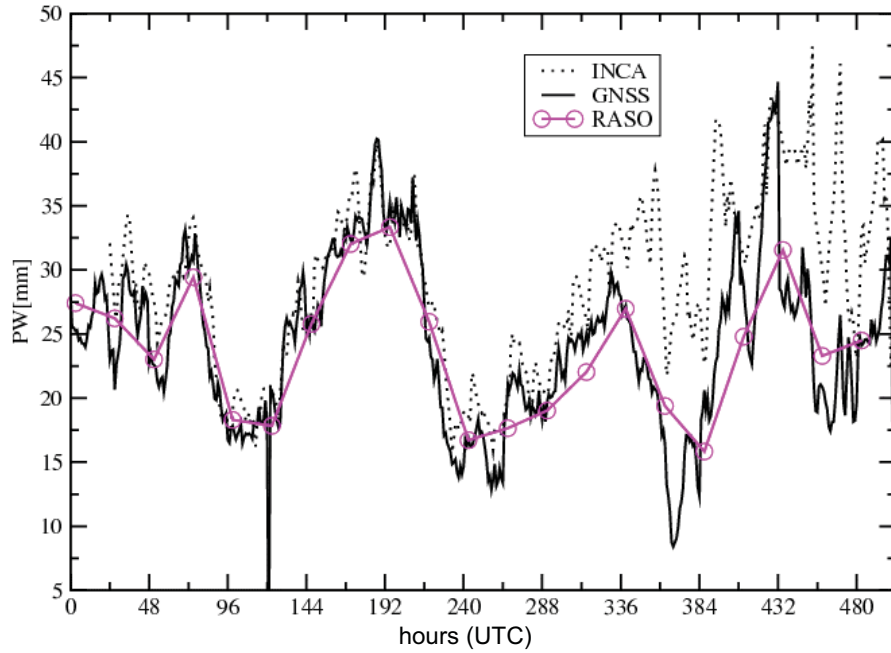


Figure 5.11: Comparison of PW determined by the INCA now-cast system, GNSS estimated and from radiosonde data at station Graz in July/2007

In a further step the GNSS PWs have to be introduced to correct the specific humidity field of the INCA model. This is quite problematic due to the integral characteristic

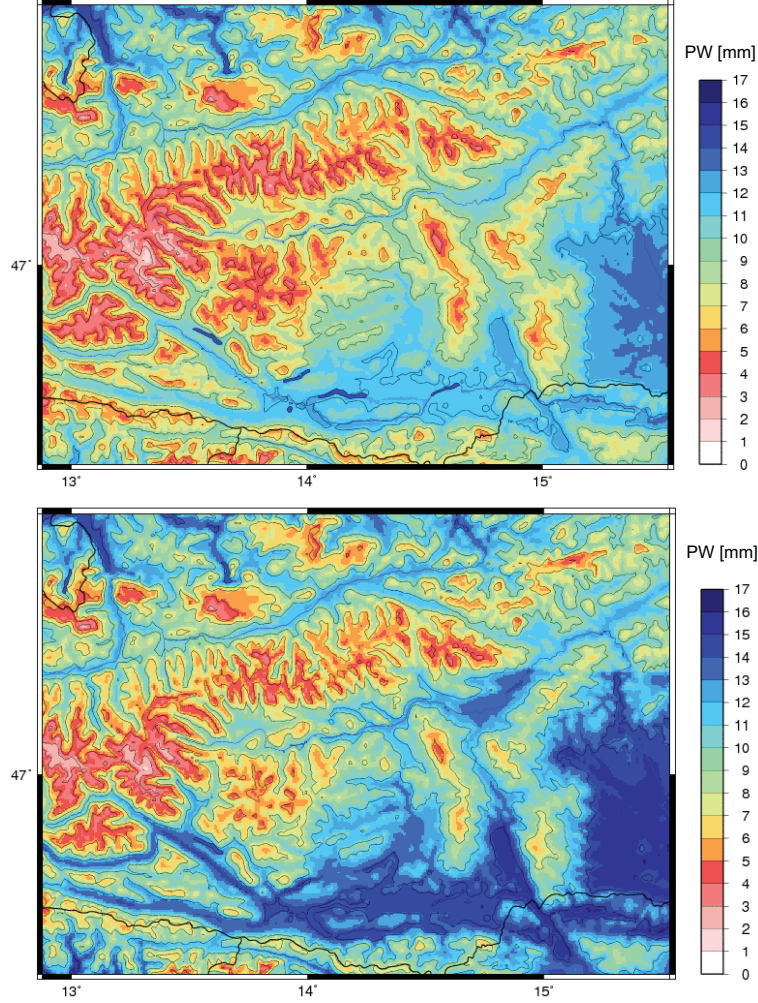


Figure 5.12: PW (in mm) over the KELSAT area on 13th October 2007 from INCA (upper panel) and assimilated GNSS estimates (lower panel)

of the GNSS estimates and the need of discrete humidity information at grid points of the INCA model. The chosen simple approach was to utilize a priori INCA humidity profiles and to apply again the f_{ij} functions to establish the GNSS corrected specific humidity $q_{ij}(h)$ at all grid points:

$$q_{ij}(h) = f_{ij}q_{ij}^{INCA}(h), \quad (5.14)$$

h indicating the grid point height. This procedure (factor common to profile) is quite promising but can also be problematic in case that the *a priori* information does not

cover the shape of the profile sufficiently. The comparison of the humidity profiles for October 18th 2007 at 3 UTC and October 19th 2007 at 3 UTC (Fig. 5.10) confirms a very good agreement between the radiosonde observation and GNSS assimilated data. For comparison, the radiosonde-pair Graz/Schöckl was used where one station is located in the valley (Graz) and the other one on the nearby mountain (Schöckl).

Fig. 5.12 provides the PW over the KELSAT area for 13th October 2007 at 3 UTC. The upper panel illustrates the raw INCA model and the lower panel INCA plus assimilated GNSS PW estimates (in mm). From the assimilation of the complete time series of GNSS estimates by the described procedure it can be concluded that GNSS PWs usually introduce a positive bias to the INCA humidity field which in general is not confirmed by the radiosonde measurements. In contrast, the extremely hot period in July 2007 (Fig. 5.11) was not properly accounted for by INCA and introduced a positive model bias. In this special case the GNSS PWs are confirmed by a perfect match of the radiosonde observations and allowed to reveal a model deficiency of the INCA model which was corrected shortly afterwards. However, it has to be noted that radiosonde measurements in Austria are solely available at few stations which are located in moderately mountainous areas.

Chapter 6

Troposphere monitoring using PPP

In the previous chapter, it has been shown how information about the humidity content and distribution within the atmosphere located above the network of stations can be retrieved using the GNSS ground observations. GNSS derived ZWD estimates have shown to be an important input for numerical weather models, particularly in areas with rugged topography or in cases of fast-moving weather fronts. Due to many benefits of GNSS ZWDs as an additional input for weather forecasting, national or regional GNSS networks are utilized for operational meteorology in a growing number of countries. Based on the promising results obtained from the test network KELSAT in Carinthia, a service covering the entire territory of Austria has been established. However, with the network extension a considerably larger amount of observation data has to be processed. An increased number of observations and demands for increased temporal resolution (1 hour or less) ask for a processing technique with short processing cycles without significant loss in accuracy, such as Precise Point Positioning. In order to evaluate the potential of PPP to derive the ZWD estimates with a satisfactory accuracy and time resolution, test calculations using a sub-network of stations in Austria have been performed. Static station coordinates and ZWD estimates are derived in a post-processing mode. Different test scenarios have been chosen to investigate the performance and possible shortcomings of the PPP technique.

6.1 Observation data

A network of 15 stations located in the southern part of Austria was used for this test calculations (Fig. 6.1). The selected stations are part of the EPOSA network (formerly TEPOS network), a collaborative station network of the Austrian Railway service ÖBB, the Viennese power supplier Wienstrom and the Burgenland power supplier BEWAG. Observation data of stations Sonnblick (SONN) and Kolm-Saigurn (KOLM) are provided by the Carinthian power supplier KELAG. Additionally, data from three closest IGS/EUREF stations, namely Graz in Austria (in Fig. 6.1 in red), Wettzell in south Germany and Zimmerwald in Switzerland were processed. These stations were used for a double-difference reference solution to which the PPP results were compared. Two sets of data have been selected, namely three weeks in March/April 2010 (March 27–April 16) and two weeks in June 2010 (June 13–June 26) with the goal to observe the ZWD in both an almost dry and the humid season of the year. The station constellation has been carefully selected to monitor the troposphere in extreme mountain areas as well as in valleys, i.e. to cover several levels of a vertical profile of the troposphere. As it can be seen in Tab. 6.1, the station height varies between approx. 200 m to 3100 m. The station distribution also allows to monitor fluctuation of weather events, particularly in west-east direction.



Figure 6.1: Map of sites used for this PPP study

Station	Latitude	Longitude	Ellipsoidal Height [m]
Graz (GRAZ)	47 04 01.7	15 29 36.5	538.3
Graz 2 (GRAR)	47 04 24.8	15 24 59.7	439.2
Kirschberg (KIBG)	47 26 55.3	12 18 31.1	876.7
Kolm-Saigurn (KOLM)	47 04 09.7	12 59 04.6	1679.6
Kötschach (KOET)	46 40 27.3	13 00 33.7	755.9
Leoben (LEOB)	47 23 13.0	15 05 26.3	607.7
Leibniz (LEIB)	46 46 51.0	15 32 48.2	334.4
Matrei (MATR)	47 07 37.9	11 27 09.1	1059.0
Neusiedlersee (NEUS)	47 57 38.1	16 50 11.7	224.0
Ochening Sud (OCHS)	46 56 13.6	13 12 43.6	1078.4
Rötenkogel (ROET)	47 10 12.5	12 38 27.6	2214.8
Sillian (SILL)	46 44 44.6	12 25 30.1	1146.3
Shladming (SHLA)	47 23 36.7	13 40 40.8	802.2
Sonnblick (SONN)	47 03 14.7	12 57 27.9	3168.0
Treibach (TREI)	46 51 38.8	14 27 49.6	671.4
Wolfsberg (WOBG)	46 50 31.3	14 50 19.5	523.9
Wettzell (WTZR)	49 08 39.1	12 52 44.1	666.0
Zimmerwald (ZIMM)	46 52 37.6	07 27 55.0	956.4

Table 6.1: Approximate geographic coordinates of network sites

6.2 Processing strategy

Data has been processed using the Bernese software (BSW) version 5.0 (Dach *et al.* [2007]). Traditionally designed as a double-differencing GNSS post-processing tool, this software has been updated with capabilities to process also zero-difference observations. Processing is organized within several main programs and a number of additional services to cover various user's needs. All programs offer manipulation of parameters, as well as changes in programming code and addition of custom-made processing scripts. Prior to processing, several input files have to be made available:

- observation data,
- orbit information and satellite clock corrections,
- general files including definition of the geodetic datum, a receiver information file, a phase center eccentricities and variation file, a satellite information file, a

satellite problem file, specification of the used nutation and sub-daily pole model, a pole offset file, etc.,

- a differential code biases file,
- an *a priori* coordinate file and a station name abbreviation file.

The general files are normally distributed with the software installation, however, the user is required to update them regularly. The Bernese software allows creation of an automated processing file, called Processing Control File (PCF) which lists all programs to be executed in a given sequence, or in parallel. The PCF file is executed through the Bernese Processing Engine (BPE), a service for automated and both interactive and non-interactive processing.

Data processing consists of several steps including the data import, orbit preparation, clock synchronization, cycle slip detection and parameter estimation. These steps are described in more detail in Appendix A.

6.3 Parameter estimation

Parameter estimation is based on the observation model given with Eqs. (3.27) and (3.28), and on a least square adjustment procedure described in Section 3.3. Daily 30 second phase and smoothed code observations are processed and the ionospheric-free linear combination of the observations is utilized to cancel the impact of the ionosphere. The IGS final orbits along with high-rate 30 second satellite clock corrections (Tab. 3.1) are applied to achieve the highest possible precision. The elevation cut-off angle is set to 5° . Observations at low elevations are generally much more sensitive to tropospheric refraction and multipath effects than those at high elevations. Unmodeled systematic errors decrease the quality of the results. Using low-elevation observations, however, enhances the geometry and allows decorrelation of ZWD- and coordinate height-estimates. The estimation of the tropospheric zenith delays and, consequently, the vertical component of the station positions is therefore improved. In order to optimize the use of low-elevation observations, an elevation-dependent weighting is used (Dach *et al.* [2007]). The introduced weighting function is defined by

$$w(z) = \cos^2(z), \tag{6.1}$$

with z being the zenith angle of the satellite.

Currently, the zero-difference processing mode within the BSW allows to process only GPS observations. There are two reasons why GLONASS observations cannot be used: (1) up to now there are no high-rate satellite clock corrections available for GLONASS, and (2) the GLONASS receiver code biases are not implemented. It is expected that in the near future many upgrades and additional software capabilities will be implemented to overcome these deficiencies.

Three groups of parameters are estimated in each processing run: troposphere parameters (ZWD), station coordinates and receiver clock offsets. ZWD estimates are modeled as piece-wise linear functions with chosen time resolution (e.g. every 1 hour), whereas the station coordinates and the receiver clock corrections are estimated in each epoch. There are no constraints applied to station coordinates. The receiver clock corrections are pre-eliminated epoch-wise to avoid large computational time. Epoch-wise parameter pre-elimination is possible because no correlation is assumed between the epoch parameters.

6.4 Estimation of zenith wet delay by PPP

With regard to troposphere estimation, several *a priori* models and program options have to be specified. The Saastamoinen model (Eq. (4.30)) was used to describe the *a priori* zenith hydrostatic delay. The Global Pressure and Temperature model (GPT, Böhm *et al.* [2007]) was applied with a height-dependent extrapolation of the pressure as described in Eq. (4.31). Any deviation of air pressure from the GPT model, and therefore the deviation of the calculated hydrostatic part of the tropospheric delay, will be captured within the estimated zenith wet delays. ZWD parameters were set up with a time resolution of 1 hour and the observations were mapped from the relevant elevation angle to the zenith by means of the Global Mapping Function (GMF, Böhm *et al.* [2006b]). Based on various test calculations investigating constraints between 0.1 mm and 1 cm “relative” constraints of 1 mm between consecutive tropospheric parameters have been specified which shaped up as the best trade-off between noise and mirroring real changes in PW at the hourly time scale.

Figs. 6.2 show the time series of ZWD estimates for March 27th, 2010 for all tested stations. The station sequence, from upper left to lower right panel, is set according to their ellipsoidal height starting from the nethermost one, namely station Neusiedlersee (NEUS) to the highest one, station Sonnblick (SONN), with three IGS/EUREF stations

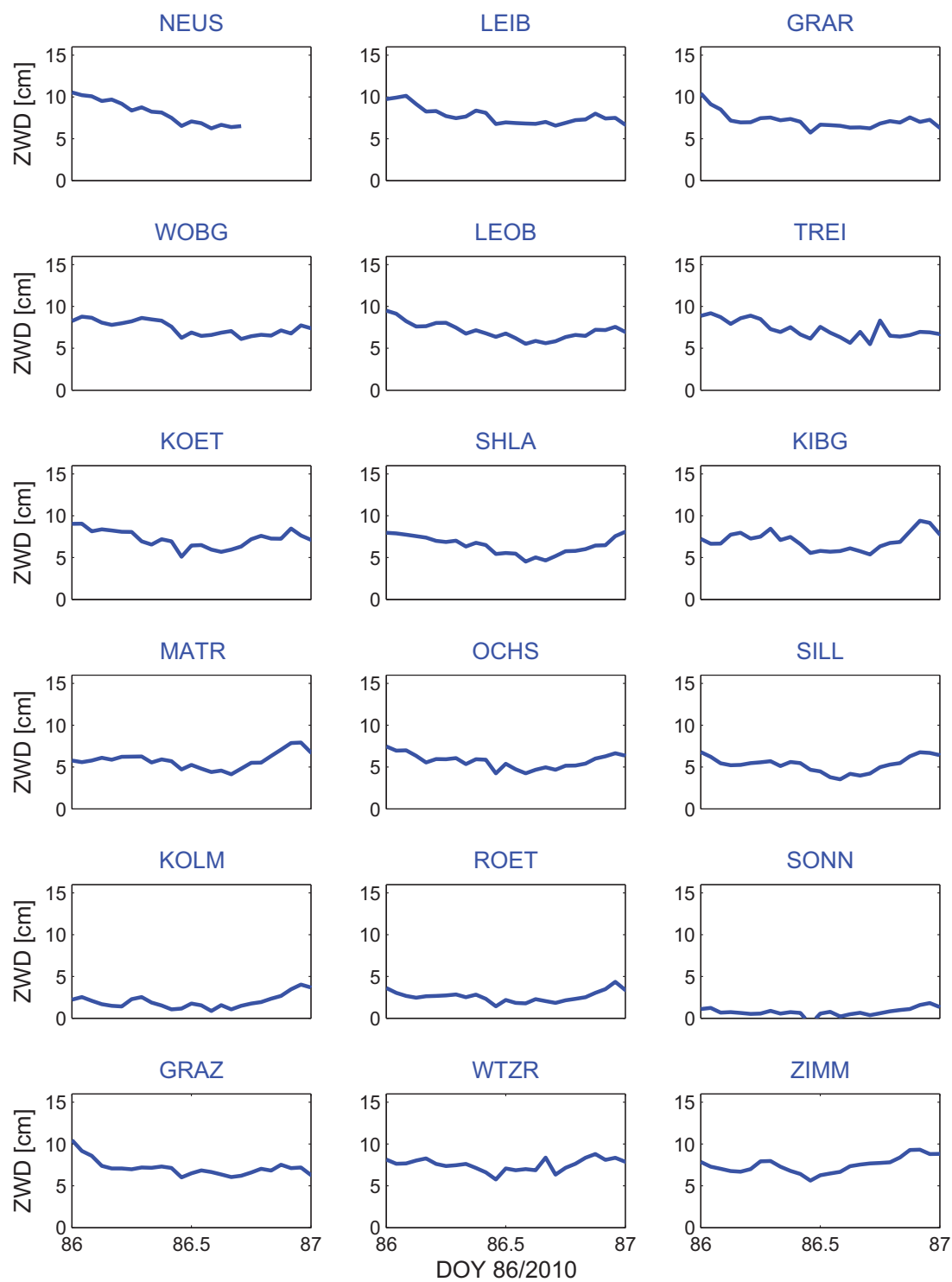


Figure 6.2: ZWD time series (in cm) of all stations on March 27th, 2010

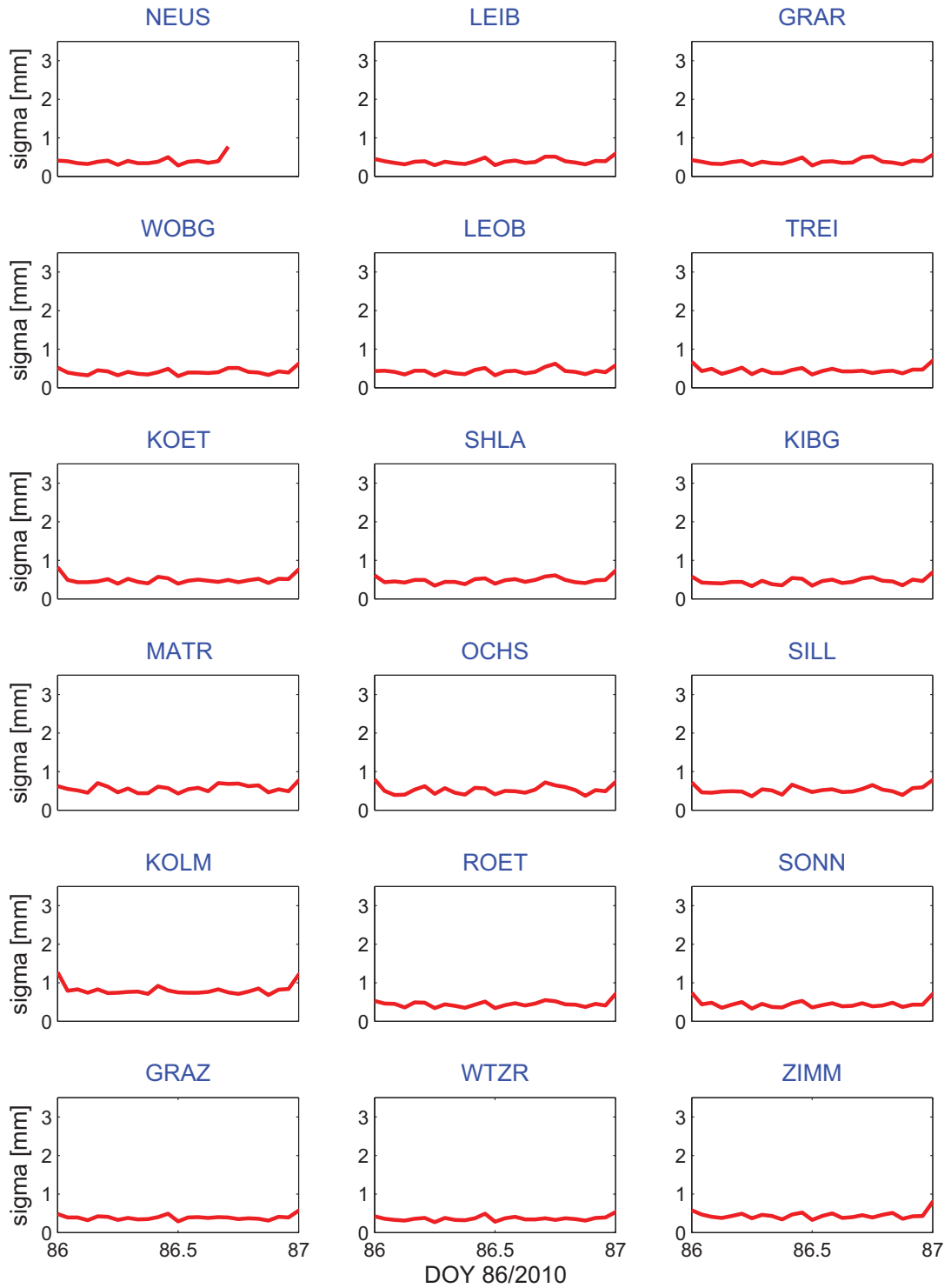


Figure 6.3: Formal errors of ZWD estimates (in mm) of all stations on March 27th, 2010

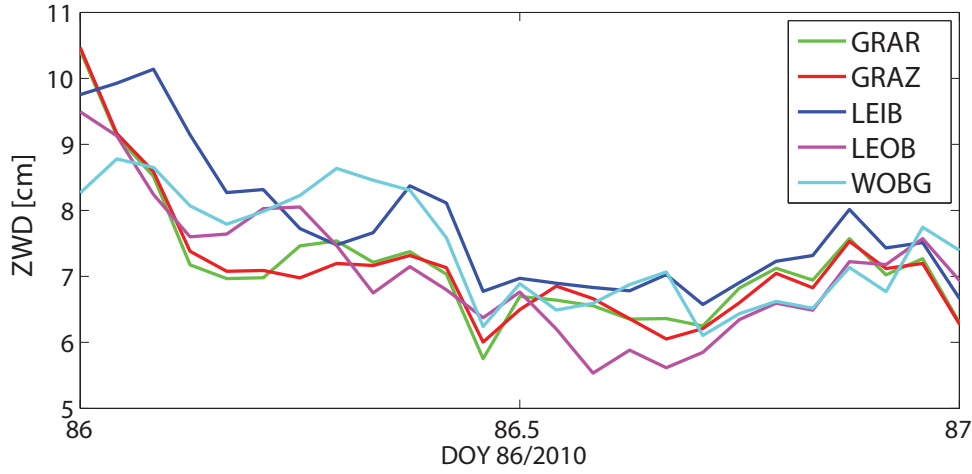


Figure 6.4: ZWD for station Graz and nearby stations on March 27th, 2010

Graz (GRAZ), Wettzell (WTZR) and Zimmerwald (ZIMM) displayed for completeness and comparison in the bottom row. It is clearly visible how the ZWD decreases with station height, indicating a lower amount of water vapor observed at higher stations. For a group of closely located stations, e.g. stations GRAR, GRAZ, LEIB, LEOB and WOBG, a similar time series behavior is noticeable, as the listed stations are under similar weather conditions. The similarity is also shown in Fig. 6.4 where the ZWD for the five aforementioned stations is displayed in more detail.

Fig. 6.5 shows the ZWD estimates of the two closest stations, namely Graz (GRAZ) and Graz 2 (GRAR). Estimates almost overlap as the same weather situation affects both stations. An offset of ZWD time series is visible in the case when the height difference between two horizontally close stations is huge. An example for this scenario is the station constellation SONN–KOLM. Station KOLM is situated at the foot of the mountain Sonnblick, and the station SONN is located at the very peak of the mountain, and their vertical distance amounts to ~ 1500 m (see Fig. 5.5).

Using Eq. (3.40), the formal errors of ZWD parameters are estimated. Following the display sequence of Fig. 6.2, the respective formal errors of the ZWD estimates of each station are shown in Fig. 6.3. Formal errors are in general less than 1 mm. Increased formal errors are common at the day borders; this is due to the utilization of 24-hour orbital batches and processing of 24-hour observation files.

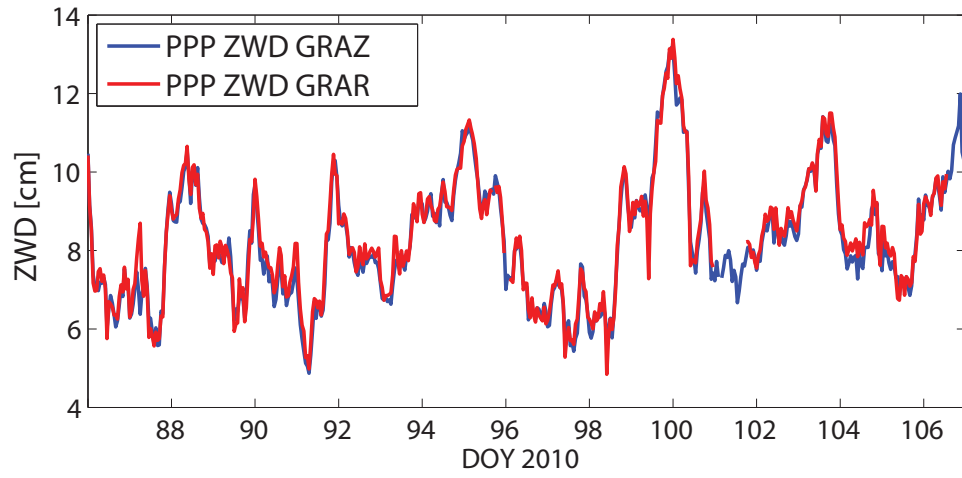


Figure 6.5: ZWD for station GRAZ and the nearby station GRAR (March 27–April 16, 2010)

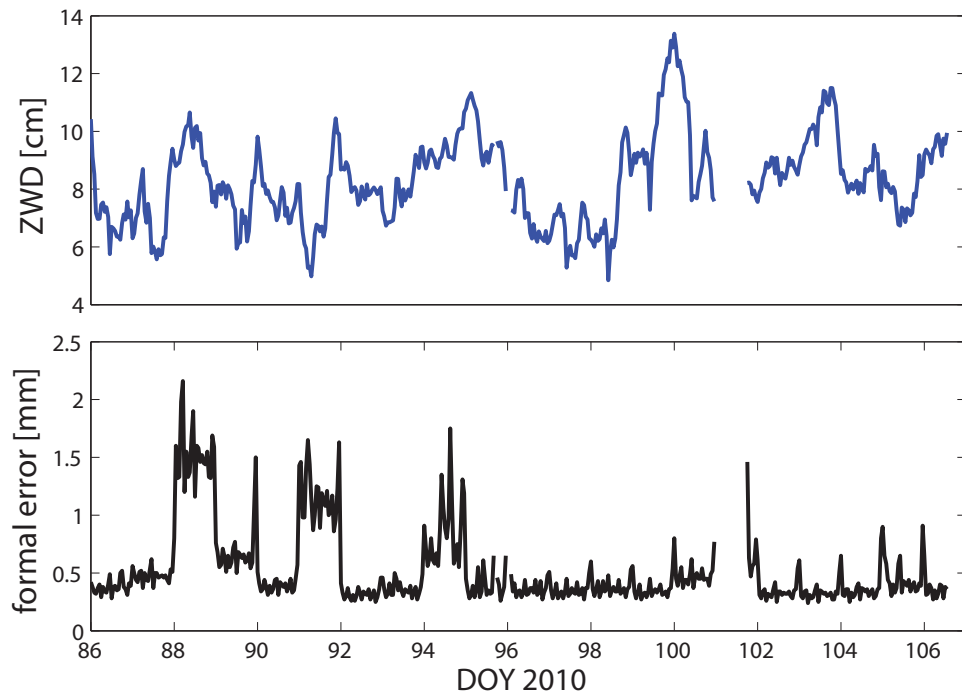


Figure 6.6: ZWD and formal errors of ZWD for station GRAR (March 27–April 16, 2010)

The ZWD time series and their respective formal errors over a three weeks time span (March 27–April 16, 2010) for station GRAR¹ are displayed in Fig. 6.6. The figure shows a relatively “peaceful” period with respect to the ZWD with the usual increase of ZWD in the mid-day hours due to the increased evaporation and consequently a decrease in the night hours. A steep increase in humidity content is obviously captured between DOY 98 and DOY 101 (April 8–11). On the lower plot the respective formal errors of ZWD estimates are displayed. On several days (DOY 88, 91 and 94) an increased formal error can be noticed, which is in most cases a consequence of incomplete observation data. Also, PPP is much more sensitive to inaccurately modeled errors such as satellite clock errors or satellite orbit errors. An increased formal error can further result from data gaps, such as in case of DOY 101, or occasional outliers.

Considerably higher formal errors and in general noisier behavior of the ZWD estimates is a common for station KOLM (see Fig. 6.7). This station, as it was mentioned

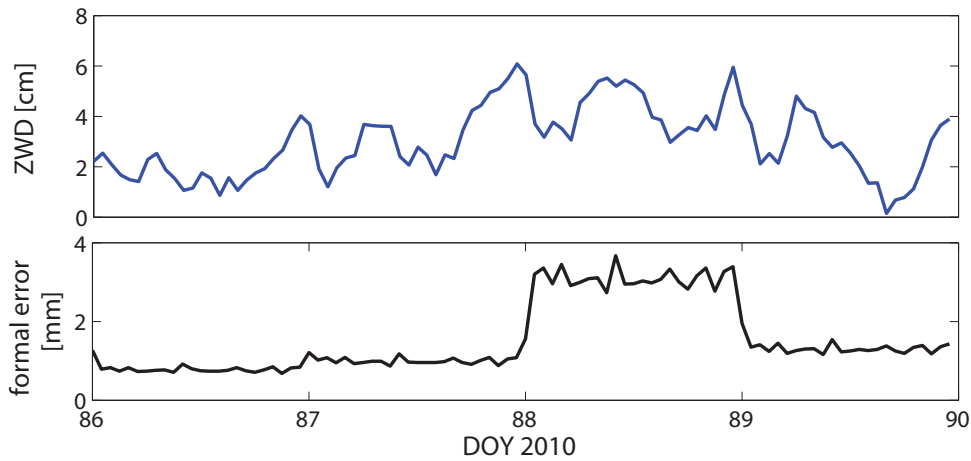


Figure 6.7: ZWD and formal errors of ZWD for station KOLM (March 27–March 29, 2010)

before, is situated at the mountain foot, and has a highly obstructed observation window with a lowest observed satellite’s elevation angle of about 16° and hence a lower amount of observations (about 30–40% less observations). The sky plot for station KOLM displayed in Fig. 6.8 visualizes the situation. For comparison, the sky plot for the non-obstructed station SONN is also provided.

¹Results and accompanying graphics for other stations are presented in Appendices B and C.

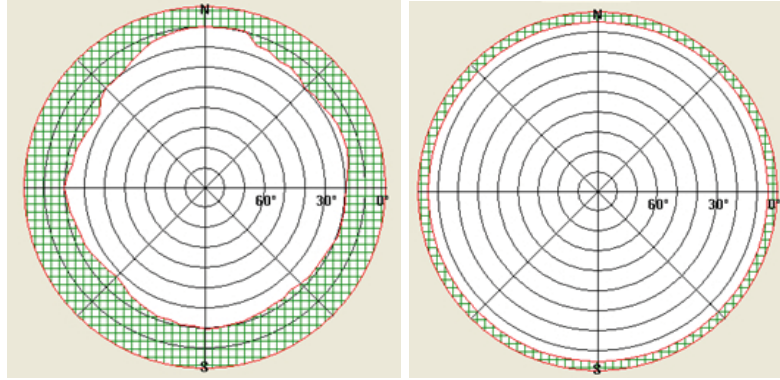


Figure 6.8: Sky plots for stations KOLM (left) and SONN (right)

Time series of ZWD estimates in the more humid period are shown in Fig. 6.9. Displayed are all tested stations in the same order as in Fig. 6.2. Fig. 6.10 displays the accompanying formal errors of the ZWD estimates. A first inspection reveals that the ZWD values are larger than in the colder, “drier” season (by a factor of 2–3), indicating an increased air humidity. The humid season is also characterized by steeper and more frequent changes of the ZWD value (see Fig. 6.11). Unfortunately, for the tested humid period data gaps and incomplete observation data files are present which can lead to increased formal errors. In the case of very fast passing weather fronts that cause rapid changes in air humidity, the formal errors of estimates can slightly increase. That is due to the fact that very frequent changes cannot be captured sufficiently by the selected temporal resolution of ZWD estimates and due to too tight constraints on consecutive (e.g. hourly) ZWD estimates.

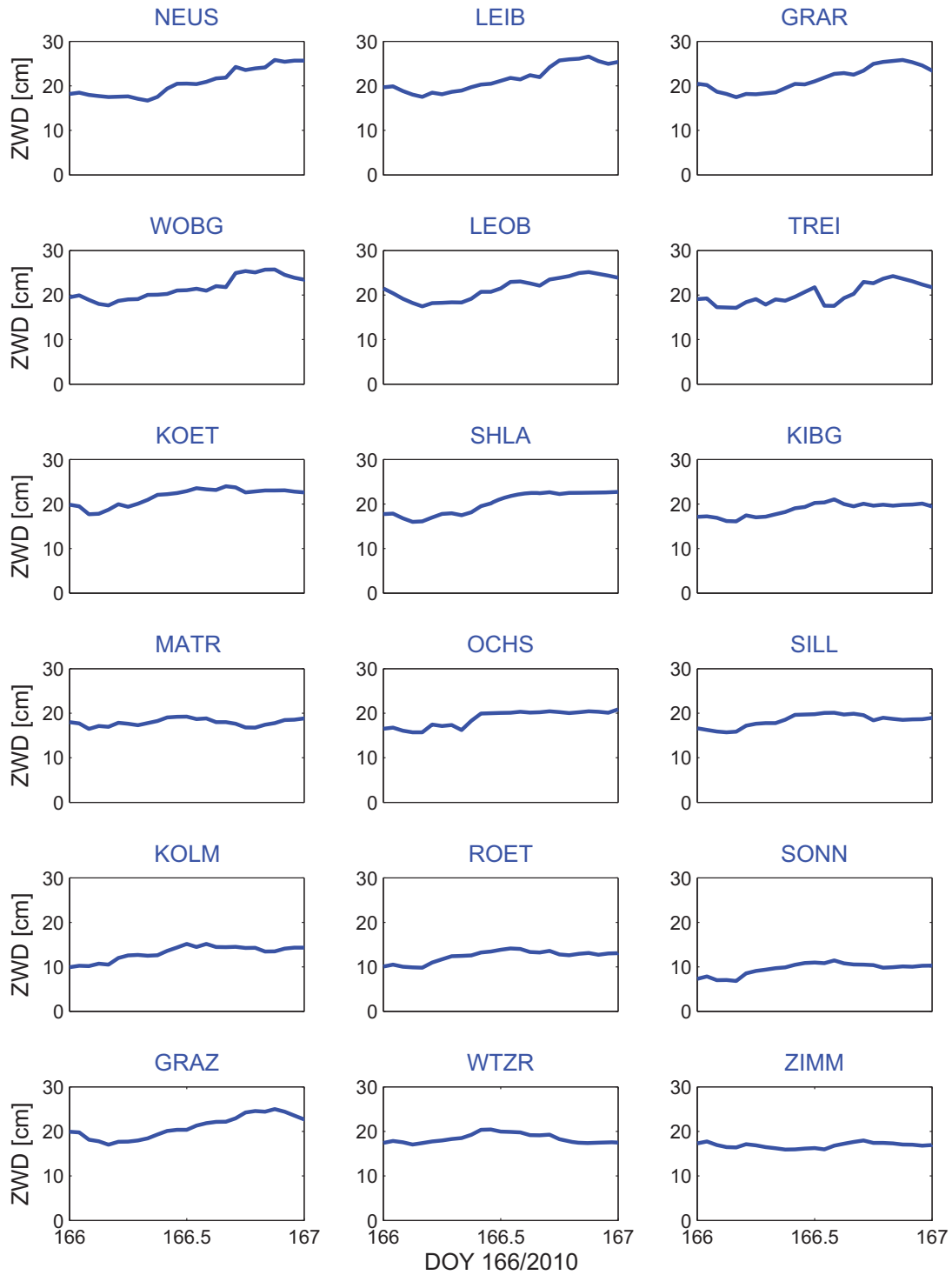


Figure 6.9: ZWD time series (in cm) of all stations on June 15th, 2010

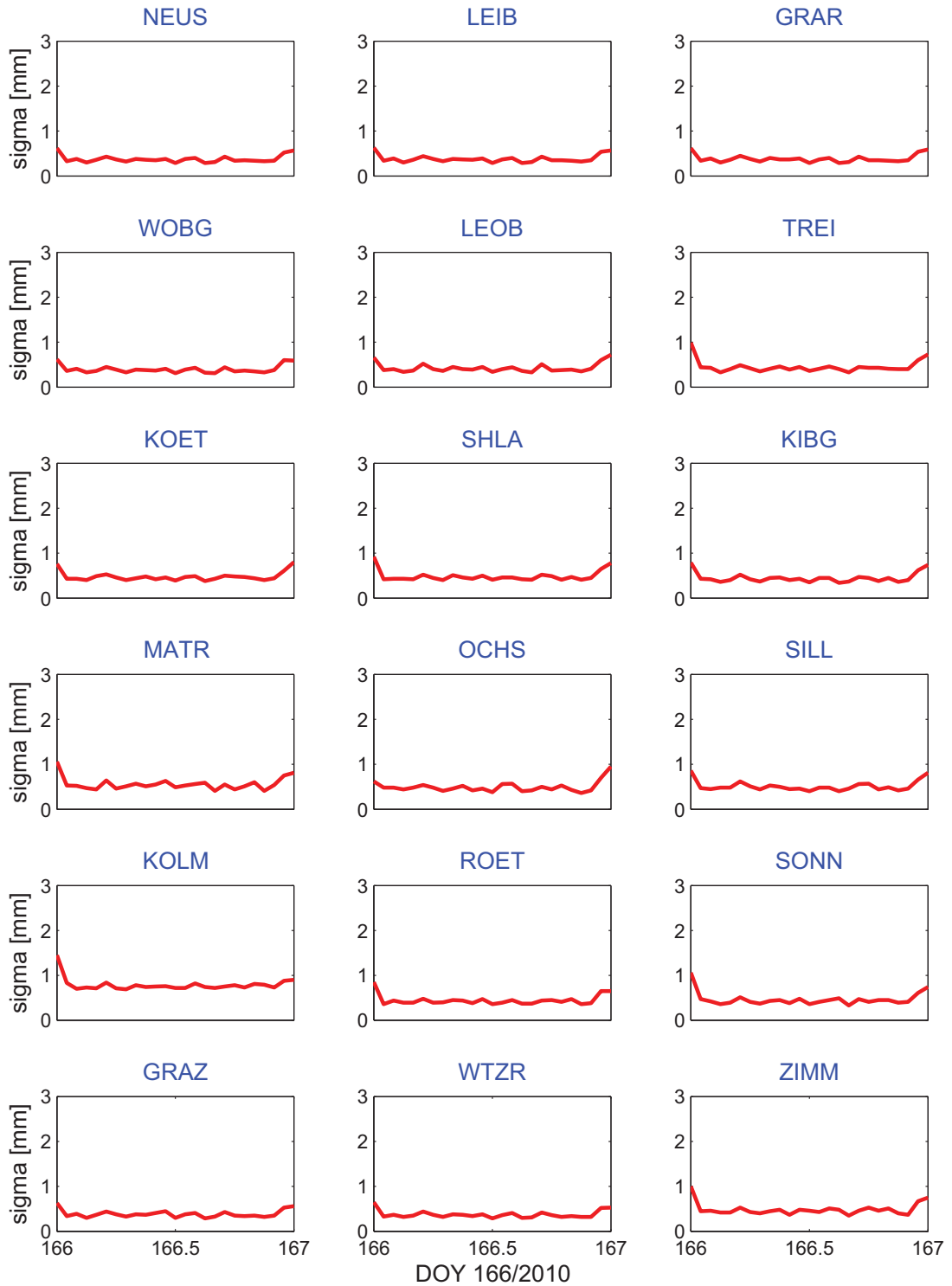


Figure 6.10: Formal errors of ZWD estimates (in mm) of all stations for June 15th, 2010

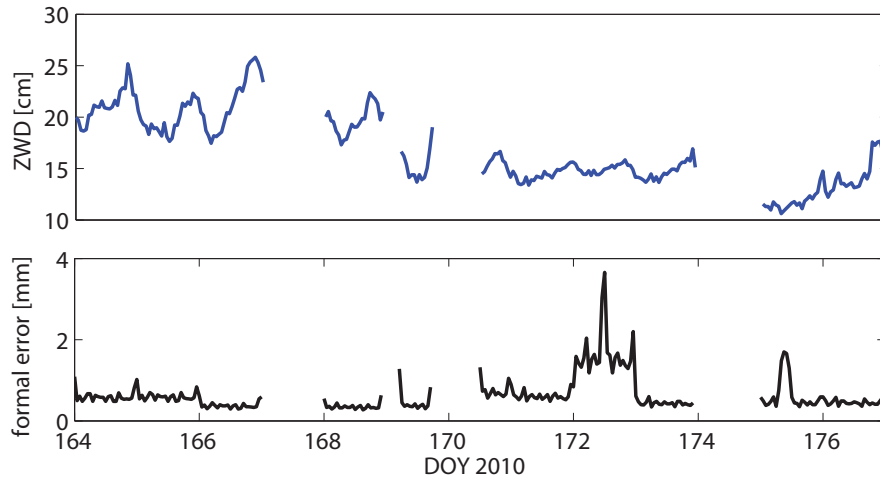


Figure 6.11: ZWD estimates and their formal errors of ZWD for station GRAR (June 13–25, 2010)

Fig. 6.12 displays the zoom-in of the ZWD for several stations for period June 13–15, 2010. The stations were selected to represent diverse height levels, which is clearly

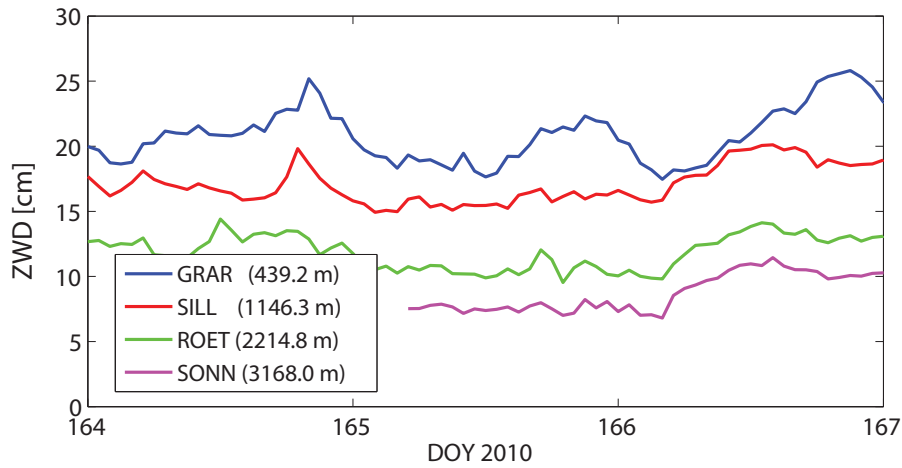


Figure 6.12: ZWD estimates for four stations on different station heights (June 13–15, 2010)

reflected by the vertically shifted ZWD estimates. The nethermost station GRAR experiences the largest variations of the air humidity, i.e. ZWD estimates, whereas the stations at higher altitudes show a more smooth change of humidity. Nevertheless, all

stations are affected in a similar way by the passing weather front.

6.5 Validation of the ZWD estimates

6.5.1 PPP versus double-difference solution

To validate the PPP solution, the ZWD estimates are compared to results of a double-difference (relative) network solution. The stations Graz, Wettzell and Zimmerwald were used as reference stations in a double-difference (baseline) solution. Baselines from each of the reference stations to each of the test stations were created. The same elevation angle (5°), *a priori* atmosphere model (GPT), mapping function (GMF) and ZWD constraints (1 mm relative constraints, with an hourly resolution) were used. Fig. 6.13 shows the comparison between ZWD estimates from the PPP solution and from the relative solution for station GRAR, for the period March 27–April 16, 2010.

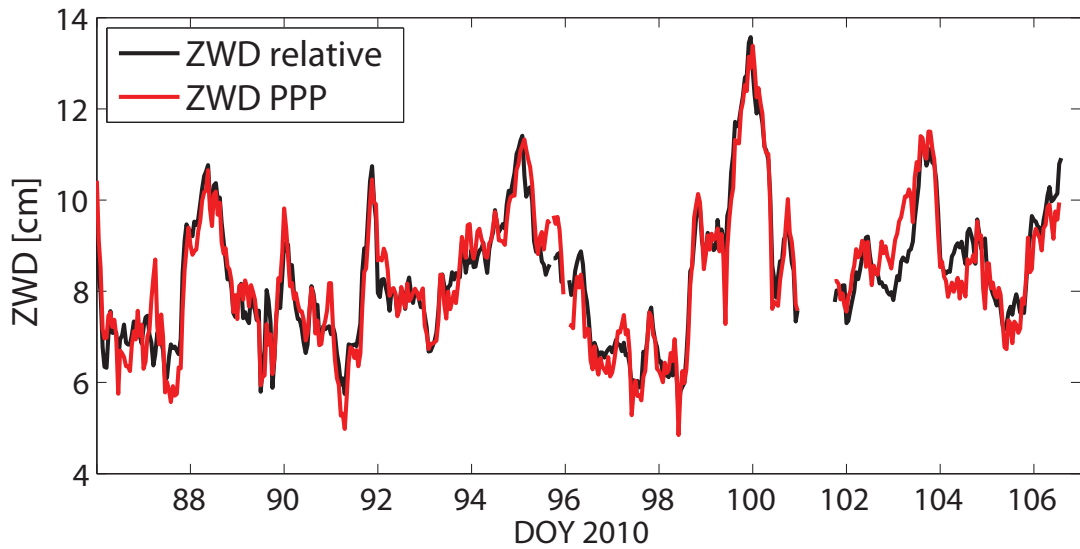


Figure 6.13: Comparison of ZWD estimates derived from PPP and double-difference solution for station GRAR (March 27–April 16, 2010)

Tab. 6.2 lists the mean formal errors of the ZWD estimates for the double-difference and the PPP solutions and the median and maximal differences between the two solutions per station. For all stations the mean formal error is less than 1 mm, although in the case of PPP it is slightly increased. Differences between ZWD estimates are

Station	mean σ_{DD} [mm]	mean σ_{PPP} [mm]	median ZWD diff. [cm]	max. ZWD diff. [cm]
GRAR	0.4	0.5	0.33	2.08
GRAZ	0.3	0.5	0.34	1.54
KIBG	0.4	0.6	0.38	5.77
KOET	0.4	0.6	0.36	3.89
KOLM	0.6	1.5	0.49	1.45
LEIB	0.4	0.5	0.31	2.21
LEOB	0.4	0.6	0.36	2.49
MATR	0.5	0.8	0.38	3.61
NEUS	0.4	0.5	0.32	1.95
OCHS	0.5	0.7	0.35	2.34
ROET	0.4	0.6	0.34	3.50
SHLA	0.4	0.7	0.35	5.01
SILL	0.4	0.7	0.36	3.15
SONN	0.4	0.5	0.34	2.26
TREI	0.4	0.6	0.41	13.43
WOBG	0.4	0.5	0.32	2.14

Table 6.2: Mean formal errors, and median and maximal differences of double-difference and PPP solution for all stations

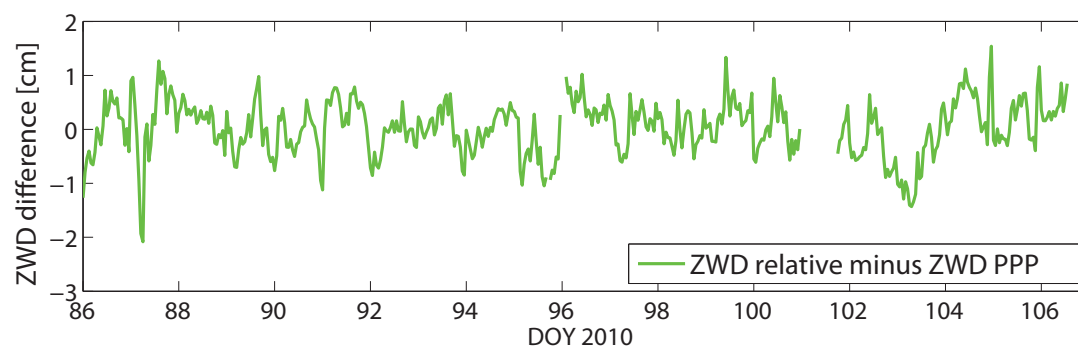


Figure 6.14: Difference of ZWD from PPP and double-difference solution for station GRAR (March 27–April 16, 2010)

normally in the range of ± 1 cm (Fig. 6.14¹), however, occasionally large outliers can occur as in the case of stations KIGB, SHLA and TREI. The mean ZWD difference is for almost all stations zero. In the case of station KOLM we experience a slight shift from zero (approx. 1.5 mm) probably originating from a reduced number of observations.

Comparing the formal errors of the estimates reveals that the level of consistency is rather high (Fig. 6.15). PPP estimates are, however, much more sensitive to data gaps, incomplete data records, misbehaving satellites and unmodeled outliers, and for that reason we can expect a more noisy behavior of the ZWD time series also documented by larger formal errors.

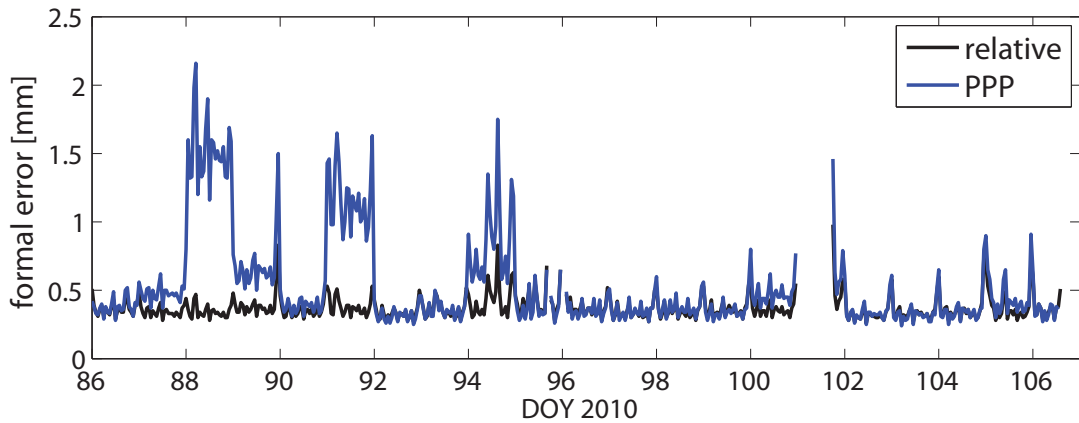


Figure 6.15: Comparison of formal errors of ZWD estimates from PPP and double-difference (relative) solution for station GRAR (March 27–April 16, 2010)

Table 6.3 lists the *a posteriori* root mean square (RMS) of the unit weight of the double-difference (DD) and the PPP solution during the period of March 27–April 15, 2010. This number should be in the order of 1–2 mm when elevation-dependent weighting is applied. The RMS of the PPP solution should be less than ~ 1.5 mm. An increased RMS could indicate poor data quality or preprocessing problems.

¹The figure depicts the ZWD differences for station GRAR. Differences for all other tested stations are shown in Appendix C.

DOY	86	87	88	89	90	91	92	93	94	95
DD	1.1	1.1	1.0	1.1	1.0	1.1	1.0	1.0	1.0	1.0
PPP	1.3	1.6	5.1	2.2	1.3	3.6	1.1	1.1	2.2	1.1
DOY	96	97	98	99	100	101	102	103	104	105
DD	1.0	1.0	1.0	1.0	1.1	1.1	1.0	1.0	1.0	1.0
PPP	1.1	1.1	1.2	1.1	1.6	1.5	1.1	1.1	1.1	1.3

Table 6.3: A posteriori RMS (in mm) of unit weight of double-difference and PPP solution for March 27–April 15, 2010

6.5.2 Comparison of results with IGS solution

The Troposphere Working Group of the IGS provides daily ultra-rapid and final tropospheric zenith total delay (ZTD) estimates for IGS stations as a contribution to meteorology, climatology and other related environmental disciplines. Eight¹ IGS analysis

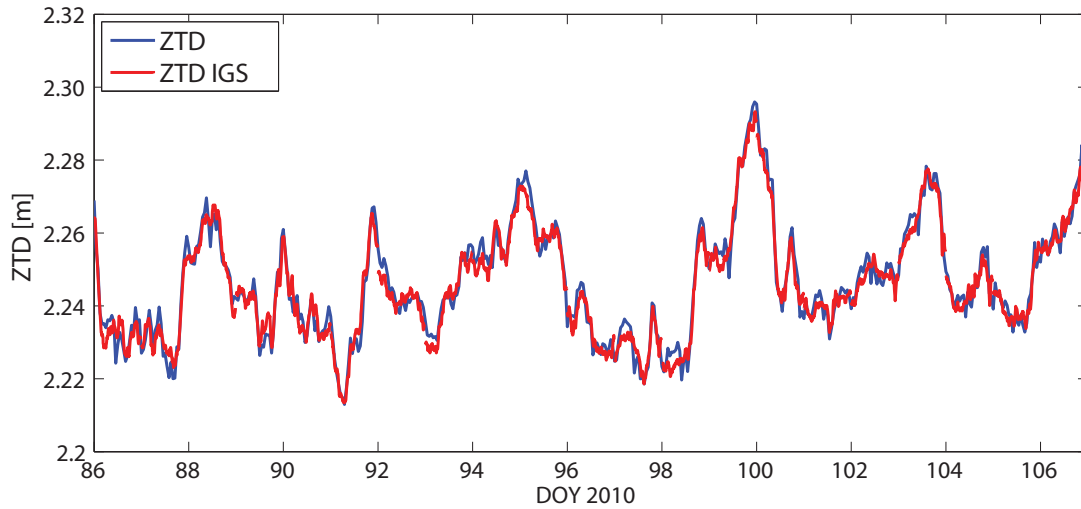


Figure 6.16: Comparison of PPP ZTDs provided by IGS and estimated within this thesis for station Graz

centers provide the troposphere products: CODE, NRCAN, ESOC, GFZ, GOP, JPL, SIO and USNO. The IGS troposphere coordinator collects the individual solutions of the analysis centers and publishes the daily files at the IGS web page².

¹<http://igs.cb.jpl.nasa.gov/projects/tropo/index.html>

²ftp://cddis.gsfc.nasa.gov/pub/gps/products/trop_new/

The ZTD time series for the period March 27–April 16, 2010 (DOY 86–106) of the IGS station Graz were downloaded from this web page and compared to the estimated PPP ZTD (Fig. 6.16). The IGS ZTDs with a 5-minute resolution were estimated by JPL using the PPP GIPSY software. Daily 30 s GPS-only data was used along with the IGS final orbit and clock products. The elevation cut-off angle was set to 7° and the tropospheric signal delays were mapped to the zenith using the Global Mapping Function. An increased temporal resolution of 5 min as opposed to hourly estimates is a reason for increased formal errors shown in Fig. 6.17 (12 times more estimates lead to almost three times larger formal errors). Both solutions utilize 24-hours processing batches, which is reflected in the increased standard deviation at day boundaries.

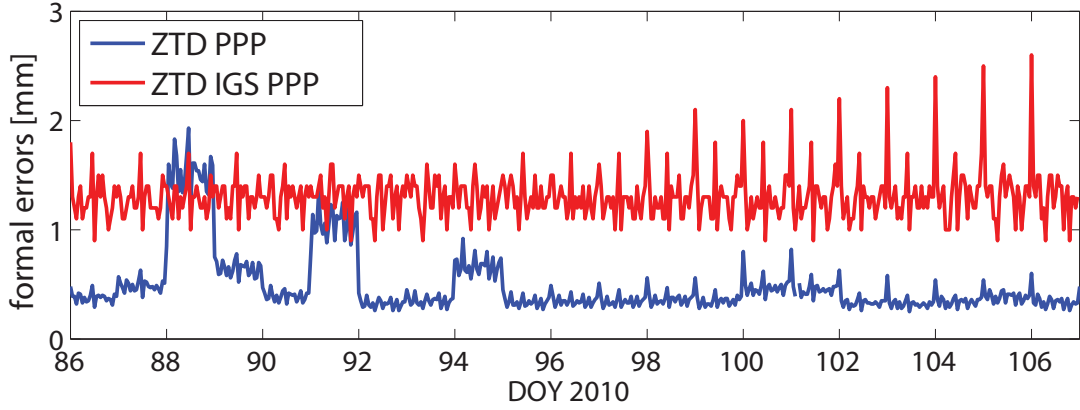


Figure 6.17: Standard deviation of the IGS PPP ZTD and PPP ZTD estimates established in this thesis (station Graz)

The difference between the two solutions is shown in Fig. 6.18. The differences between the IGS ZTD and our solution are generally between ± 5 mm, but the time series show an extremely periodical (12- and 24-hour) behavior. The periodical behavior could be caused by the difference of constraints for the ZTD estimates. The IGS ZTD estimates were constrained to 3 cm per hour (random walk), whereas the test calculations use much tighter constraints (1 mm). Note, that the temporal resolution of the IGS estimates is 5 min, and the constraints are given with an hourly resolution. However, to draw a firm conclusion, more insight into the processing algorithm used for the IGS ZTD estimation should be provided.

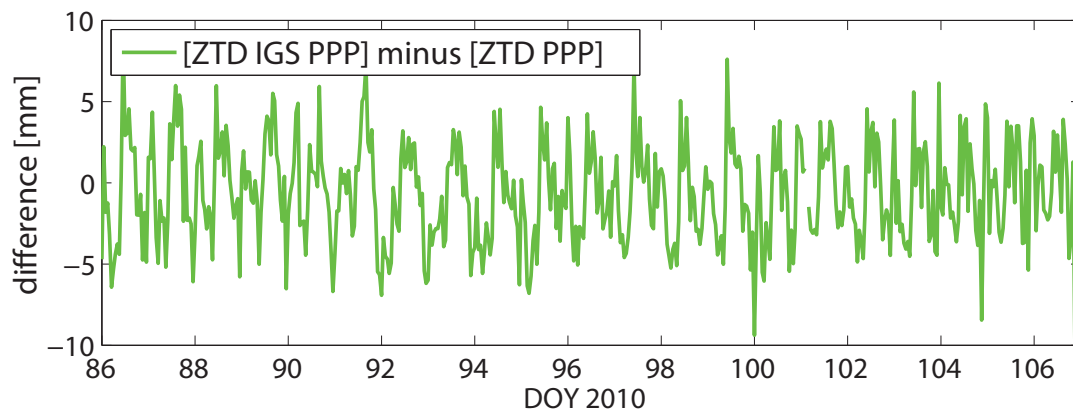


Figure 6.18: Difference between the IGS PPP ZTD and PPP ZTD time series (station Graz)

6.5.3 Meteorological data

The variability of the tropospheric wet delays is also mirrored in observed meteorological data such as temperature, pressure and precipitation. The Austrian Meteorological

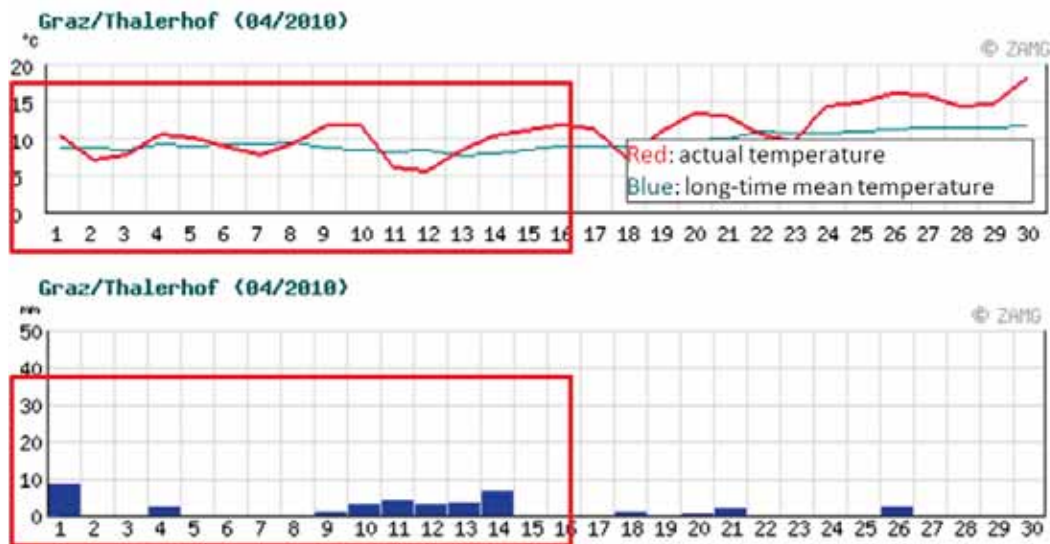


Figure 6.19: Meteo records of temperature (upper panel) and precipitation (lower panel) for station Graz in April 2010 (source: ZAMG)

Agency (ZAMG) publishes the monthly and daily evolution of mean temperature and

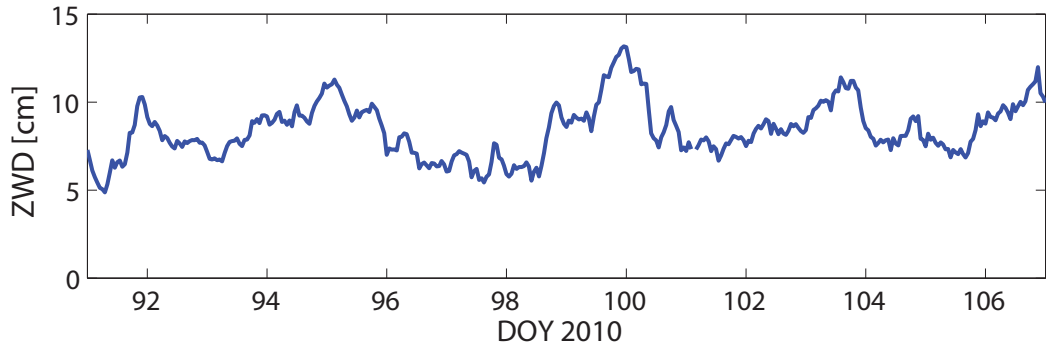


Figure 6.20: ZWD for IGS station GRAZ (March 27–April 16, 2010)

precipitation (Fig. 6.19) for a selected number of stations in Austria. One of those is the meteorological station Graz. The comparison of ZWD estimates (Fig. 6.20) with temperature and precipitation series reveals a certain correlation. A temperature change of 5–6 degrees that occurred in the period of April 7–11 (corresponding to DOY 97–101), accompanied by rain can be also recognized in the ZWD estimates. A closer

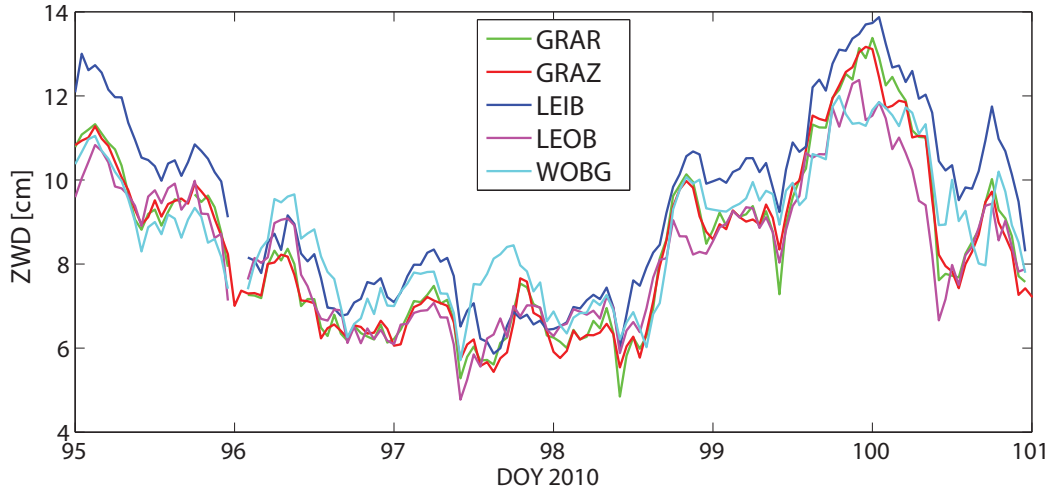


Figure 6.21: ZWD time series of IGS station GRAZ and several nearby stations (April 5–11, 2010 (DOY 95–101))

look at the ZWD estimates for the aforementioned period depicted on Fig. 6.21 for station Graz and several surrounding stations can also give hints about the weather front that affected the region, and its direction. Inspecting the geographical station

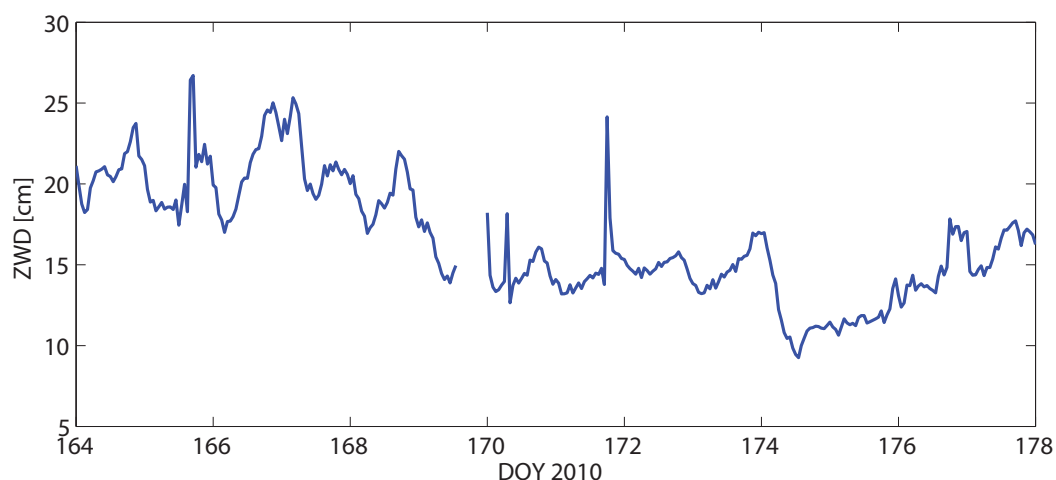


Figure 6.22: ZWD of IGS station GRAZ and nearby stations (June 13–26, 2010 (DOY 164–177))

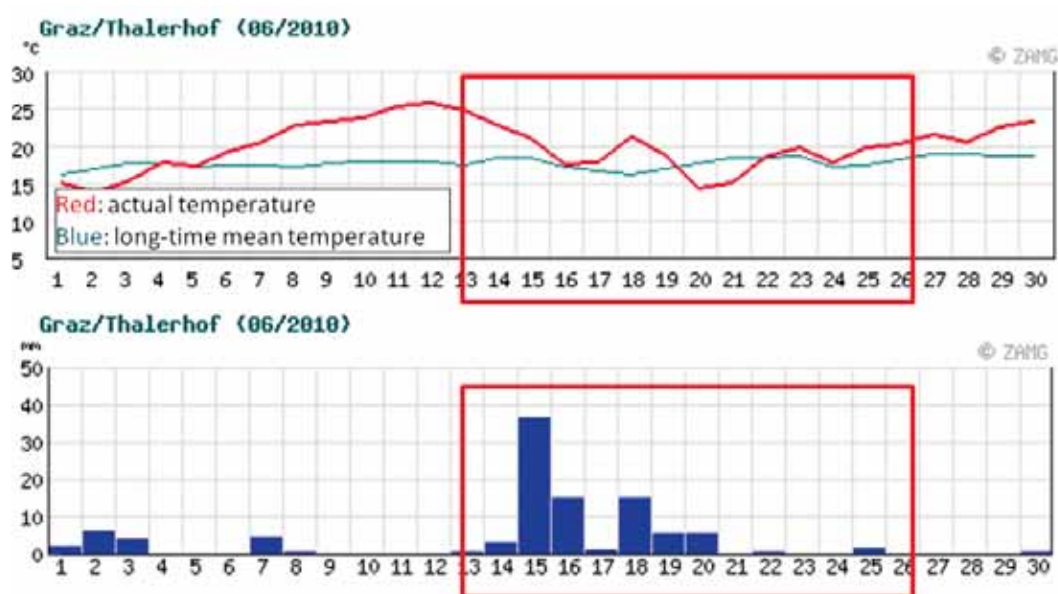


Figure 6.23: Meteo records of temperature (upper panel) and precipitation (lower panel) for station Graz in June 2010 (source: ZAMG)

distribution (Fig. 6.1), it can be noticed that the stations were affected by a weather front from west to east, arriving first at stations WOBG and LEOB, moving towards GRAZ and GRAR, and finally passing station LEIB.

More humid summer months note steeper decreases and increases of ZWDs (Fig. 6.22, station Graz). The very humid period of DOY 164–165 (June 13–14) followed by the strong precipitation on DOY 166–167 (June 15–16) shown in meteorological records (Fig. 6.23) is mirrored in the estimated ZWD values. An increase of temperature, as it occurred at the end of June, is usually accompanied by an increase in air humidity, hence an increase in ZWD values.

6.6 Solution parameters

6.6.1 Satellite orbits

The 15-minute IGS final orbit products were used to establish the PPP solution. These orbits are a combined product of about eight contributing IGS analysis centers using six independent software packages, namely Bernese, GAMIT, GIPSY, NAPEOS, EPOS and PAGES software (Kouba [2009]). The solution is usually available approx. 13 days after the last observation is collected. From Tab. 3.1 we learn that the accuracy of the orbits is on a 2 cm level with a satellite clock accuracy of about 75 ps. Fig. 6.24 displays the weighted RMS of the individual AC orbit solutions with respect to the IGS final product. The IGS rapid orbits (IGR), available about 17 hours after the last observation, have improved drastically in the past years to an accuracy comparable to the final products.

When choosing the orbit products for PPP analysis, it is important to keep in mind: (1) the accuracy of the applied products, (2) the availability of products, and (3) the consistency with other applied products such as the earth orientation parameters (ERP) and the satellite clock corrections. As long as the consistency is ensured, using the final combined IGS solution or final solution of the individual analysis center should not lead to any relevant changes in the estimated ZWD parameters or the station coordinates. Fig. 6.25 shows the ZWDs estimated using the IGS final orbit and ERP products versus the final products provided by the CODE analysis center. The difference between the two solutions is up to ± 4 mm and can be considered as almost negligible. A similar conclusion is drawn when comparing the ZWDs estimated using the IGS final and the IGS rapid orbit products.

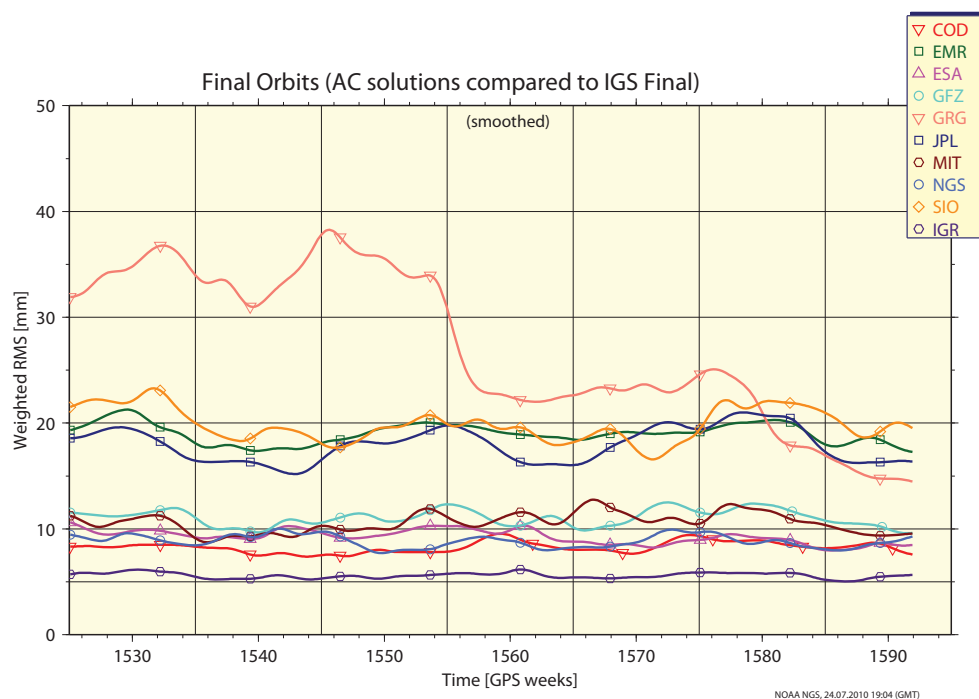


Figure 6.24: Weighted RMS of the individual AC orbit solutions with respect to the IGS final product (April 15, 2009 – July 4, 2010)

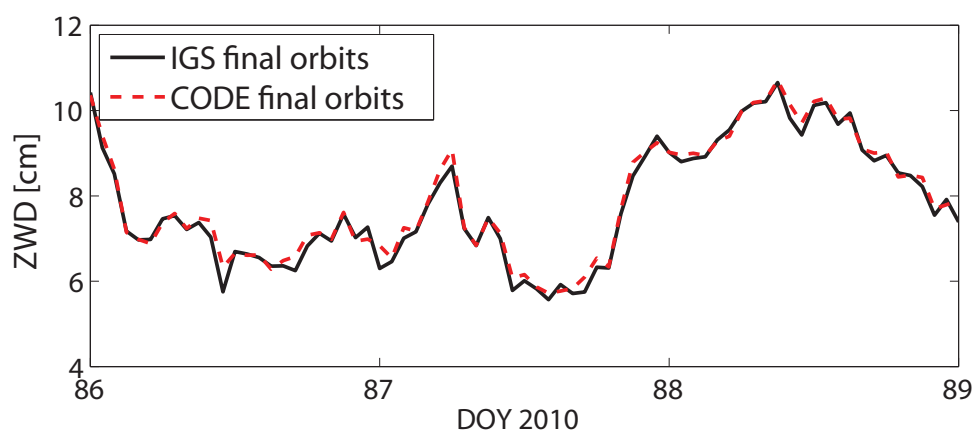


Figure 6.25: PPP ZWD for station GRAR using IGS final orbits and CODE final orbits

6.6.2 Satellite clock corrections

Along with the precise satellite orbit solution, the satellite clock corrections are provided with an accuracy of about 75 picoseconds or better and a time resolution of 15 min. While the accuracy of the satellite clock correction is on a high level, large errors in

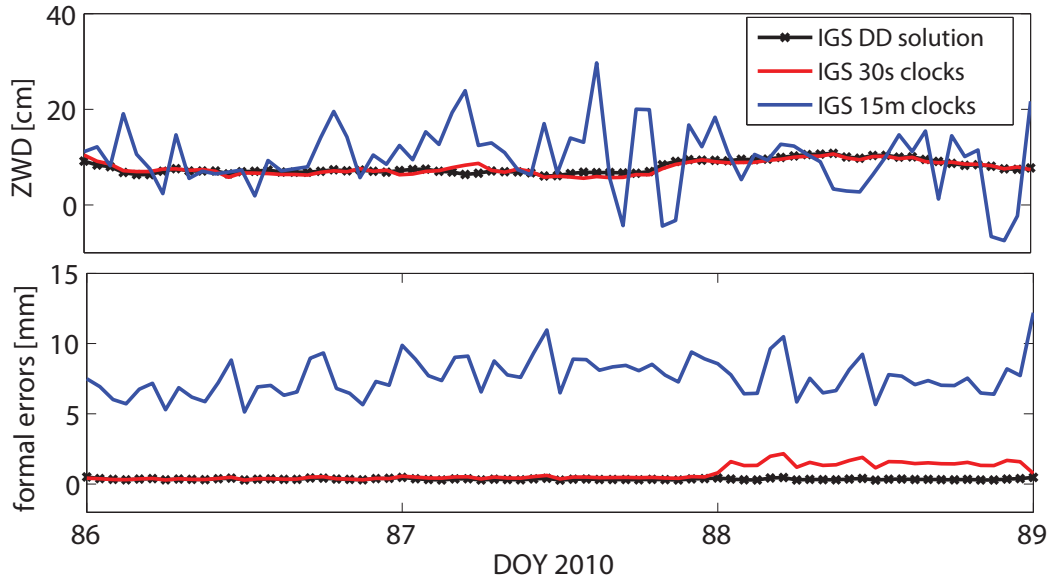


Figure 6.26: PPP ZWD estimates (upper panel) and respective formal errors (lower panel) for station GRAR using 15-minute and 30-second satellite clock corrections compared to the DD solution

the estimates at intermediate epochs are enforced due to clock correction interpolation to each observed epoch. Fig. 6.26 shows a comparison of the ZWD estimates when using the satellite clock corrections provided within the SP3 final orbit file, and the precise satellite clock corrections with a 30-second time resolution. Currently, the IGS provides separately from orbit products final and rapid satellite clock corrections with 5-minute time resolution, and final high-rate 30-second satellite clock corrections. The CODE analysis center in addition provides final clock correction data with a 5-second time resolution (for processing the high resolution observation data). A higher clock correction rate is in particular useful in case of a comparable observation data rate.

6.6.3 Observation selection

The number of available observations conditioned by the data sampling rate, the number of observed satellite system, the choice of elevation mask, etc. plays an important

role in PPP. For the presented test calculations, a set of 30-second GPS-only observation data files have been used. An increased data rate does not necessarily change the estimated troposphere parameters (and coordinates), but it can certainly influence the standard deviation of the estimates. Fig. 6.27 shows the estimated PPP ZWDs with an hourly resolution using a 30-second data rate along with CODE 30-second satellite clock corrections, and using a 15-second data rate and 5-second CODE satellite clock corrections. In both cases the final CODE orbit products were used to keep the consistency. We can see that there is no change in the estimated ZWD values, but the increased data rate has a slight impact on formal errors of the estimates (Fig. 6.27, lower panel). On the other hand, these reduced formal errors reflect primarily the correlations between subsequent observations which are not accounted for in the present processing scheme. Thus these decrease of formal errors cannot be mapped directly to an increase of accuracy of the estimates.

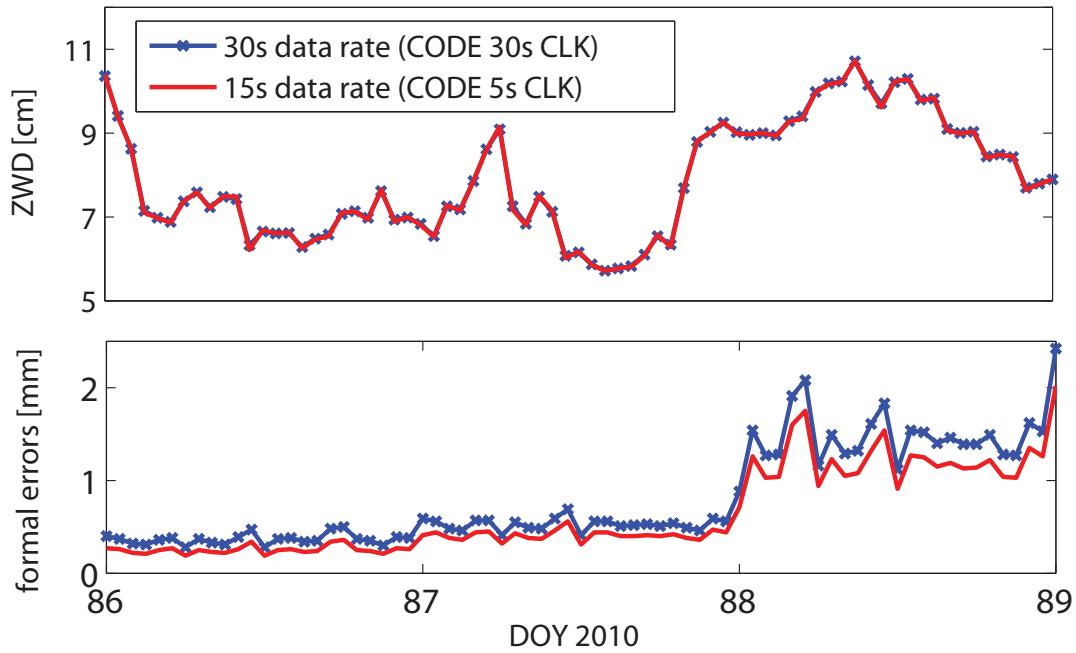


Figure 6.27: Hourly PPP ZWD estimates (upper panel) and respective formal errors (lower panel) for station GRAR using 30-second and 15-second data rate

An increased number of observations per epoch is a main precondition for an increased temporal resolution of the troposphere parameters. Including additional signals from GLONASS and the future Galileo system will allow to reduce the estimate's rate

to 30 min and less without loss of accuracy. Currently the Bernese software allows only to process GPS observations in zero-difference mode. Increasing the ZWD temporal resolution leads to slightly noisier solutions and increased formal errors (Fig. 6.28). An increased number of signals will be specially beneficial for obstructed stations, like this is the case for station Kolm-Saigurn (KOLM).

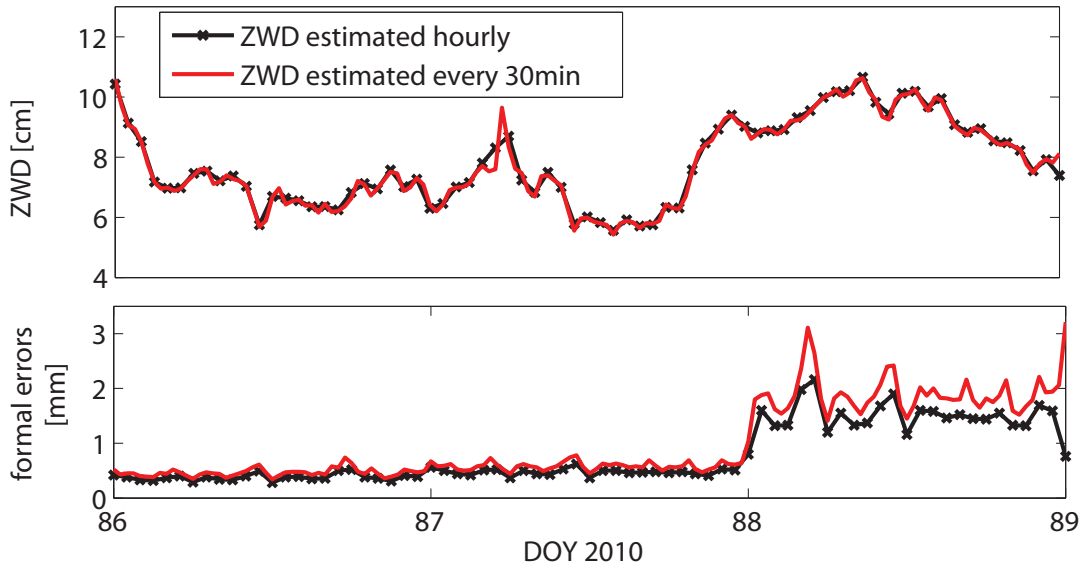


Figure 6.28: PPP ZWD estimates (upper panel) and respective formal errors (lower panel) for station GRAR with higher temporal resolution

The selection of the elevation cut-off angle also impacts the number of observations per epoch. A low elevation angle ($<5^\circ$) might decrease the accuracy of the estimates, since low elevation observations are more affected by multipath and potential imperfections of the mapping function. Setting a higher elevation angle on the other hand reduces the number of available observations, degrades the geometry and subsequently increases the standard deviation of the estimates.

6.6.4 Setup of troposphere criteria

Prior to troposphere delay estimation, adequate criteria have to be selected. This includes the choice of an *a priori* atmosphere model, a choice of a mapping function and the setup of parameter constraints. As it was mentioned earlier, the current version of BSW supports the implementation of Global Pressure and Temperature

model and the Global Mapping Function, which were used in all test calculations. Test calculations performed by applying the widely used Niell Mapping Function revealed no changes in ZWD estimates nor in the respective formal errors. Differences could be expected in periods of extreme weather anomalies.

The constraints between consecutive ZWD estimates were set to 1 mm. Seemingly very tight, this choice of constraints allowed to eliminate physically non-meaningful jumps in the ZWD estimates. Setting the constraints to more loose values, or omitting them completely, led to almost no changes at non-obstructed stations (see Fig. 6.29 for station GRAR, or Fig. 6.30 for station ROET). However in the case of e.g. station KOLM omitting the constraints resulted in a quite noisy solution with increased formal errors (Fig. 6.31).

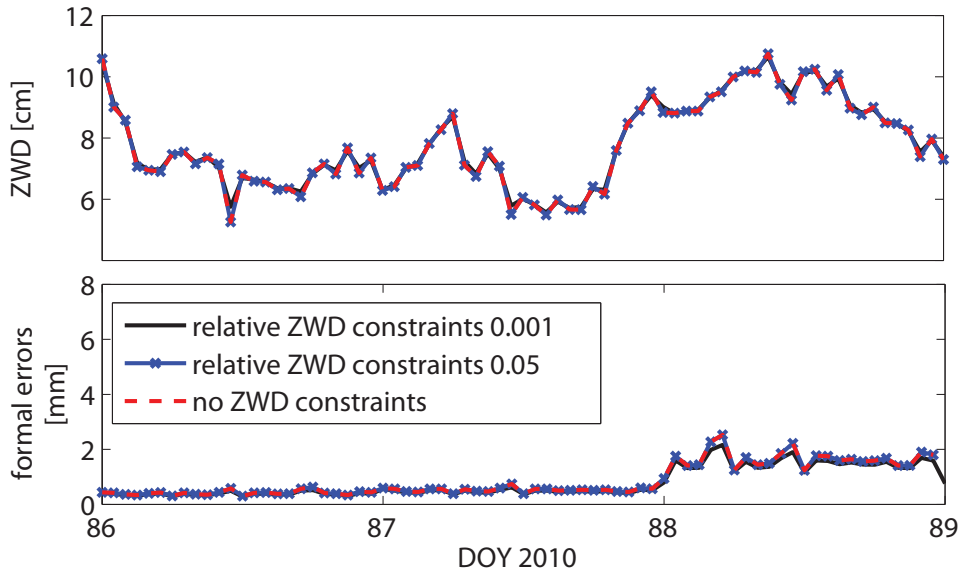


Figure 6.29: ZWD estimates (upper panel) and respective formal errors (lower panel) for station GRAR with different constraints

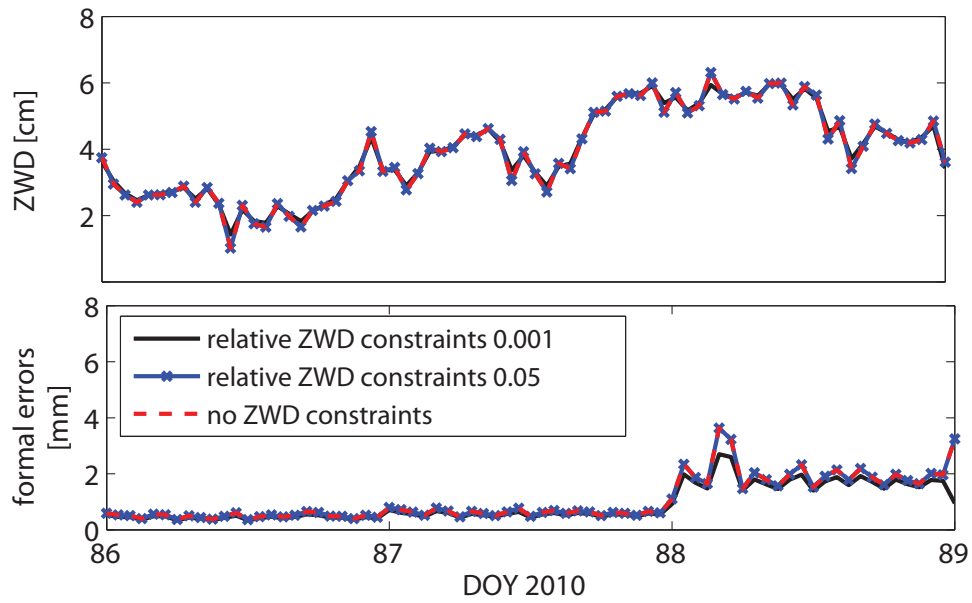


Figure 6.30: ZWD estimates (upper panel) and respective formal errors (lower panel) for station ROET with different constraints

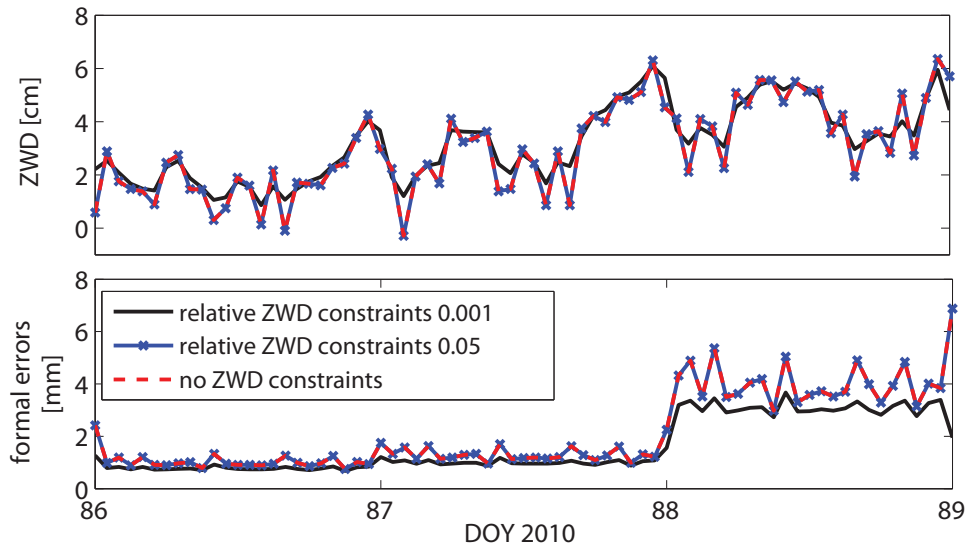


Figure 6.31: ZWD estimates (upper panel) and respective formal errors (lower panel) for station KOLM with different constraints

6.7 Impact on station coordinates

In addition to the hourly ZWD estimates, the station coordinates have been estimated as static and kinematic parameters. In the static mode, one coordinate solution was estimated for the entire processed session, i.e. one set of coordinates per day. In the kinematic mode, the station coordinates were estimated epoch-wise (every 30 seconds). The estimated PPP coordinates have been compared to the static double-difference solution. In order to compare the PPP and double-difference results, the effect of the plate motion has to be taken into account. For that reason the ITRF2005 coordinates of the reference stations (Graz, Wettzell, Zimmerwald) were introduced with the epoch set to March 27th, 2010 (DOY 86/2010). The PPP coordinate solution is tied to the satellite's coordinates frame provided always in the current ITRF solution (currently ITRF2005) and the epoch of the processed day. Therefore, a consistency of the coordinate solution on DOY 86/2010 can be stated, and sufficient consistency of the remaining 20 days is assumed.

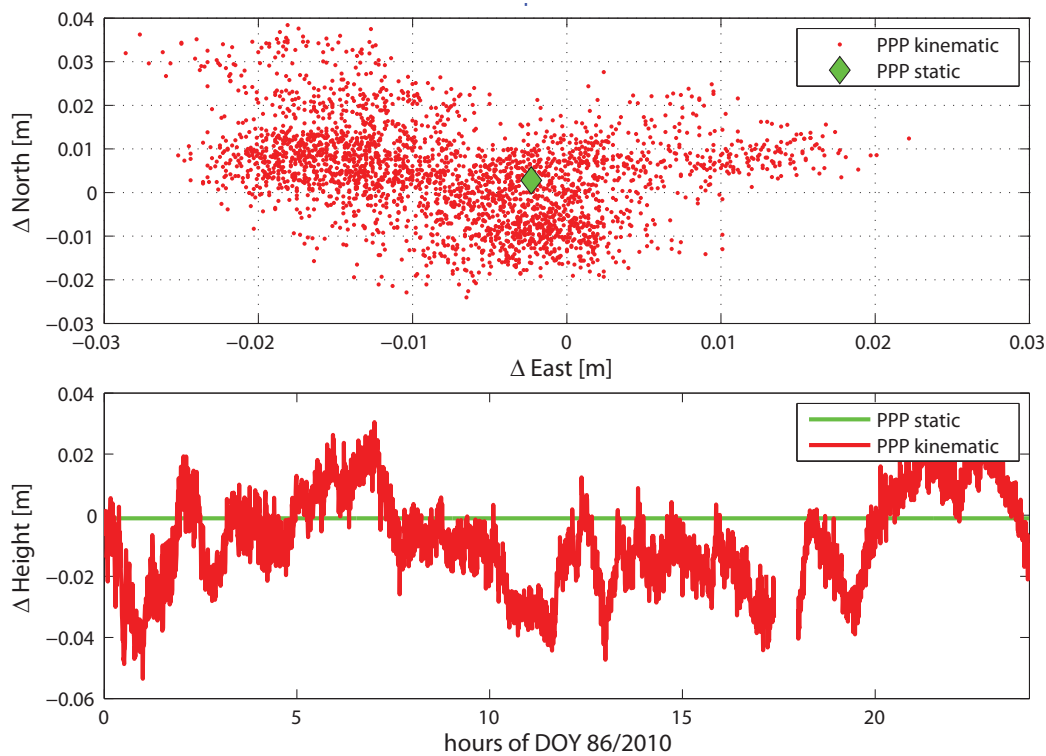


Figure 6.32: Station GRAR: station displacement in the north-, east- and up-component for March 27th, 2010

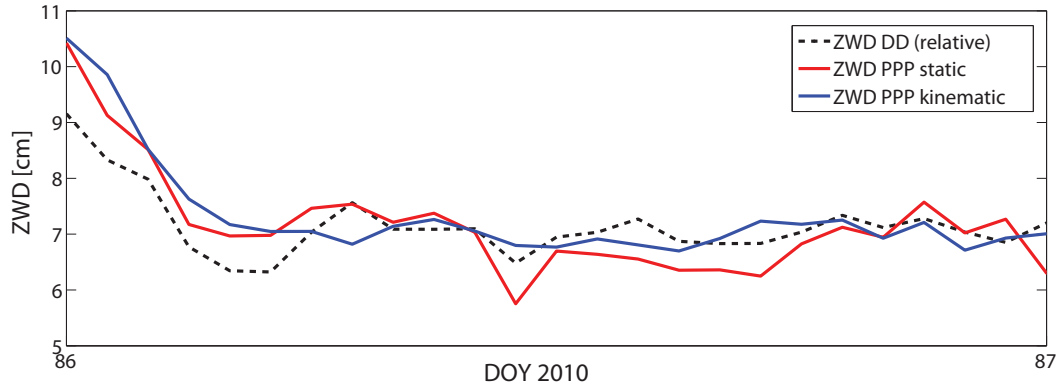


Figure 6.33: ZWD estimates for station GRAR on March 27th, 2010

The station displacement of station GRAR with respect to the double-difference solution is displayed in Fig. 6.32. The static solution, represented with a green diamond sign, shows a displacement to the reference double-difference solution in the sub-cm level. The static solution is basically a mean value estimated in epoch-wise mode, which shows a displacement of up to ± 4 cm in horizontal and a slightly larger displacement in the vertical component. The vertical component is particularly interesting since it can be directly related to the zenith tropospheric delays. Any error in modelling of the ZTD will map directly into the vertical component. Fig. 6.33 shows the ZWD estimates for station GRAR on March 27th, 2010 (DOY 86/2010). Displayed are ZWD time series from double-difference solution where the reference station coordinates were fixed, compared to PPP ZWD time series obtained from static and kinematic solutions. Differences at the cm-level can occur due to the different constraining of the coordinates and different processing approaches. Furthermore, the effect of the atmospheric loading could be monitored if air pressure measurements on site would be available.

6.8 Summary

In this chapter, a comprehensive evaluation of the Precise Point Positioning technique used for troposphere monitoring was presented. Observations from a network of stations located in Austria have been utilized. Two sets of observation data were processed, namely three weeks in March/April 2010 and two weeks in a more humid period in June 2010. For parameter estimation the ionosphere-free linear combination of observations is chosen, with an elevation mask set to 5° . Furthermore, the Saastamoinen model to describe the *a priori* zenith hydrostatic delay based on Global Pressure and

Temperature model is applied. The estimates were mapped to the zenith using the Global Mapping Function. The PPP solution has been validated through a comparison with a double-difference solution. The comparison has shown a very good agreement of the ZWD estimates from DD and PPP solution, with mean differences of less than 1 cm. An additional validation of the troposphere estimates for IGS/EUREF station Graz was performed via comparison with the zenith total delay provided by the IGS Troposphere Working Group. Finally, an investigation of selected estimation parameters, i.e. satellite orbits and clock correction products, observation selection and ZWD constraints, was given.

Chapter 7

Future improvements

The Precise Point Positioning technique has shown potential to become the standard technique for the estimation of ZWD from ground based GNSS observations gathered from large networks. However, PPP is a work in progress. Further improvements are foreseen with respect to the PPP algorithm and opportunities provided by the modernization of GNSS. Future work in the area of troposphere monitoring by means of PPP includes e.g. the investigation of advantages of new GNSS components and new signals, utilization of state-of-the-art troposphere models and mapping functions, and exploration of benefits of troposphere tomography models.

7.1 Geometry effects

The accuracy of the determined station position and troposphere parameters depends on the number of available observations and the satellite-receiver geometry. The effect of geometry of the satellites on the position error is called dilution of precision (DOP). Usually, GDOP (geometric dilution of precision) or PDOP (position dilution of precision) are used to express the quality of the satellite geometry. In addition, we have TDOP (time dilution of precision), HDOP (horizontal DOP) and VDOP (vertical DOP). The combined observation of GPS and Galileo satellites allows to track slightly more than the doubled number of satellites compared to the GPS-alone case (factor 1.05) due to a larger semi-major axis of the Galileo satellite orbits. In case of hybrid GPS+Galileo receivers the mean PDOP ratio (averaged over 24 hours) of GPS+Galileo versus GPS-only is about 0.6 (ratio <1 indicates an improvement in geometry), which represents an improvement of about 40% (Weber *et al.* [2008a]). Although DOP numbers characterize in principle the observation geometry at a single epoch, this improvement will also result in an increased accuracy of the ZWD estimates determined by

a least-squares approach over a defined period and under the precondition of resolved ambiguities. The use of hybrid GPS+Galileo receivers promises an accuracy improvement with respect to horizontal positioning of about 30% and in height of about 50% due to the increased number of observations, an improved satellite geometry and a better de-correlation between the height and the tropospheric delay.

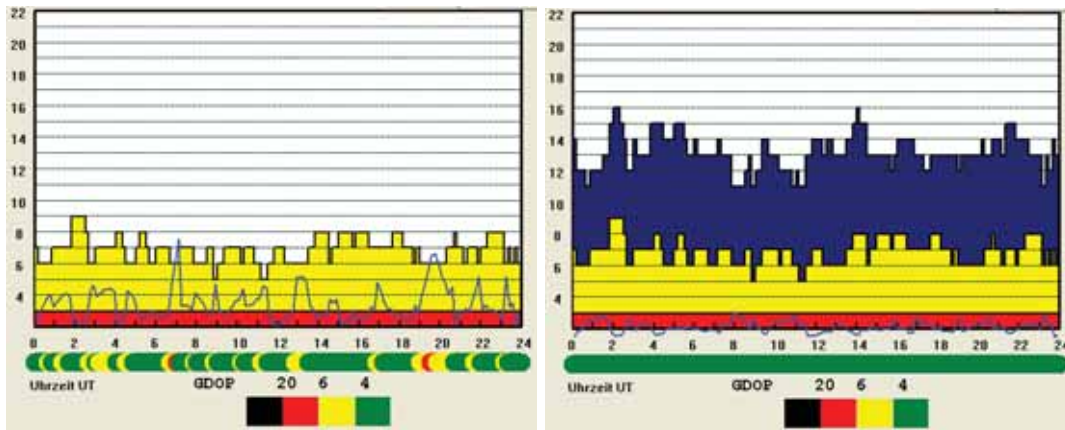


Figure 7.1: The number of visible satellites and GDOP for station KOLM in the case of GPS-only (left) and simulated GPS+Galileo scenario

In particular, the obstructed sites will profit from an increased number of observations brought by GNSS modernization. As an example we focus on station Kolm-Saigurn (KOLM, Sect. 6.1), a highly obstructed site with a lowest elevation angle of observation of approx. 16° . Fig. 7.1 displays the number of visible satellites and the respective GDOP for the GPS-only and the GPS+Galileo scenario. It is clearly visible that with the inclusion of Galileo the number of visible satellite doubles and the GDOP remains under 4 the whole day.

The current GNSS offers a full GPS constellation and 21 operational GLONASS satellites. However, a comparison of ZWD estimates and respective formal errors from GPS-only and GPS+GLONASS¹ scenario shown in Fig. 7.2 reveals little or no improvement (less than 15% for formal errors). This is due to deficiencies in modeling intra-system biases like GLONASS differential signal biases and inter-system biases at the receiver side like antenna phase center offsets and variations and again differential

¹This comparison is valid for double-difference mode because the Bernese software currently does not provide the routines to process multiple GNSS in PPP mode.

code biases, and due to the impossibility to fix the integer number of double-difference ambiguities.

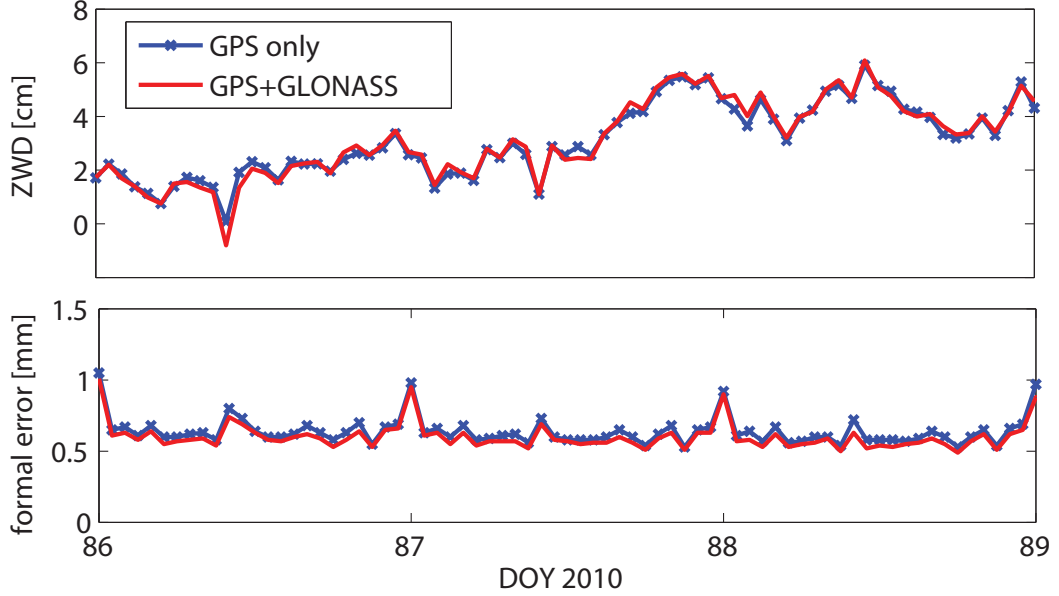


Figure 7.2: Comparison of GPS-only and GPS+GLONASS derived ZWD estimates (upper panel) and respective formal errors (lower panel) from DD solution for the station Kolm-Saigurn

7.2 New linear combinations

From an improved satellite geometry as well as the availability of new carrier bands and signals, an increased accuracy and temporal and spatial resolution of the estimates (e.g. coordinates and troposphere parameters) is anticipated (Weber & Karabatić [2009]). It is obvious that the use of new signals (GPS: L5, L2C, L1C; Galileo: E1B, E1C, E5a, E5b, E6A) will allow the formation of additional phase and code linear combinations (LC) based on three to five individual frequencies. Potential improvements can be observed with respect to ambiguity fixing (wide wavelengths, low phase noise), ionosphere cancellation (low noise) or low code and phase multipath. To have a closer look on advantages and disadvantages of optional new linear combinations the overall expression for combining three carrier phases Φ_1 , Φ_2 and Φ_3 is given as follows

$$\Phi_{n,m,k} = n\Phi_1 + m\Phi_2 + k\Phi_3, \quad (7.1)$$

with n , m and k integer values. Thus, the apparent frequency $f_{n,m,k}$ and the apparent wavelength $\lambda_{n,m,k}$ of the new linear combination can be calculated as follows

$$f_{n,m,k} = nf_1 + mf_2 + kf_3 \quad \text{and} \quad \lambda_{n,m,k} = \frac{c}{f_{n,m,k}}. \quad (7.2)$$

The linear combinations are usually more sensitive to ionospheric refraction than GPS L1 carrier phase which can be expressed by the ionospheric amplification factor but on the other hand they may also have longer wavelengths. The ionospheric amplification factor kI reads

$$kI = \frac{\frac{n}{f_1} + \frac{m}{f_2} + \frac{k}{f_3}}{nf_1 + mf_2 + kf_3} f_1^2. \quad (7.3)$$

Furthermore, all linear combinations increase the phase noise σ compared to L1 (depending on the integer numbers n , m , k), i.e.,

$$\sigma_{n,m,k} = \sqrt{n^2 + m^2 + k^2} \sigma_{L1}, \quad (7.4)$$

and are more susceptible to multipath effects. Multipath is mainly dependent on the modulation scheme, but also on the bandwidth of the incoming signal and on the reflecting environment. Eissfeller *et al.* [2007] assume 1–2 dm multipath of Galileo code signals at almost not obstructed sites and at high satellite elevation angles. The Galileo E5 AltBOC modulation will show an even better performance of <5 cm. Simsky *et al.* [2008] confirm these assumptions by investigating already available GIOVE-B data.

n (L1)	m (L2)	k (L5)	λ [m]	Ionosphere amplification	Iono/ λ
1	-1	0	0.862	-1.283	-1.49
0	1	-1	5.861	-1.719	-0.29
1	0	-1	0.751	-1.339	-1.78
1	-4	3	1.011	-1.208	-1.20

Table 7.1: GPS linear combinations

Tab. 7.1 lists the wavelength and the ionospheric amplification factor calculated for a few basic linear combinations of GPS L1, L2 and L5. Particularly interesting is the widelane L2–L5 LC providing a huge wavelength of 5.86 m and moreover a low iono/wavelength factor. A similar table is provided for Galileo linear combinations

n (E1)	m (E5a)	k (E5b)	l (E5)	r (E6)	λ [m]	Ionosphere amplification	Iono/ λ
0	1	-1	0	0	9.768	-1.748	-0.18
0	1	0	-1	0	19.537	-1.770	-0.09
0	2	-3	0	-1	29.305	-0.769	-0.03
1	4	1	-3	-3	3.907	-0.001	-0.00
3	-5	0	0	3	0.112	0.000	0.00
4	-3	1	1	0	0.109	-0.000	-0.00

Table 7.2: Galileo linear combinations

(Tab. 7.2). Some potential LCs were listed either with long wavelengths, fair ionospheric amplification and competitive noise behavior or almost ionospheric free LCs based on 3–5 frequencies with usually 11 cm wavelength and increased noise amplification. Although it is not very likely that future (affordable) receivers will be able to process all these signals, at least their individual strengths for data processing should be kept in mind. Conventional data processing for deriving reliable troposphere estimates (ZWD) is usually dependent on the possibility of fixing ambiguities. A LC close to the ionospheric free plane with modest noise amplification should allow to calculate good coordinate approximations. To minimize the search space also two or three step procedures utilizing two kinds of widelanes with varying wavelength could be taken into account. Usually in the final step a ionospheric free linear combination is used to solve the remaining 11 cm wave (narrow lane). When aiming at shorter observation spans (couple of minutes) new dual- or triple-frequency LC will keep the same ability of ambiguity resolution as regular L1/L2 solutions but allow to reduce the 3D site position error and therefore increase the accuracy of the ZWD estimates. Furthermore, the availability of at least three signals within one satellite system will allow to eliminate second-order ionosphere effects. With currently only two signals available, only the first-order ionospheric delay can be eliminated by forming the ionosphere-free linear combination. The remaining ionospheric delay maps into the estimated ZWD parameters.

7.3 Water vapor tomography

The zenith wet delay derived from GNSS observations has to be interpreted as a signal refraction due to the humid atmosphere integrated (one-dimensional) over the entire path length and mapped to the zenith. It, therefore, offers no knowledge of the vertical profile of the humidity field. To enhance the GNSS contribution to weather models,

the concept of 3D- or 4D-tomography model has been investigated by several research groups (Lutz *et al.* [2010], Bender & Raabe [2007]).

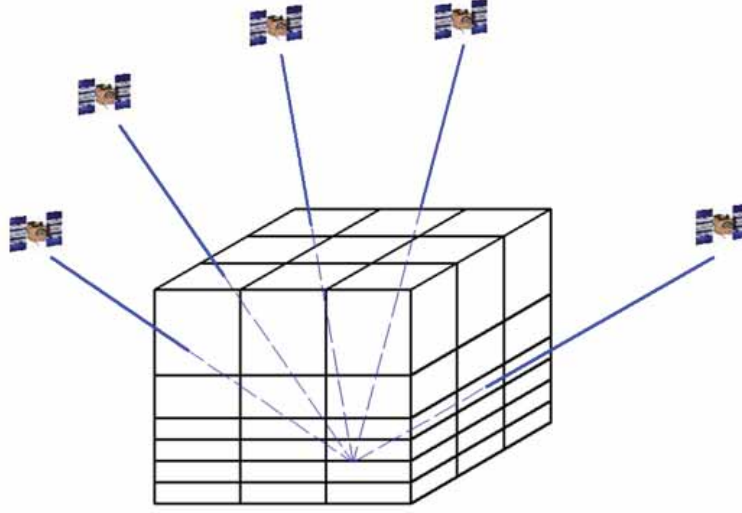


Figure 7.3: Tomography model

A tomography model is represented by a voxel (volumetric pixel) model where the troposphere is divided into smaller volume elements (Fig. 7.3). Similar to three-dimensional medical imaging using X-rays, the structure of the humidity field in the atmosphere above the network of receivers can be determined using the radio waves (Lutz *et al.* [2010]). The refractivity model can be determined using simultaneous rays passing through the same voxel. The wet refractivity of the air is assumed to be constant per voxel. The wet refractivity profile between satellite and receiver can be obtained by solving a linear system of equations given by:

$$\Delta\rho_w = 10^{-6} \sum_{m=1}^{M_v} N_w(m)d(m), \quad (7.5)$$

where $\Delta\rho_w$ is the slant wet tropospheric delay, M_w is total number of voxels which are passed by the signal, $N_w(m)$ is the wet refractivity of voxel m and $d(m)$ is the distance traveled by the signal in voxel m (Nilsson [2008]).

A simulation of such a tomography model has been carried out utilizing an example network with a mean station distance of about 60 km (typical for RTK purposes). A 12x12 horizontal grid with a regular spacing of 10 km and 8 unequally spaced



Figure 7.4: Simulated raytraced tomography model using GPS-only and GPS+Galileo observations (number of observations per voxel)

vertical layers as indicated in Fig. 7.4 were set. Current tomography models, such as the one developed by the Geodesy and Geodynamic Lab of Institute of Geodesy and Photogrammetry, ETH Zurich for the area of Switzerland (Lutz *et al.* [2010]), utilize typically only the GPS observations. As it can be seen in Fig. 7.4, the number of observations doubles when Galileo data is included. However, sparse station distribution leads to a low number of observations in lower layers even with Galileo included. The distance between the reference stations should therefore be decreased to about 10 km to cover also the most humid surface layers up to 2 km in height. Densified networks allow the operation of the tomography model without the need of tight constraints between the vertical estimation levels. The increased number of available observations due to Galileo and the improved geometry will facilitate an increased temporal and spatial resolution of vertical profiles of the humidity field. The temporal resolution might be increased to 30 min and less. Such a station densification is unfortunately expensive and currently hardly feasible.

As already mentioned in Sec. 7.1, an increased number of observations when using the hybrid GPS+Galileo system and hence an improved GDOP will lead to increased

accuracies of estimated humidity field by approx. 40%. The anticipated increase is primarily due to an increased number of observations and due to the slightly improved geometry provided by a fully established Galileo space segment. Similar conclusions are derived from simulations performed by the aforementioned ETH group (see Fig. 7.5). Compared are standard deviations of tomography results derived from GPS-only and GPS+Galileo solutions for the station network AGNES (Automated GNSS Network of Switzerland). Fig. 7.5 also shows the effect of a station network extension on the accuracy of the water vapor derived from a tomography model. The station network AGNES, a network of 30 operating stations with a station density of about 50 km, is augmented by 72 meteorological stations of the Automated Swiss Weather Station Network (ANETZ).

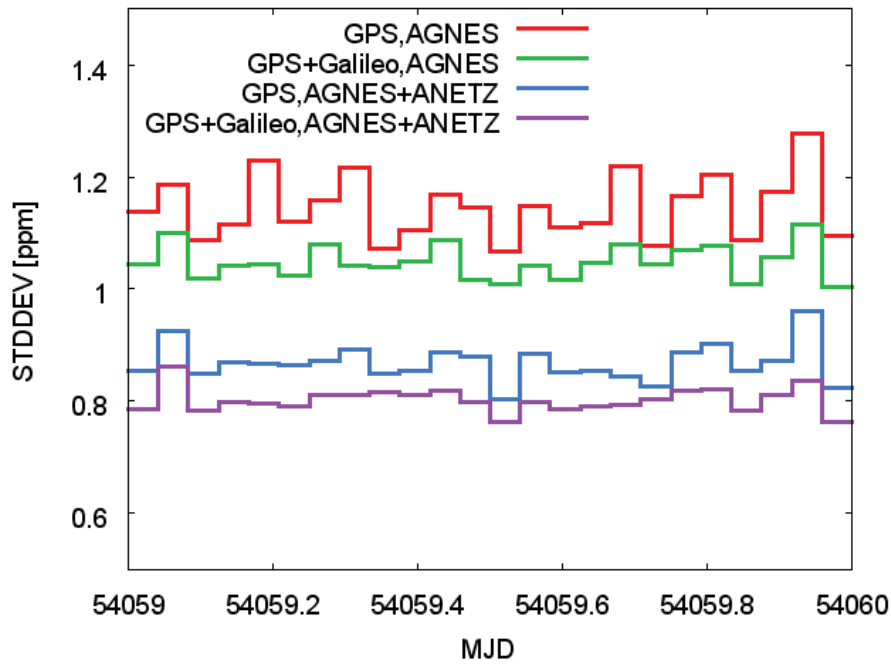


Figure 7.5: The impact of additional GNSS observations and network extension on tomography results (*source: Institute of Geodesy and Photogrammetry, ETH Zurich*)

Chapter 8

Conclusions

8.1 Summary

The work presented in this dissertation deals with monitoring the humidity content of the atmosphere using observations of global navigation satellite systems. Zenith wet delay information obtained from GNSS ground data is a function of the humidity along the signal path between the satellite and the receiver and is of special interest to meteorology as an additional data source for Numerical Weather Prediction (NWP). The observations from current global navigation systems, namely GPS and GLONASS, can be used to derive the station coordinates with accuracy on centimeter level and zenith wet delay estimates with accuracy on millimeter level. For this work, data of a fixed network of stations has been investigated. The analysis is performed in post-processing mode using the GNSS analysis package Bernese v5.0. Daily observation files were used along with IGS precise products to derive the static station coordinates and hourly ZWD estimates.

It has been shown that passing weather fronts can be analyzed in more detail by introducing GNSS derived tropospheric wet delays. The observed ZWDs are influenced by changes in humidity in the free atmosphere, whereas the data at the meteorological ground stations react to these changes only with a time delay. This allows to forecast heavy rainfall causing potentially local floodings more reliably and to narrow down the affected region. The timeliness and accuracy requirements for meteorology were fulfilled by delivery of ZWD estimated by a double-difference approach, with a delay of less than one hour and an overall accuracy better than 5 mm (1 mm in PW). The hydrostatic part is calculated from ground based meteorological measurements at or nearby the GNSS stations. The corrected values for the ZWD have been assimilated

into the real-time forecast system INCA. Model improvements obtained due to the assimilation of GNSS wet delays are mostly visible during summer months (GNSS constraints on forecast models during periods of high humidity are more tight) and in times of quickly passing weather fronts.

In order to process large networks with an increased timeliness, the potential of the PPP technique has been investigated in more detail. Since the 1990s PPP became a popular technique for processing the GNSS data of an isolated station. To achieve ultimate accuracy, PPP requires pseudo-range and carrier phase observations on at least two frequencies, precise orbit and satellite clock correction products, proper models to account for error effects and sophisticated analysis software. It has to be kept in mind that due to a number of error sources that cancel when processing in double-difference (relative) mode, the PPP approach is much more sensitive to improper modeling of the individual effects. Therefore, a critical assessment of effects degrading the PPP accuracy reveals the quality of orbit and clock correction products, the effect of un-modeled error sources, the tie to the appropriate reference frame, the noise amplification of the used ionospheric free linear combination and the inability to fix the integer phase ambiguities. On the other hand, no reference station data is required for data processing which makes this technique cost effective compared to the classic relative technique.

The PPP observation model includes a number of effects affecting the GNSS satellites, the propagation of the signal and the station receiver. Assuming that effects such as relativity, satellite and receiver antenna phase center variations, phase wind-up, system biases and station displacement are properly handled and observations are free of multipath effects, the modeling of the signal propagation delay is investigated. The utilization of the ionosphere-free linear combination allows the elimination of the first-order ionosphere delay, capturing approx. 99% of the total signal delay caused by the ionosphere. The use of two GNSS frequencies, however, does not allow to eliminate the effects of the neutral atmosphere. Hence, it has to be modeled properly. The modeling of the neutral atmosphere, i.e. the troposphere includes an *a priori* model for the hydrostatic part (GPT) and an estimation of the remaining wet component. Both are referred to their respective zenith values by application of a GMF mapping function.

A carefully selected network of 15 stations located in Austria has been utilized to derive the ZWD estimates for different case scenarios. To observe the humidity content at different elevations, the station height varies from about 200 m to 3100 m. Two sets of observation data have been used to monitor the ZWD in dry and humid period of

the year. It has been shown that hourly ZWD estimates can be obtained with formal errors of less than 1 mm, which is a main precondition for the assimilation in numerical weather models. A comparison of the PPP and double-difference (baseline) derived ZWDs reveals differences of less than a centimeter, with slightly increased formal errors in the case of PPP.

8.2 Outlook

The IGS precise orbit and clock correction information is always consistent with the most recent ITRS realization (currently ITRF2005). To tie the PPP positions to former ITRS realizations, continental frame realizations (e.g. ETRF) or local reference frames a spatial similarity transformation has to be applied subsequently. The parameters of this transformation have to account for the correct epoch of the chosen frame. Improvements in quality and timeliness of provided orbit and clock products are a permanent issue for organizations like the IGS. Further work is required to provide satellite clock corrections with high accuracy and increased temporal resolution for (near) real-time applications. To minimize ranging errors, PPP requires the most precise orbit information specially since the derived station positions are tied to a specific reference frame by means of satellite orbit information. All additional external products like satellite clock corrections or ionospheric models have to be consistent with the chosen frame.

GPS modernization as well as the upcoming Galileo system will provide new signals on a third frequency. These signals will offer the opportunity to choose less noisy ionospheric free linear combinations and allow to model higher order ionospheric effects to be accounted for before estimating ZWD. The formal errors of the derived tropospheric delays could be improved by up to 40% compared to the current level by inclusion of Galileo data. This number is primarily based on the increased number of observations and on the slightly improved geometry provided by a fully established Galileo space segment. Under the assumption of no further un-modelled systematic inter-system biases, this improvement will also map into an increased accuracy of the ZWDs. To make use of the modernization advantages, the current analysis softwares should be upgraded with routines for processing the new signals and state-of-the-art troposphere models.

Furthermore, an increased number of available observations due to Galileo and an improved geometry will allow for an increased temporal and spatial resolution of

the respective products. The temporal resolution might be increased to 30 min and less. This close to real-time availability of ZWD estimates is an urgent need for GNSS contributions to weather forecast. The improved spatial resolution (more observations in additional azimuth and zenith distances) will allow to operate 3D- or 4D-tomography models.

Appendix A

Processing with Bernese Software v5.0

GNSS data processing was performed using the post-processing package Bernese v5.0 (Dach *et al.* [2007]), developed at the Astronomical Institute of the University of Bern, Switzerland. The most recent public version, namely the version 5.0 released in April 2004 allows in addition to traditional double-difference data processing the handling of zero-difference observations. Hence, the PPP analysis is possible. Due to number of error sources that cannot be eliminated in zero-difference mode (see Ch. 6), PPP still cannot compete with double-difference methods in achievable accuracy. Therefore, in addition to formal errors, the PPP solution was validated through the comparison with the double-difference solution (Sec. 6.5). In the following, both processing routines are explained in more details.

The routines are executed using the Bernese Processing Engine (BPE), the tool that allows automated data processing. For this purpose a Processing Control File (PCF) had to be created. In this file the subroutines to be executed by the software were defined and listed in a logical sequence.

Double-difference (relative) solution

The PCF file for the double-difference solution consists of following steps:

001	FTP_IGSN	PHDN_GEN	ANY	1
002	FTP_REF	PHDN_GEN	ANY	1

The numbers 001 and 002 define the processing ID numbers (PIDs). The scripts to be executed (FTP_IGSN and FTP_REF) are user-defined Perl scripts used to download the orbit information files, earth rotation parameters (ERP) and reference station (GRAZ, ZIMM, WTZR) data. Precise orbit information data and ERPs are downloaded from

IGS ftp server and saved in the campaigns' ORB directory. The reference station data are saved in directory RAW where the remaining station data already reside. Input parameters for each of subroutines are stored in specific OPT subdirectory, in this case subdirectory PHDN_GEN. After download of all necessary files the preparation of pole and orbit data is done through the following steps:

101	CCPREORB	PHDN_GEN	ANY	1 001
102	POLUPD	PHDN_GEN	ANY	1 101
103	PRETAB	PHDN_GEN	ANY	1 102
104	ORBGEN	PHDN_GEN	ANY	1 103

Program CCPREORB merges the GPS and GLONASS orbit informations into one orbit file in SP3 format with 15 min time resolution. The downloaded ERP informations are extracted and formatted from IERS into a Bernese pole file using the program POLUPD. GNSS orbit files given in Earth-fixed frame are converted into tabular positions in the inertial frame within the program PRETAB. It is very important that the set of orbit information data and earth rotation parameters is consistent through-out the entire processing. It is also possible to extract the satellite clock informations using PRETAB. This clock data are provided with the same resolution like satellite positions (15 min). Program ORBGEN uses the orbital positions from tabular files and equation of motion to create a Bernese standard orbit files. The orbits of the satellites are represented by six osculating elements and nine dynamical parameters associated with radiation pressure. Standard orbit files (STD files) are used with all subsequent processing steps where the orbit information is required.

201	RXOBV3	PHDN_GEN	ANY	1 002
202	CODSPP	PHDN_GEN	ANY	1 104 201

Further steps include the conversion of RINEX to Bernese observation file format (program RXOBV3) and synchronization of the receiver clocks to GPS time on a sub-microsecond level (program CODSPP). The latter program requires the *a priori* station coordinate file. The synchronization and in addition a basic outlier detection is performed on a zero-difference level using the code observations. Next step is the creation of baselines between reference stations and network stations. The predefined baseline list file was created and used within the program SNGDIF to set up single difference phase observation files.

301	SNGDIF	PHDN_GEN	ANY	1 202
302	MAUPRPAP	PHDN_GEN	ANY	1 301
303	MAUPRP_P	PHDN_GEN	ANY	1 302

Program MAUPRP screens the phase single-difference file and checks for cycle slips, unpaired L1 and L2 observations, observations below the selected mask angle and small observation pieces. This program was executed in parallel mode, meaning that each baseline is processed separately. For this reason PID 302 prepares the list of parallel scripts, i.e. the list of baselines to be processed in PID 303.

```
# Checking and screening of outliers (1st GPSEST)
# -----
401 GPSESTAP PHDN_RES ANY 1 303
402 GPSEST_P PHDN_RES ANY 1 401
#
403 RESRMS PHDN_RES ANY 1 402
404 SATMRK PHDN_RES ANY 1 403
#
#
# Ambiguity resolution (2rd GPSEST)
# -----
501 GPSESTAP PHDN_L5 ANY 1 404
502 GPSEST_P PHDN_L5 ANY 1 501
#
#
# Final solution, saving of NEQs (3th GPSEST)
# -----
601 GPSESTAP PHDN_L3 ANY 1 502
602 GPSEST_P PHDN_L3 ANY 1 601
#
#
# Normal equation stacking
# -----
701 ADDNEQ2 PHDN_FIN ANY 1 602
```

As seen above, the parameter estimation program GPSEST was executed three times but with different purpose. The first GPSEST run saves the residual files. This step along with programs RESRMS and SATMRK has a task to check for any remaining outliers. The estimation is performed using the ionosphere-free linear combination and no ambiguity resolution is done. The reference station coordinates were tightly constrained (1 mm) to their *a priori* values (ITRF2005). Saved residual files are screened with program RESRMS and identified outliers are marked in program SATMRK. In the next step the L5 ambiguities are resolved and stored (PID 502), and introduced in the next GPSEST run (PID 602). Hence the SIGMA ambiguity strategy was applied. Troposphere parameters were estimated with an hourly resolution and the Global Mapping

Function was applied. In the last GPSEST run each baseline is processed individually and in parallel, and normal equations were stored. The stored NEQs were combined using the program ADDNEQ2 to obtain the combined daily solution for all involved stations. It is obvious that individual GPSEST processing settings require separate input files, i.e. separate OPT subdirectories, otherwise each new settings would overwrite the previous ones. At this point, the Bernese processing ends. However, several custom designed tasks were programmed in Perl and adapted to be used with the BPE. Those scripts include mainly extraction of estimated data such as station coordinates and troposphere parameters.

```

801 TRPXTR_N PHDN_FIN      ANY      1 701
802 CRDXTR_N PHDN_FIN      ANY      1 801
803 CXN_NEU  PHDN_FIN      ANY      1 802

```

The PCF file ends with the definition of parallel runs:

```

302                      $302
303                      PARALLEL $302
401                      $401
402                      PARALLEL $401
501                      $501
502                      PARALLEL $501
601                      $601
602                      PARALLEL $601

```

and the definition of predefined user variables:

VARIABLE	DESCRIPTION	DEFAULT
8*****	40*****	16*****
V_ORBG	GPS orbit information	IGS
V_ORBR	GLONASS orbit information	IGL
V_ORB	Orbit information	IGGR
V_ERP	Earth orientation parameters	IGS
V_CLK	Clock information	IGS
V_PCV	Absolute/relative PCV	I05
V_ABBINF	Abbreviation table	PHD_CALC
V_APRCRD	A priori coordinates	PHD_CALC
V_BASL	Predefined baseline file	PHD_CALC

Zero-difference (PPP) solution

In addition to orbit information files and ERPs, the PPP requires the precise satellite clock information. Those are downloaded prior to processing using a similar Perl script as for orbits and ERPs download. Receiver clock corrections are estimated along with coordinates and troposphere parameters within the processing routine. In double-difference case we do not need to care about satellite and receiver clock errors, since they are eliminated by forming the differences. The clock informations are needed only for CODSPP and for that purpose 15 min satellite clock corrections extracted from SP3 files are sufficient. In a zero-difference mode precise, high-rate clock information are essential.

```
# Prepare pole information, calculate tabular and standard orbits
# extract precise satellite clocks
# -----
101 POLUPD   PHD_PPP           ANY      1 001
102 PRETAB   PHD_PPP           ANY      1 101
103 ORBGEN   PHD_PPP           ANY      1 102
104 CCRNXC   PHD_PPP           ANY      1 002
#
#
# Convert and synchronize observation data
# -----
201 RNXSMTAP PHD_PPP           ANY      1 103 104
202 RNXSMT_P PHD_PPP           ANY      1 201
203 SMTBV3   PHD_PPP           ANY      1 202
204 CODSPP   PHD_PPP           ANY      1 203
#
#
# Compute PPP solution
# -----
401 GPSEST   PHD_PPP           ANY      1 204
```

The high-rate precise satellite clock corrections were extracted using the program CCRNXC. The same routine like in double-difference case was applied to obtain the Bernese formatted earth rotation parameters and standard orbits (i.e. POLUPD, PRETAB and ORBGEN). Prior to conversion of observation data from RINEX to Bernese format, the code smoothing using the phase observation data was performed on RINEX level in program RNXSMT. Detected cycle slips and outliers are marked in this step. Smoothed observation files are then converted in the phase and code Bernese

observation files.

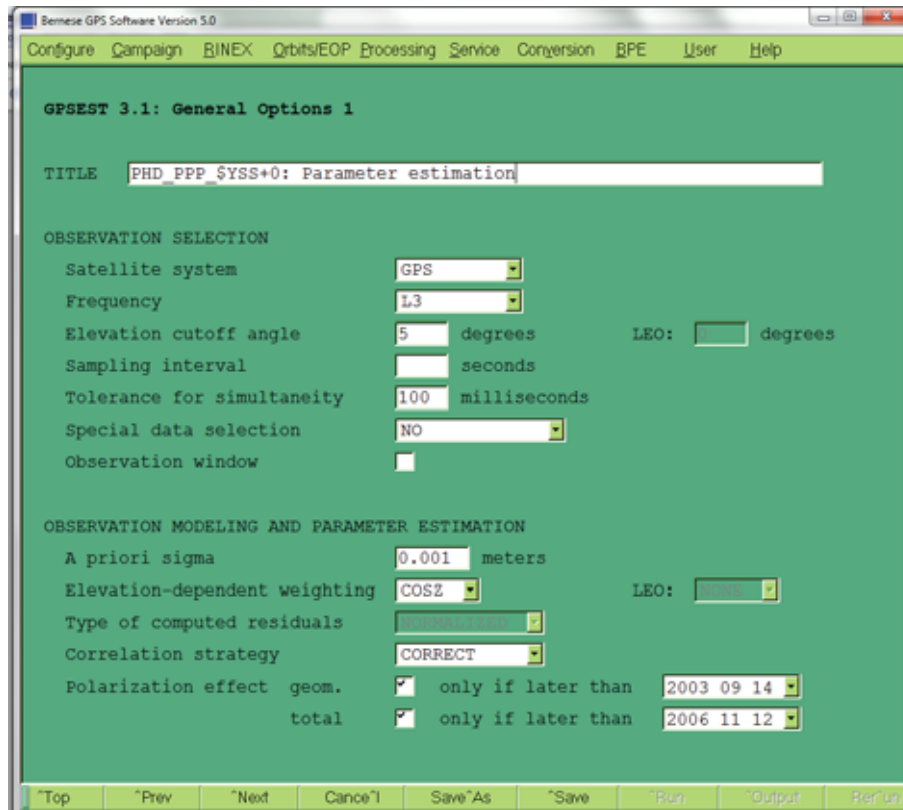


Figure A.1: Example of Bernese SW input panel

Since it is not possible to resolve the zero-difference ambiguities, no multiple runs of GPSEST were necessary. In PPP mode, the GPSEST program was used to perform the parameter estimation. The ionosphere-free linear combination was used and the elevation mask was set to 5° . For troposphere parameters estimation a similar strategy was used as in the case of double-difference solution. Note that in the PPP procedure the program MAUPRP is omitted. This is done on purpose to be able to detect bad observation data, and their impact on the PPP solution (example SONN). The cycle-slip screening was performed previously in program RNXSMT.

With regard to different test scenarios (see Sec. 6.6), different orbit and clock parameters were downloaded, and therefore different Perl scripts had to be prepared. Special care had to be therefore paid to result extraction and naming convention of extracted files.

Appendix B

Appendix B covers the complete set of figures illustrating ZWD time series and their respective formal errors per day for the entire tested period. The figures are displayed in sequence according to the ellipsoidal station height, as already shown in Figs. 6.2 and 6.3, and described in Sec. 6.4.

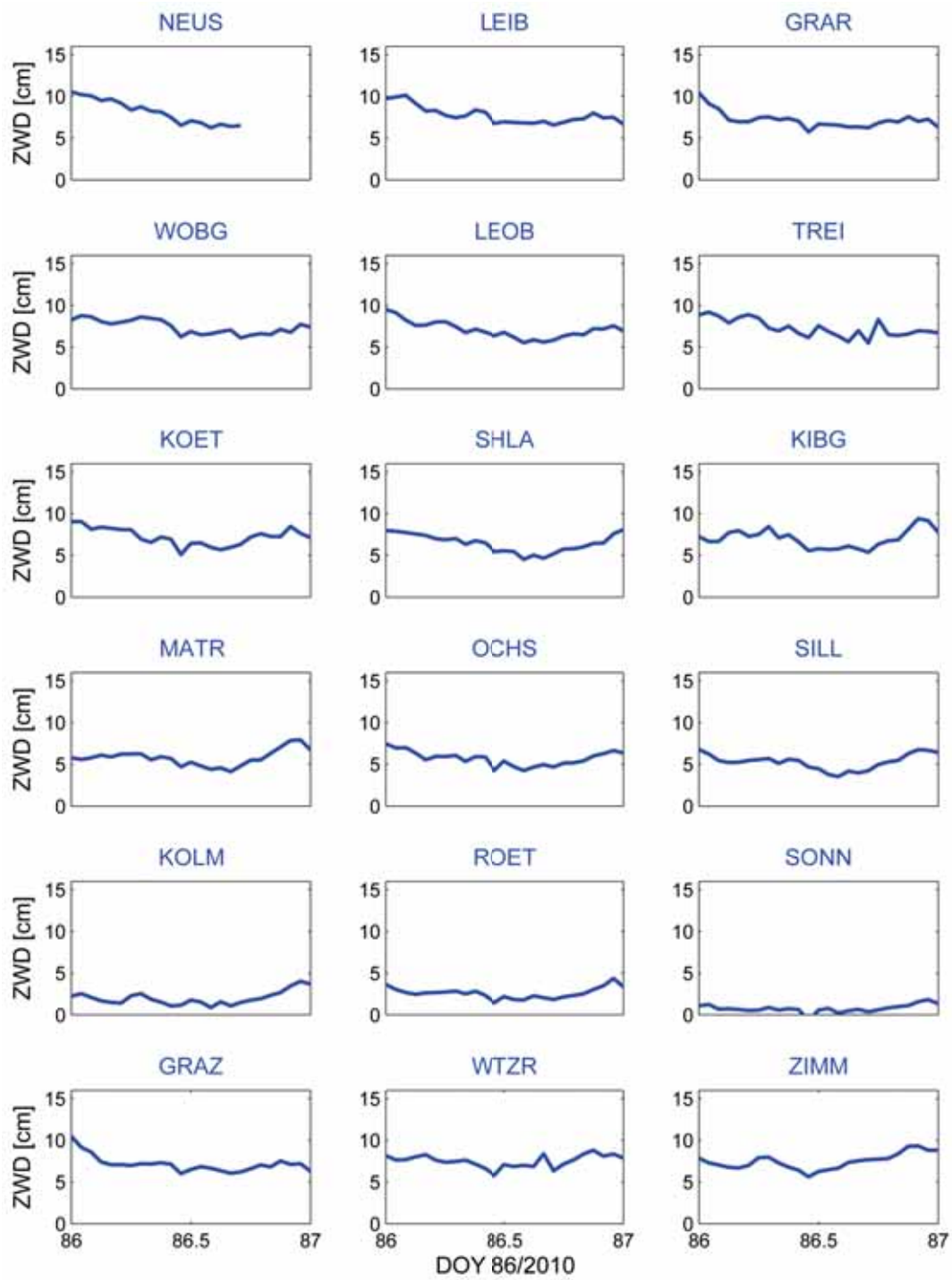


Figure B.1: ZWD (in cm) of all stations on March 27th, 2010

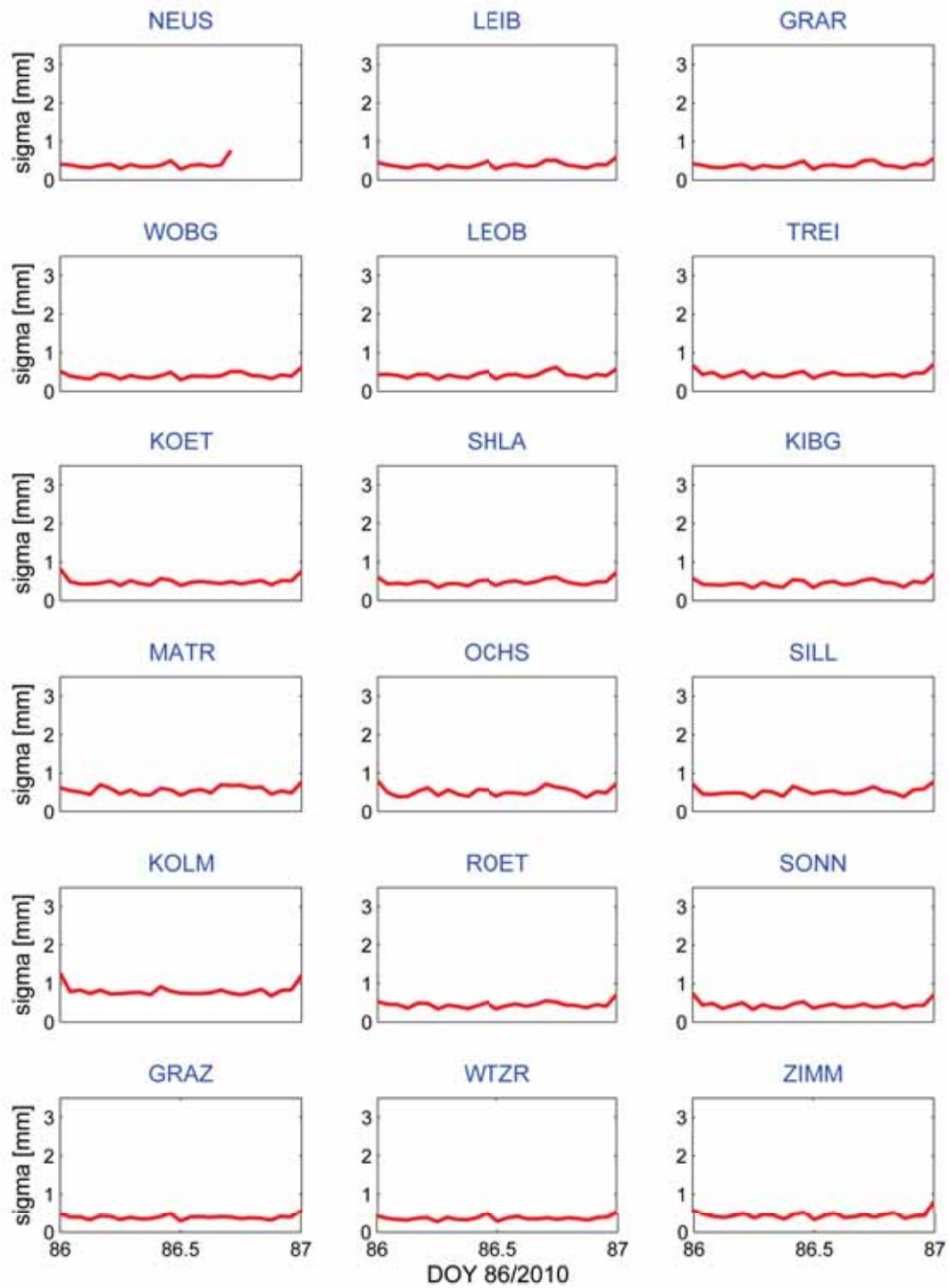


Figure B.2: Formal errors of ZWD estimates (in mm) of all stations on March 27th, 2010

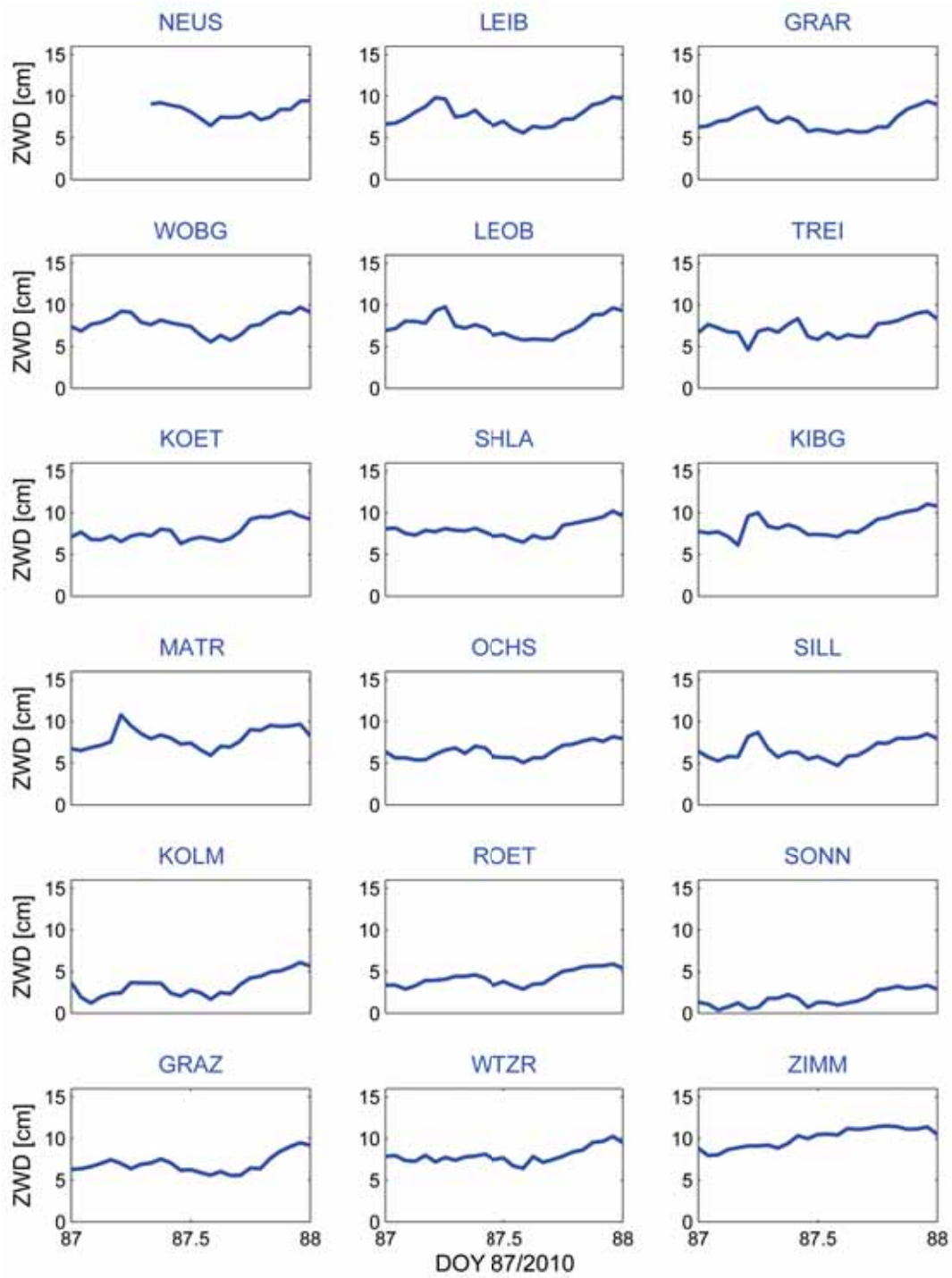


Figure B.3: ZWD (in cm) of all stations on March 28th, 2010

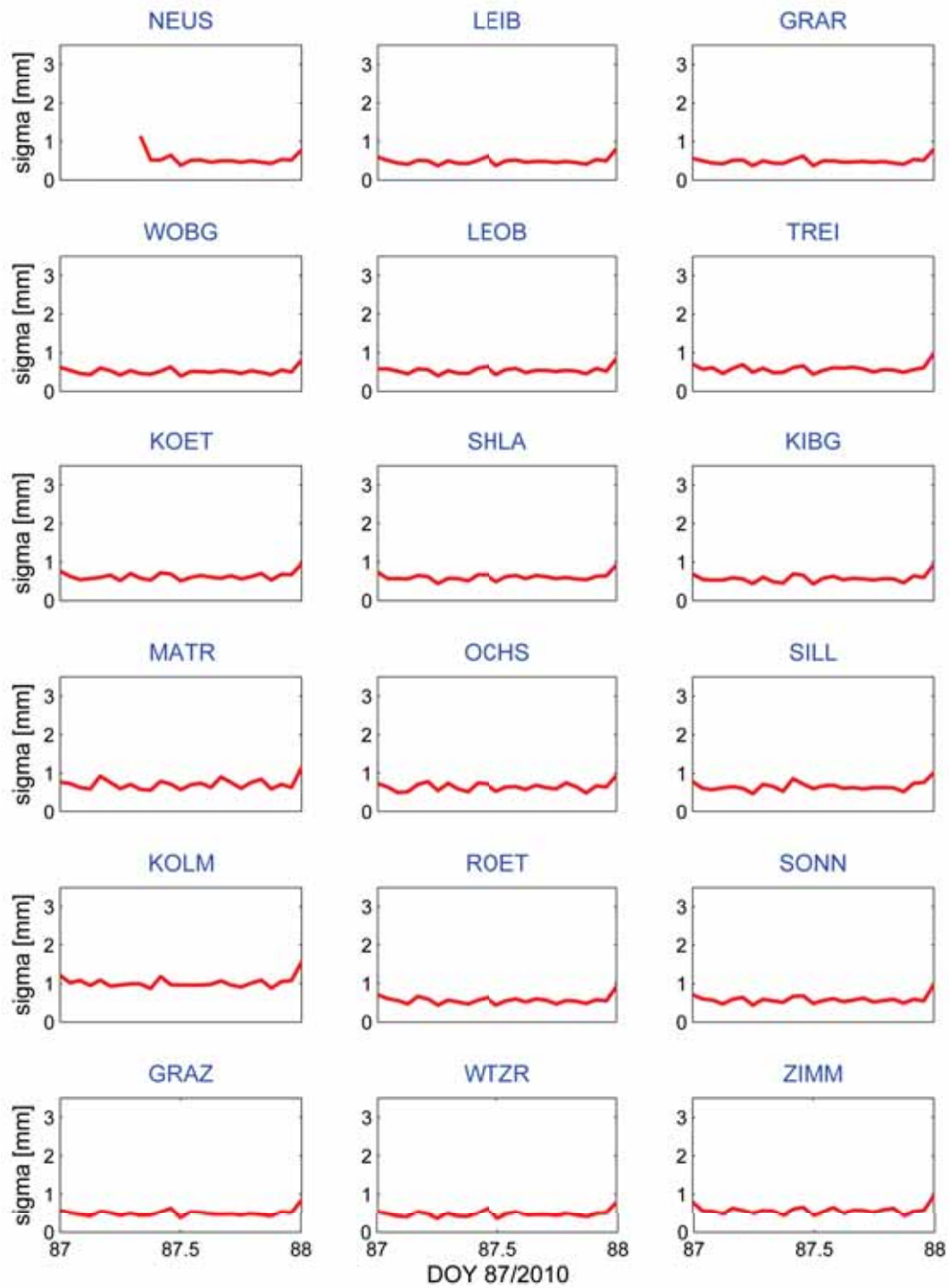


Figure B.4: Formal errors of ZWD estimates (in mm) of all stations on March 28th, 2010

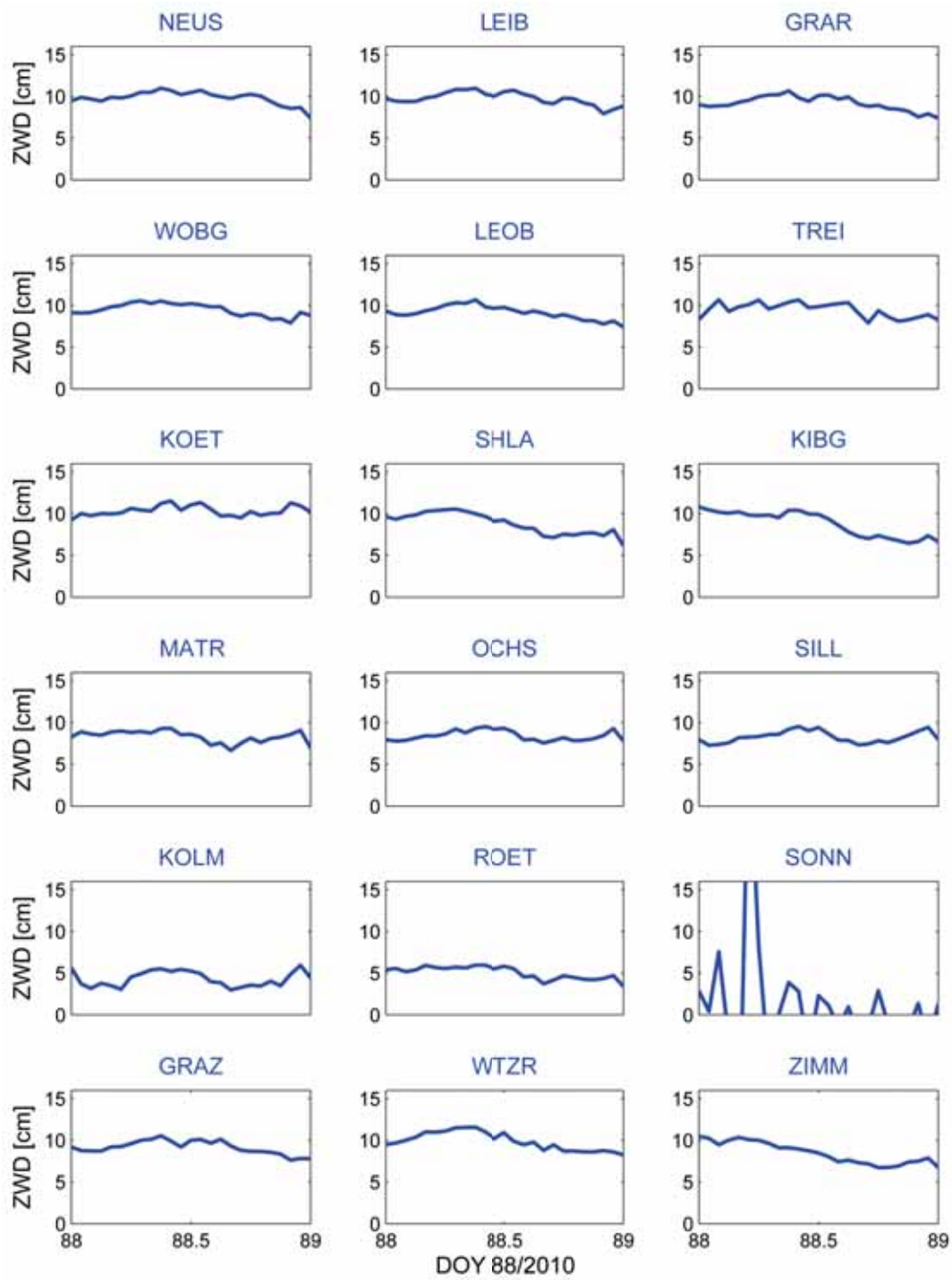


Figure B.5: ZWD (in cm) of all stations on March 29th, 2010

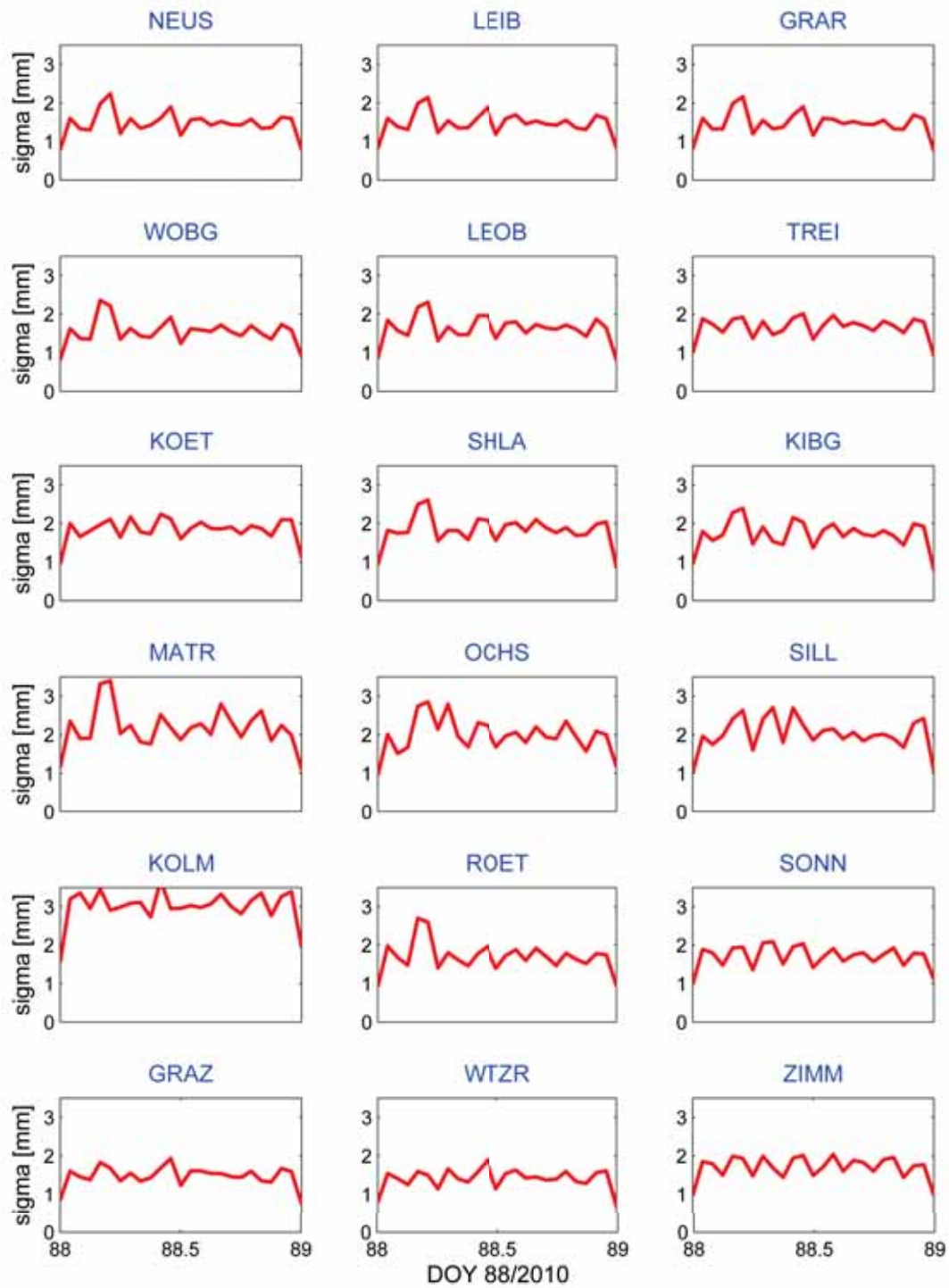


Figure B.6: Formal errors of ZWD estimates (in mm) of all stations on March 29th, 2010

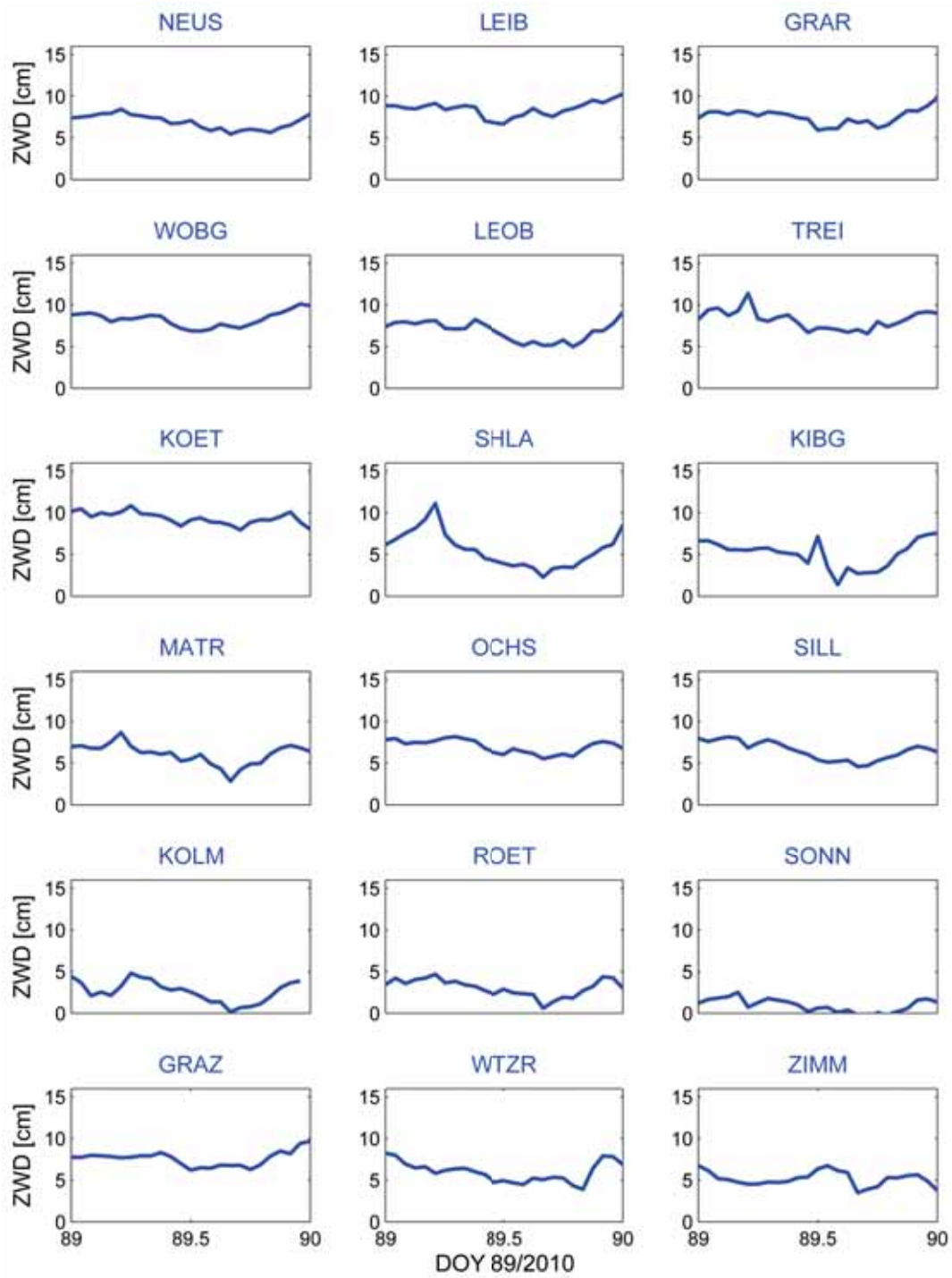


Figure B.7: ZWD (in cm) of all stations on March 30th, 2010

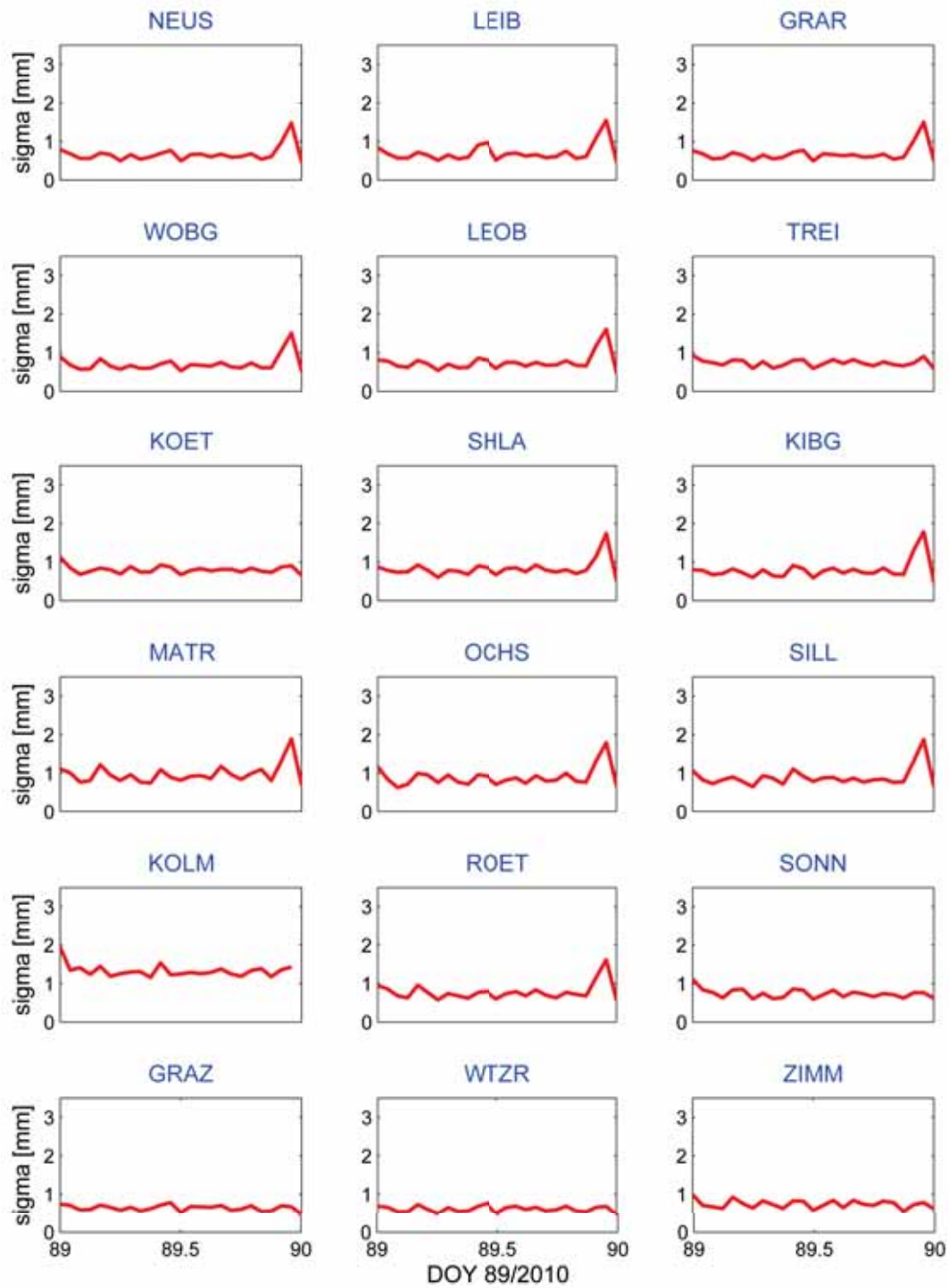


Figure B.8: Formal errors of ZWD estimates (in mm) of all stations on March 30th, 2010

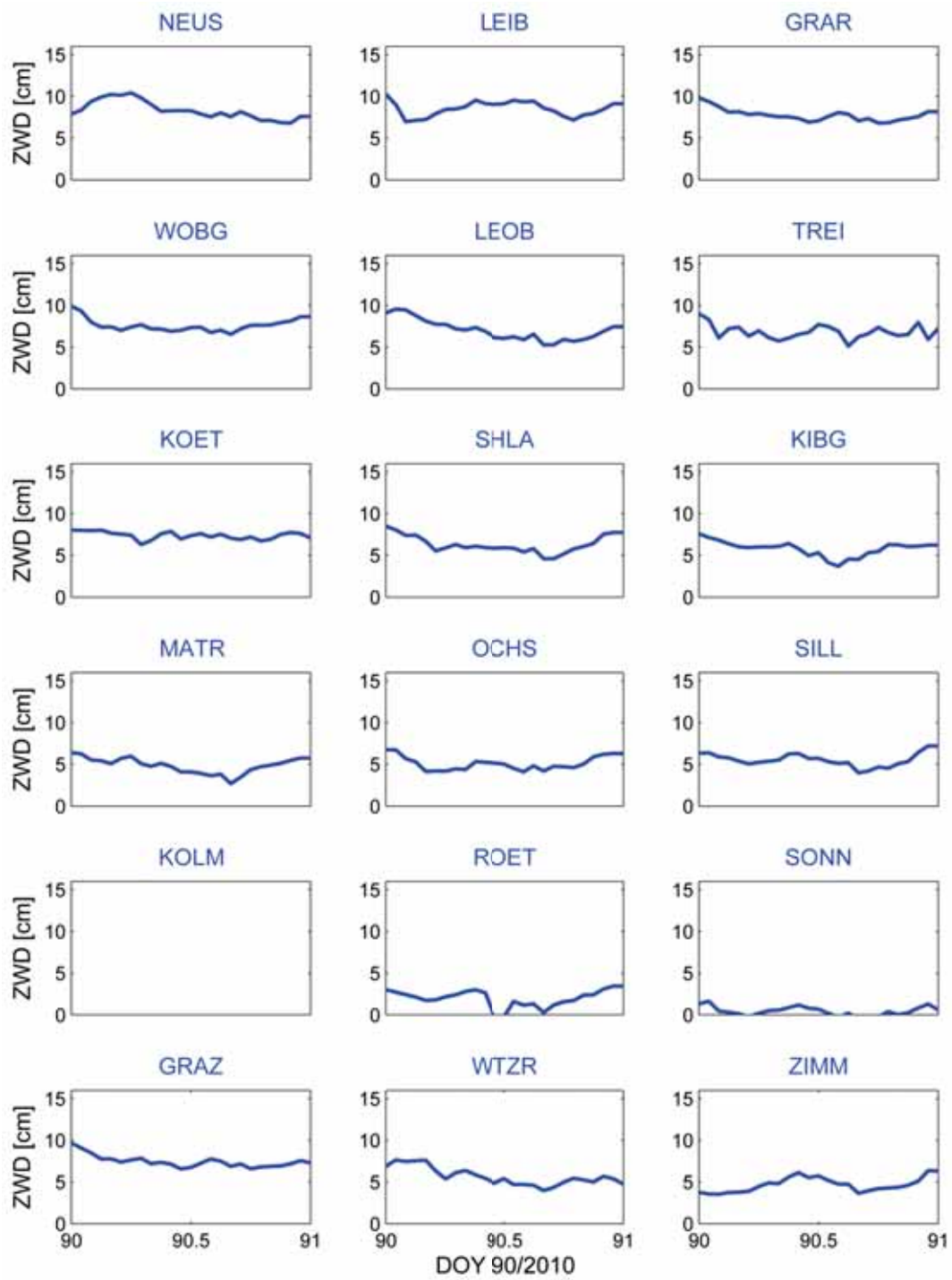


Figure B.9: ZWD (in cm) of all stations on March 31th, 2010

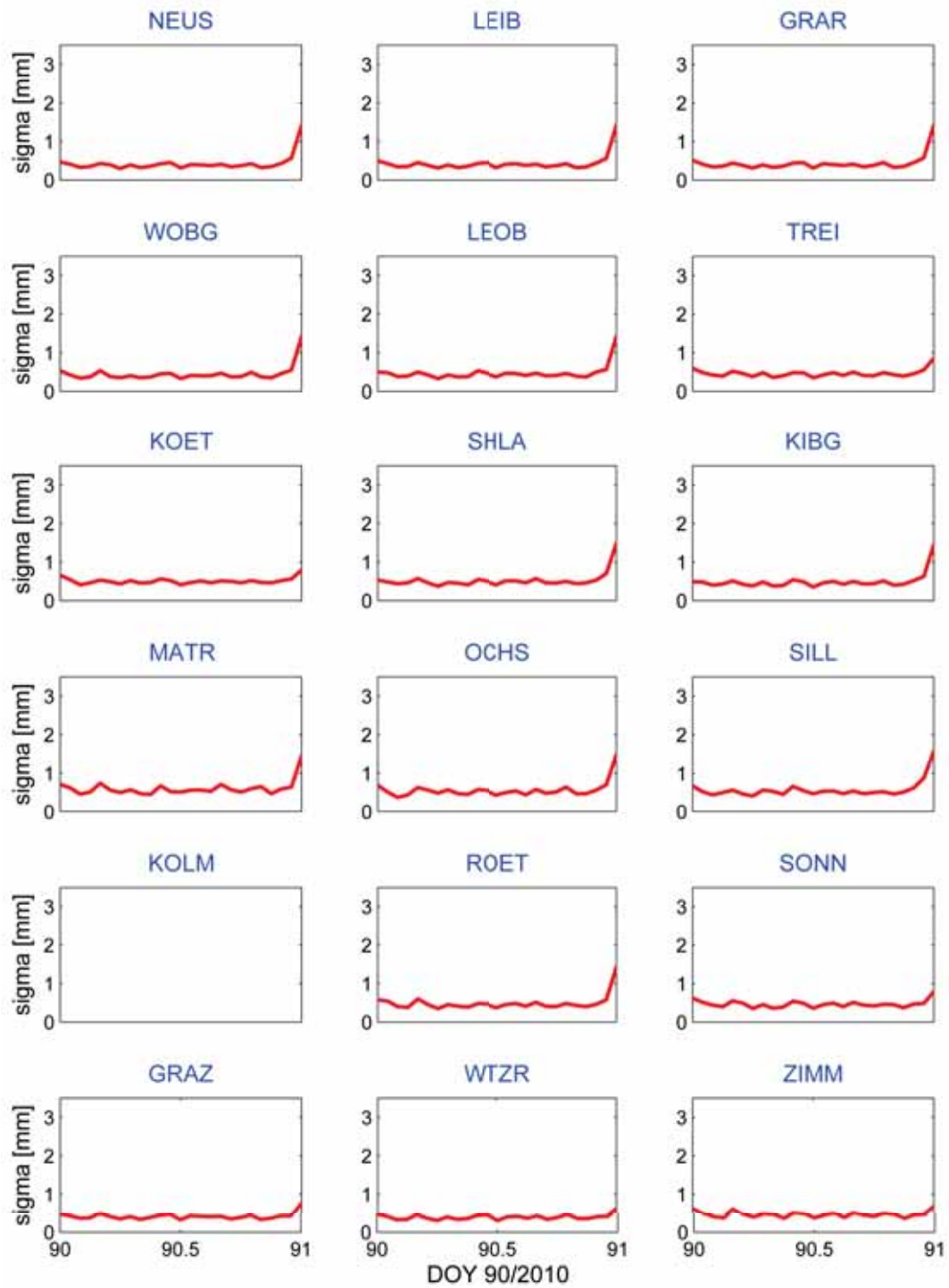


Figure B.10: Formal errors of ZWD estimates (in mm) of all stations on March 31th, 2010

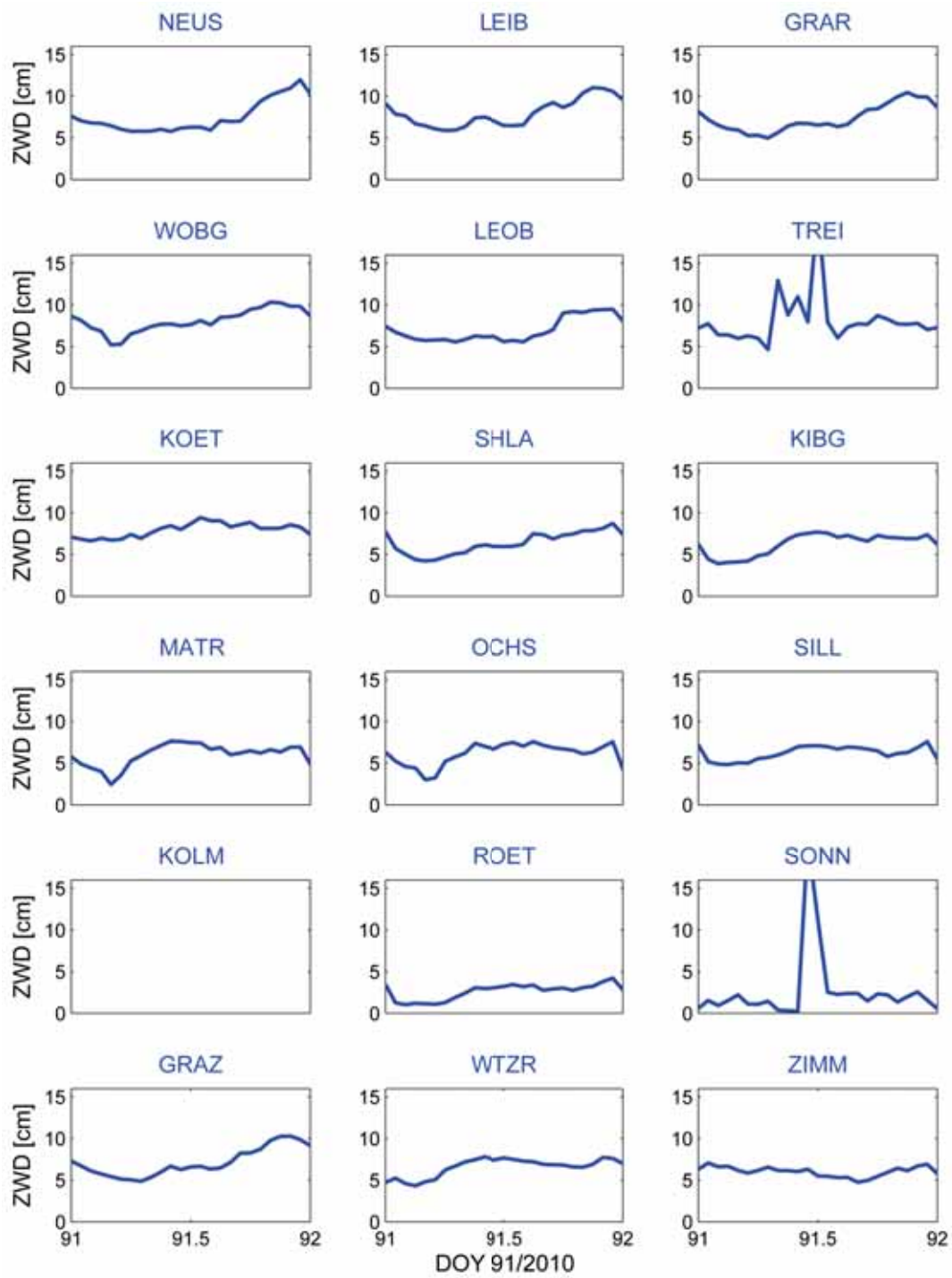


Figure B.11: ZWD (in cm) of all stations for April 1st, 2010

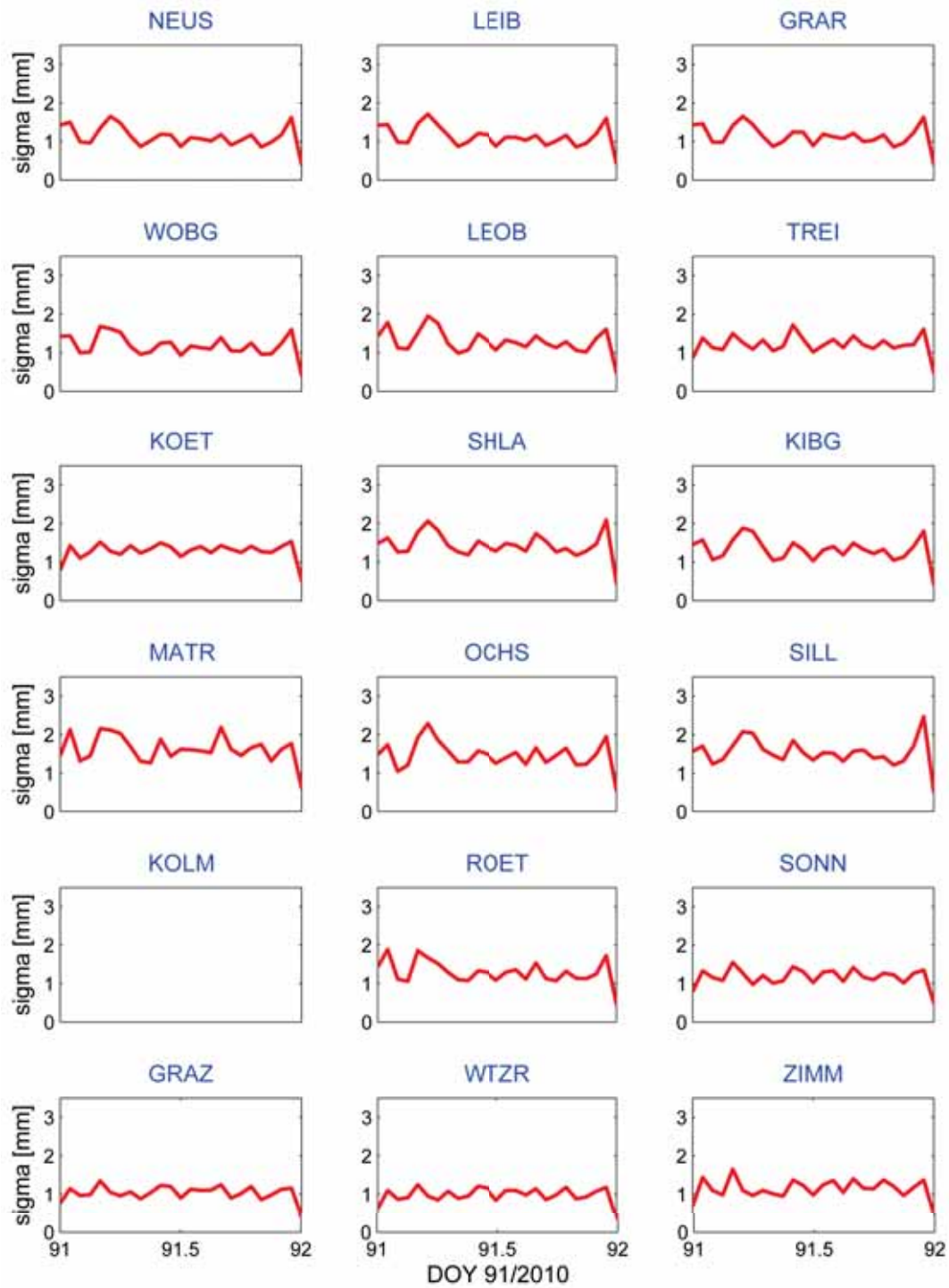


Figure B.12: Formal errors of ZWD estimates (in mm) of all stations on April 1st, 2010

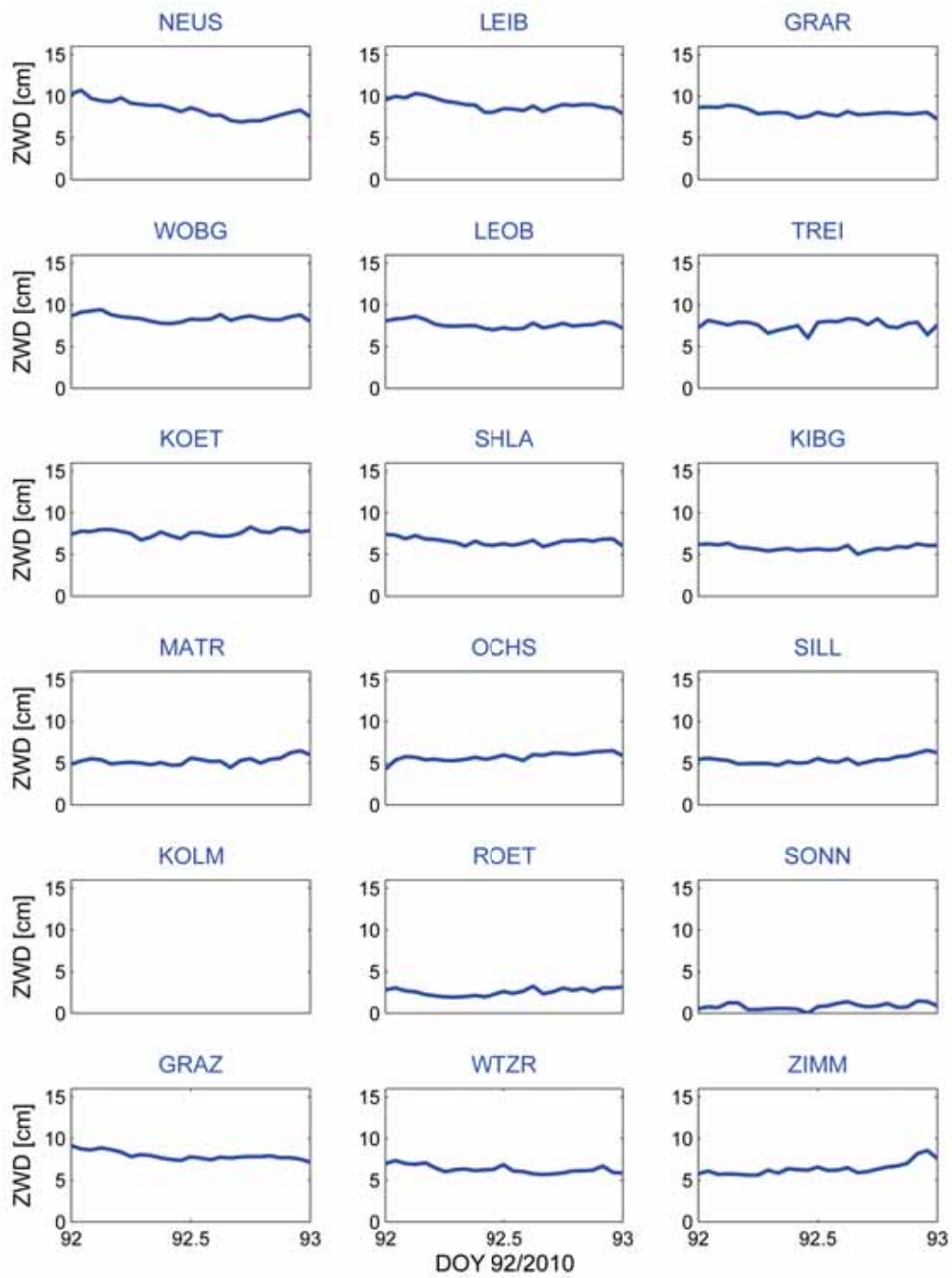


Figure B.13: ZWD (in cm) of all stations on April 2nd, 2010

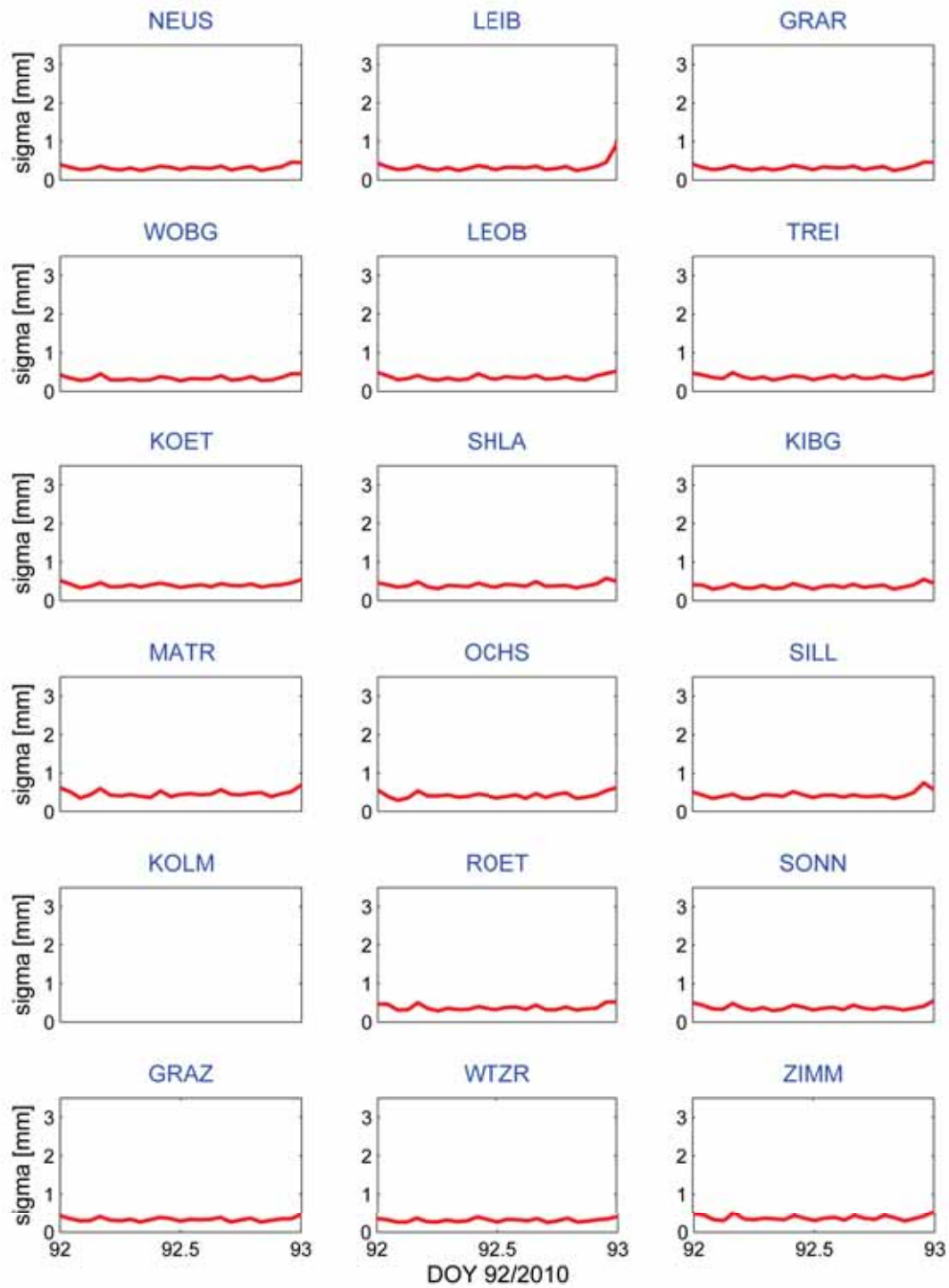


Figure B.14: Formal errors of ZWD estimates (in mm) of all stations on April 2nd, 2010

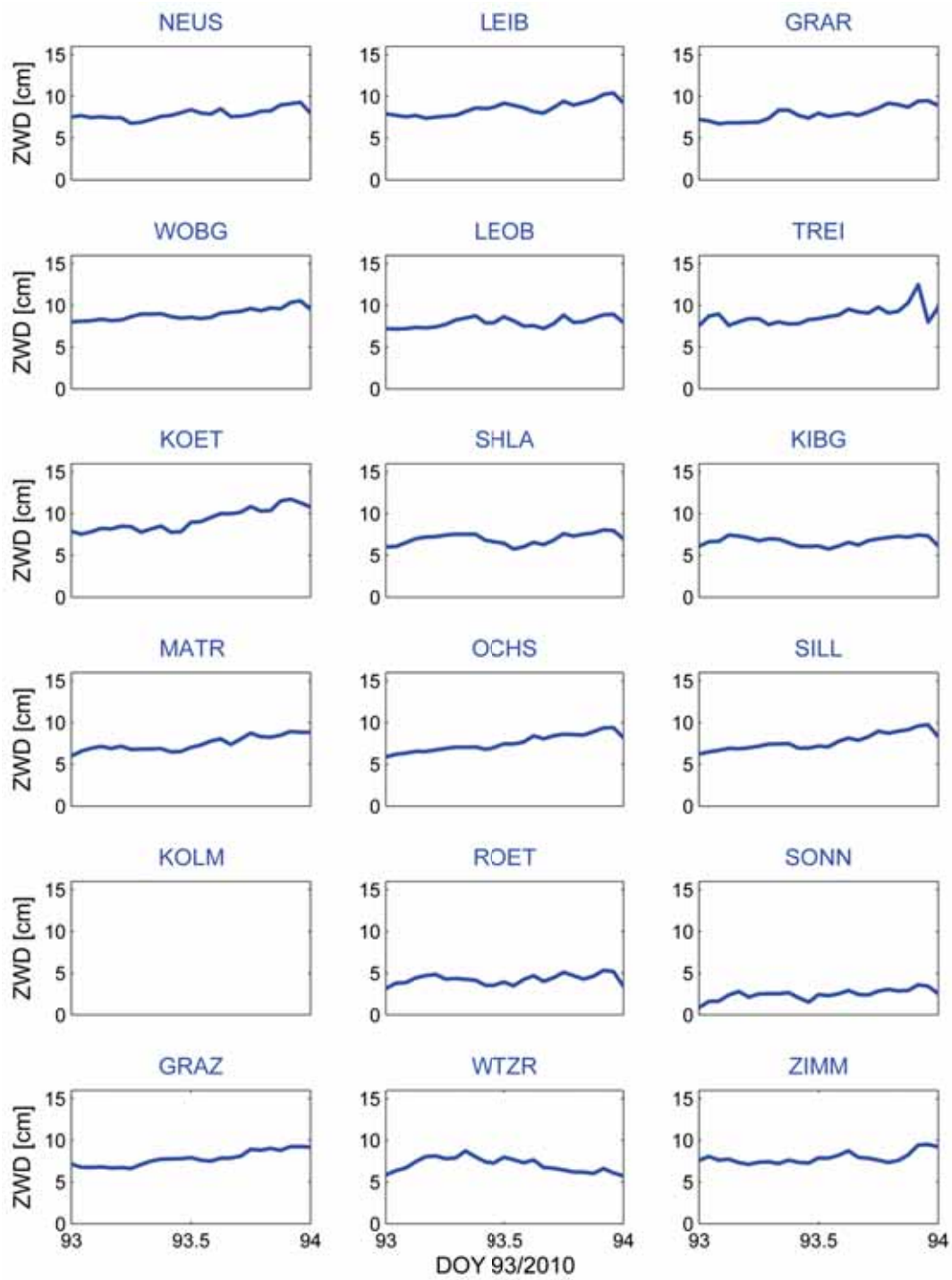


Figure B.15: ZWD (in cm) of all stations on April 3rd, 2010

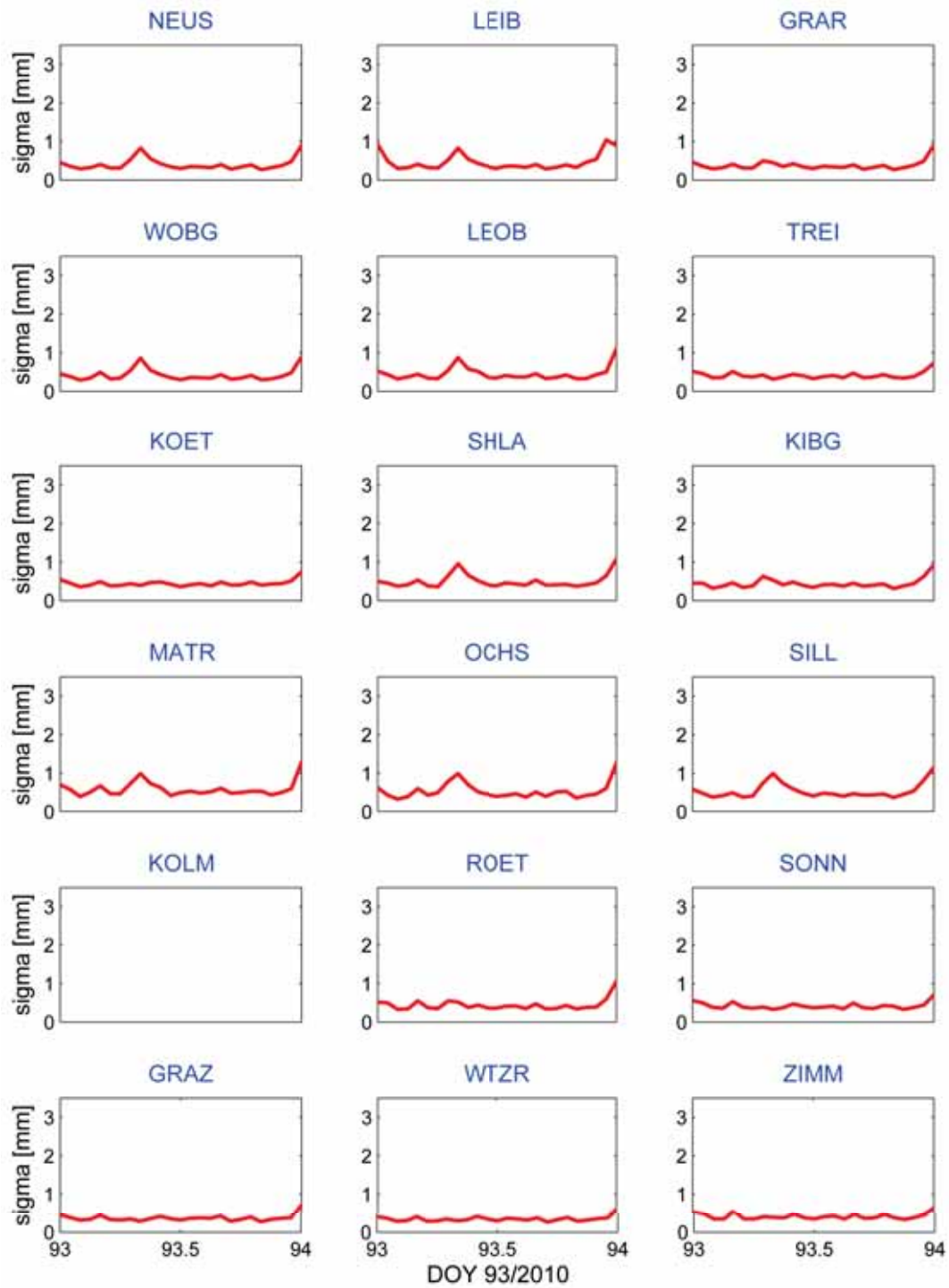


Figure B.16: Formal errors of ZWD estimates (in mm) of all stations on April 3rd, 2010

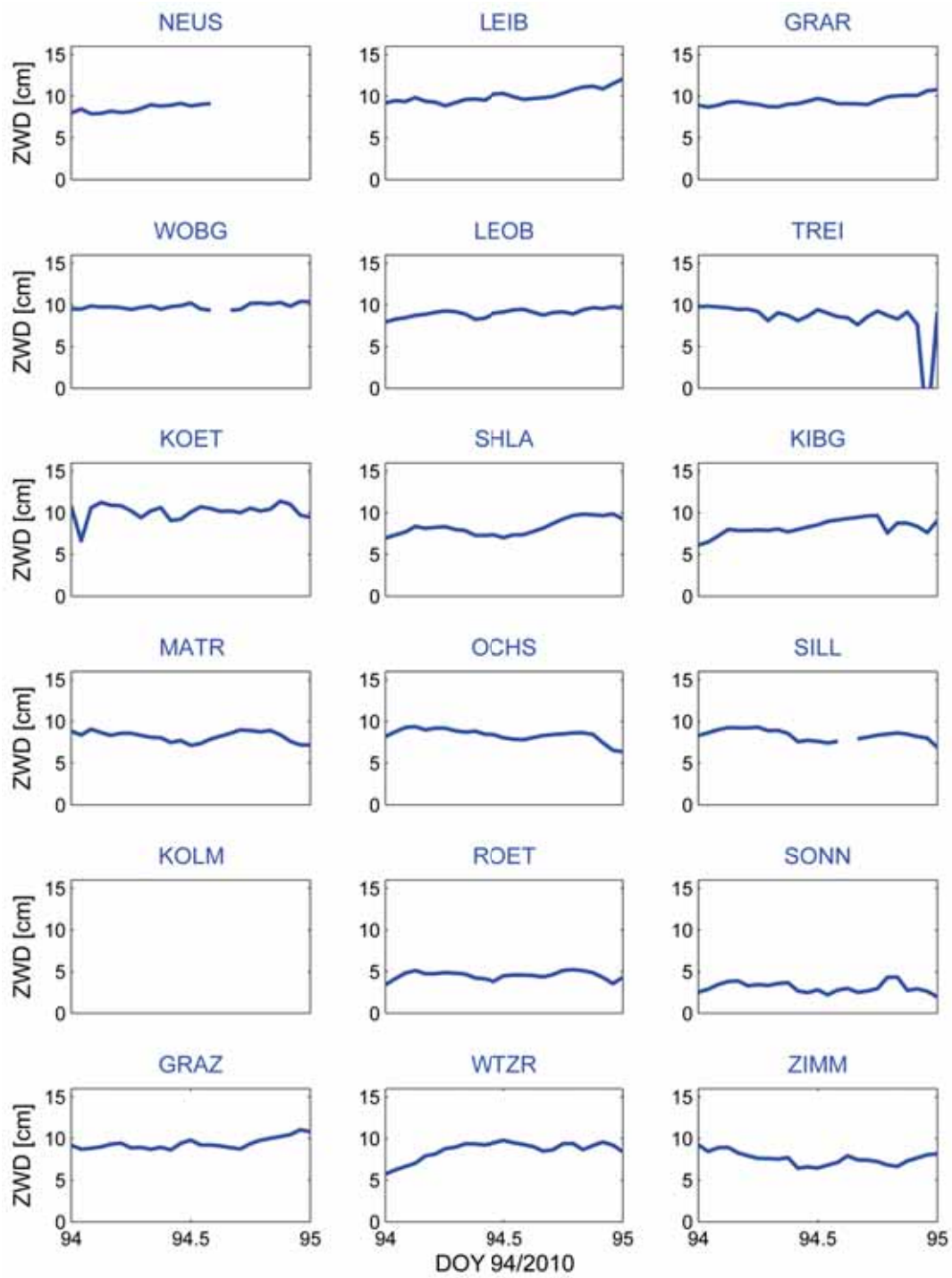


Figure B.17: ZWD (in cm) of all stations on April 4th, 2010

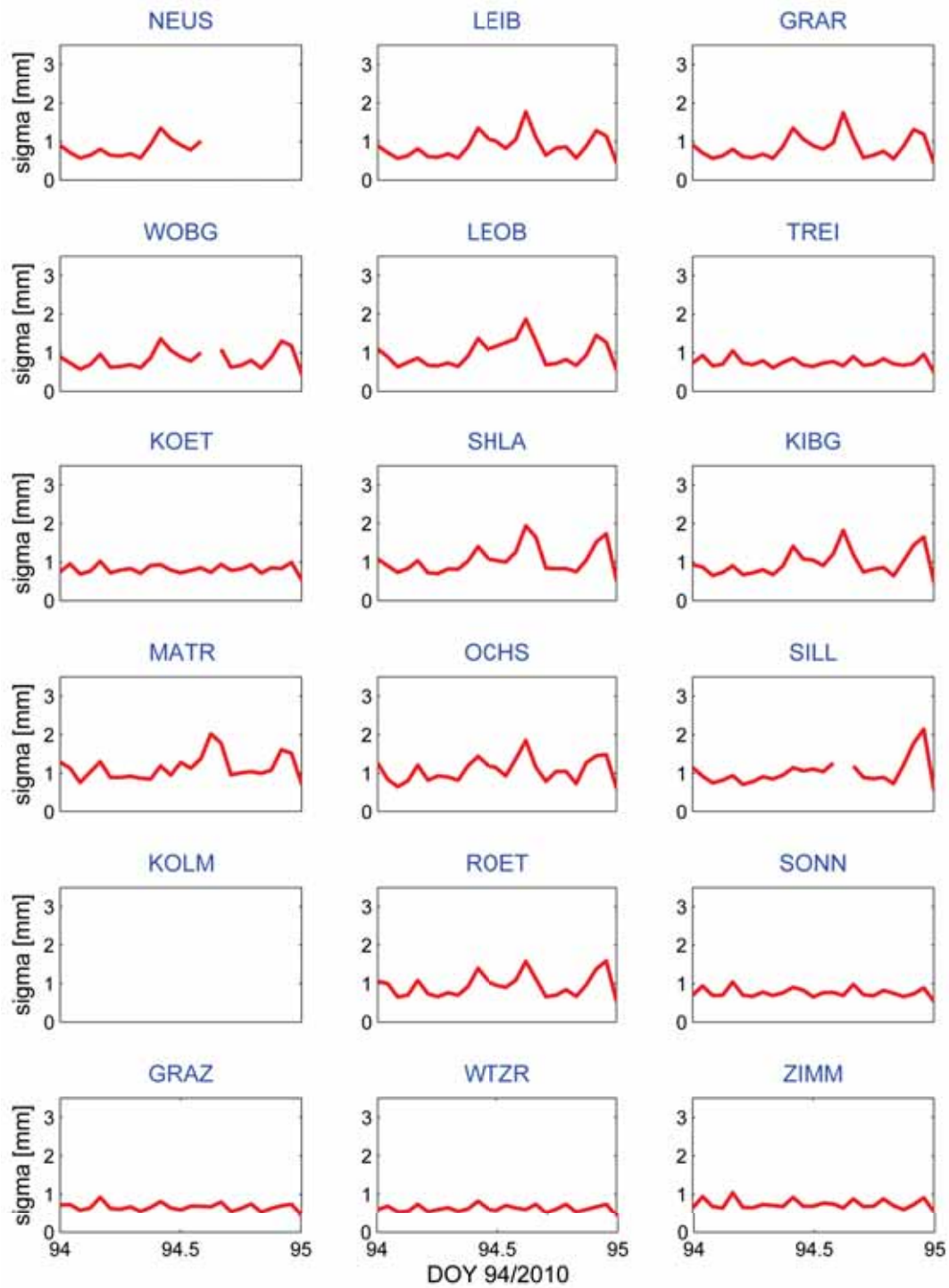


Figure B.18: Formal errors of ZWD estimates (in mm) of all stations on April 4th, 2010

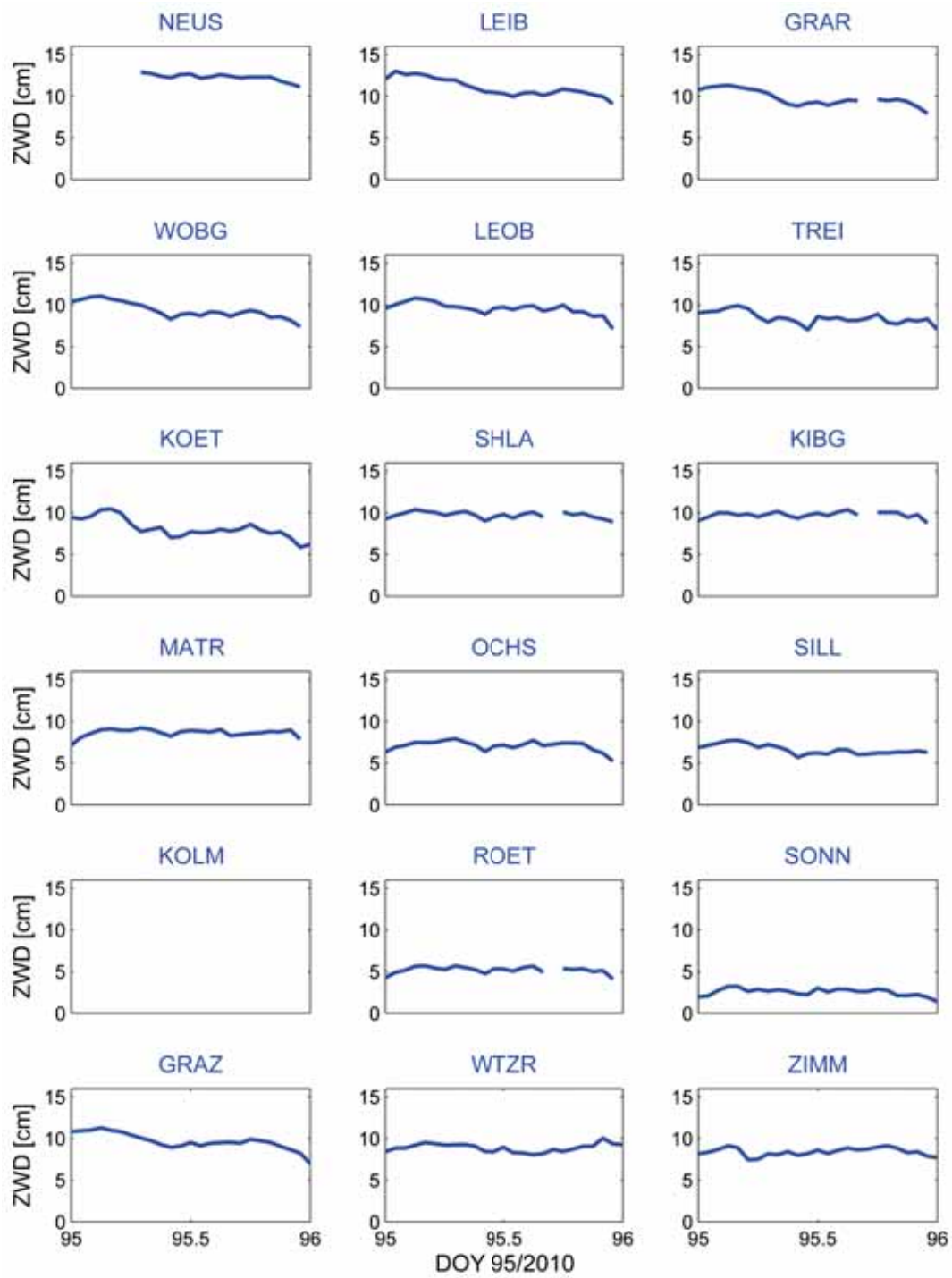


Figure B.19: ZWD (in cm) of all stations on April 5th, 2010

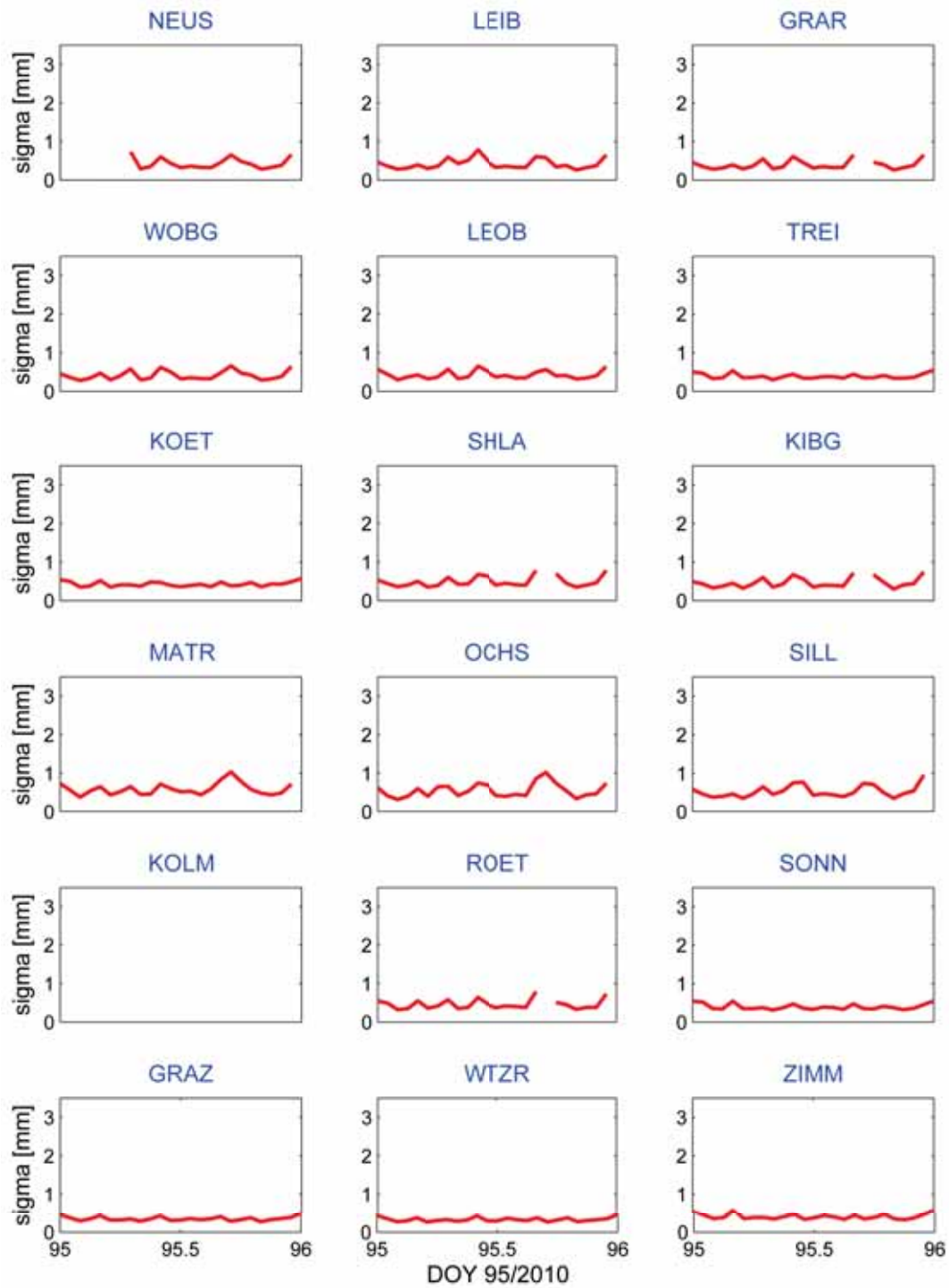


Figure B.20: Formal errors of ZWD estimates (in mm) of all stations on April 5th, 2010

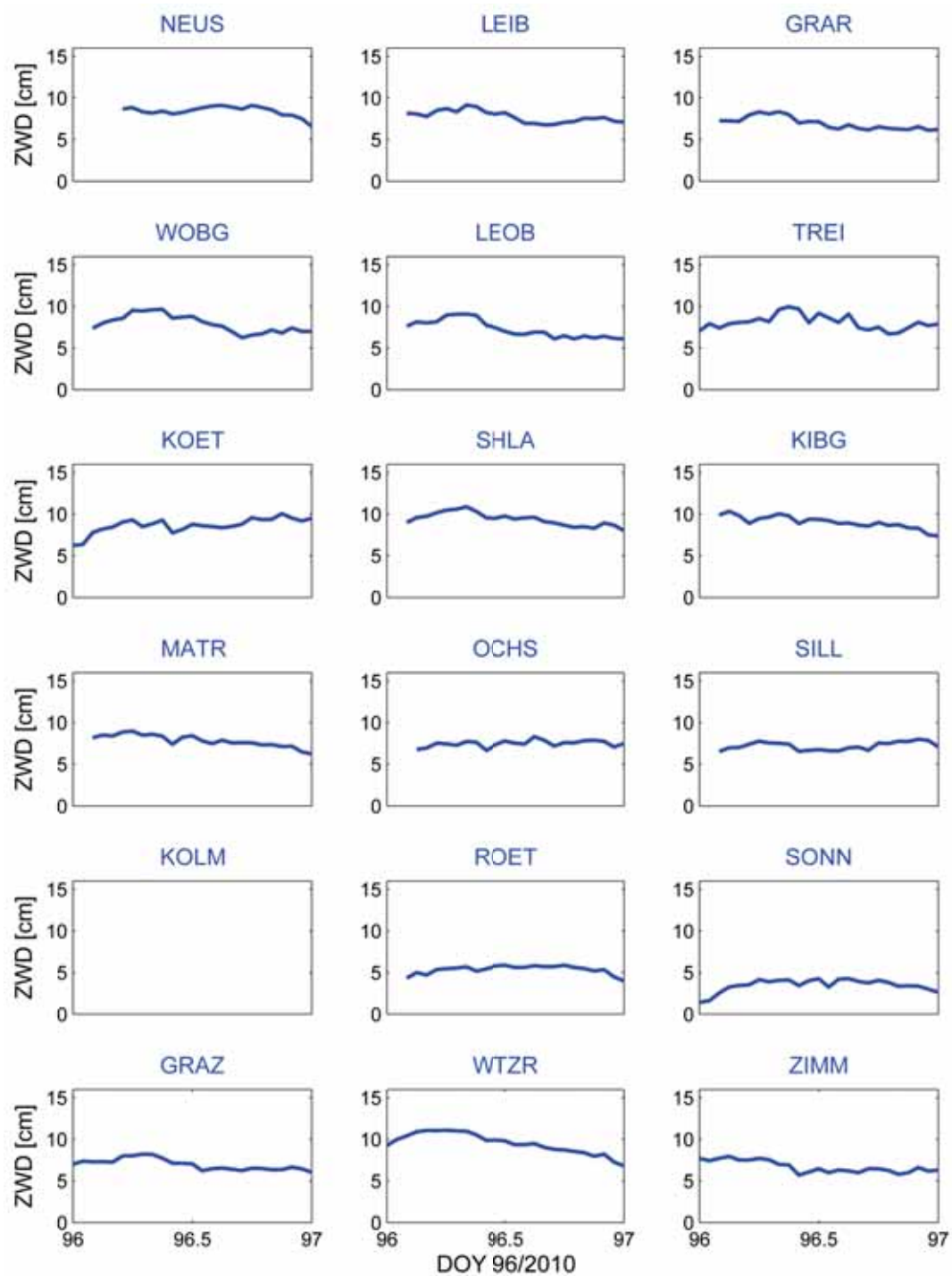


Figure B.21: ZWD (in cm) of all stations on April 6th, 2010

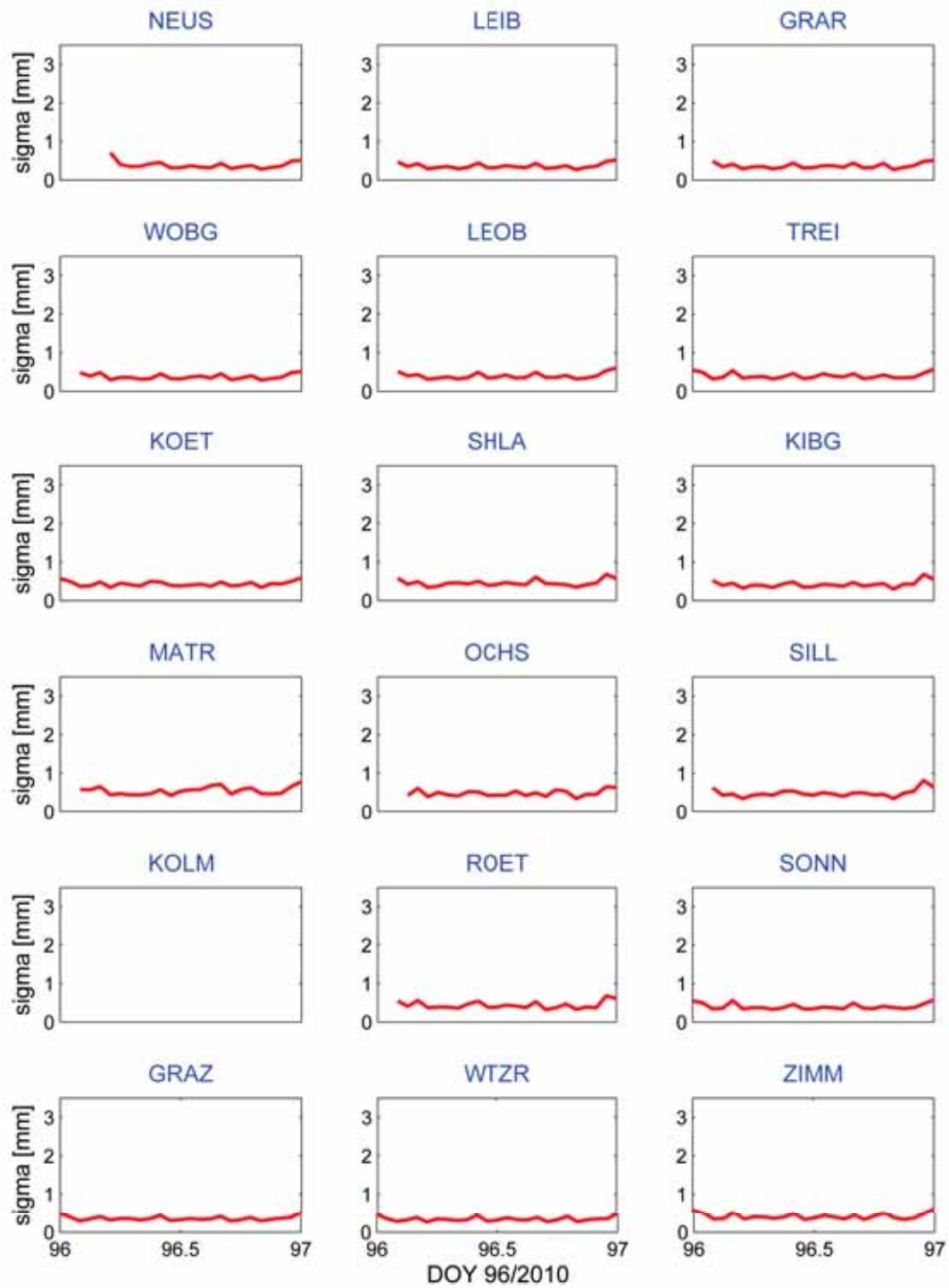


Figure B.22: Formal errors of ZWD estimates (in mm) of all stations on April 6th, 2010

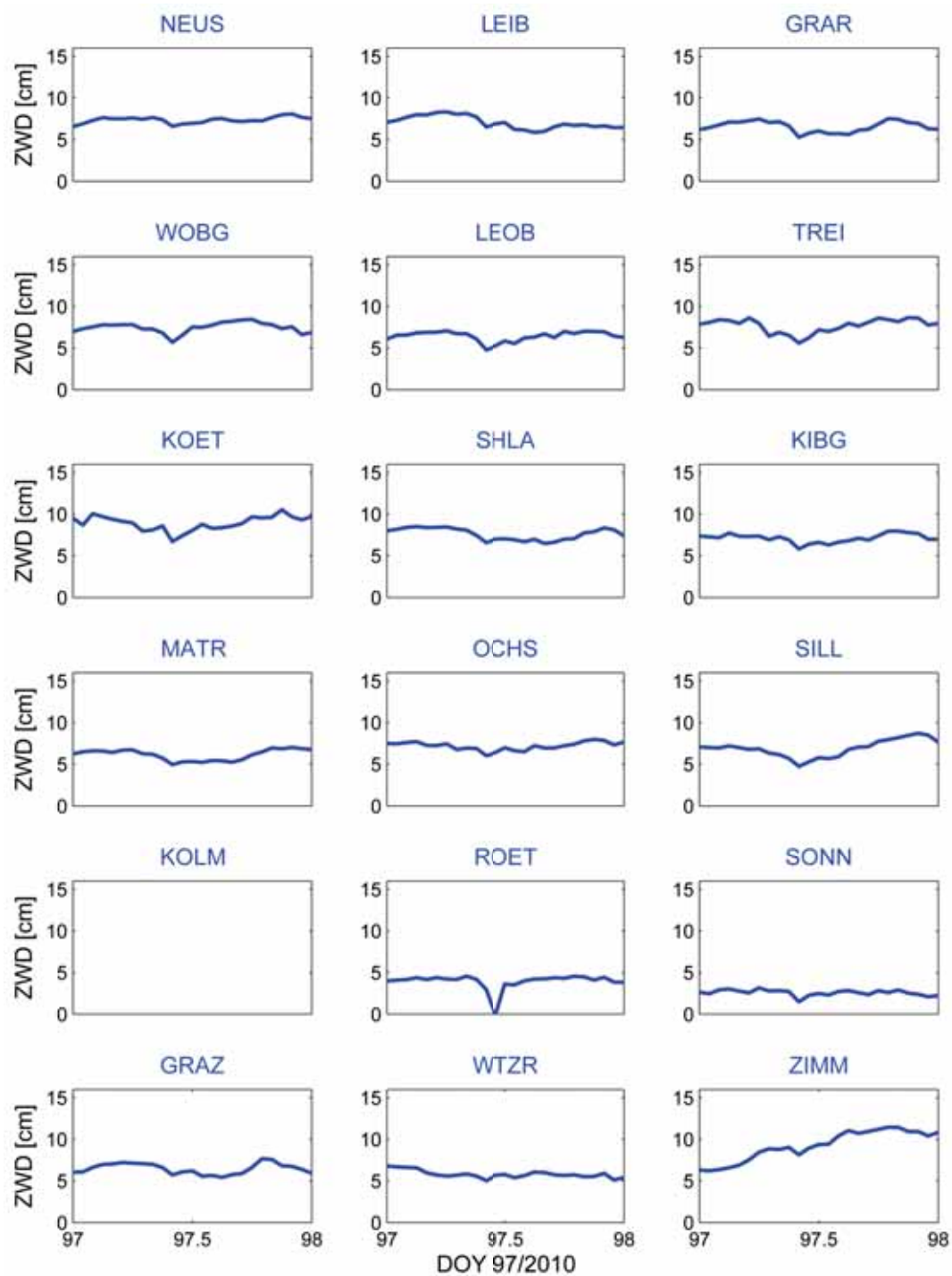


Figure B.23: ZWD (in cm) of all stations on April 7th, 2010

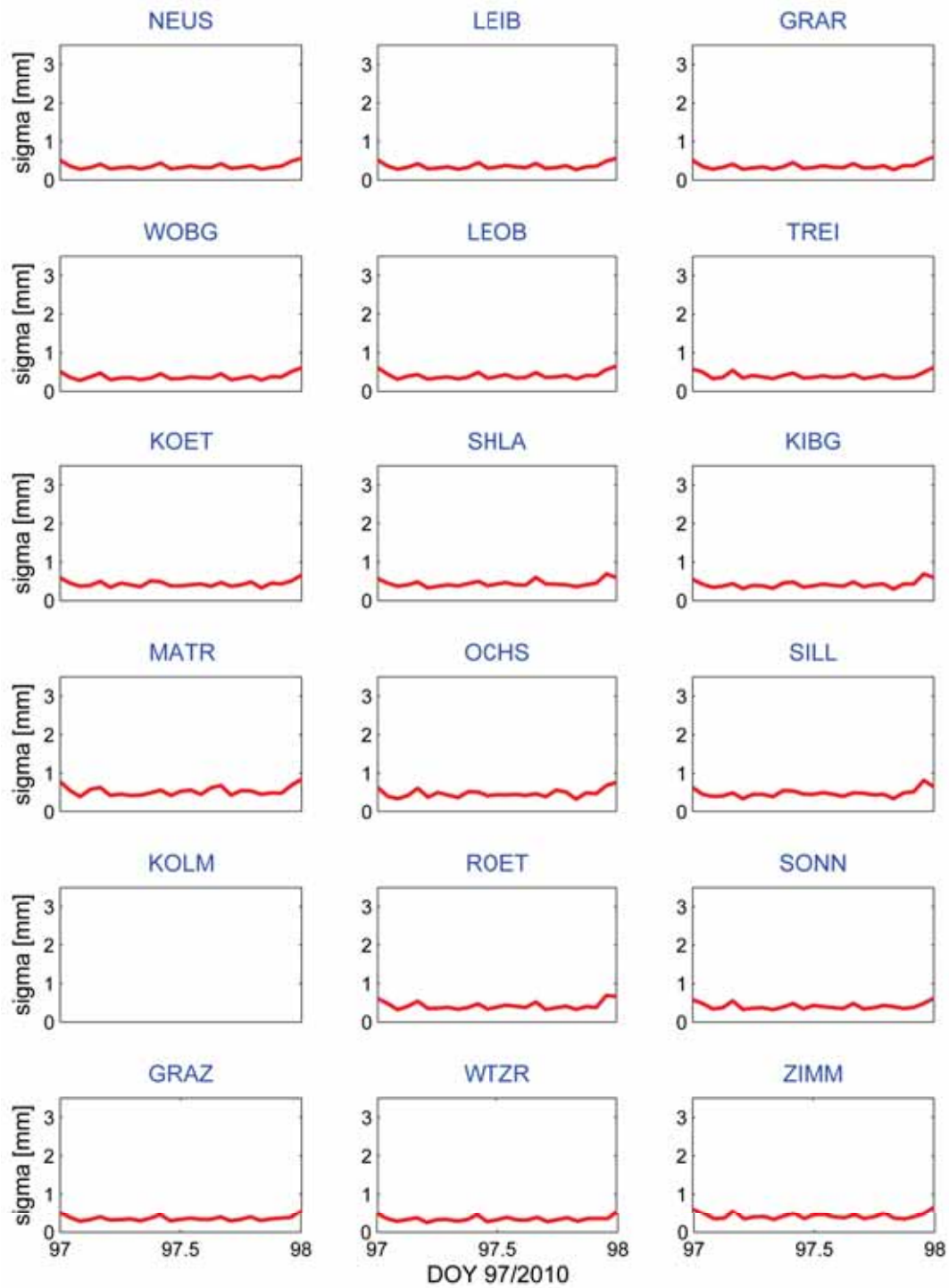


Figure B.24: Formal errors of ZWD estimates (in mm) of all stations on April 7th, 2010

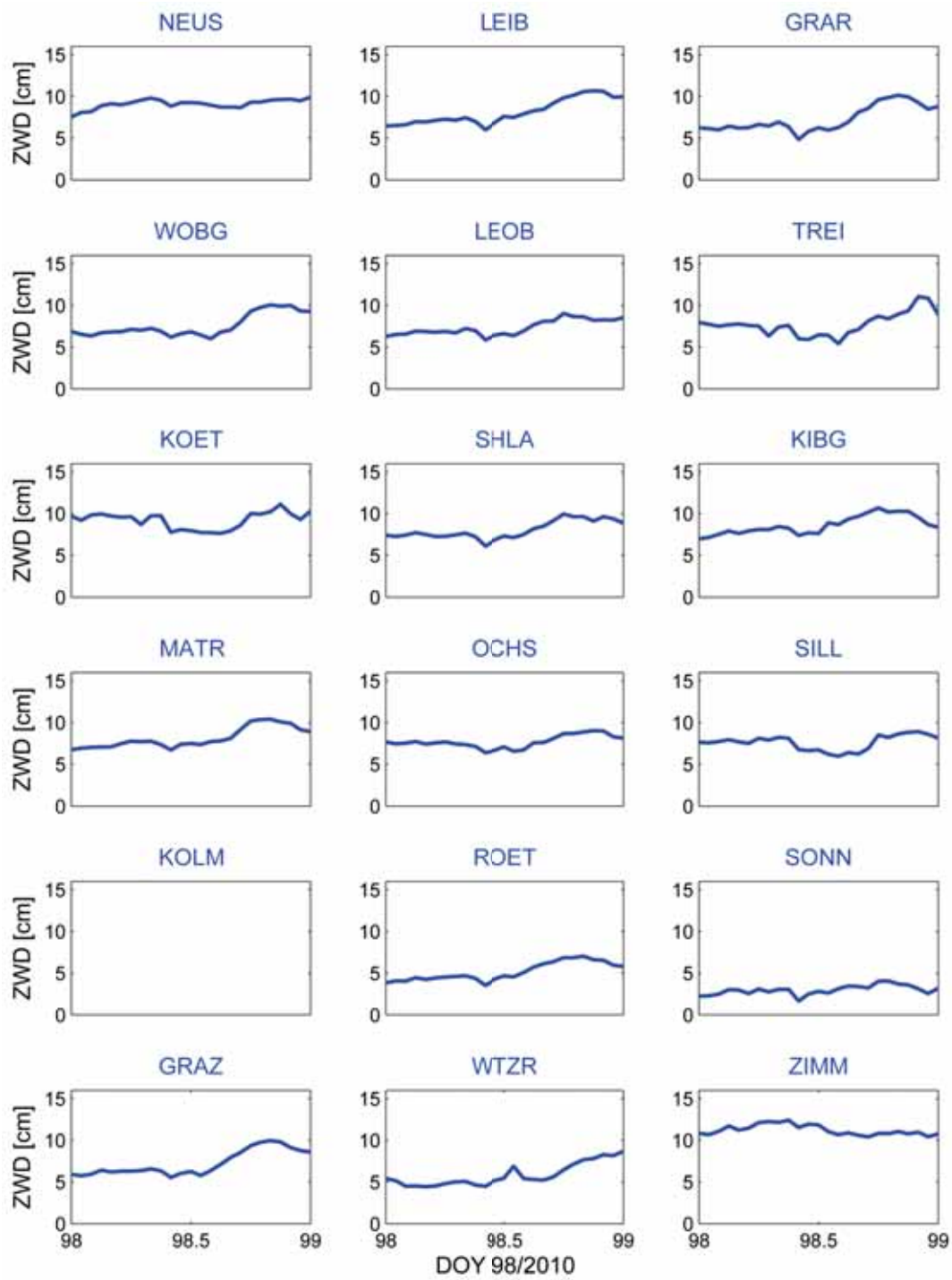


Figure B.25: ZWD (in cm) of all stations on April 8th, 2010

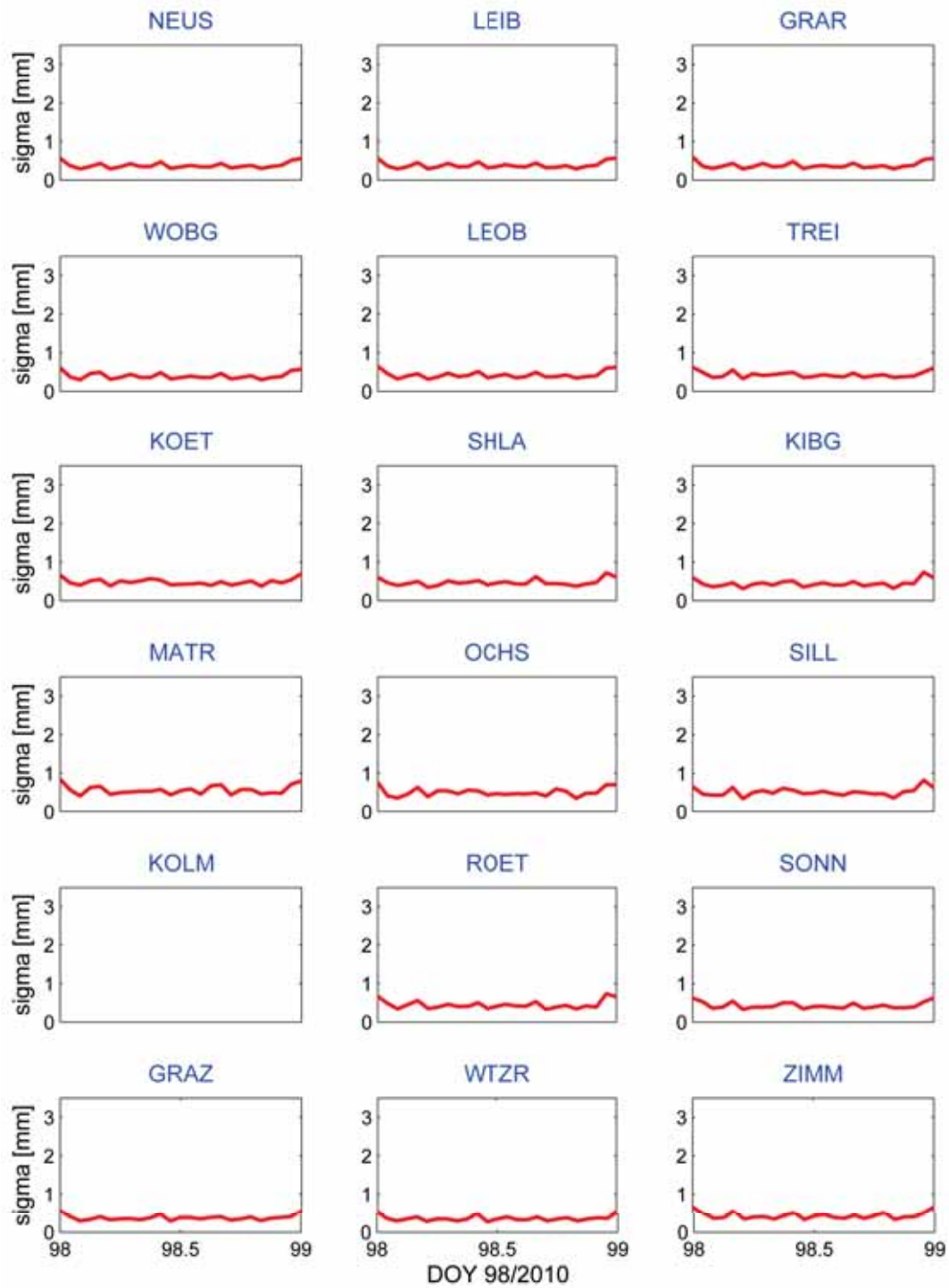


Figure B.26: Formal errors of ZWD estimates (in mm) of all stations on April 8th, 2010

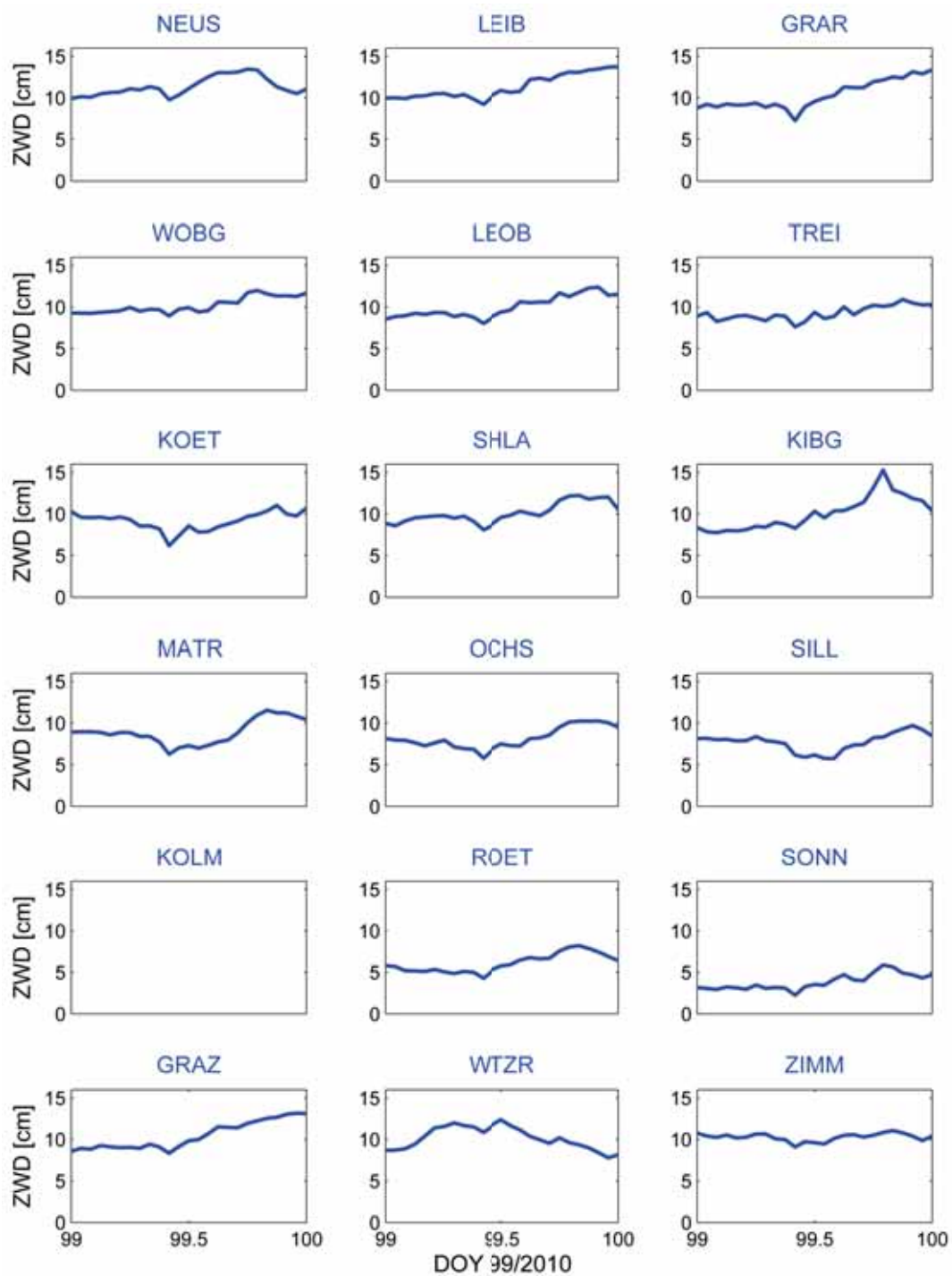


Figure B.27: ZWD (in cm) of all stations on April 9th, 2010

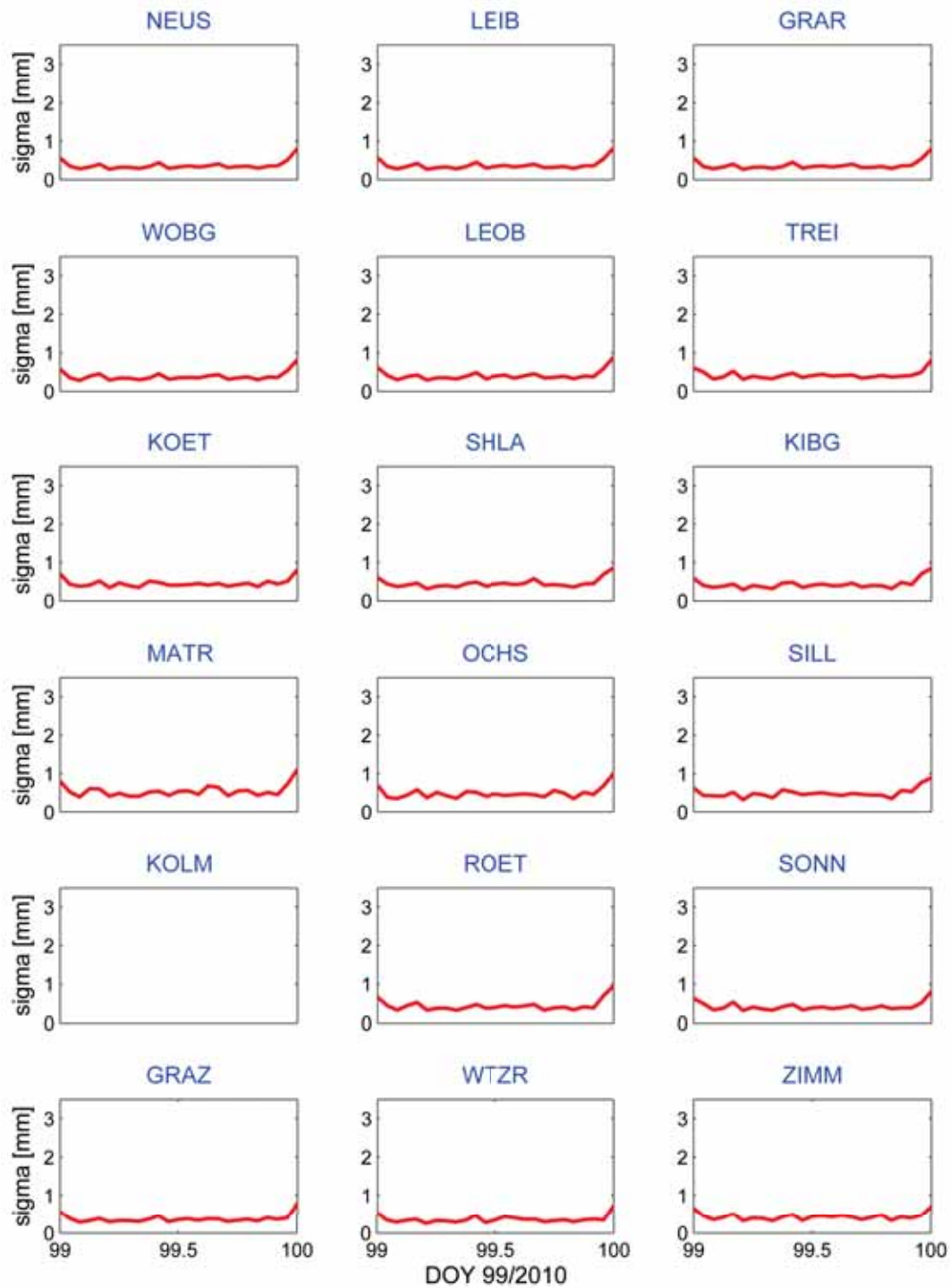


Figure B.28: Formal errors of ZWD estimates (in mm) of all stations on April 9th, 2010

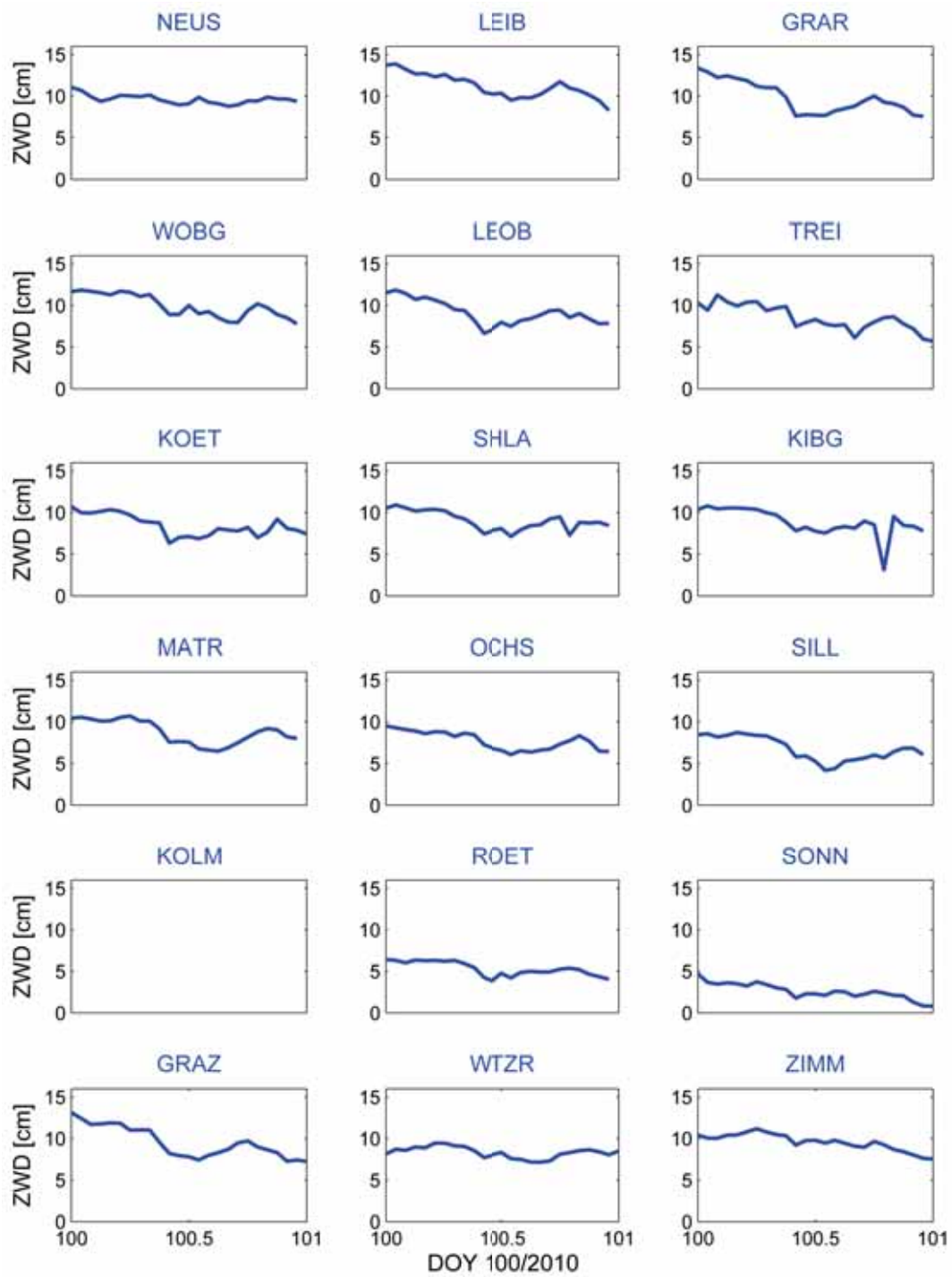


Figure B.29: ZWD (in cm) of all stations on April 6th, 2010

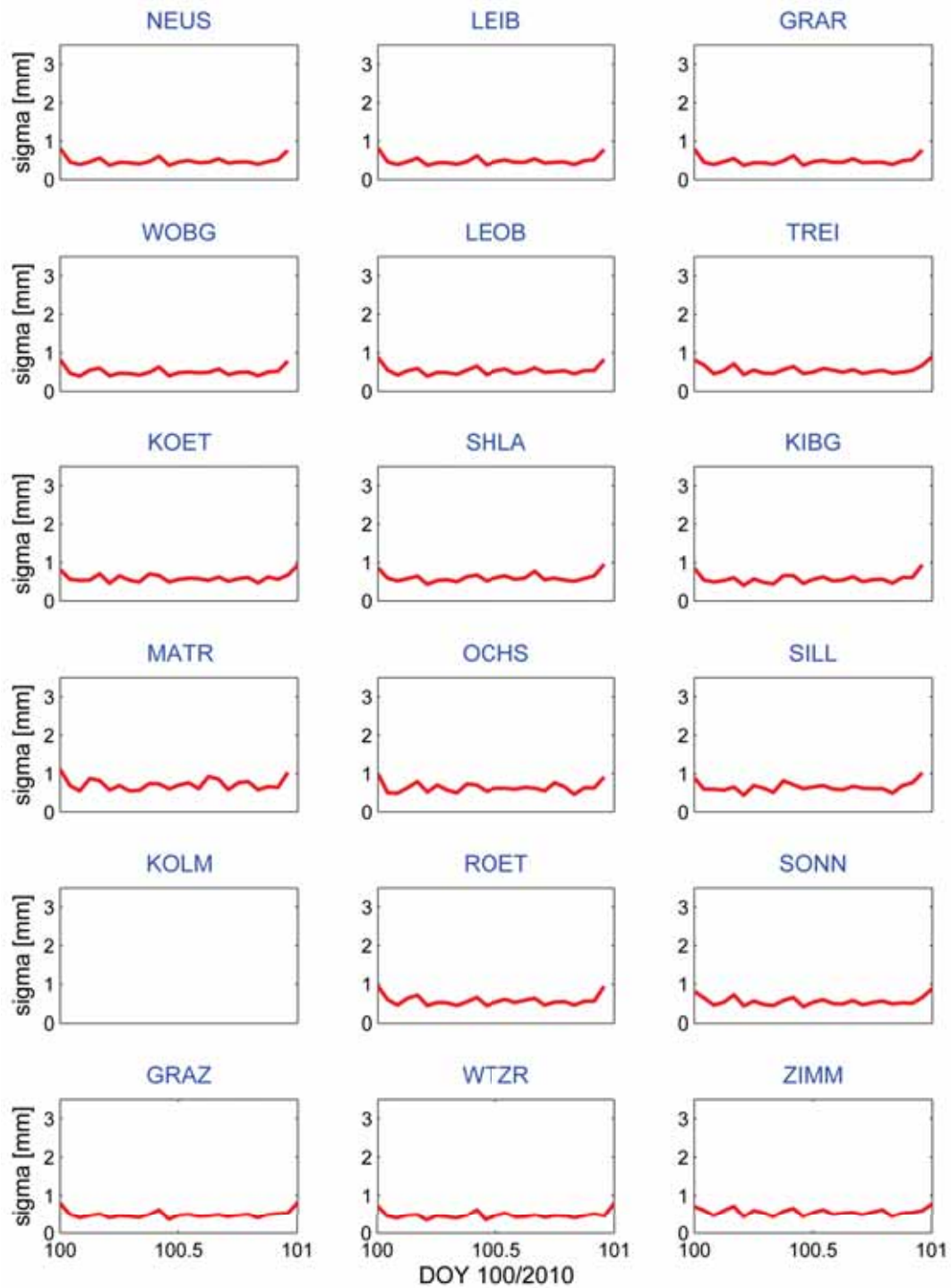


Figure B.30: Formal errors of ZWD estimates (in mm) of all stations on April 10th, 2010

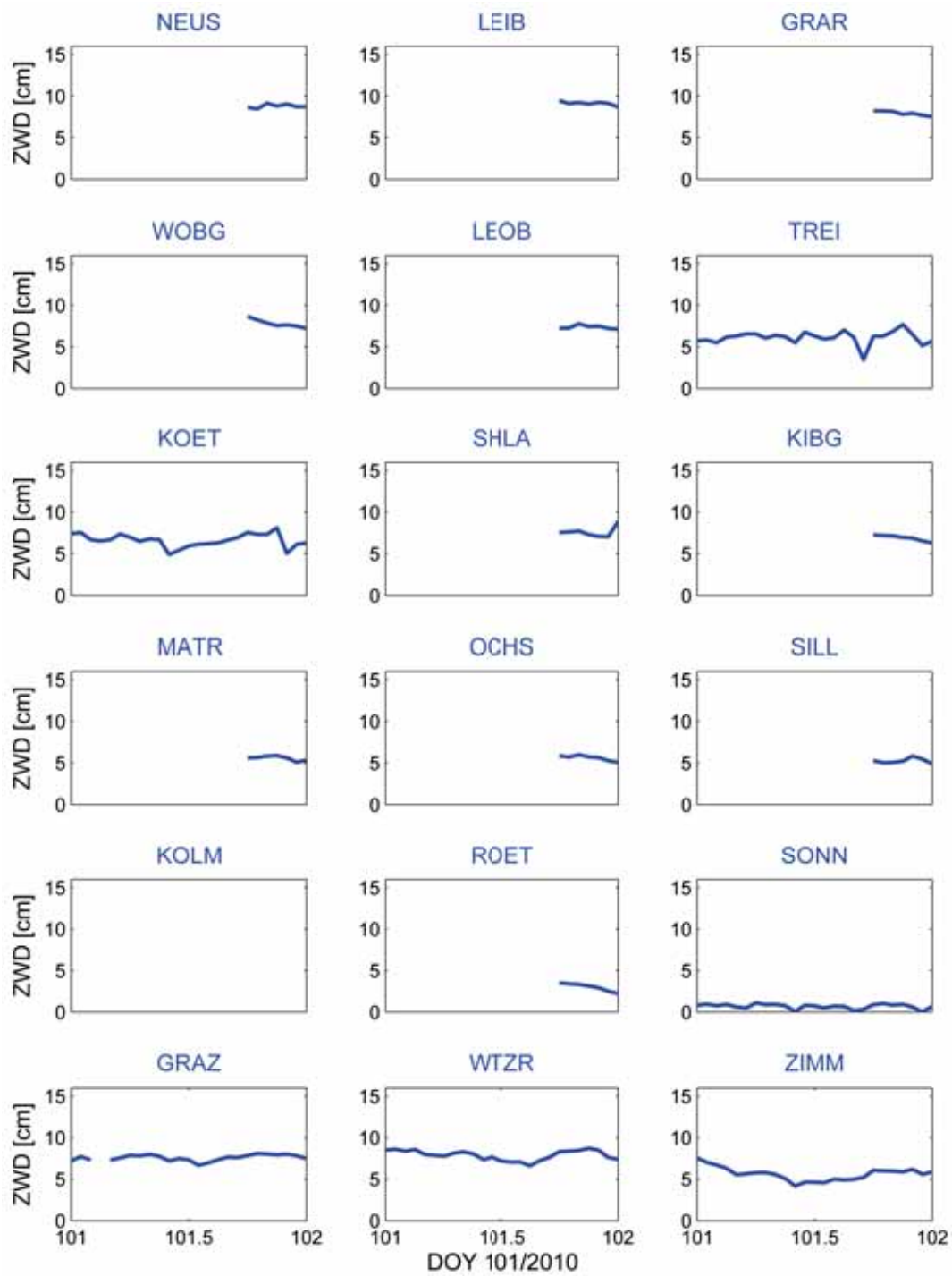


Figure B.31: ZWD (in cm) of all stations on April 11th, 2010

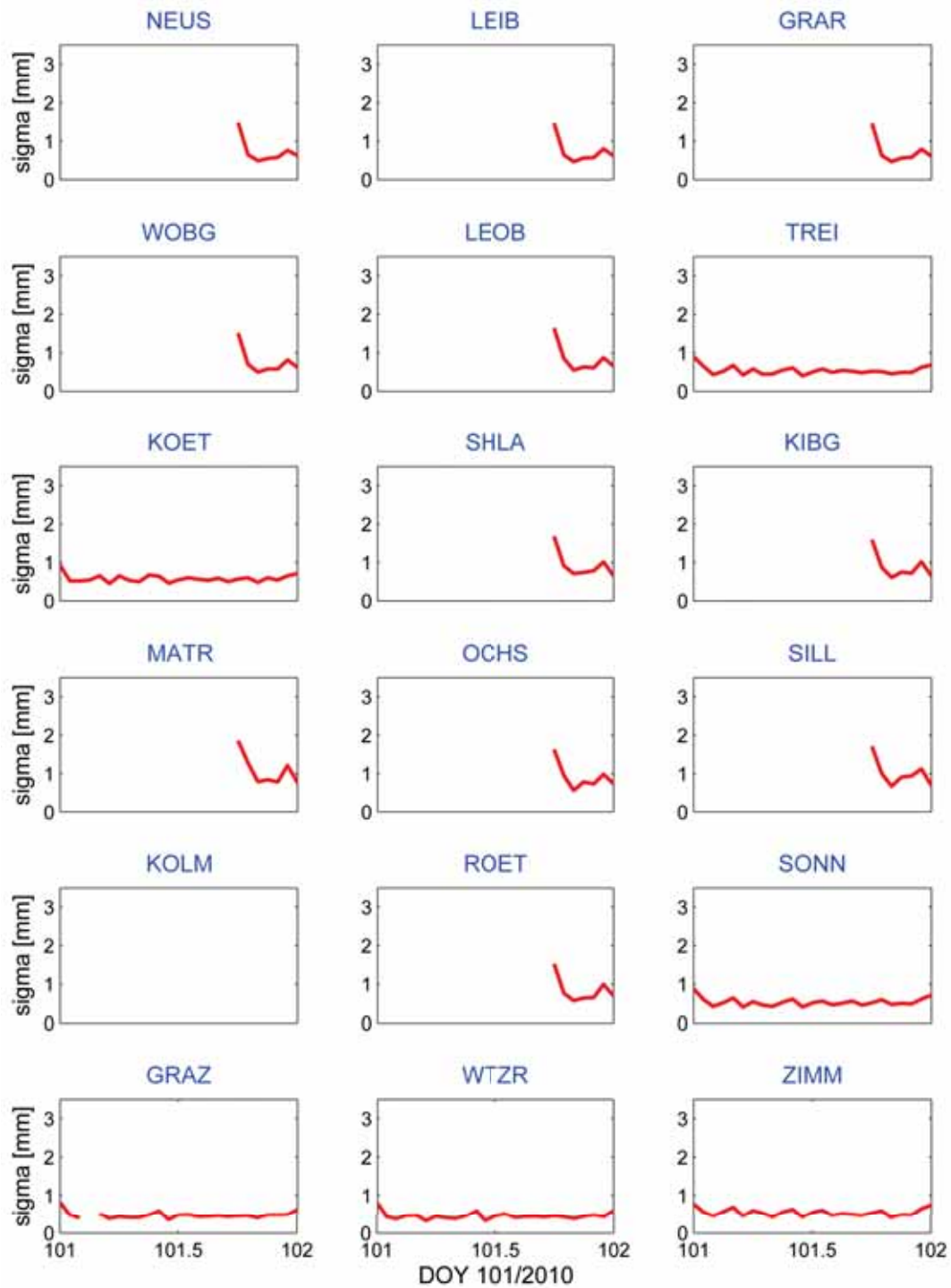


Figure B.32: Formal errors of ZWD estimates (in mm) of all stations on April 11th, 2010

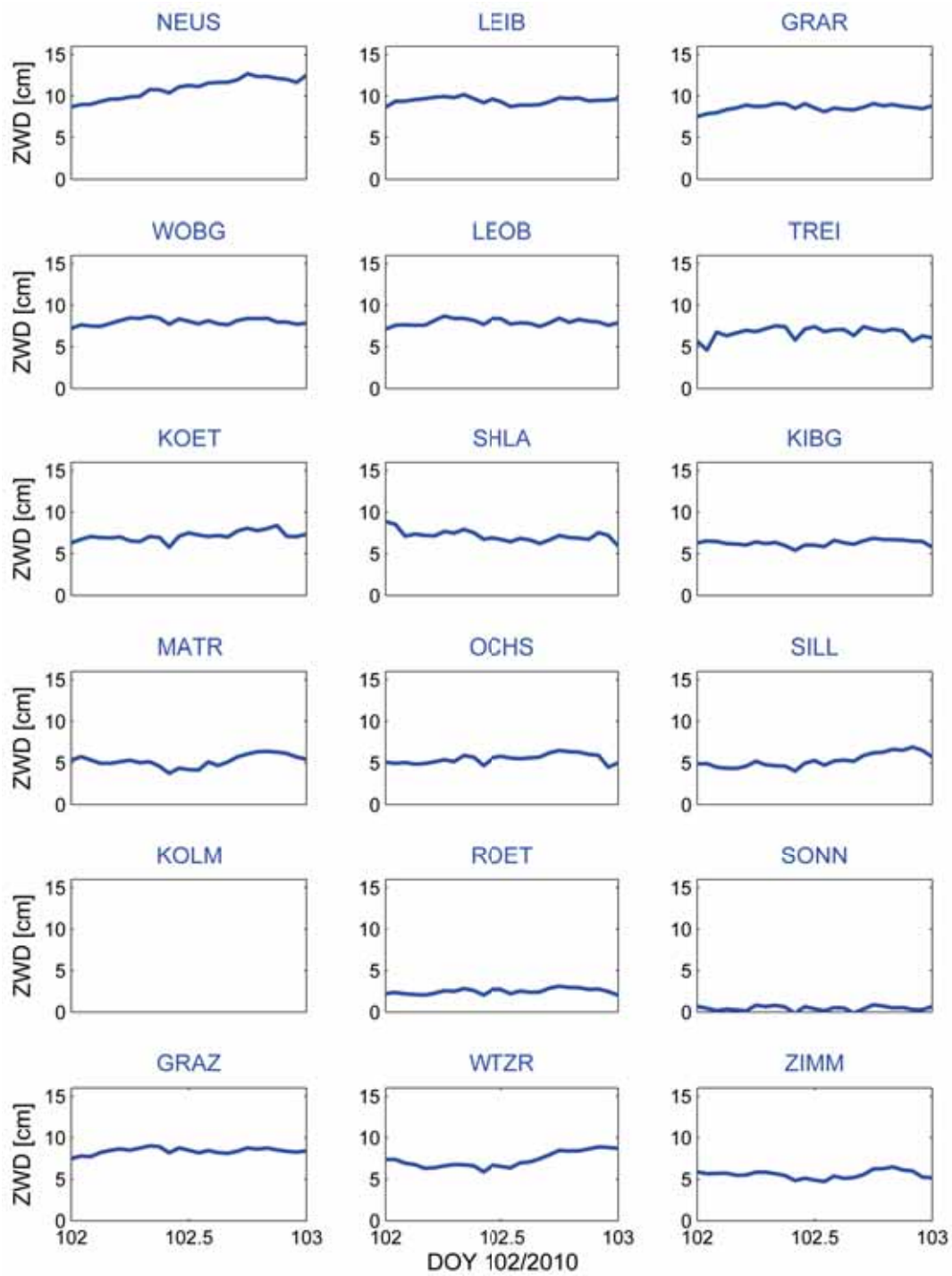


Figure B.33: ZWD (in cm) of all stations on April 12th, 2010

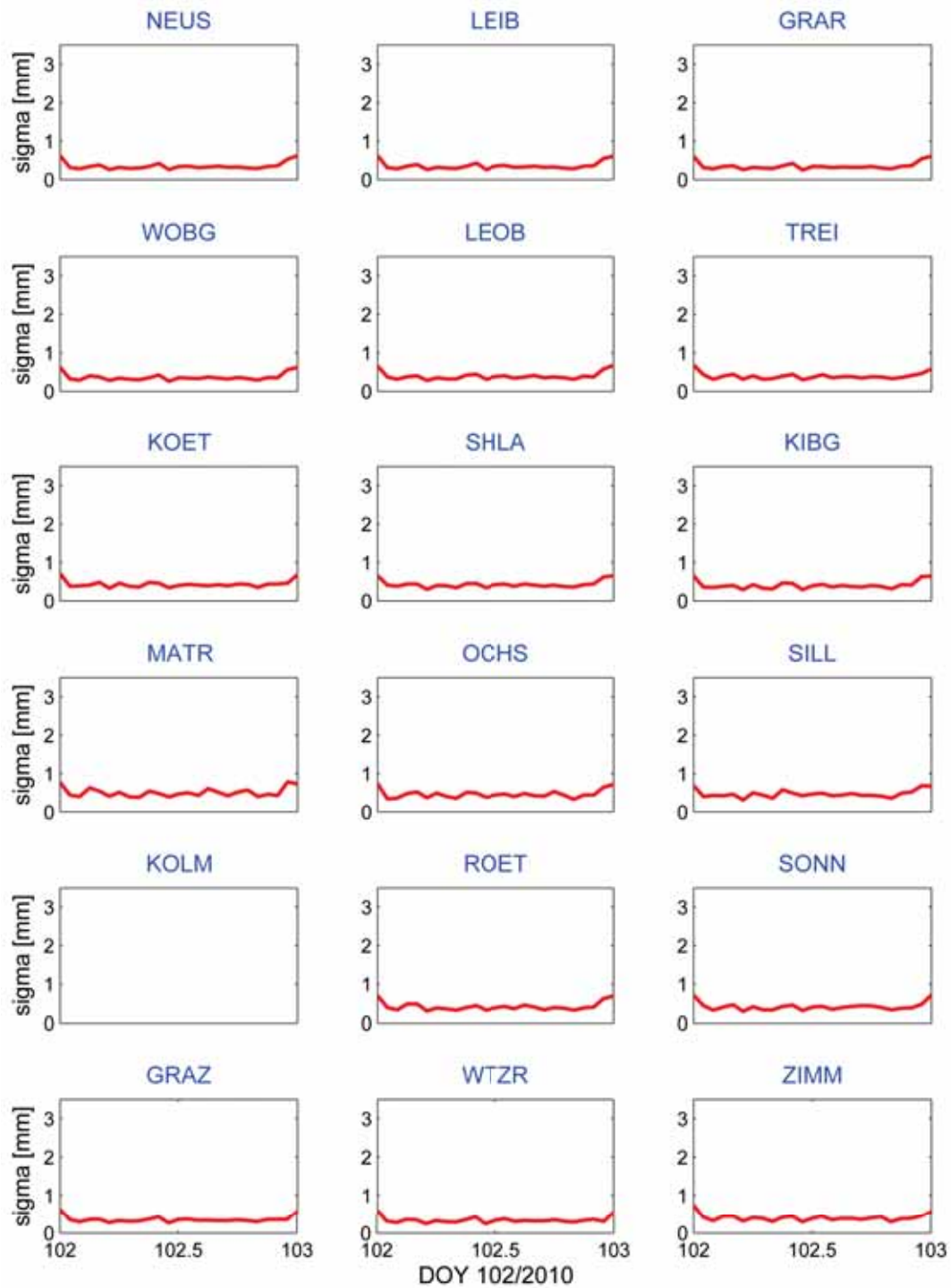


Figure B.34: Formal errors of ZWD estimates (in mm) of all stations on April 12th, 2010

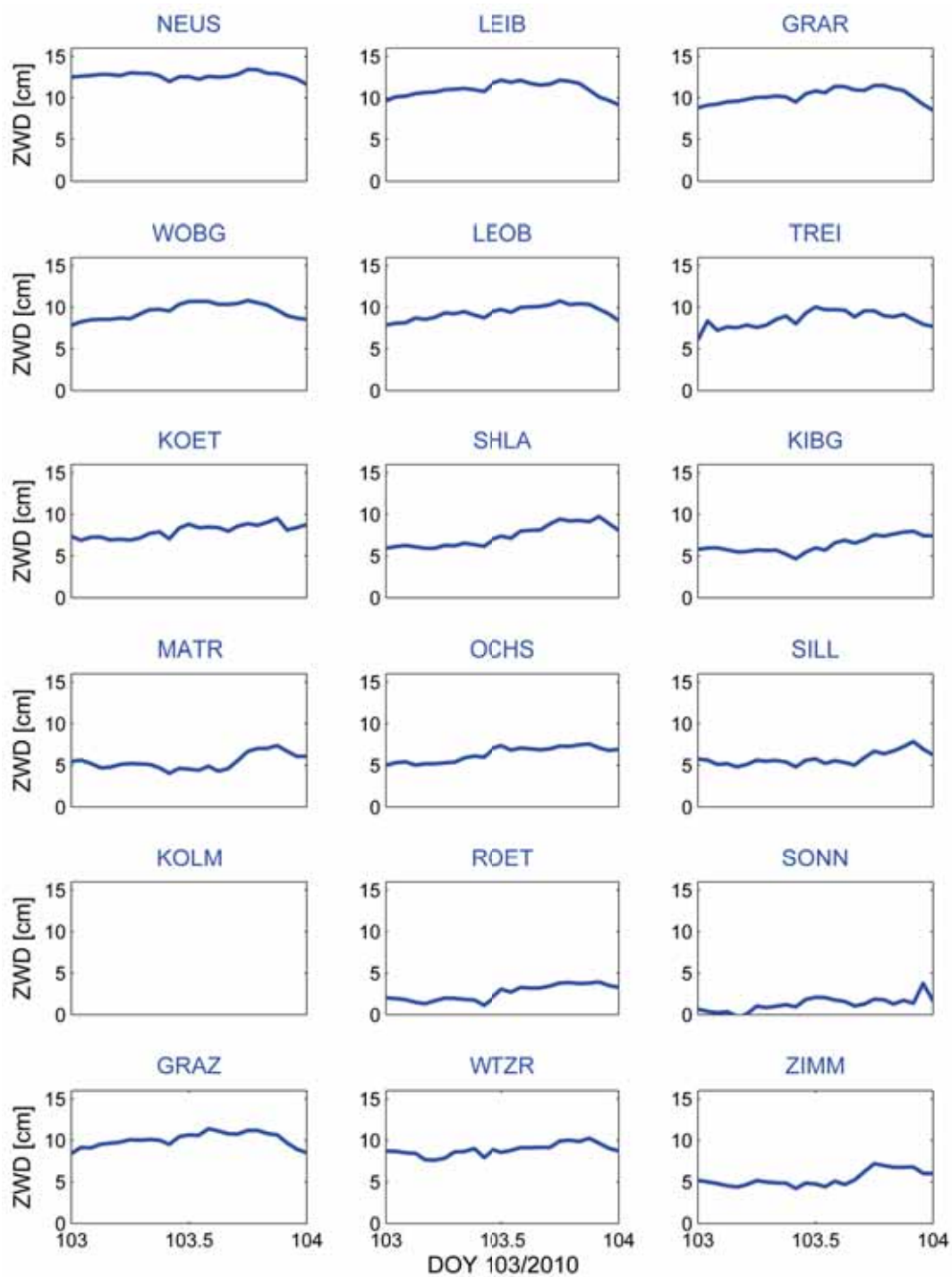


Figure B.35: ZWD (in cm) of all stations on April 13th, 2010

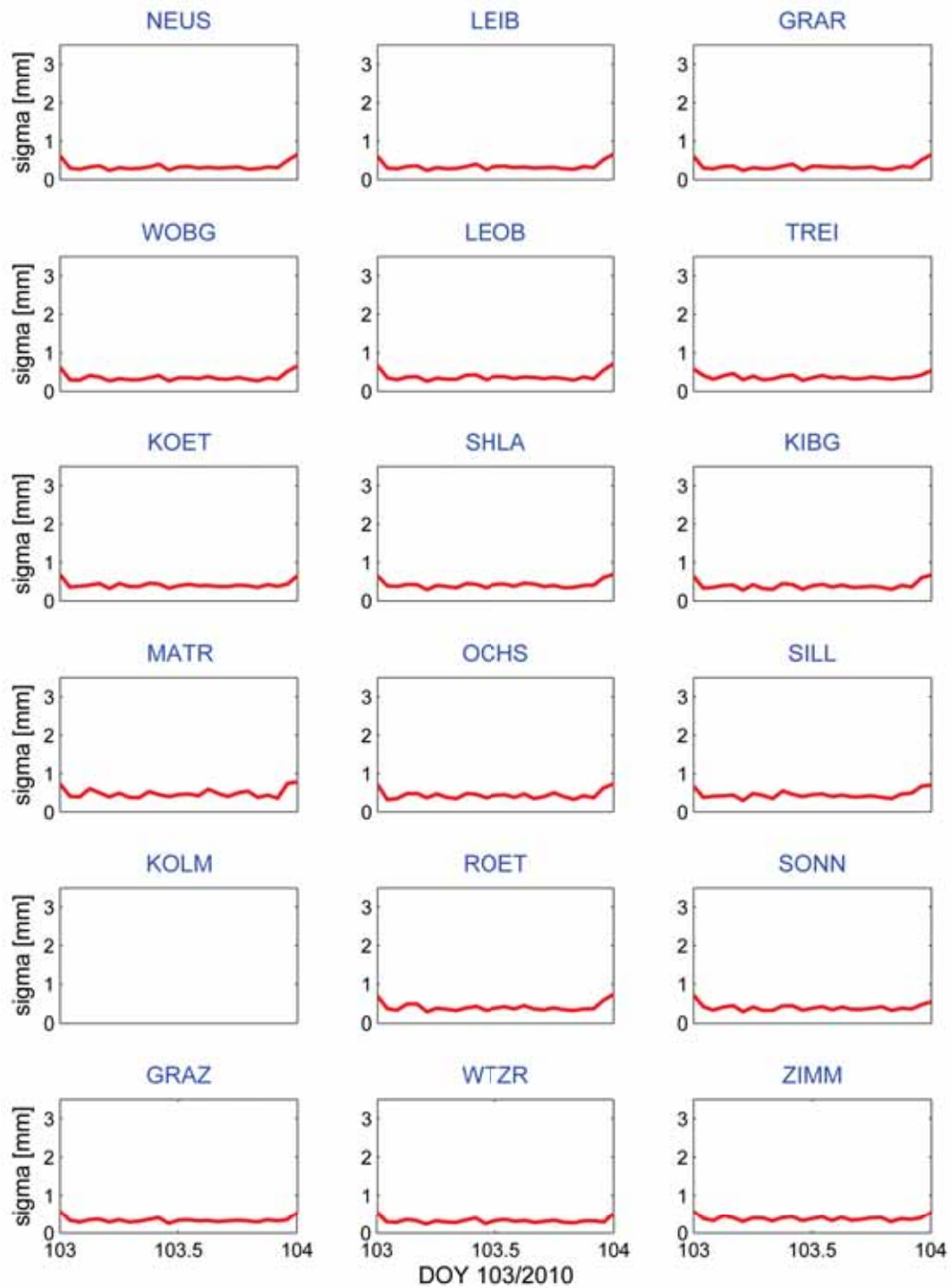


Figure B.36: Formal errors of ZWD estimates (in mm) of all stations on April 13th, 2010

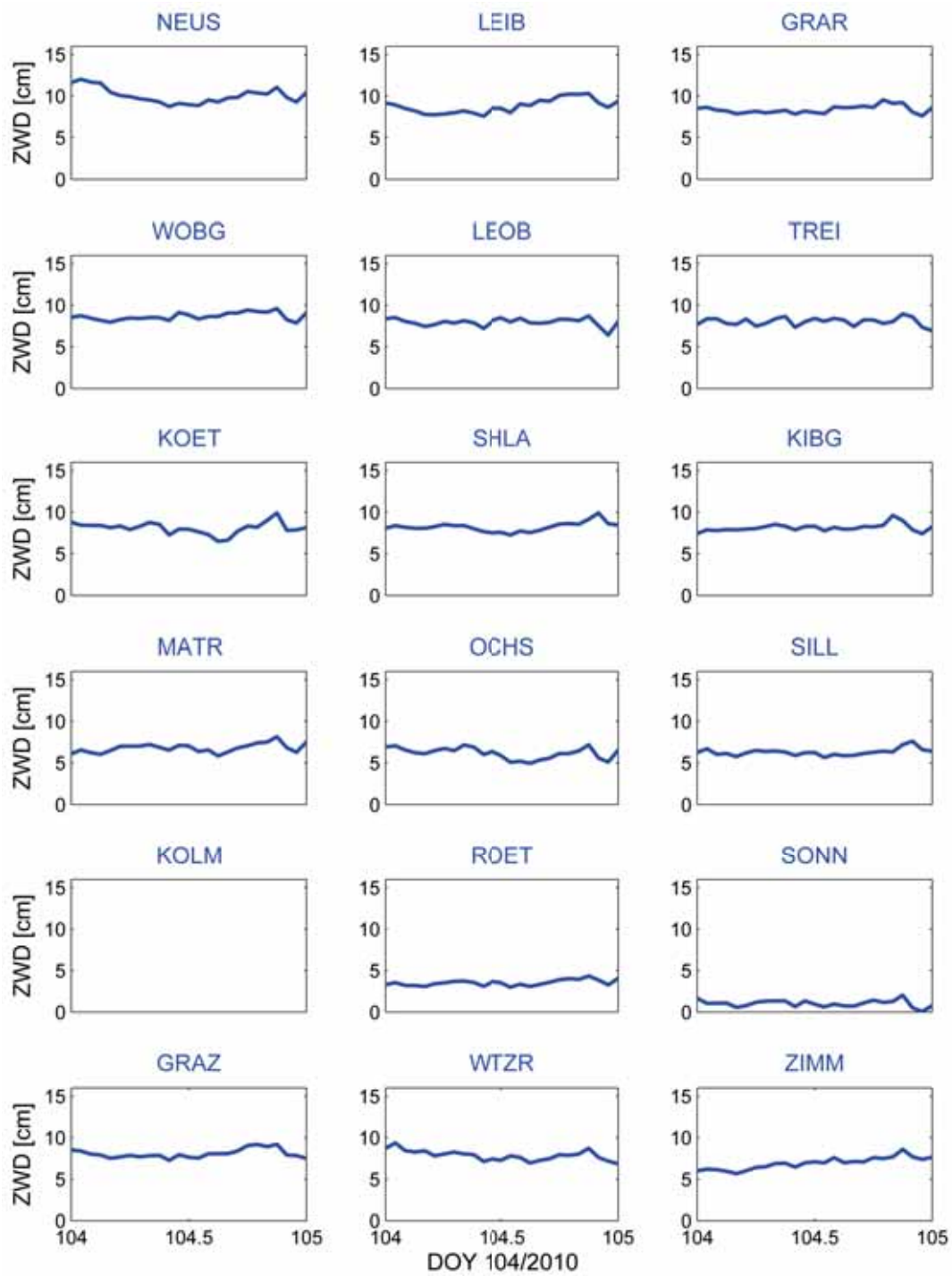


Figure B.37: ZWD (in cm) of all stations on April 14th, 2010

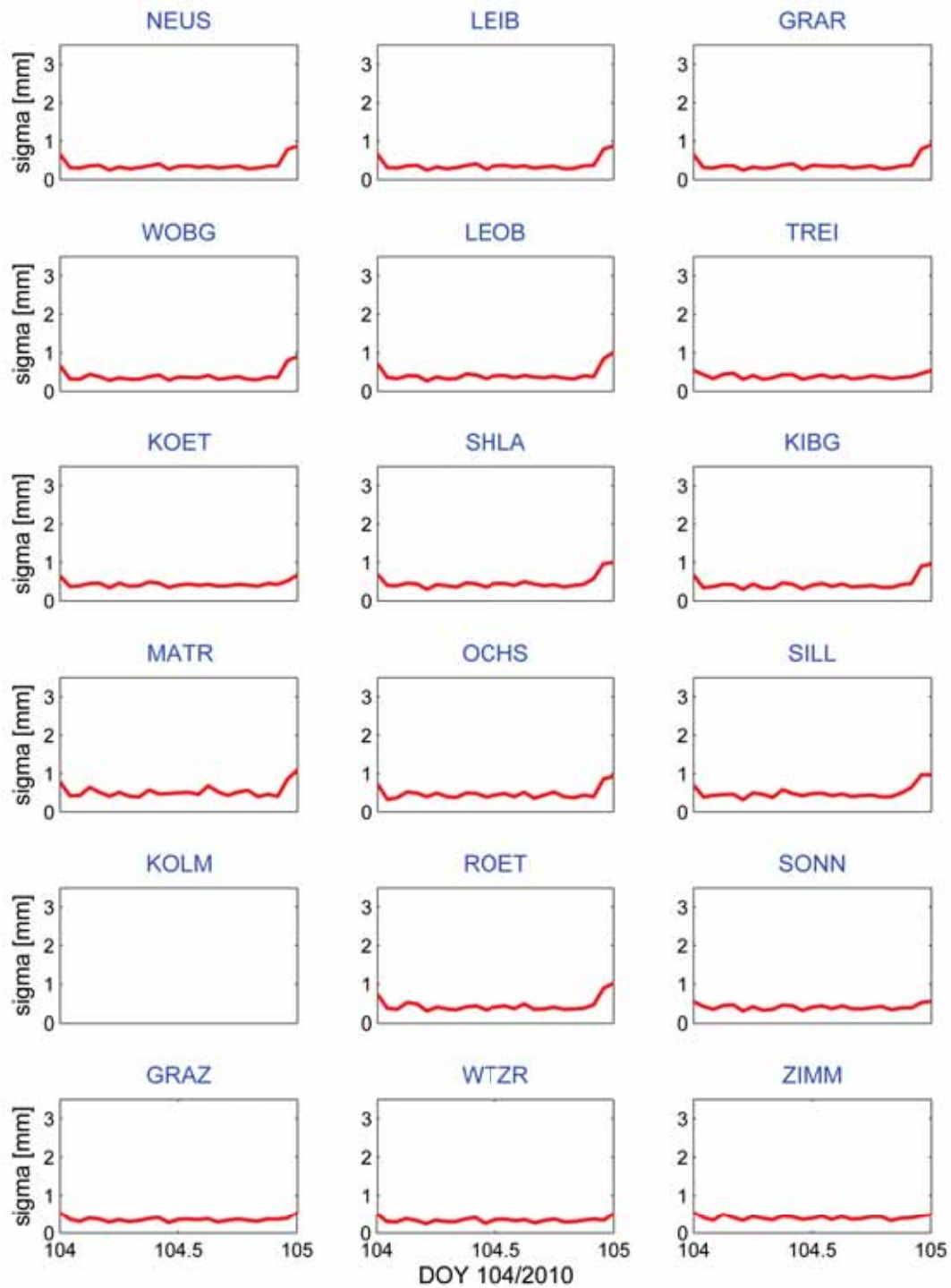


Figure B.38: Formal errors of ZWD estimates (in mm) of all stations on April 14th, 2010

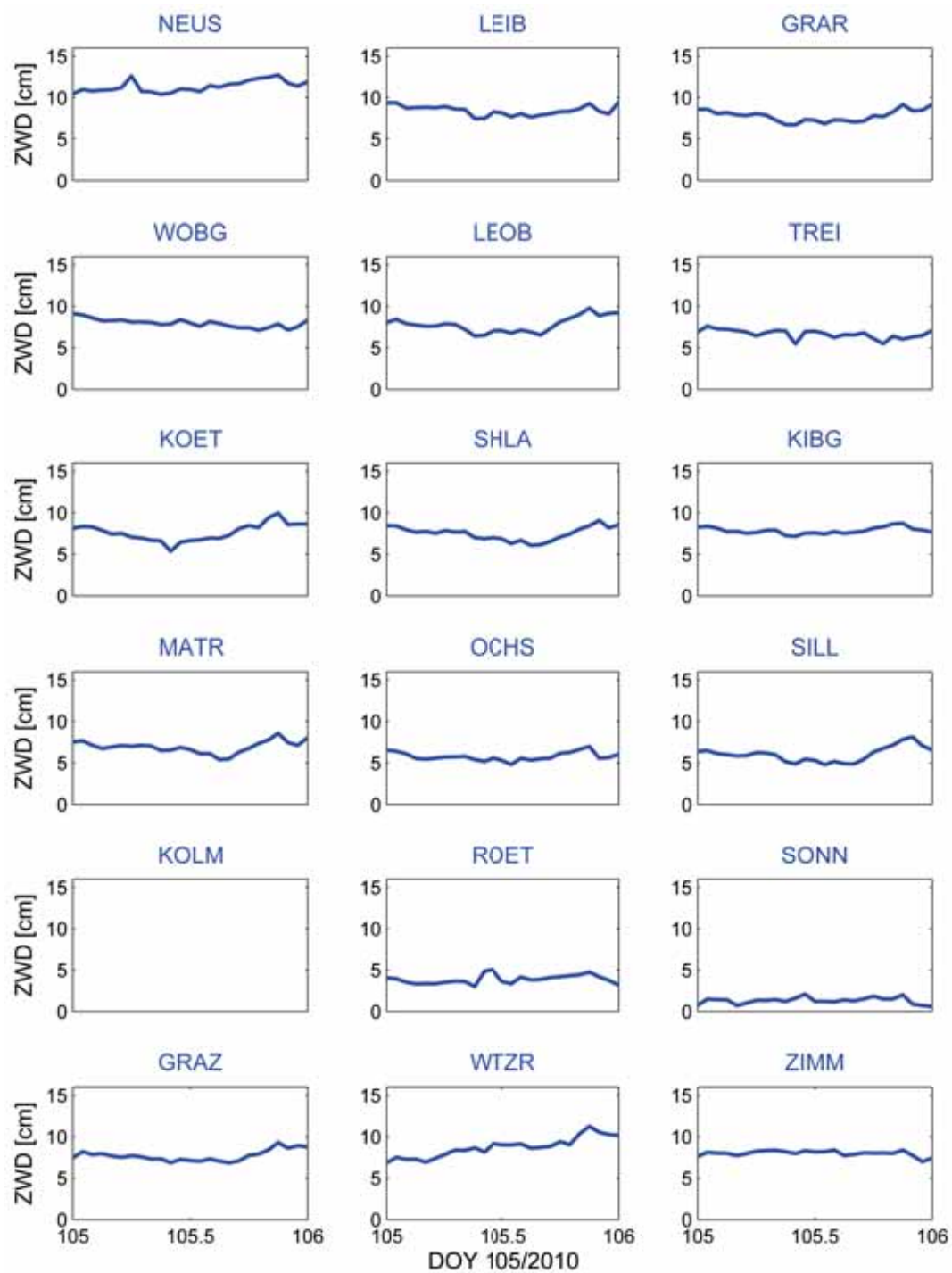


Figure B.39: ZWD (in cm) of all stations on April 15th, 2010

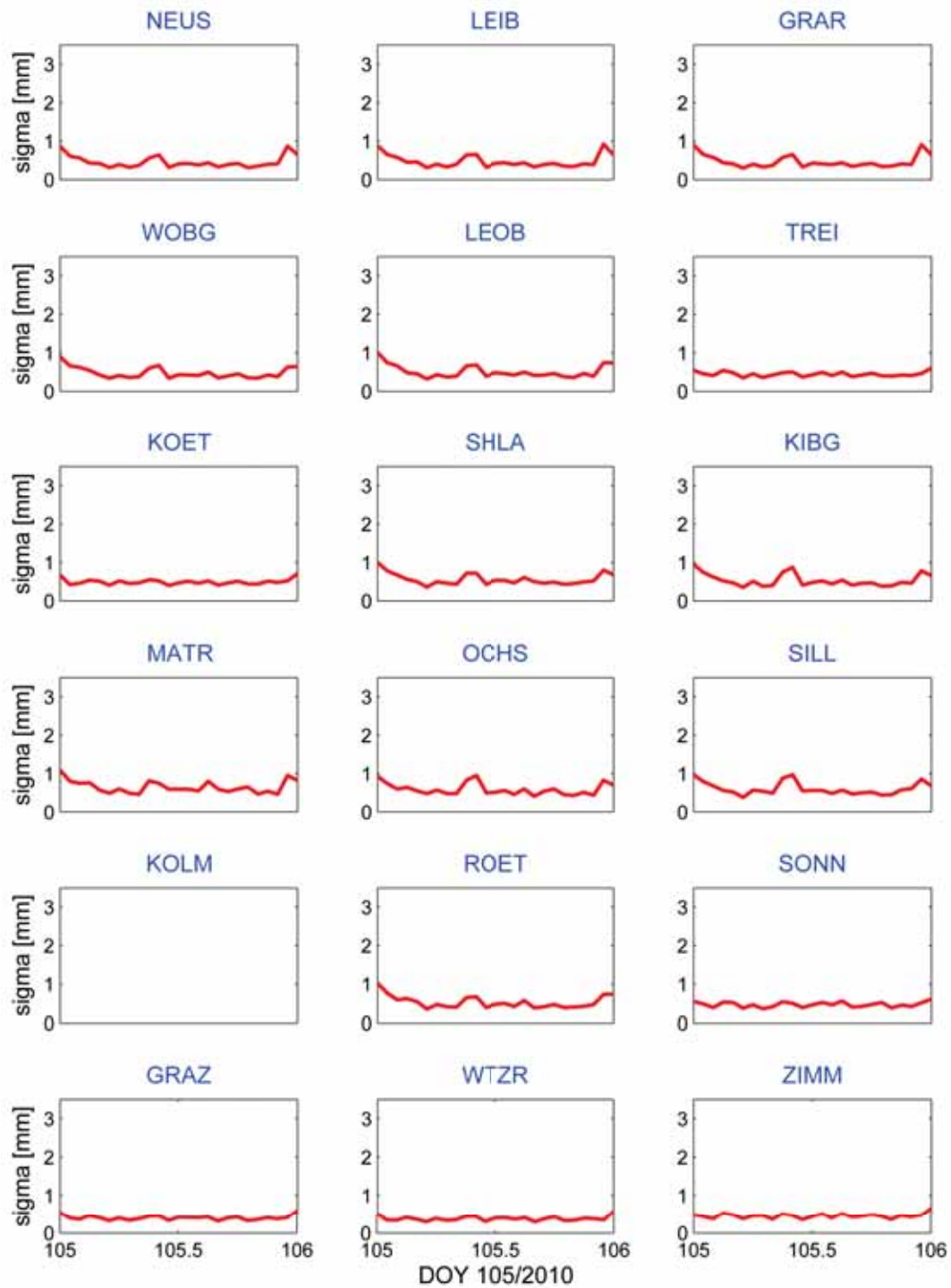


Figure B.40: Formal errors of ZWD estimates (in mm) of all stations on April 15th, 2010

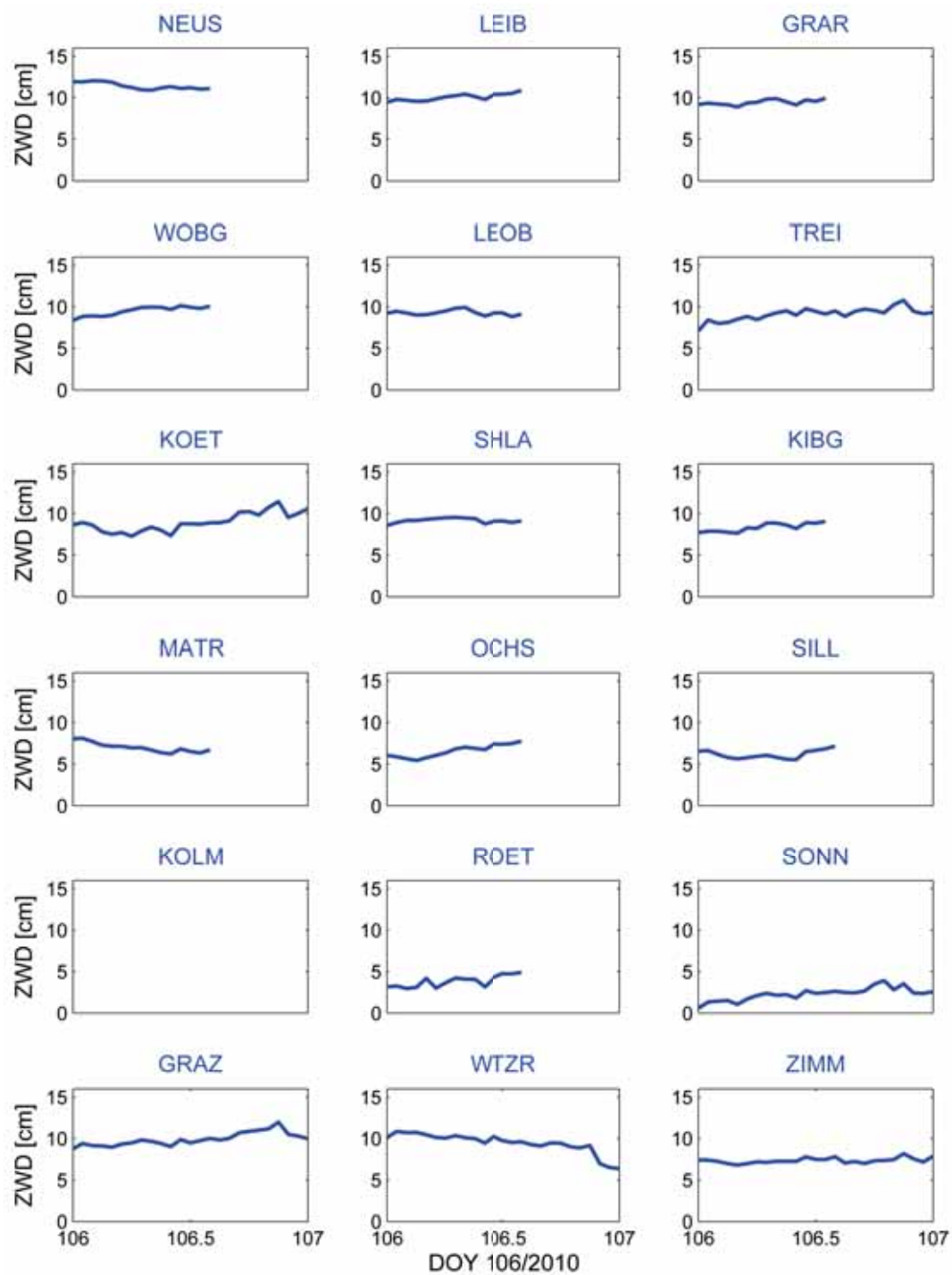


Figure B.41: ZWD (in cm) of all stations on April 16th, 2010

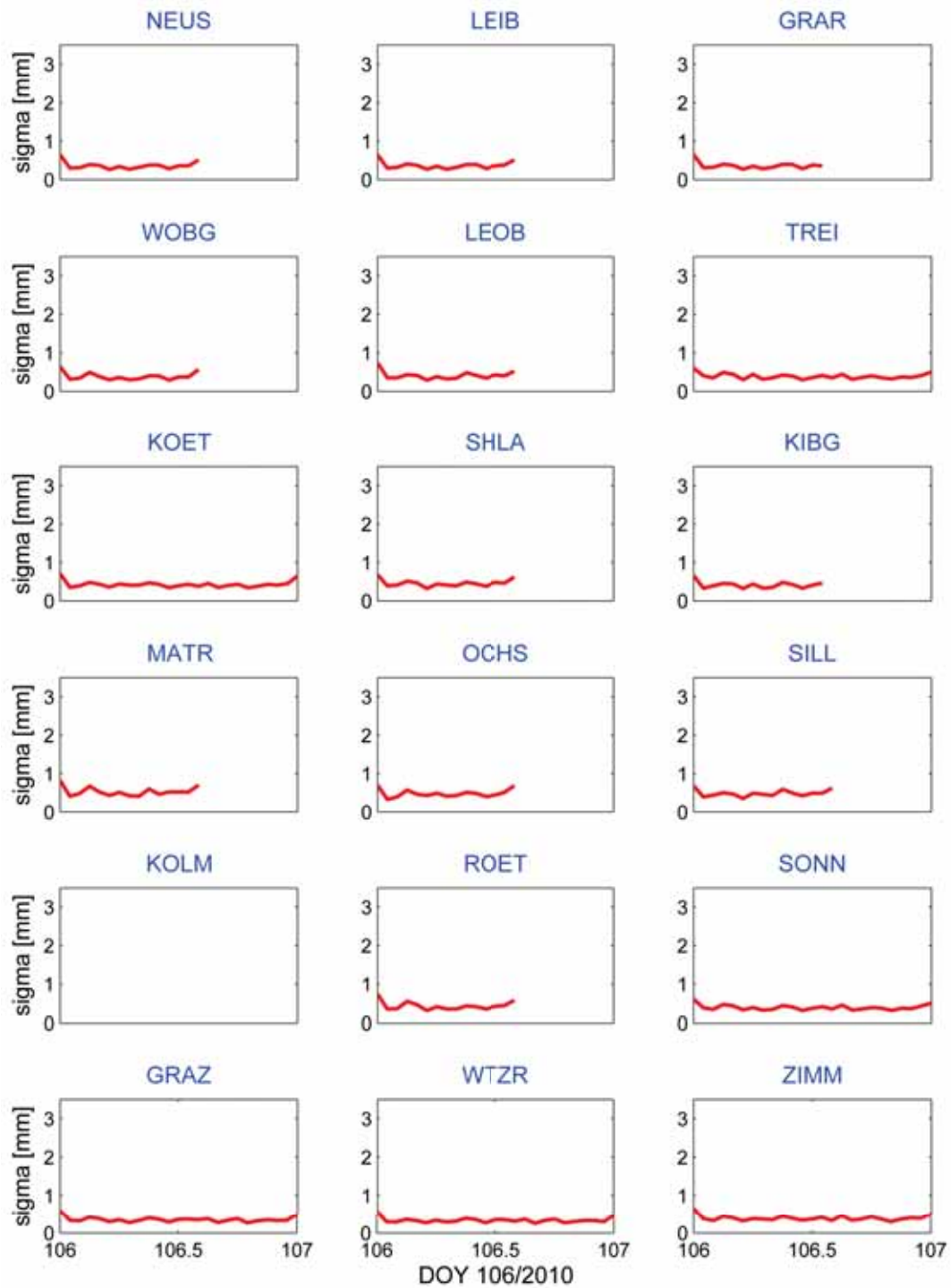


Figure B.42: Formal errors of ZWD estimates (in mm) of all stations on April 16th, 2010

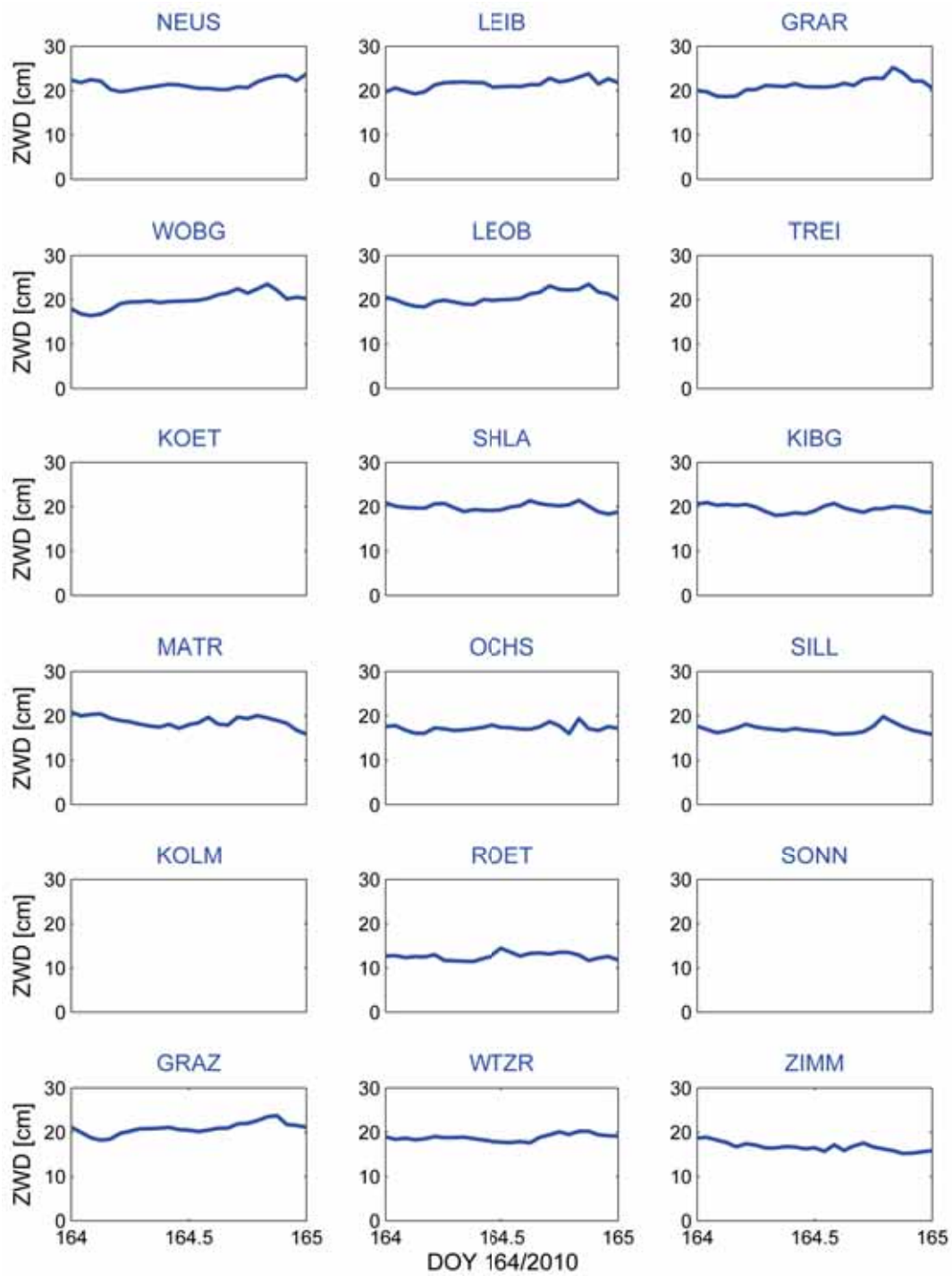


Figure B.43: ZWD (in cm) of all stations on June 13th, 2010

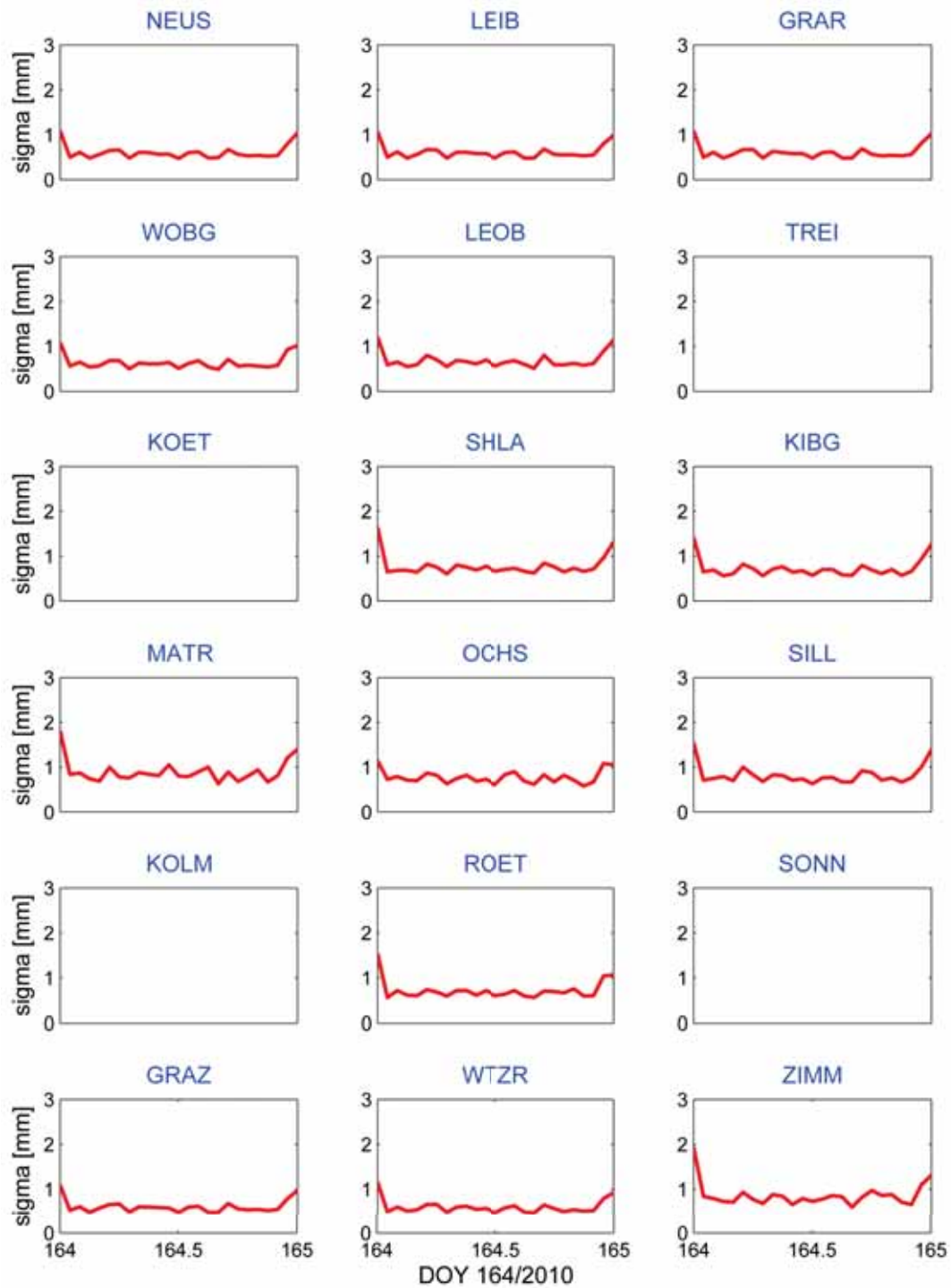


Figure B.44: Formal errors of ZWD estimates (in mm) of all stations on June 13th, 2010

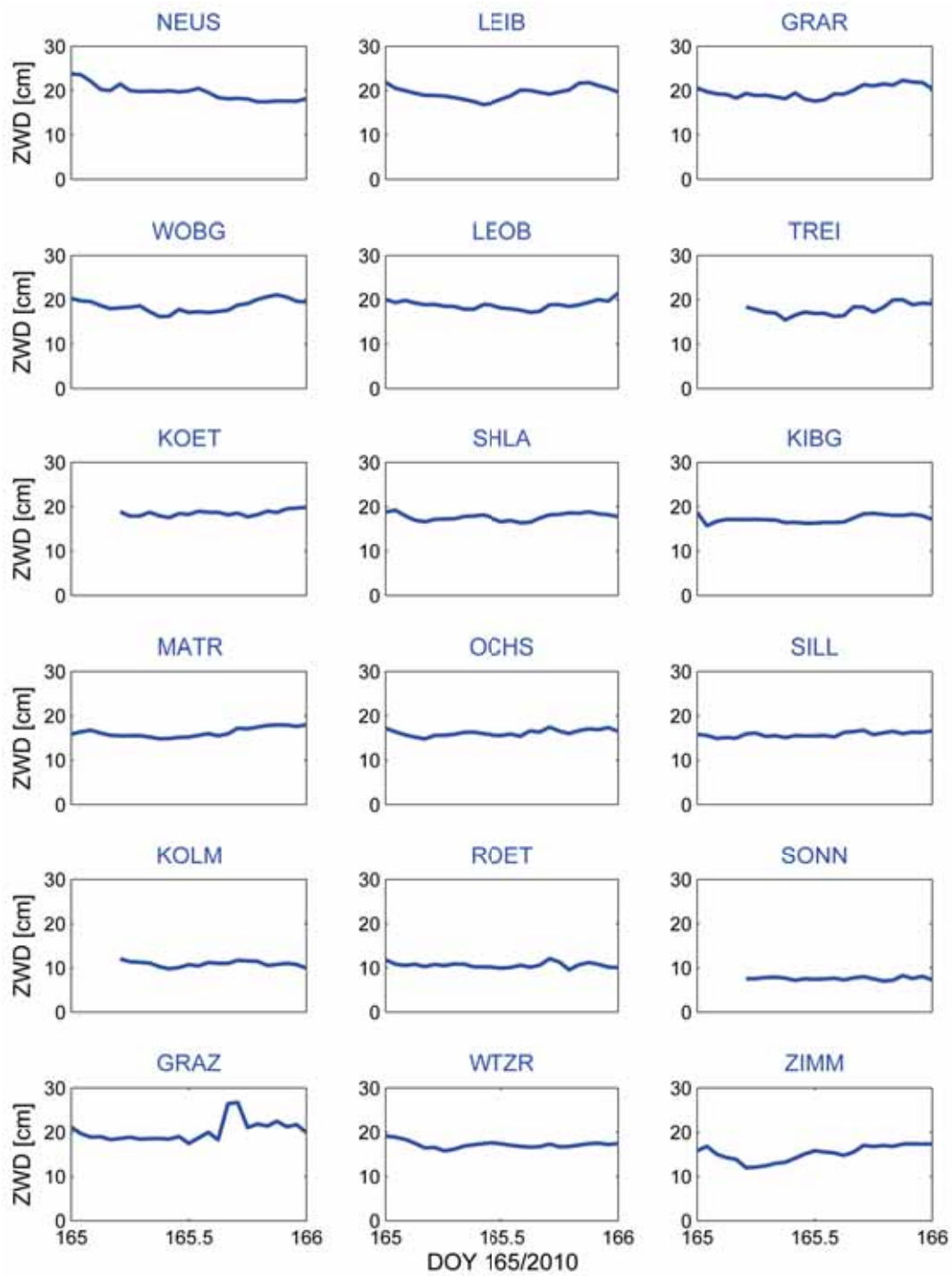


Figure B.45: ZWD (in cm) of all stations on June 14th, 2010

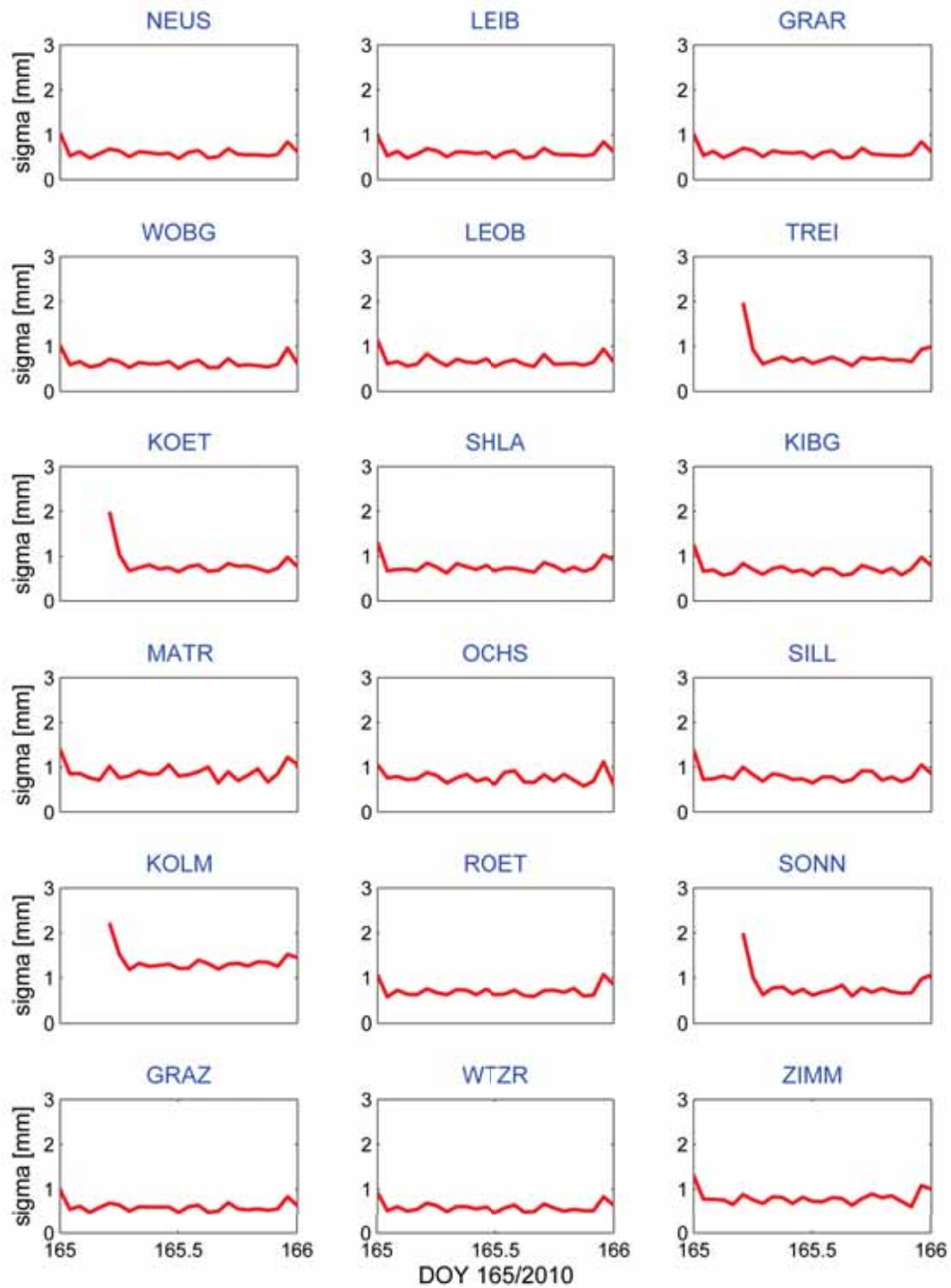


Figure B.46: Formal errors of ZWD estimates (in mm) of all stations on June 14th, 2010

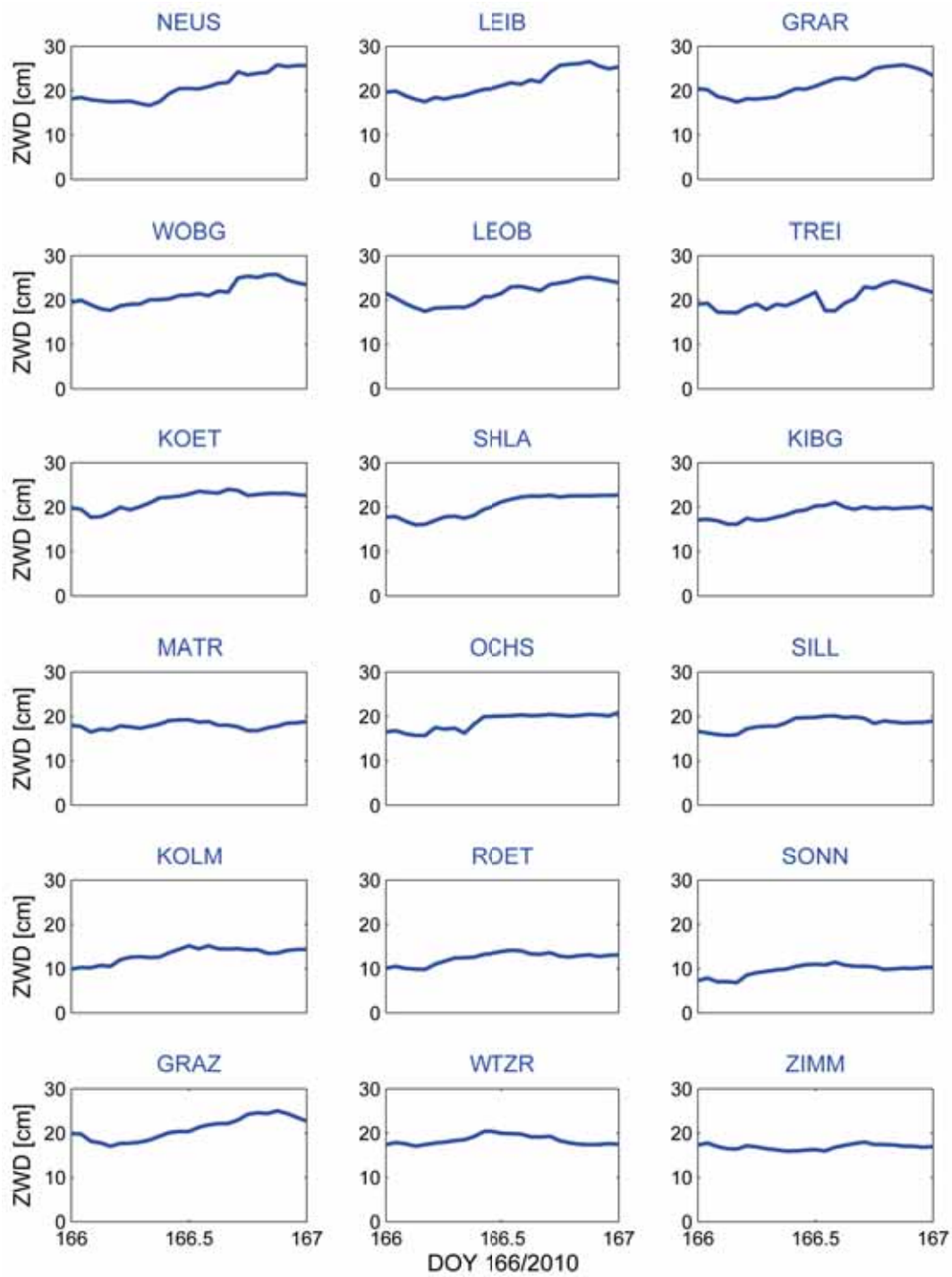


Figure B.47: ZWD (in cm) of all stations on June 15th, 2010

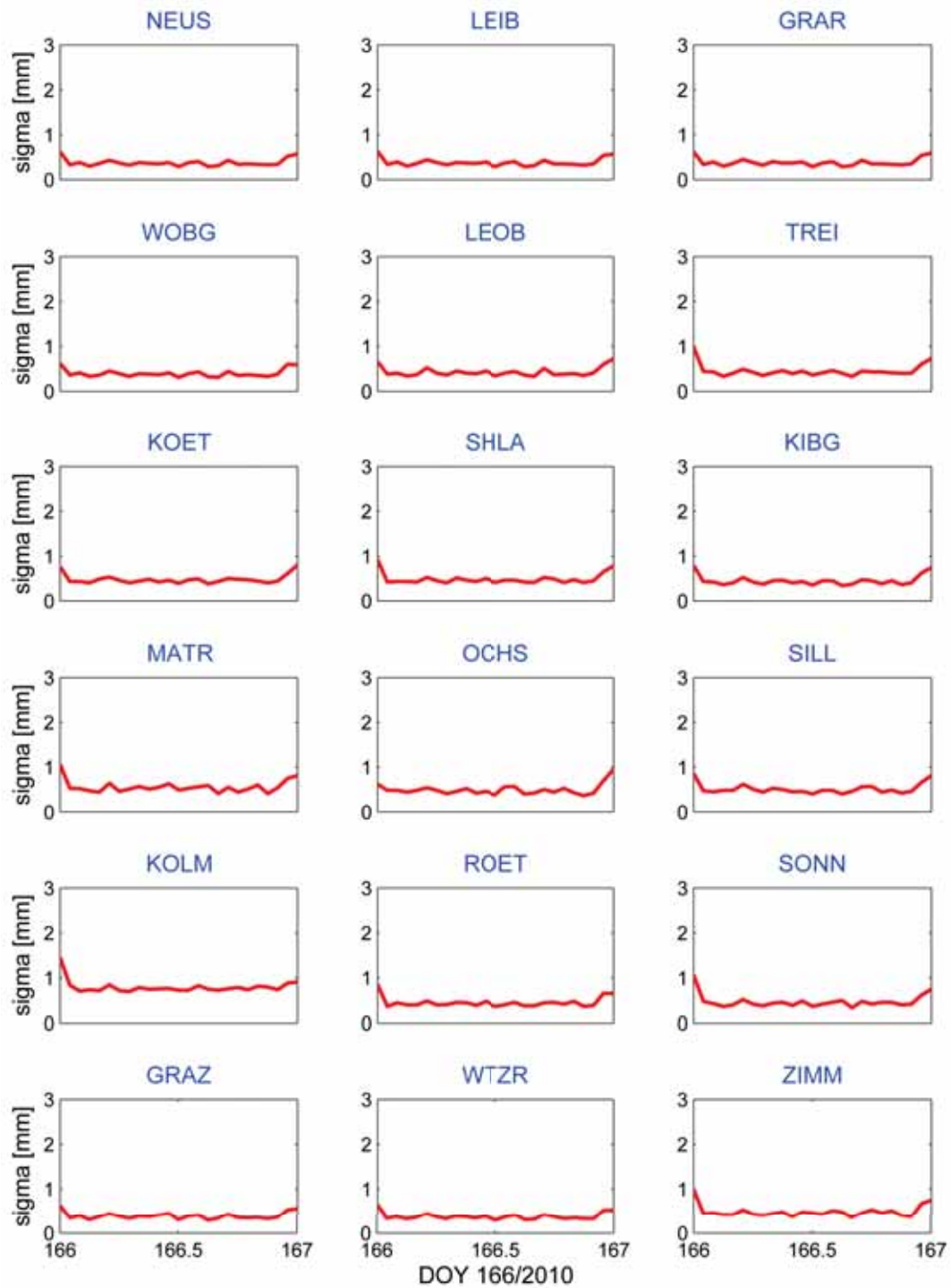


Figure B.48: Formal errors of ZWD estimates (in mm) of all stations on June 15th, 2010

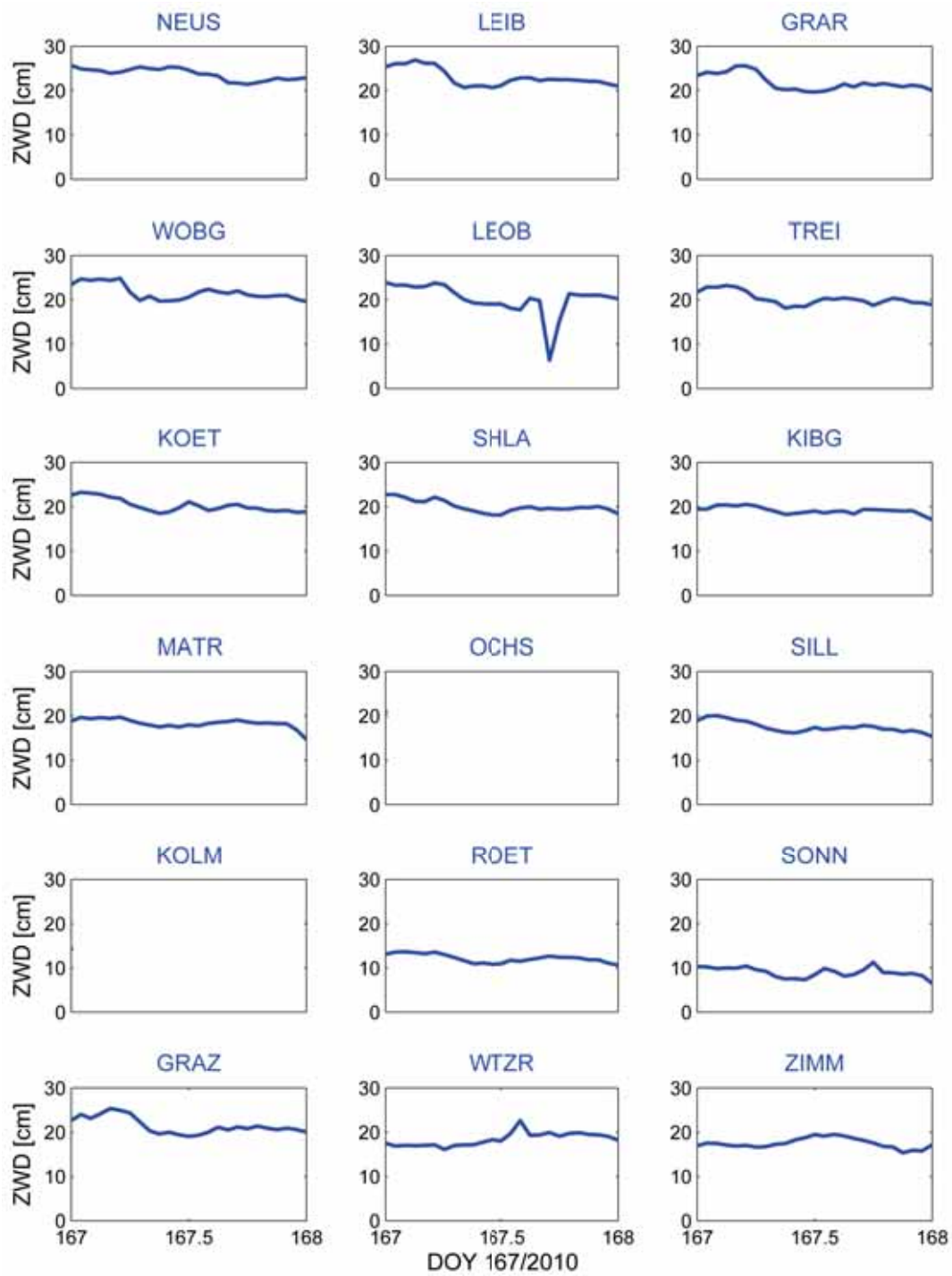


Figure B.49: ZWD (in cm) of all stations on June 16th, 2010

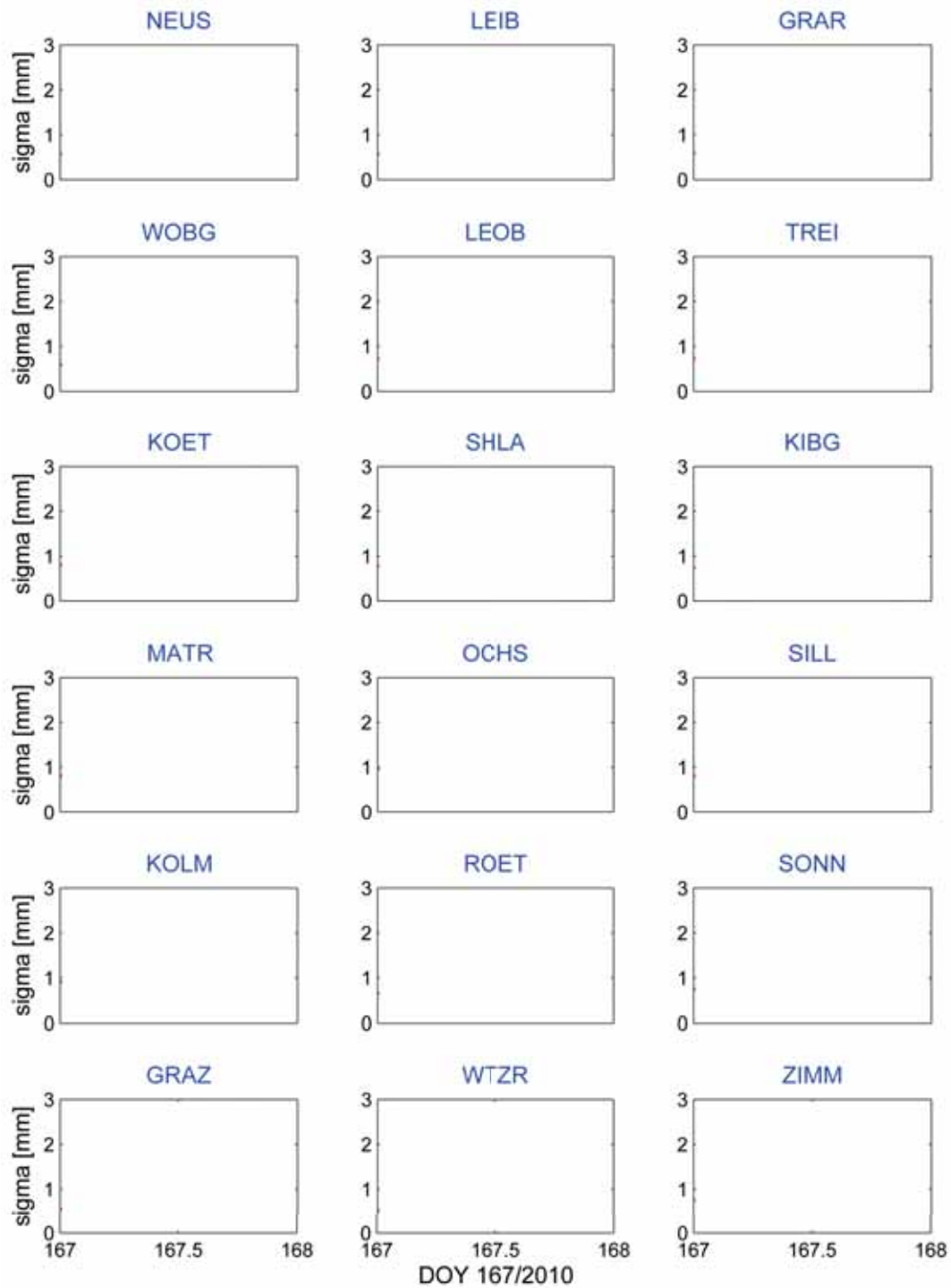


Figure B.50: Formal errors of ZWD estimates (in mm) of all stations on June 16th, 2010

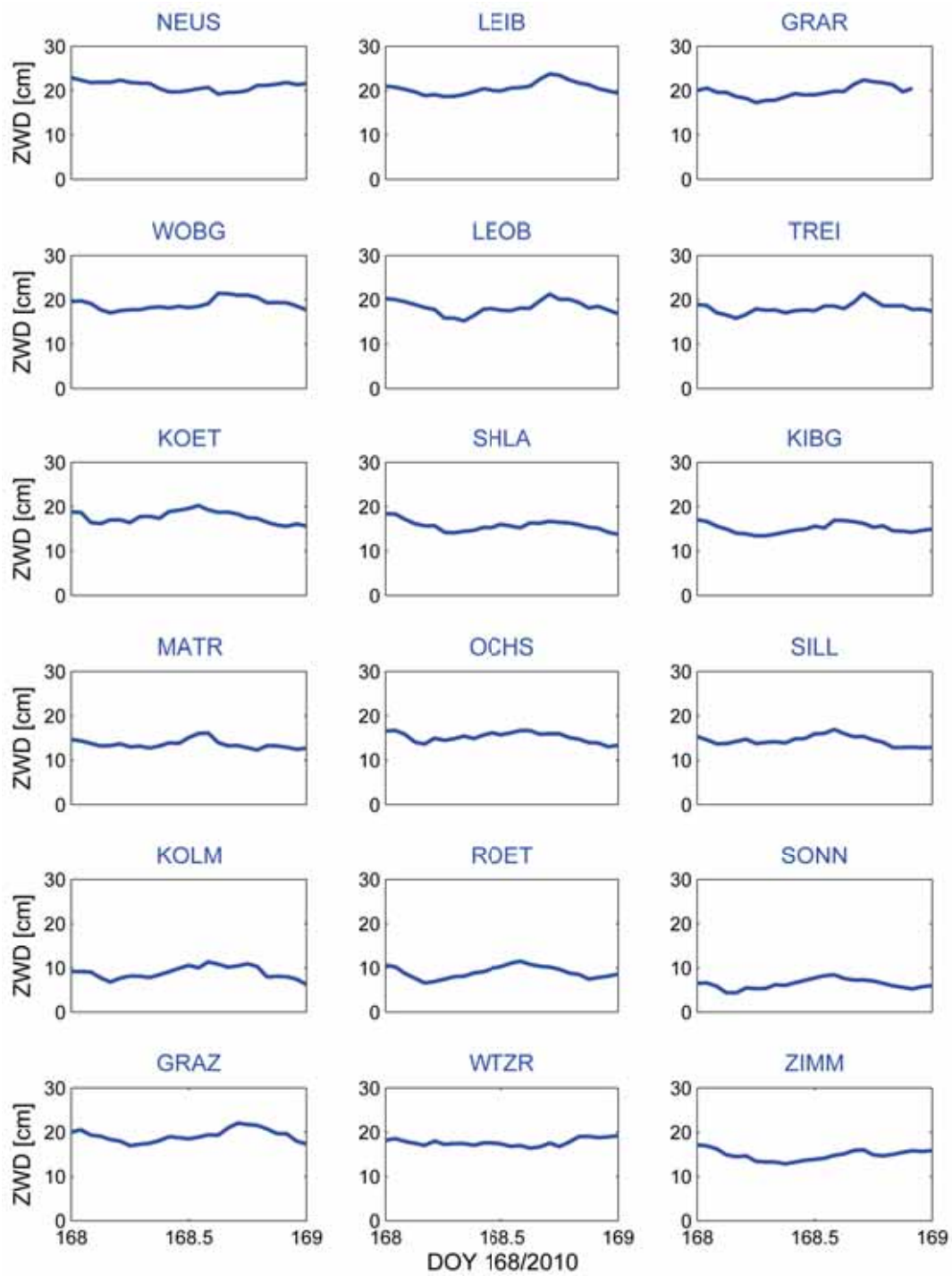


Figure B.51: ZWD (in cm) of all stations on June 17th, 2010

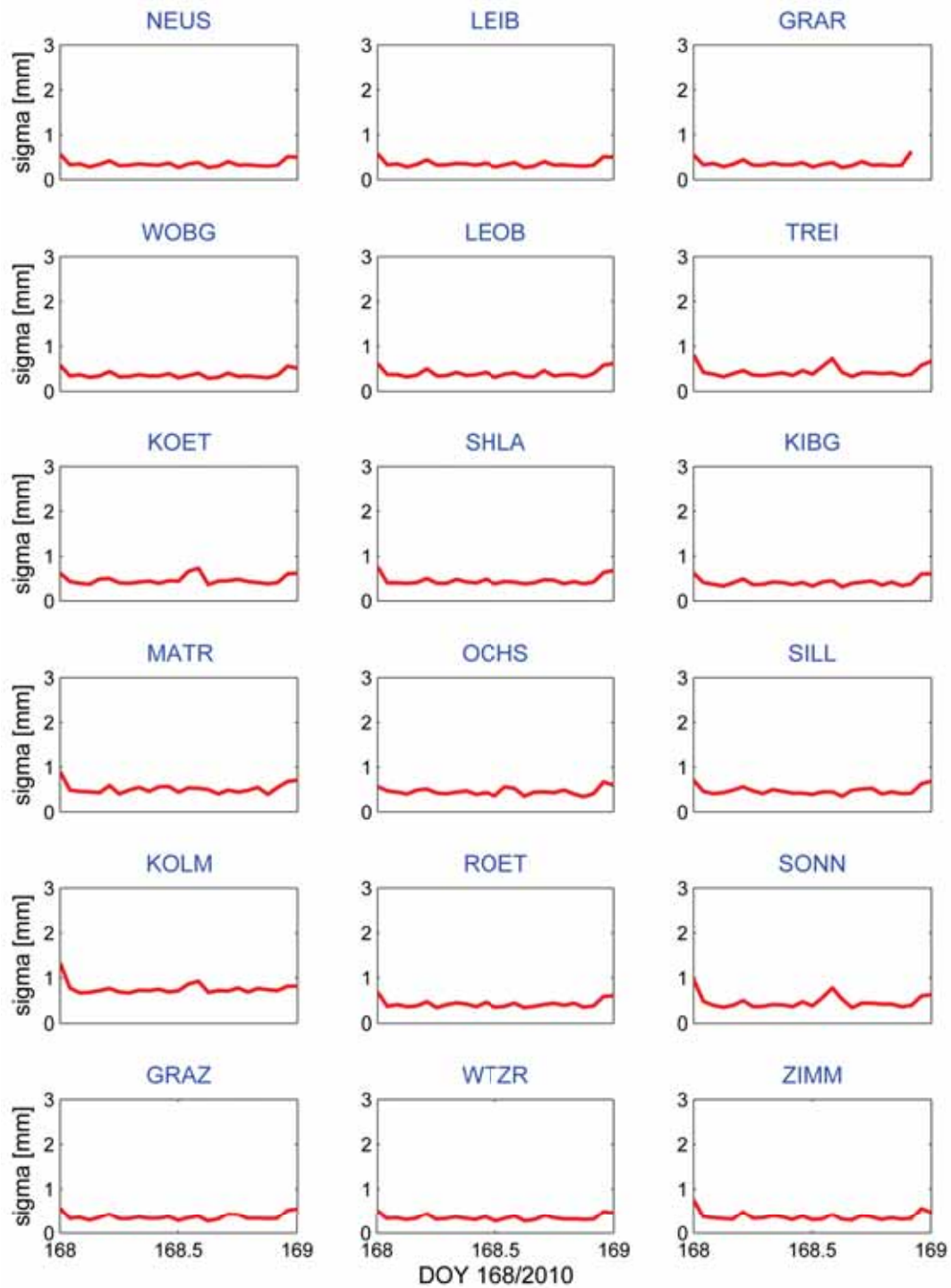


Figure B.52: Formal errors of ZWD estimates (in mm) of all stations on June 17th, 2010

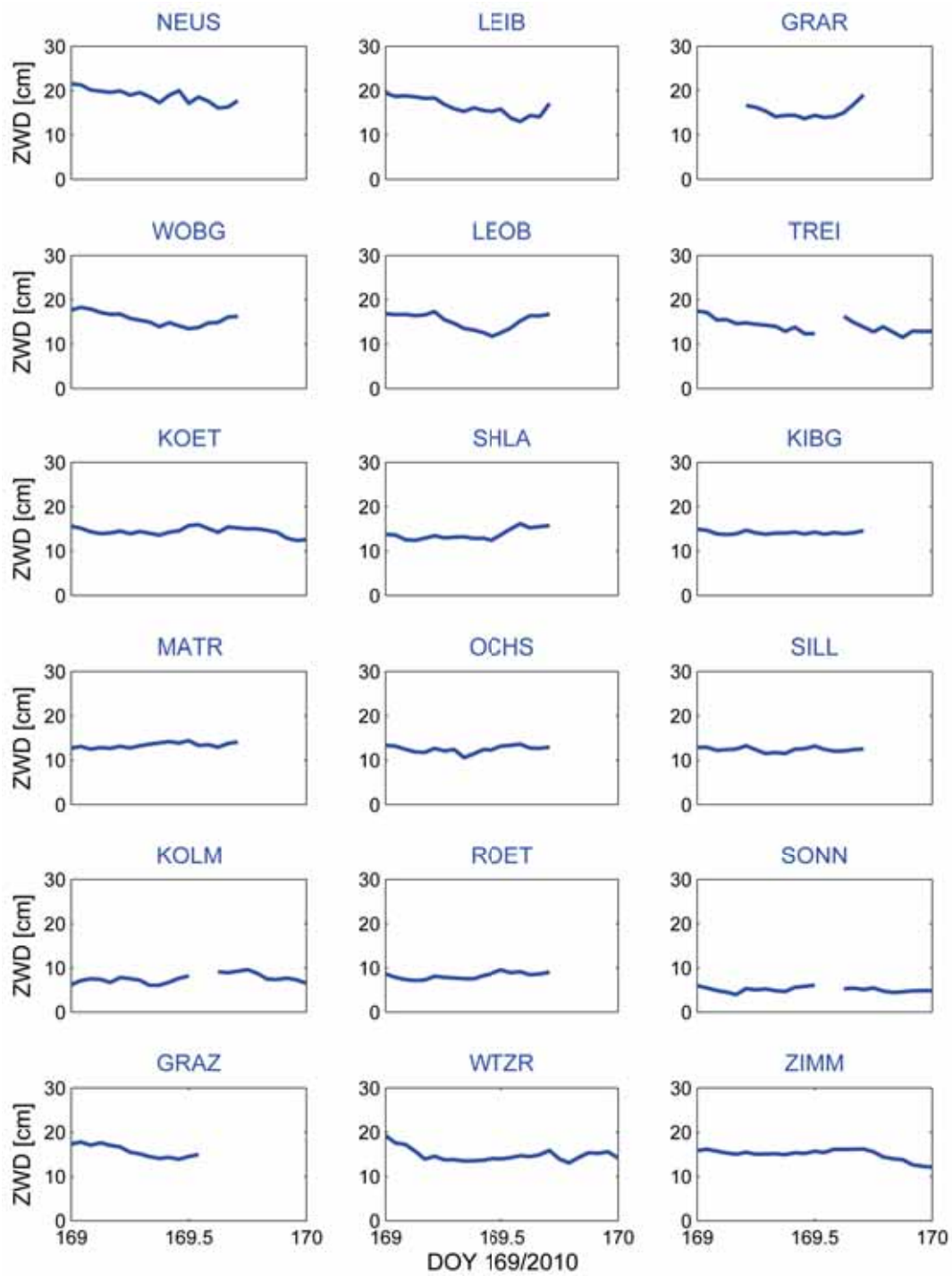


Figure B.53: ZWD (in cm) of all stations on June 18th, 2010

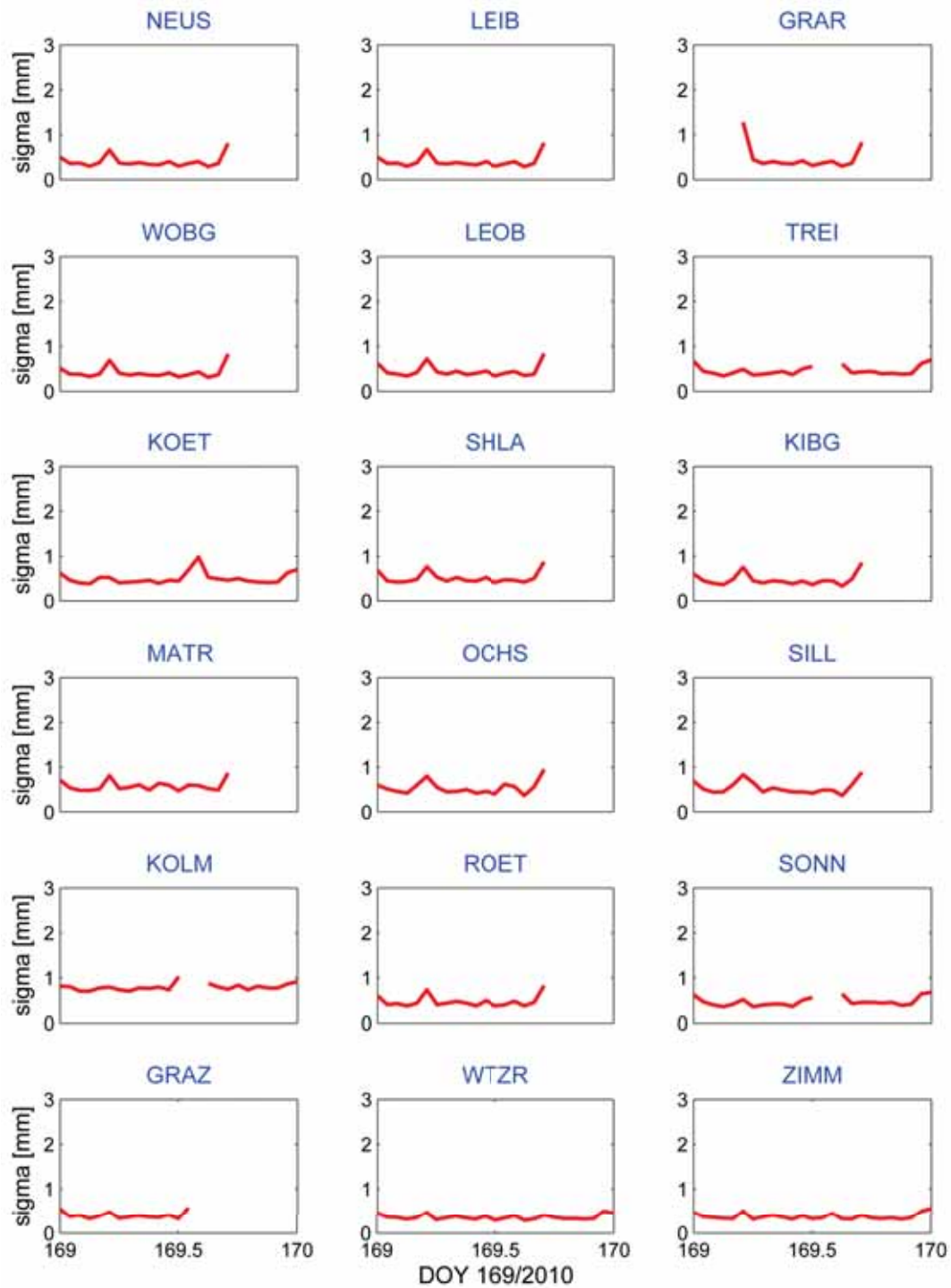


Figure B.54: Formal errors of ZWD estimates (in mm) of all stations on June 18th, 2010

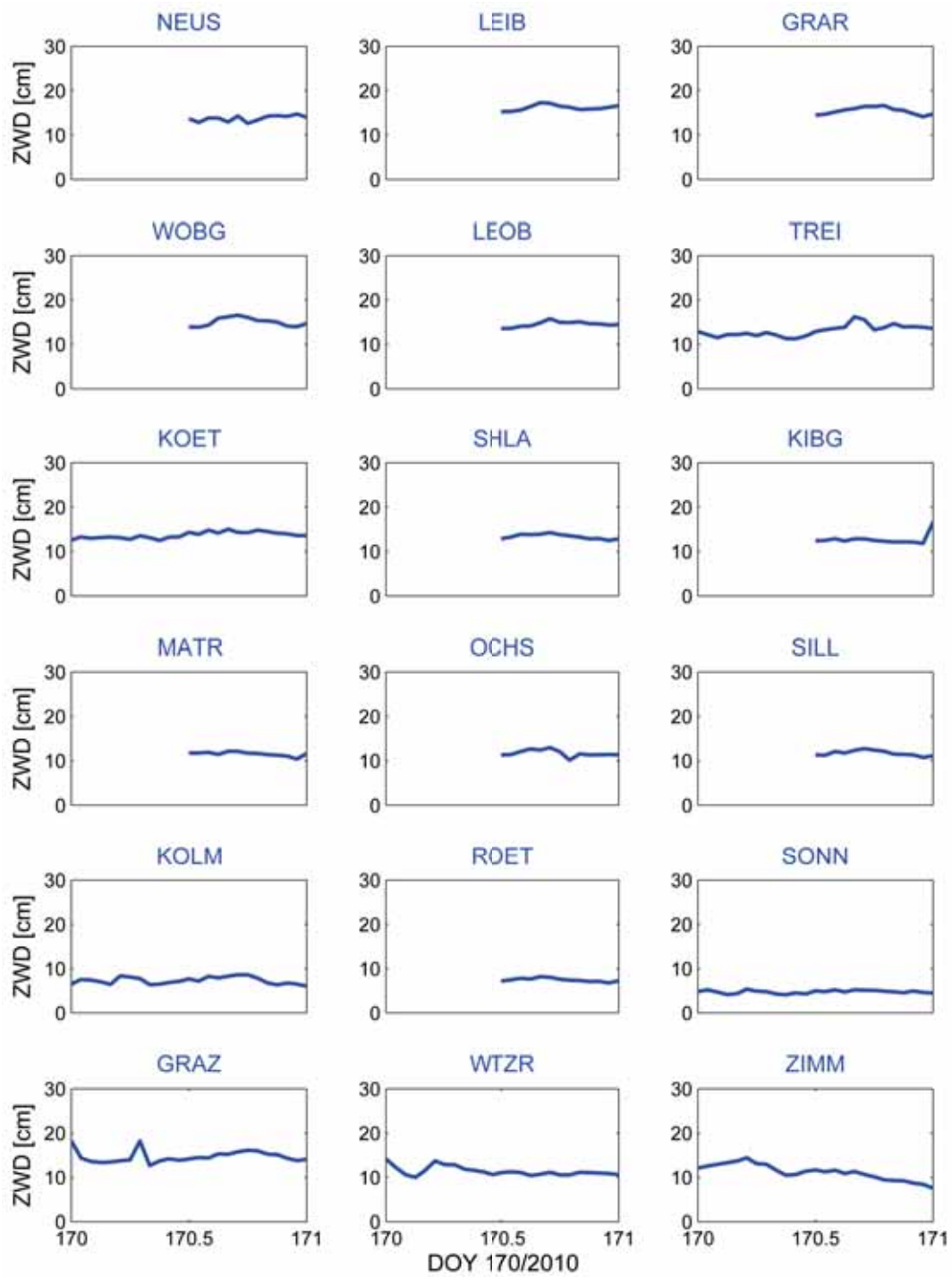


Figure B.55: ZWD (in cm) of all stations on June 19th, 2010

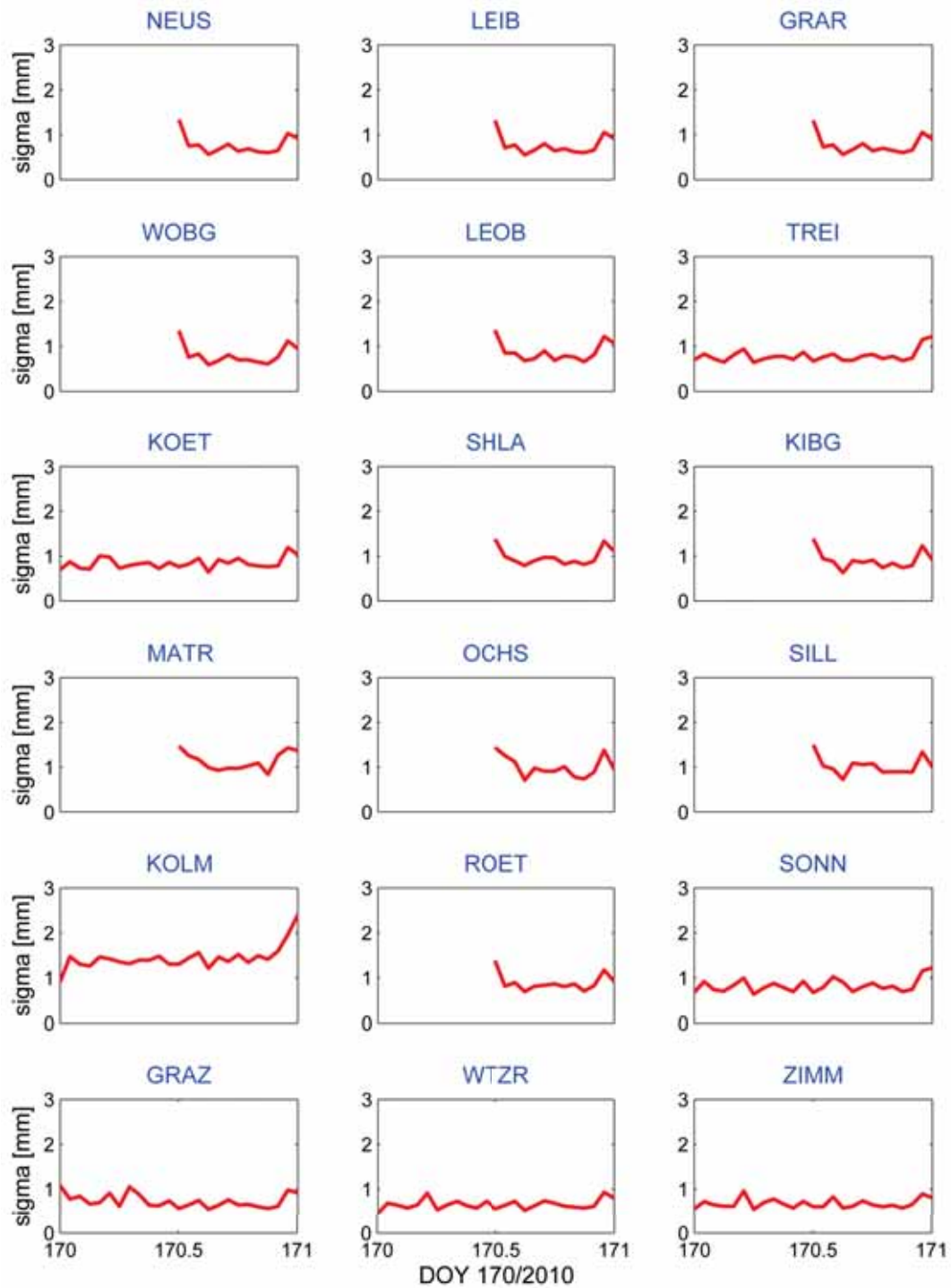


Figure B.56: Formal errors of ZWD estimates (in mm) of all stations on June 19th, 2010

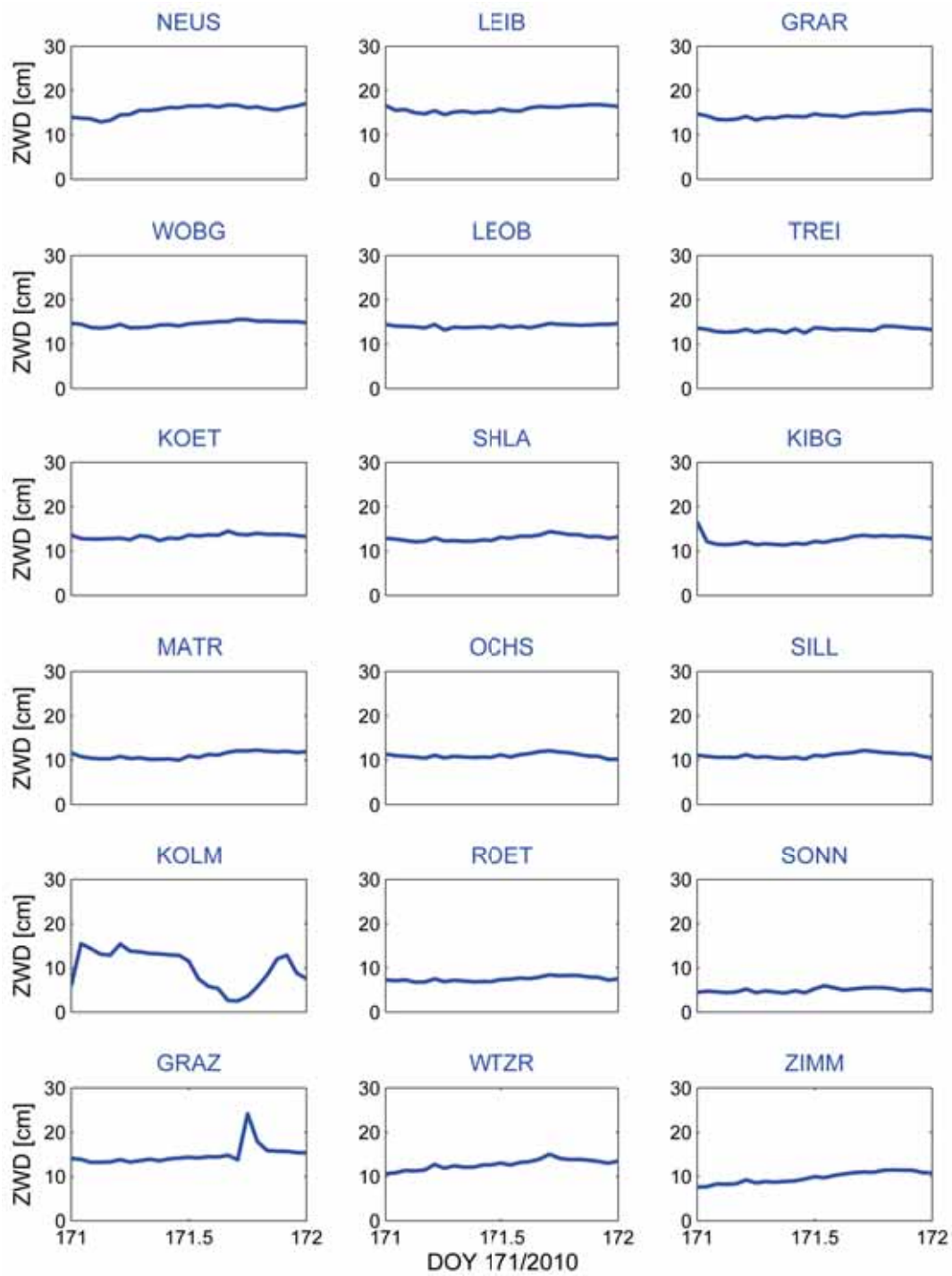


Figure B.57: ZWD (in cm) of all stations on June 20th, 2010

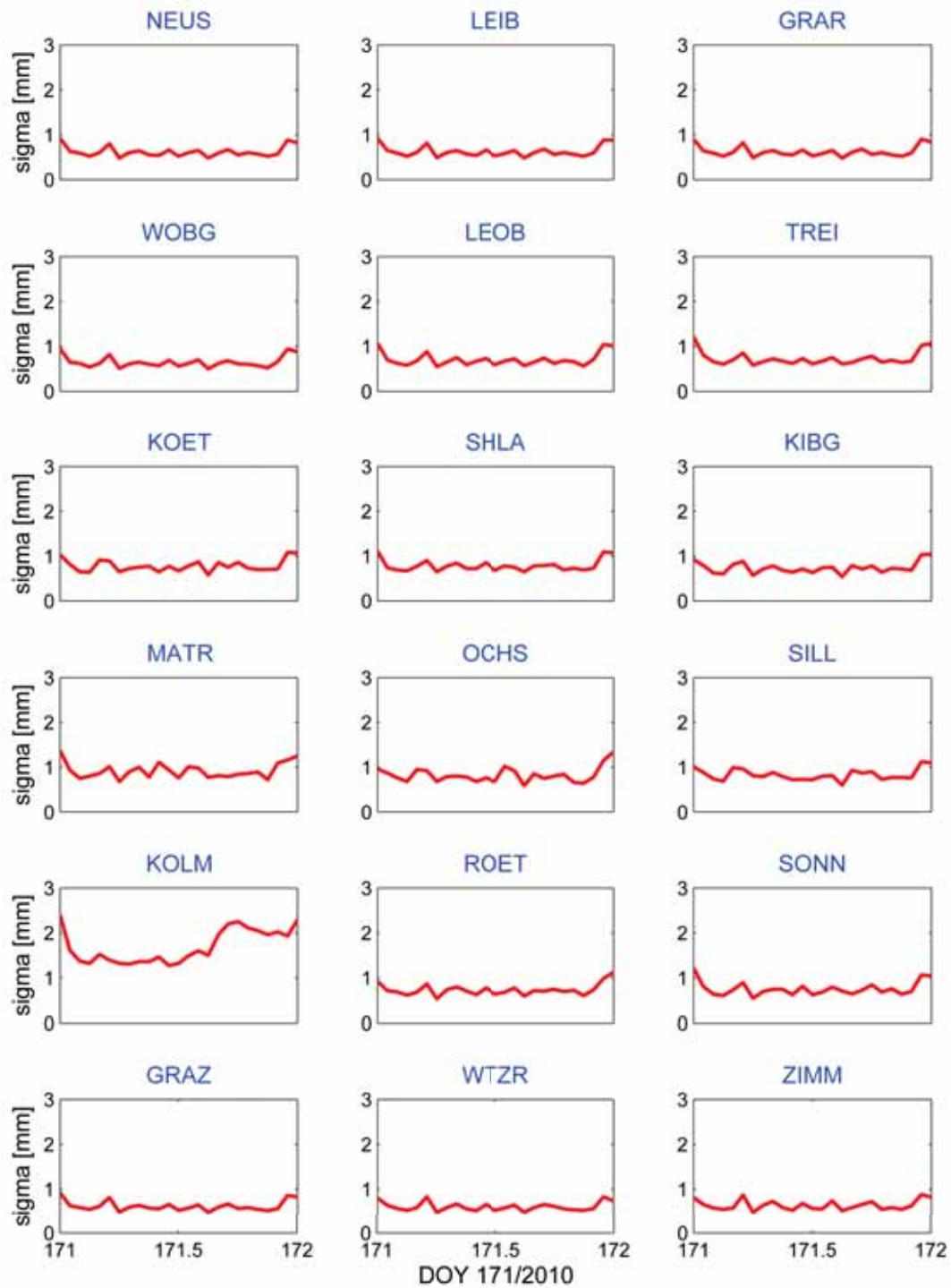


Figure B.58: Formal errors of ZWD estimates (in mm) of all stations on June 20th, 2010

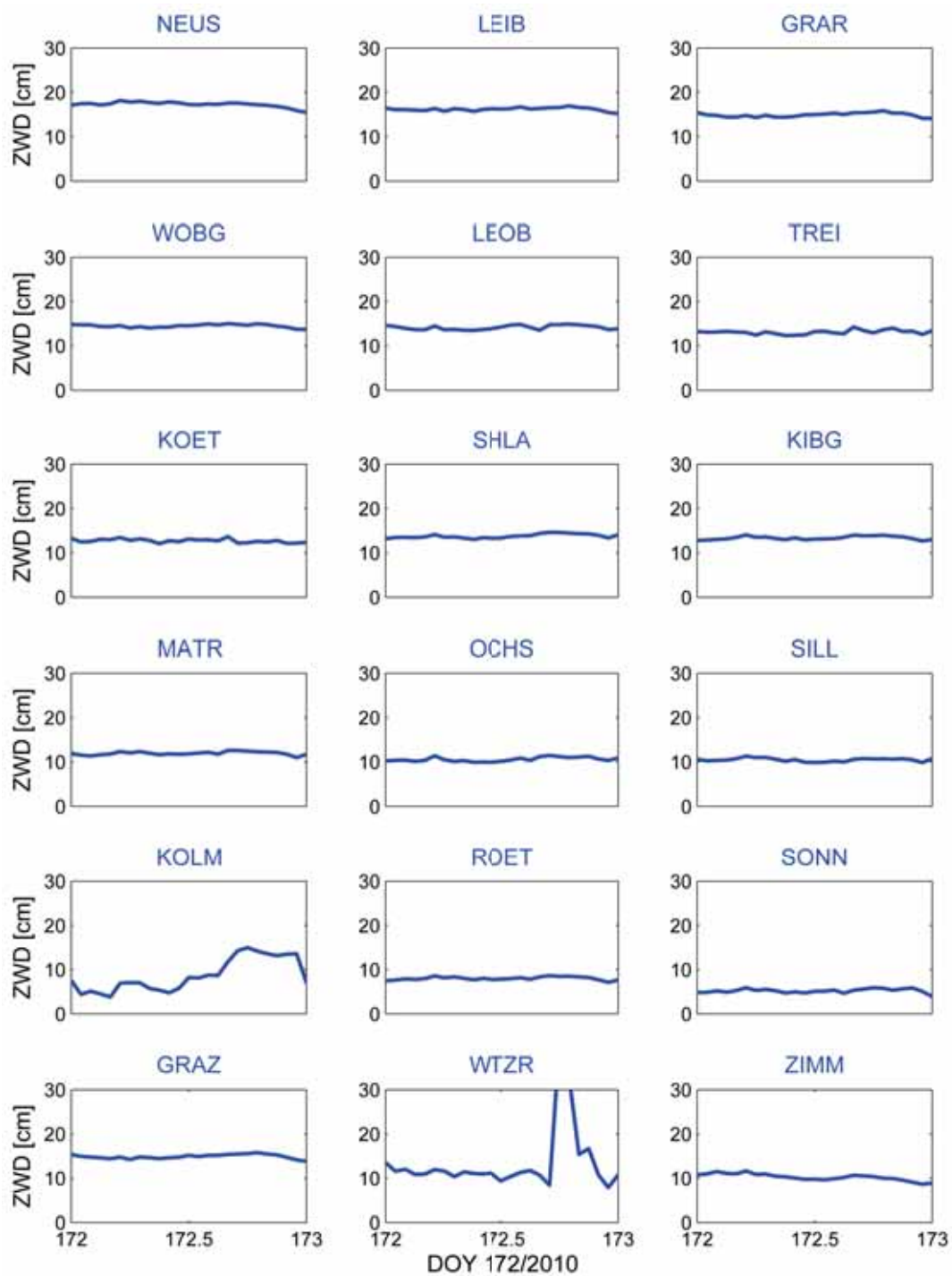


Figure B.59: ZWD (in cm) of all stations on June 21st, 2010

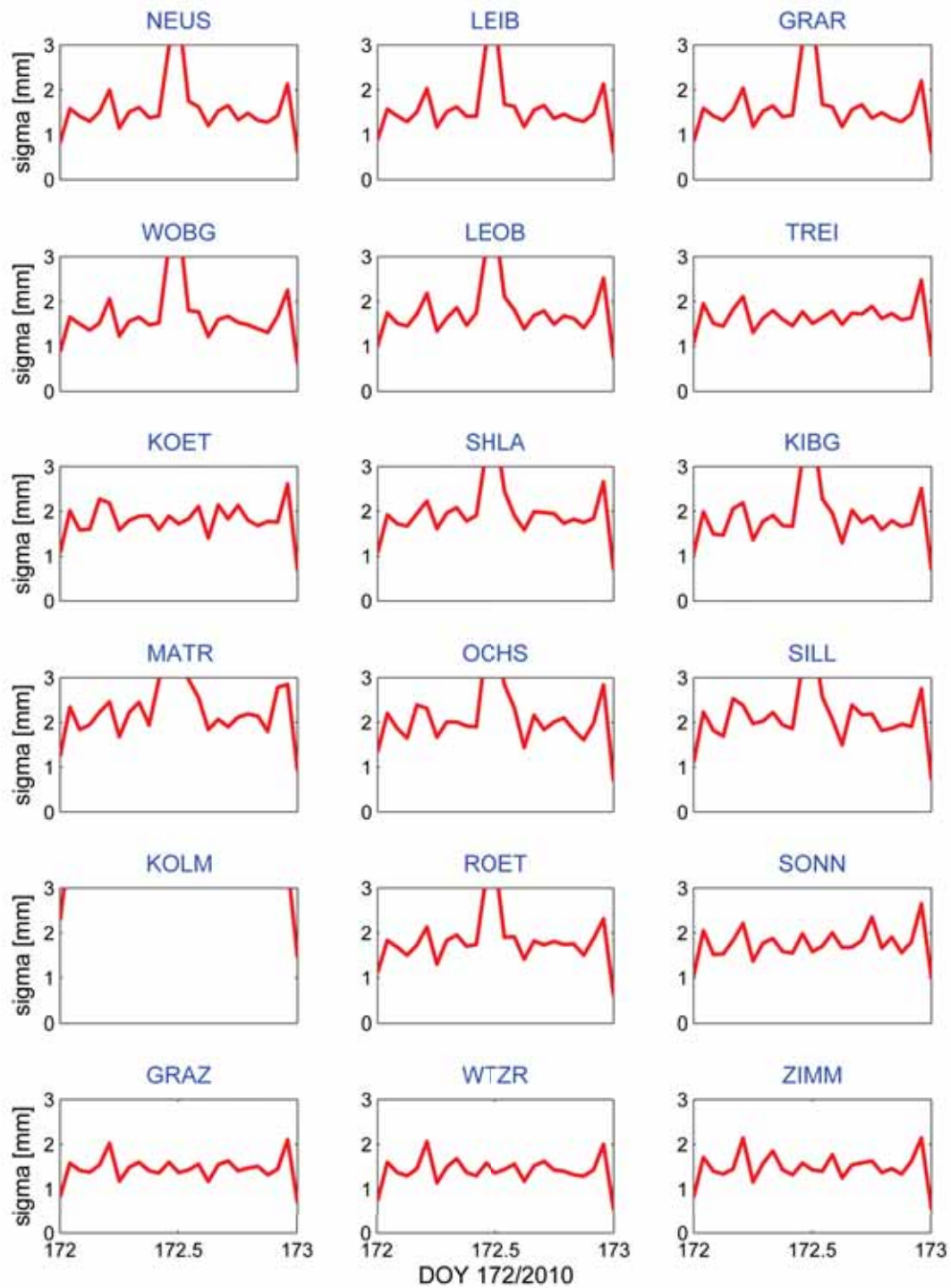


Figure B.60: Formal errors of ZWD estimates (in mm) of all stations on June 21st, 2010

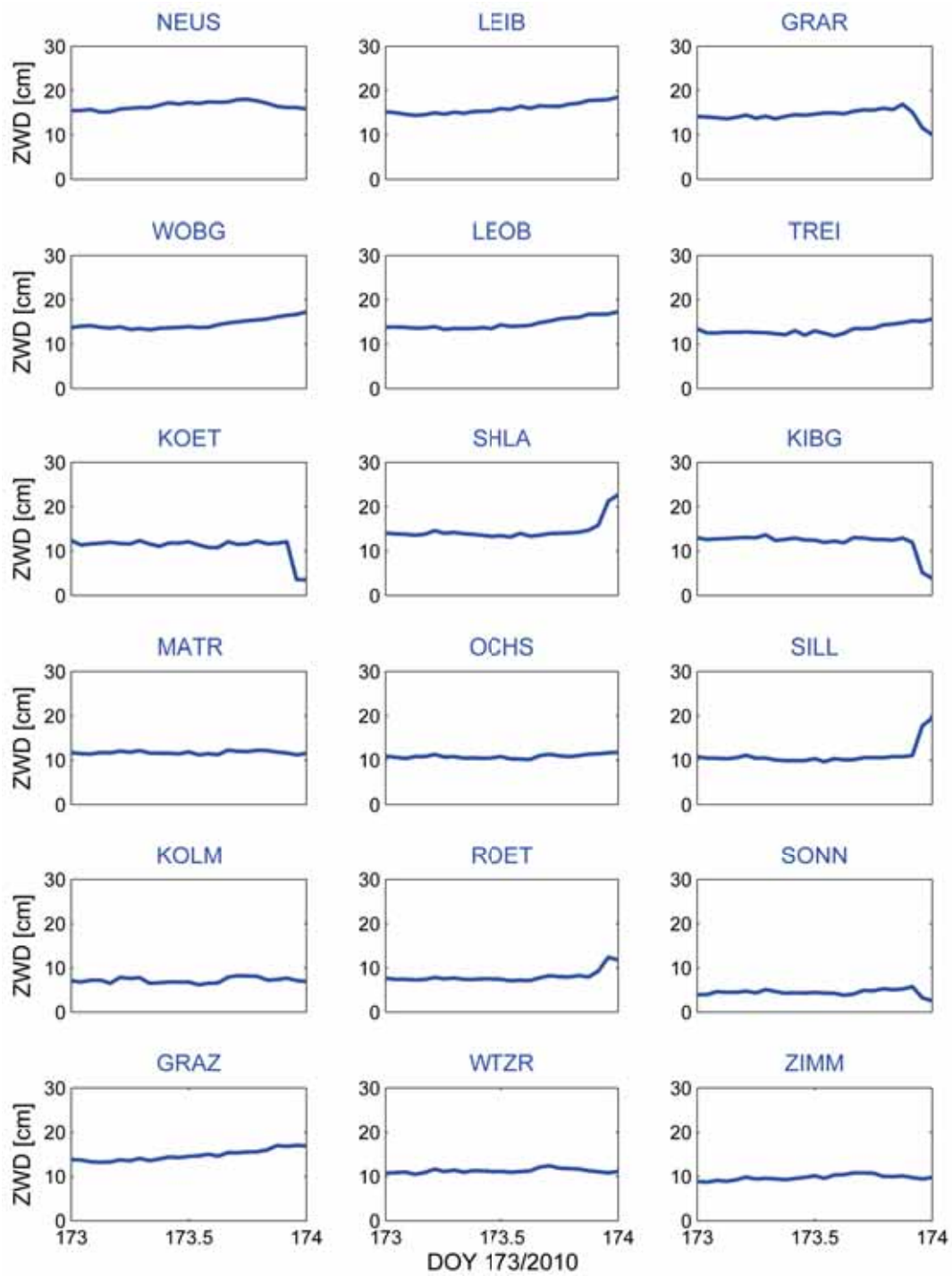


Figure B.61: ZWD (in cm) of all stations on June 22nd, 2010

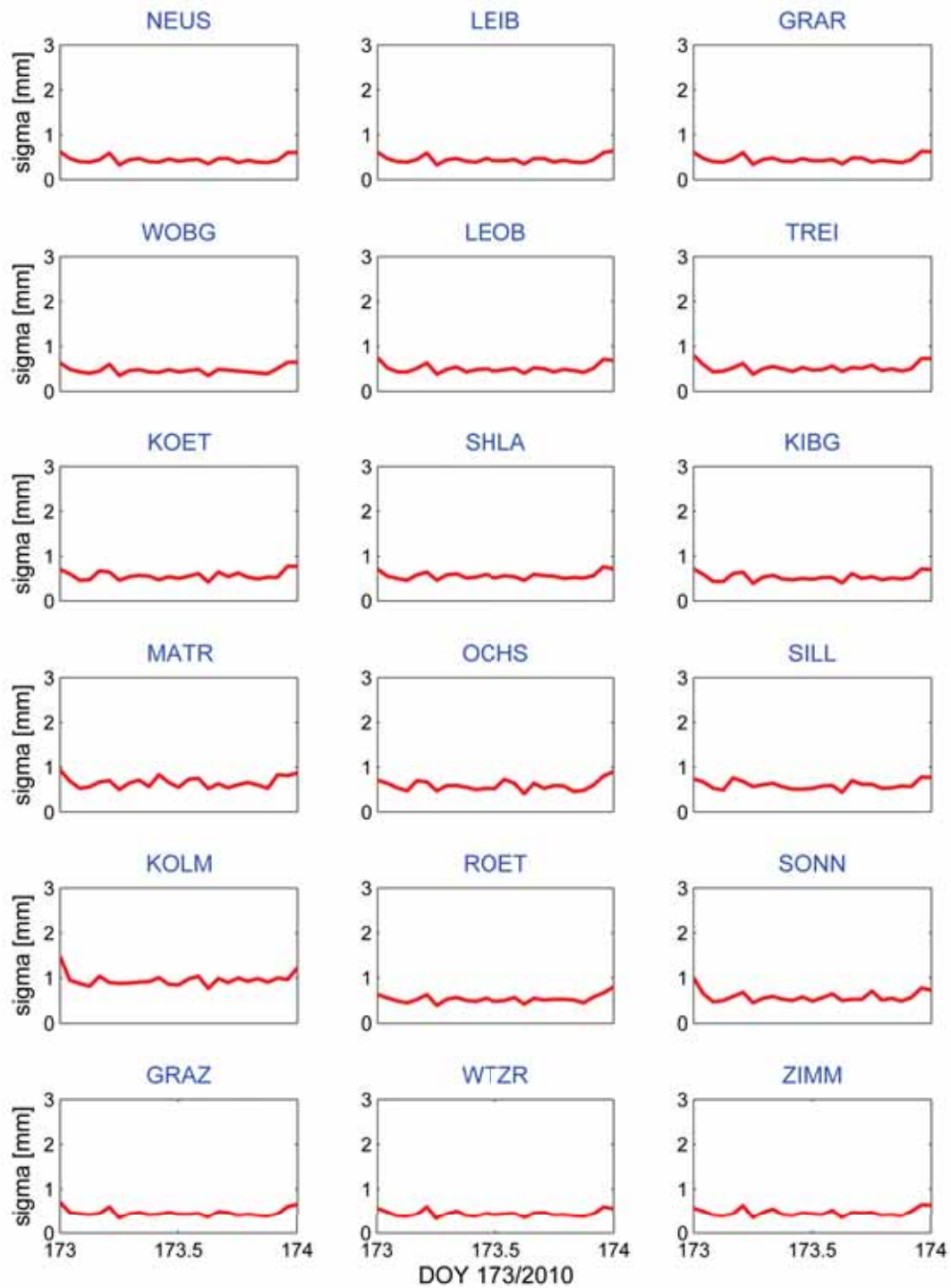


Figure B.62: Formal errors of ZWD estimates (in mm) of all stations on June 22nd, 2010

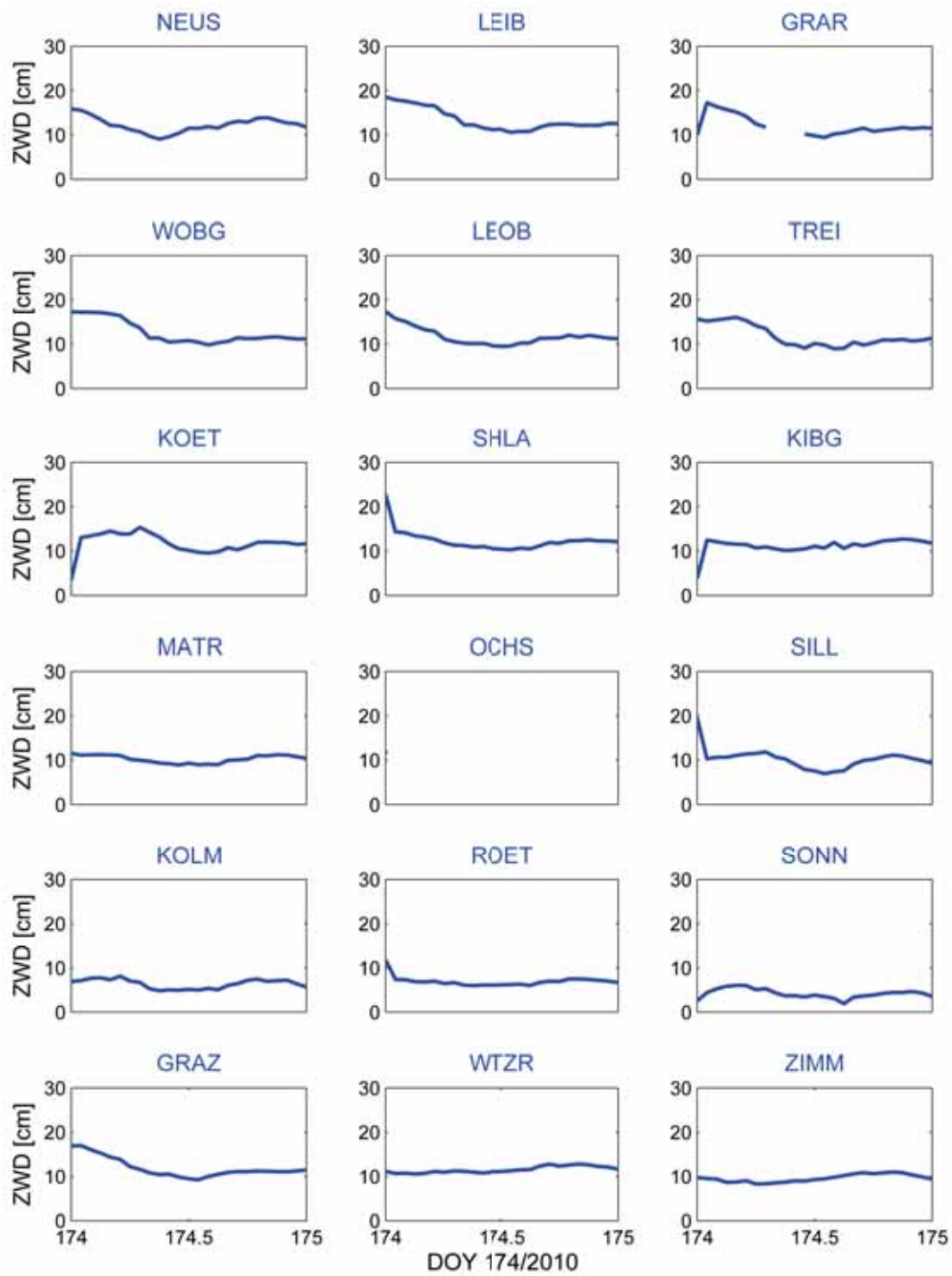


Figure B.63: ZWD (in cm) of all stations on June 23rd, 2010

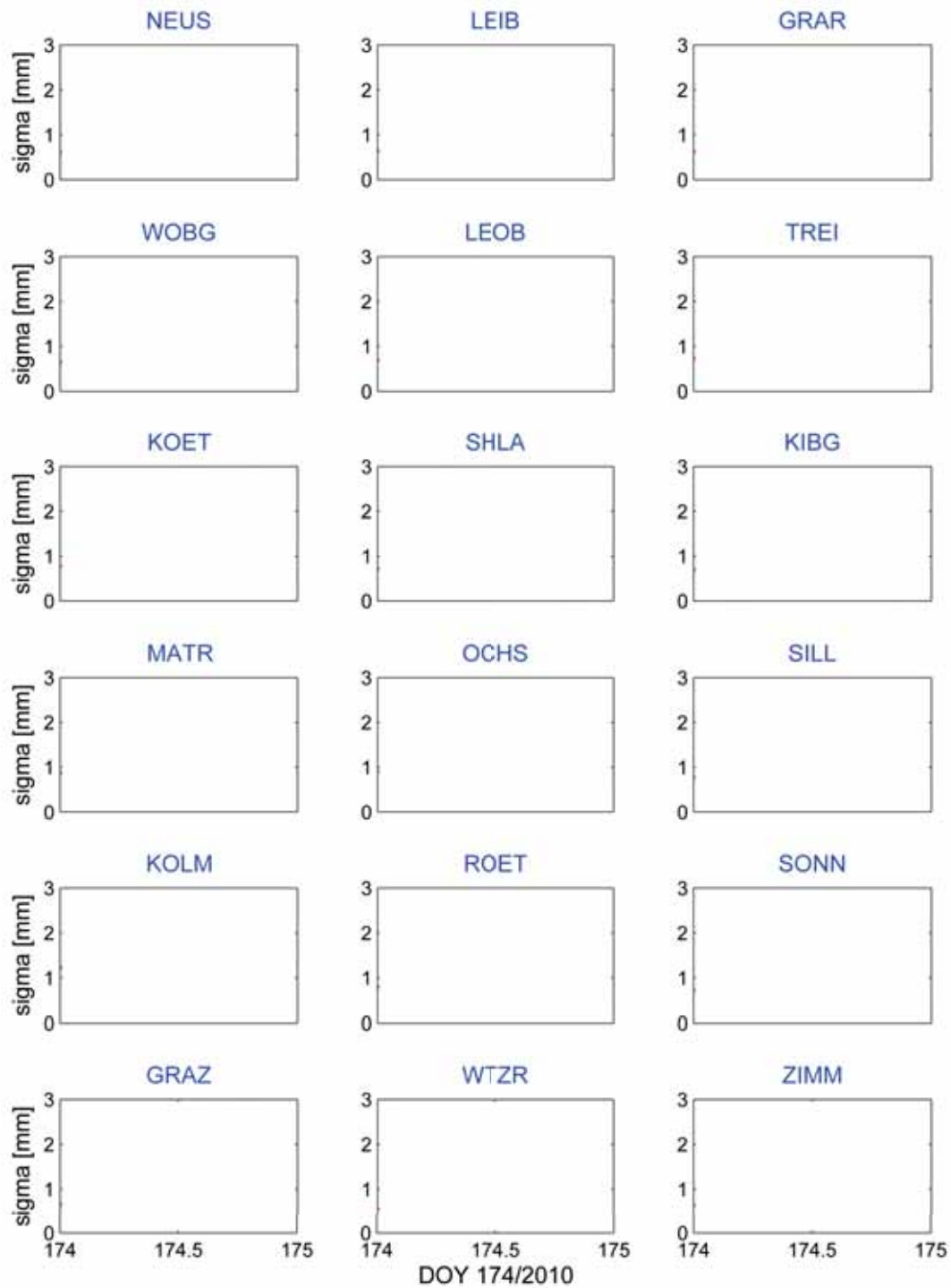


Figure B.64: Formal errors of ZWD estimates (in mm) of all stations on June 23rd, 2010

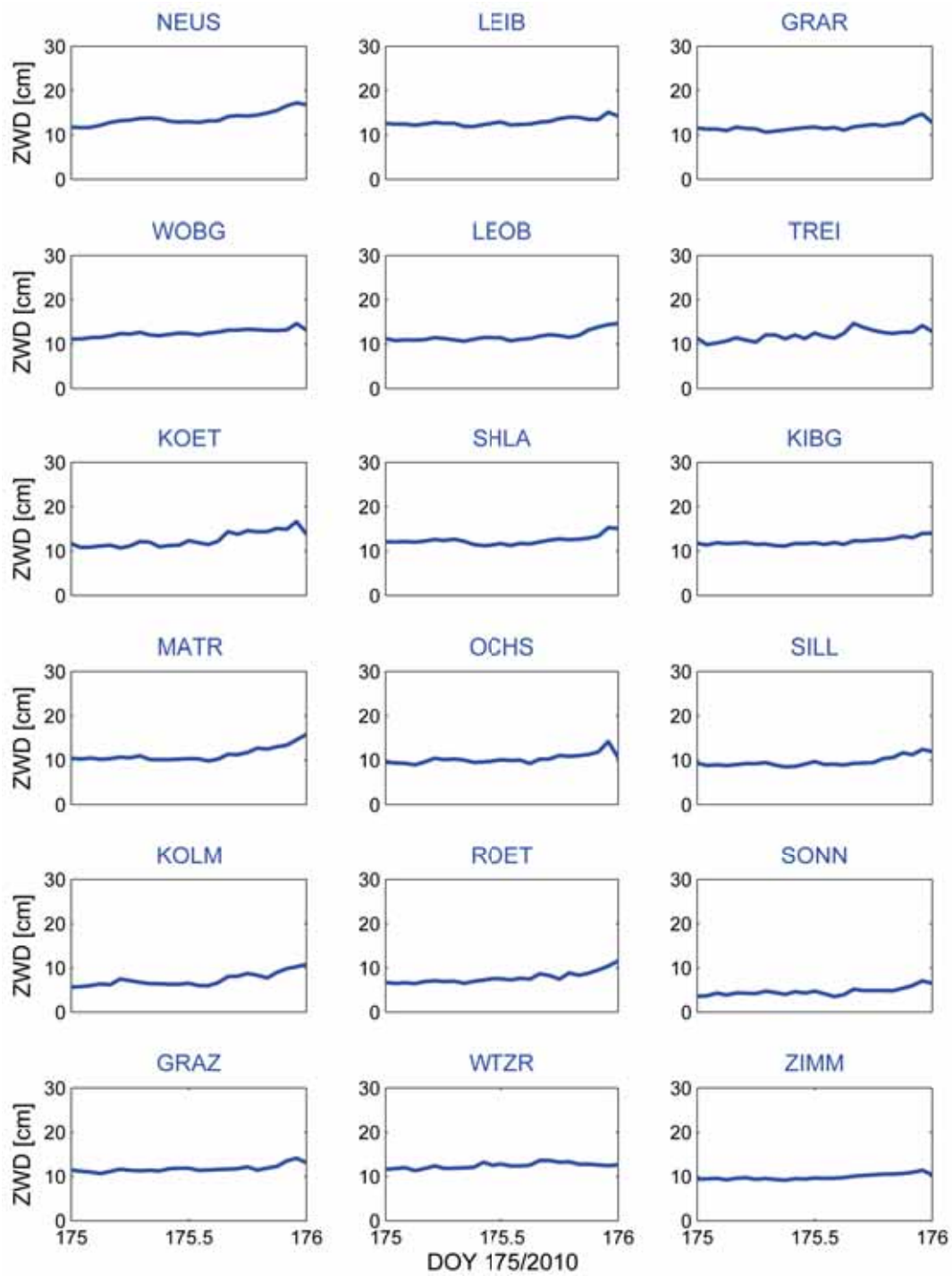


Figure B.65: ZWD (in cm) of all stations on June 24th, 2010

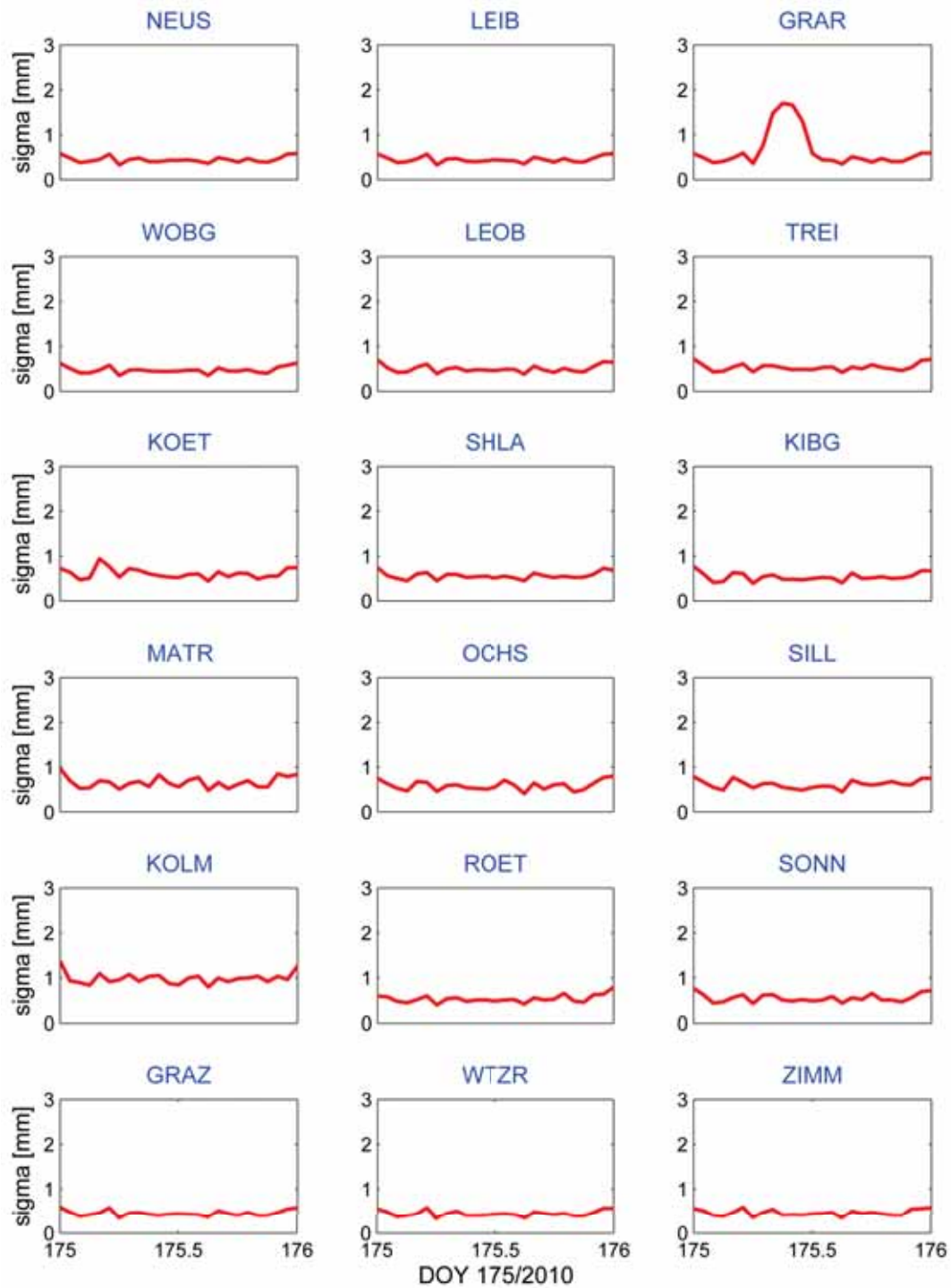


Figure B.66: Formal errors of ZWD estimates (in mm) of all stations on June 24th, 2010

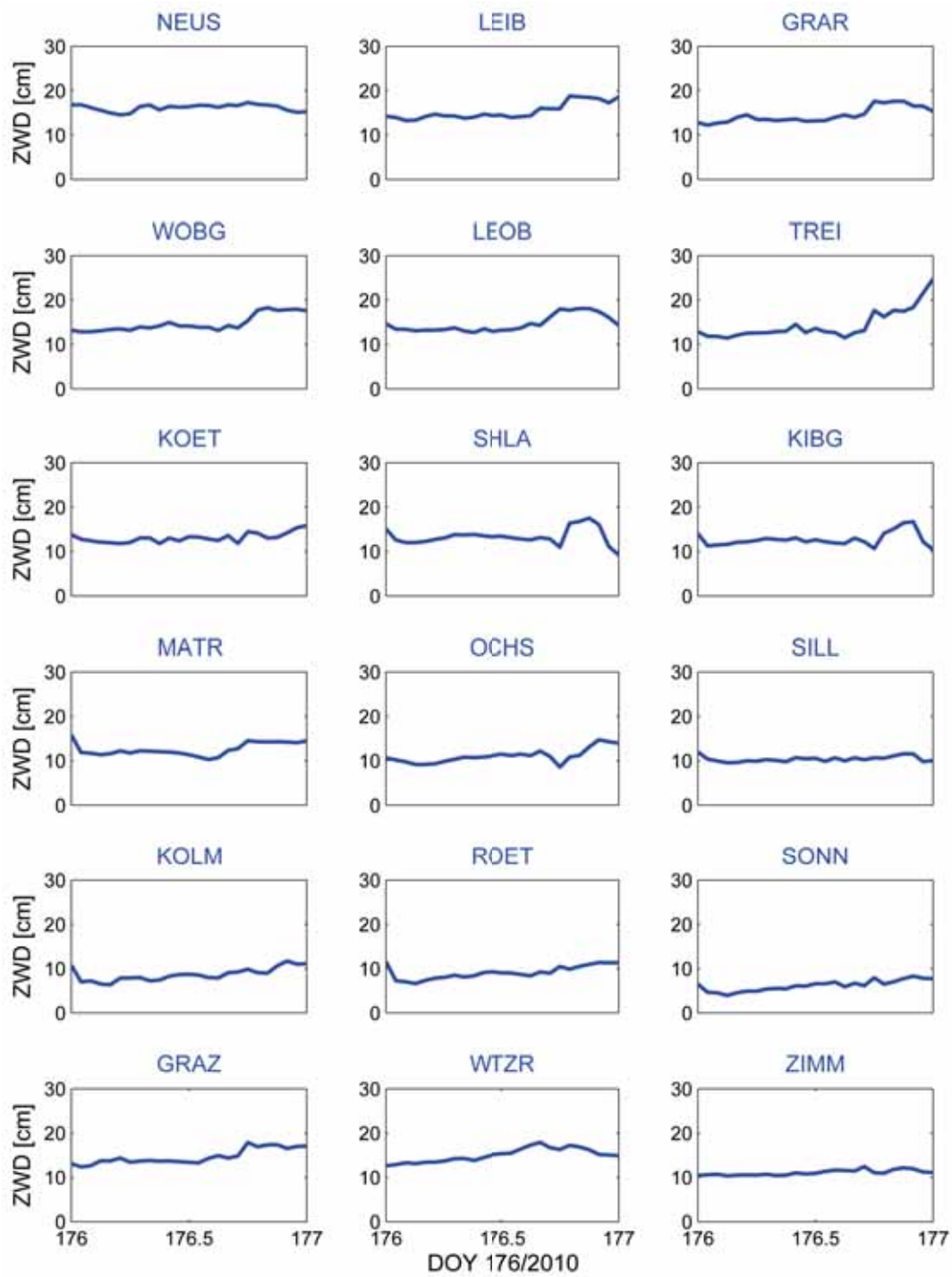


Figure B.67: ZWD (in cm) of all stations on June 25th, 2010

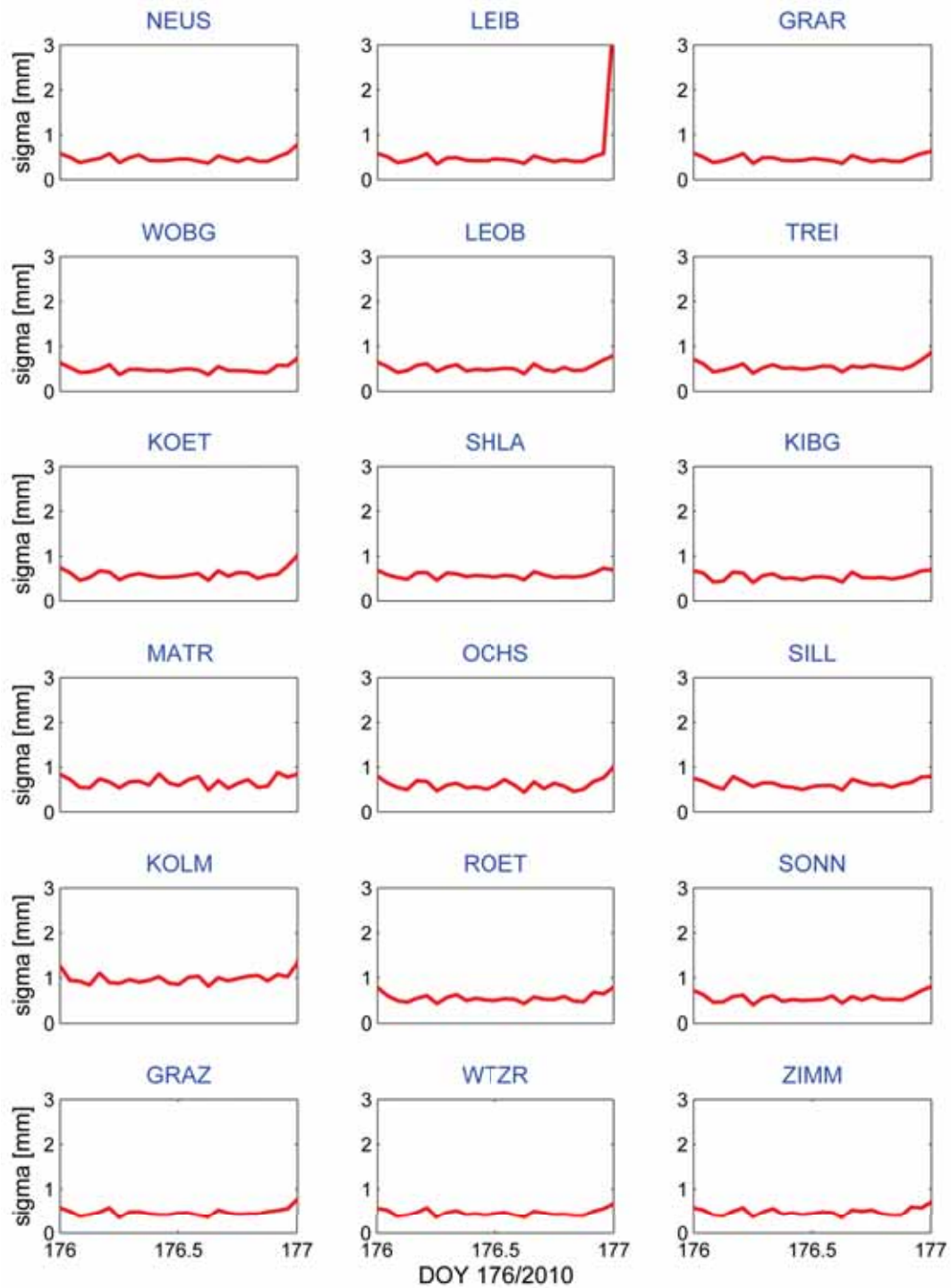


Figure B.68: Formal errors of ZWD estimates (in mm) of all stations on June 25th, 2010

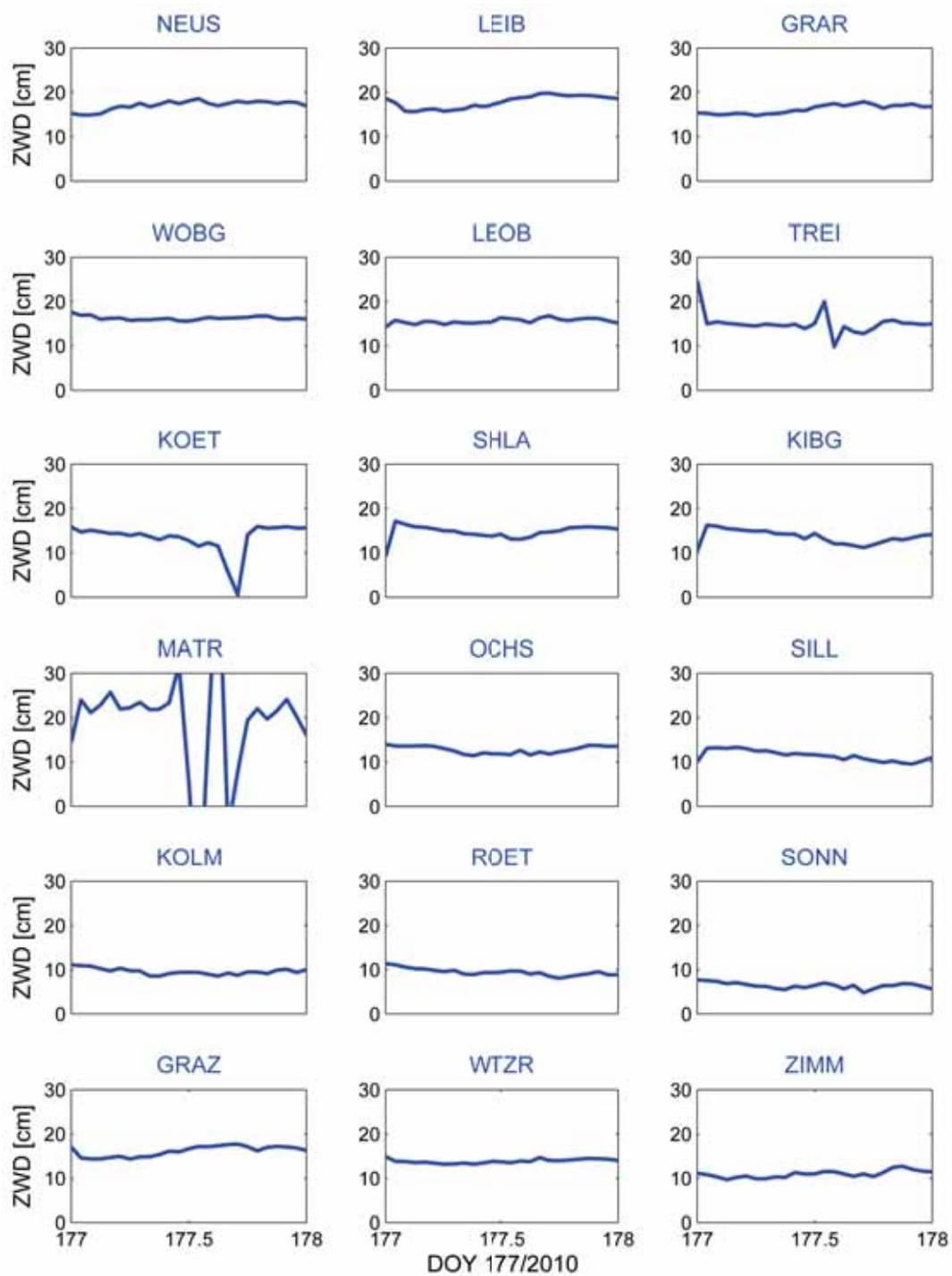


Figure B.69: ZWD (in cm) of all stations on June 26th, 2010

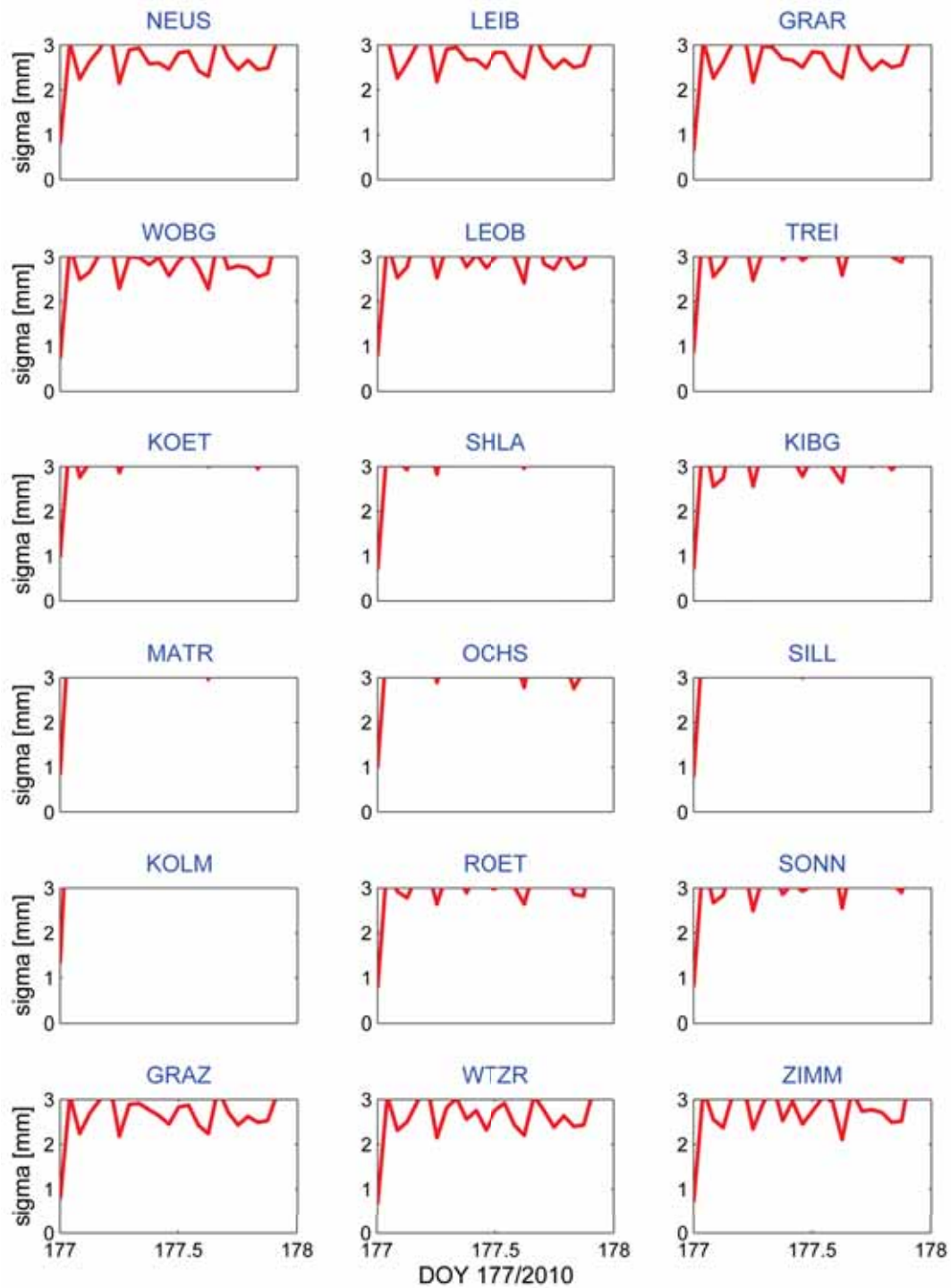


Figure B.70: Formal errors of ZWD estimates (in mm) of all stations on June 26th, 2010

Appendix C

This appendix lists the ZWD time series and the respective formal errors for each individual station, estimated by the Precise Point Positioning technique described in Ch. 6. For comparison, the estimates from a double-difference solution and the difference between the PPP and DD solution is depicted. A full description of the comparison, as well as some statistical results are already presented in Sec. 6.5.1.

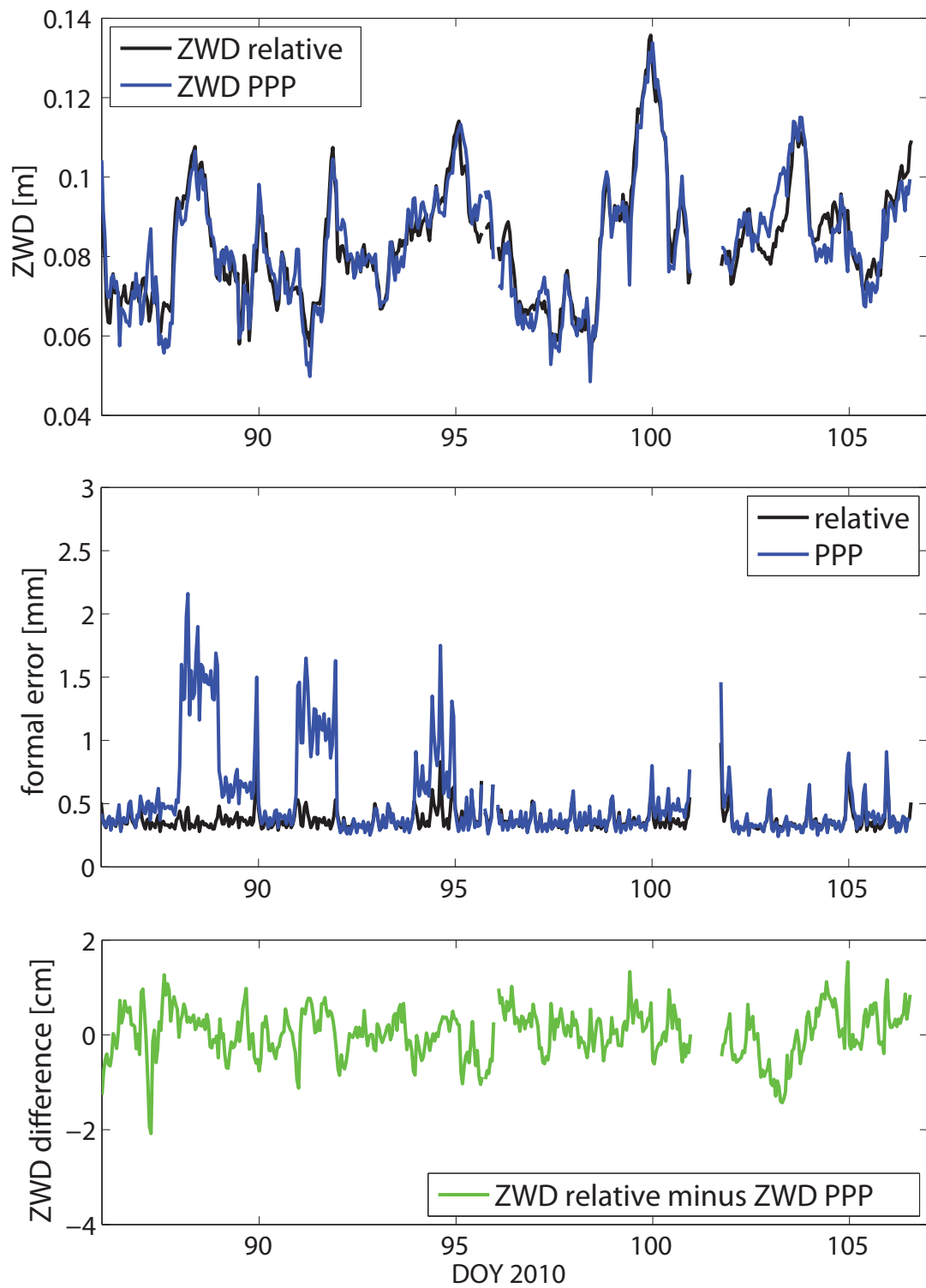


Figure C.1: Comparison of PPP and double-difference (relative) solution for station GRAR (March 27–April 16, 2010)

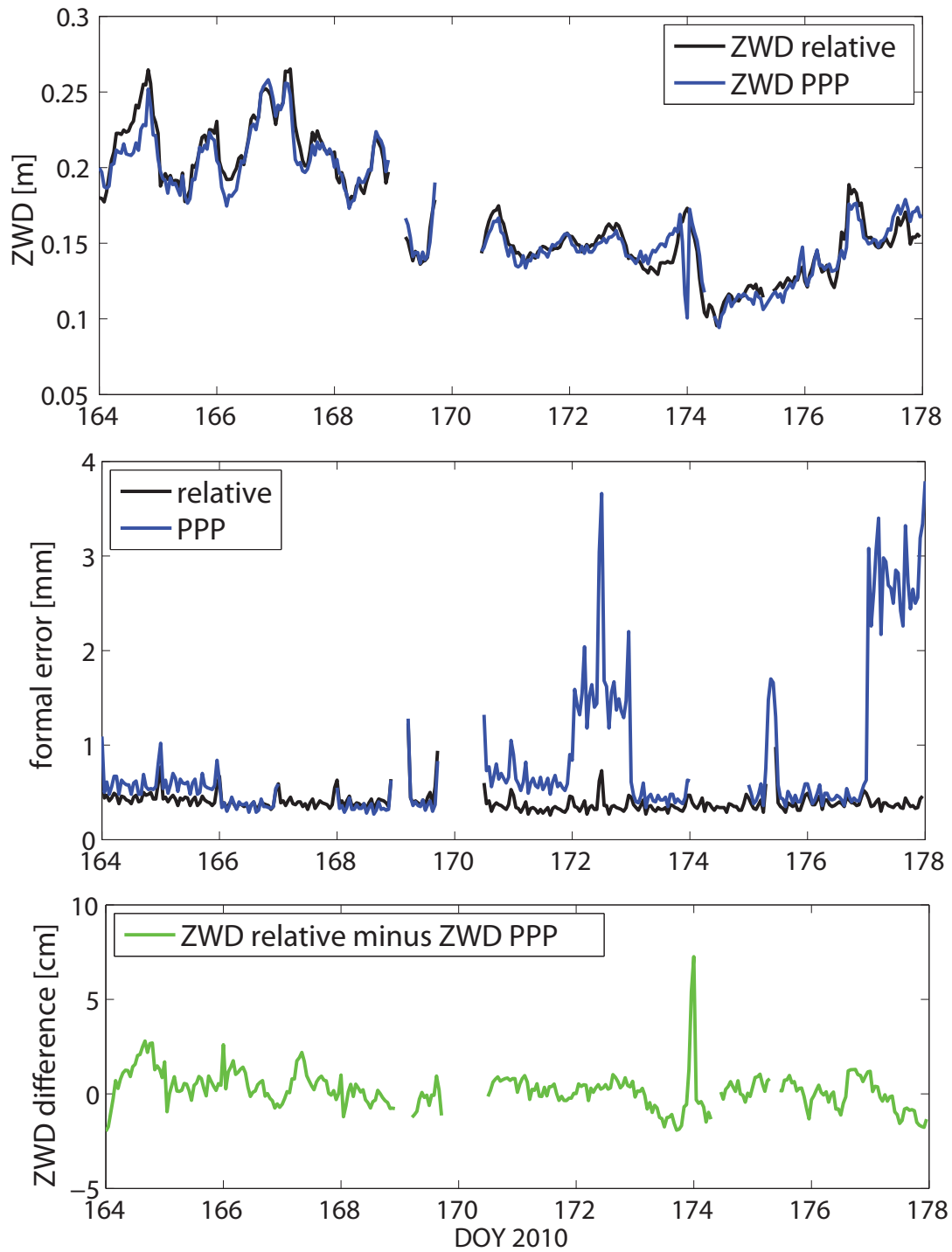


Figure C.2: Comparison of PPP and double-difference (relative) solution for station GRAR (June 13–26, 2010)

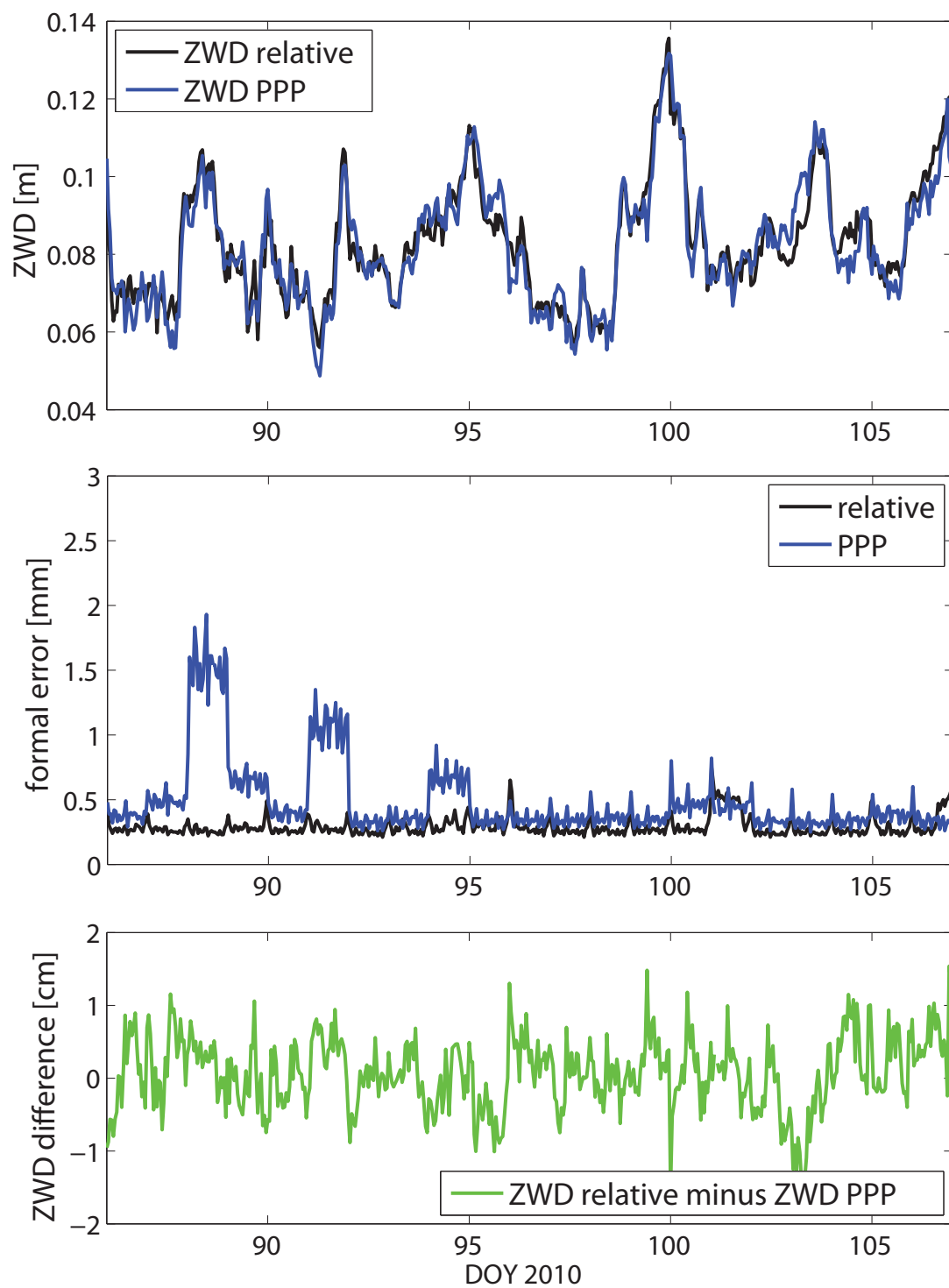


Figure C.3: Comparison of PPP and double-difference (relative) solution for station GRAZ (March 27–April 16, 2010)

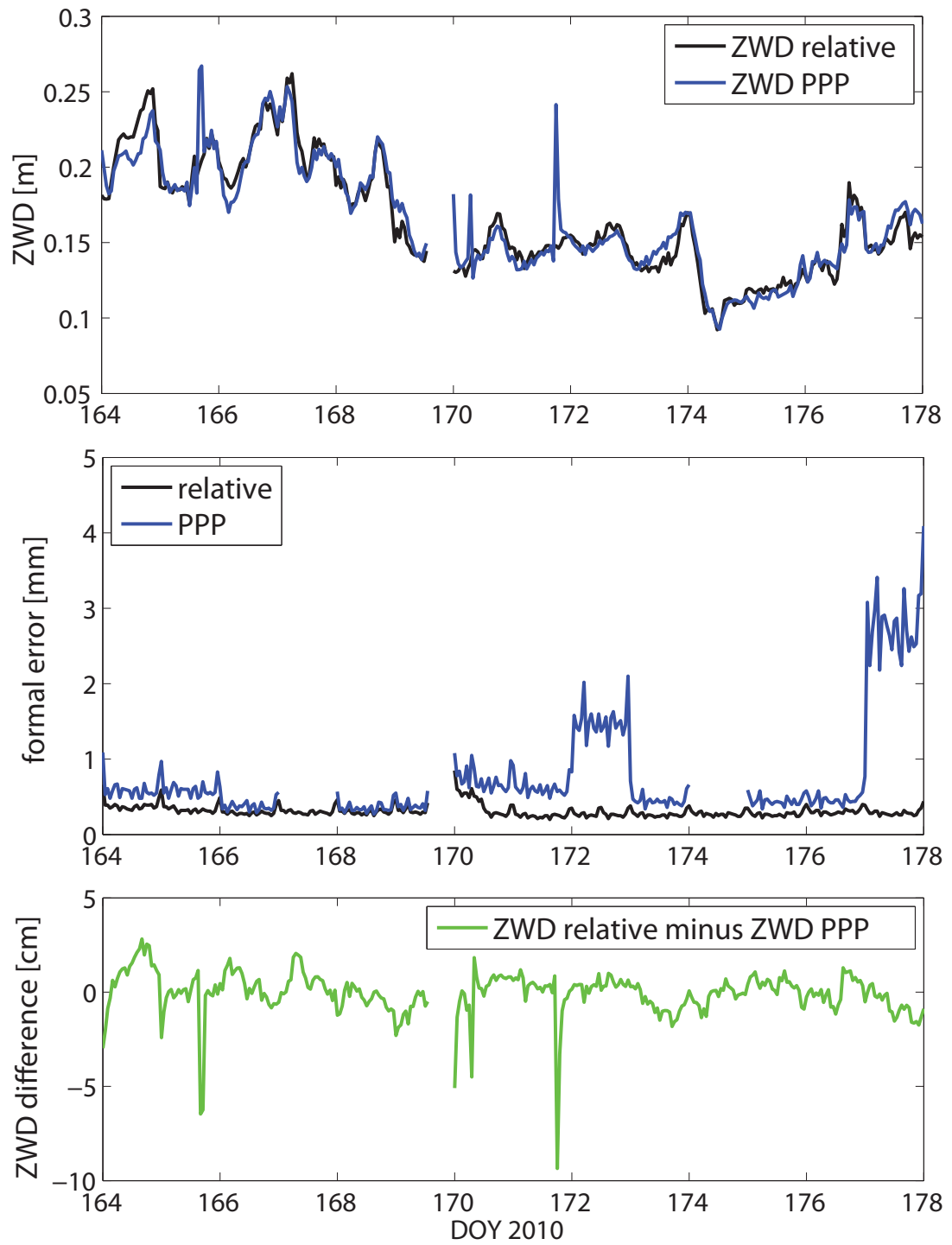


Figure C.4: Comparison of PPP and double-difference (relative) solution for station GRAZ (June 13–26, 2010)

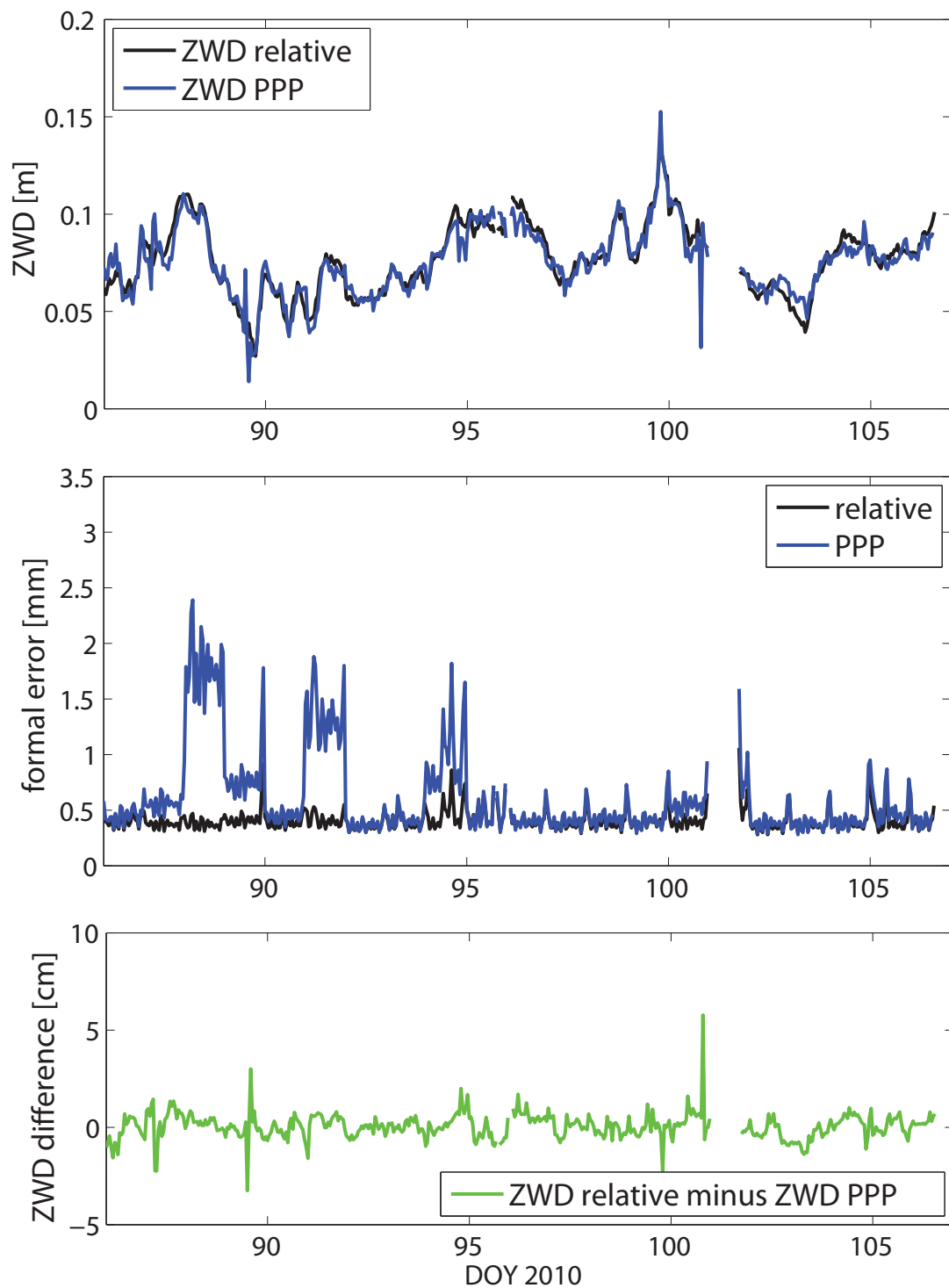


Figure C.5: Comparison of PPP and double-difference (relative) solution for station KIBG (March 27–April 16, 2010)

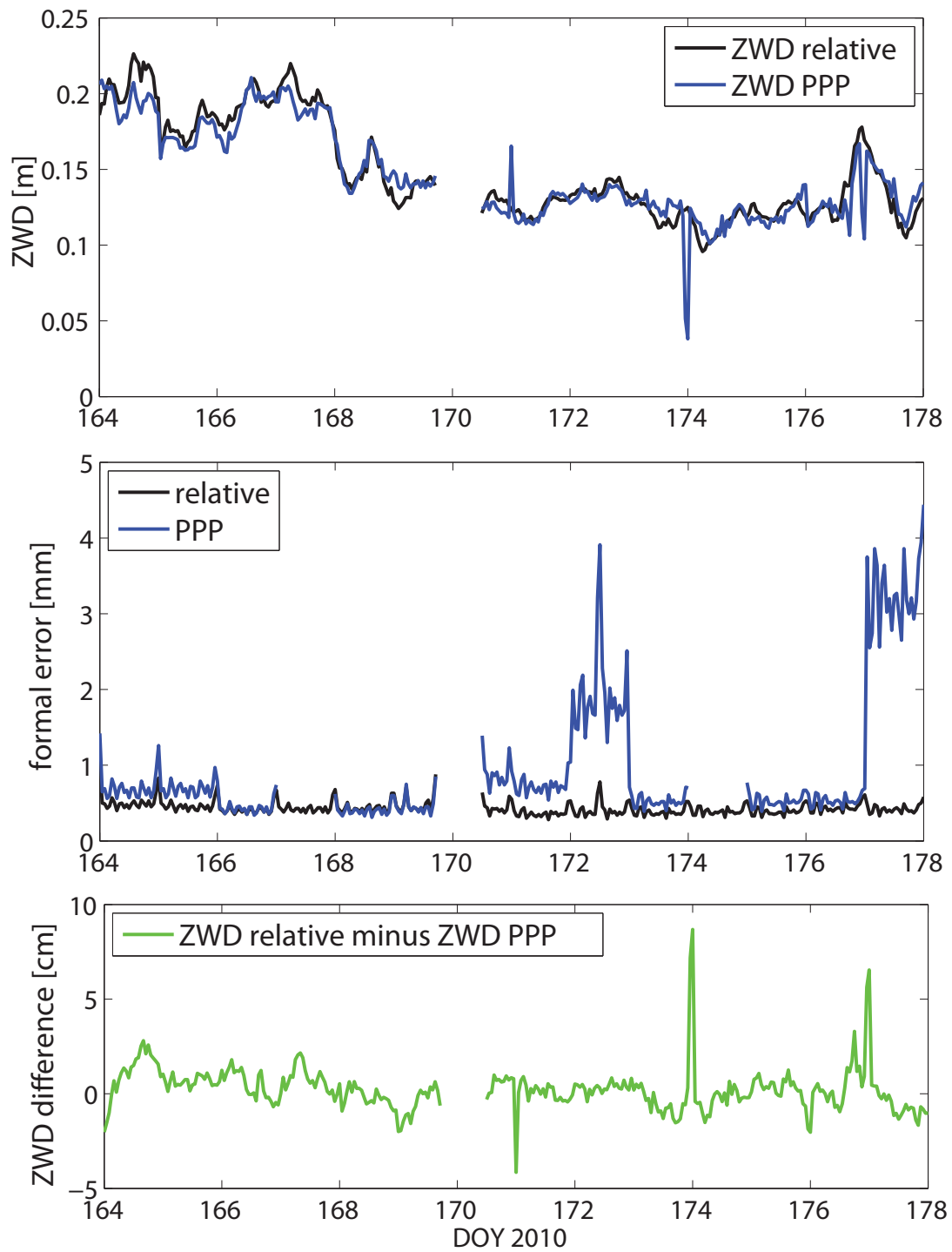


Figure C.6: Comparison of PPP and double-difference (relative) solution for station KIBG (June 13–26, 2010)

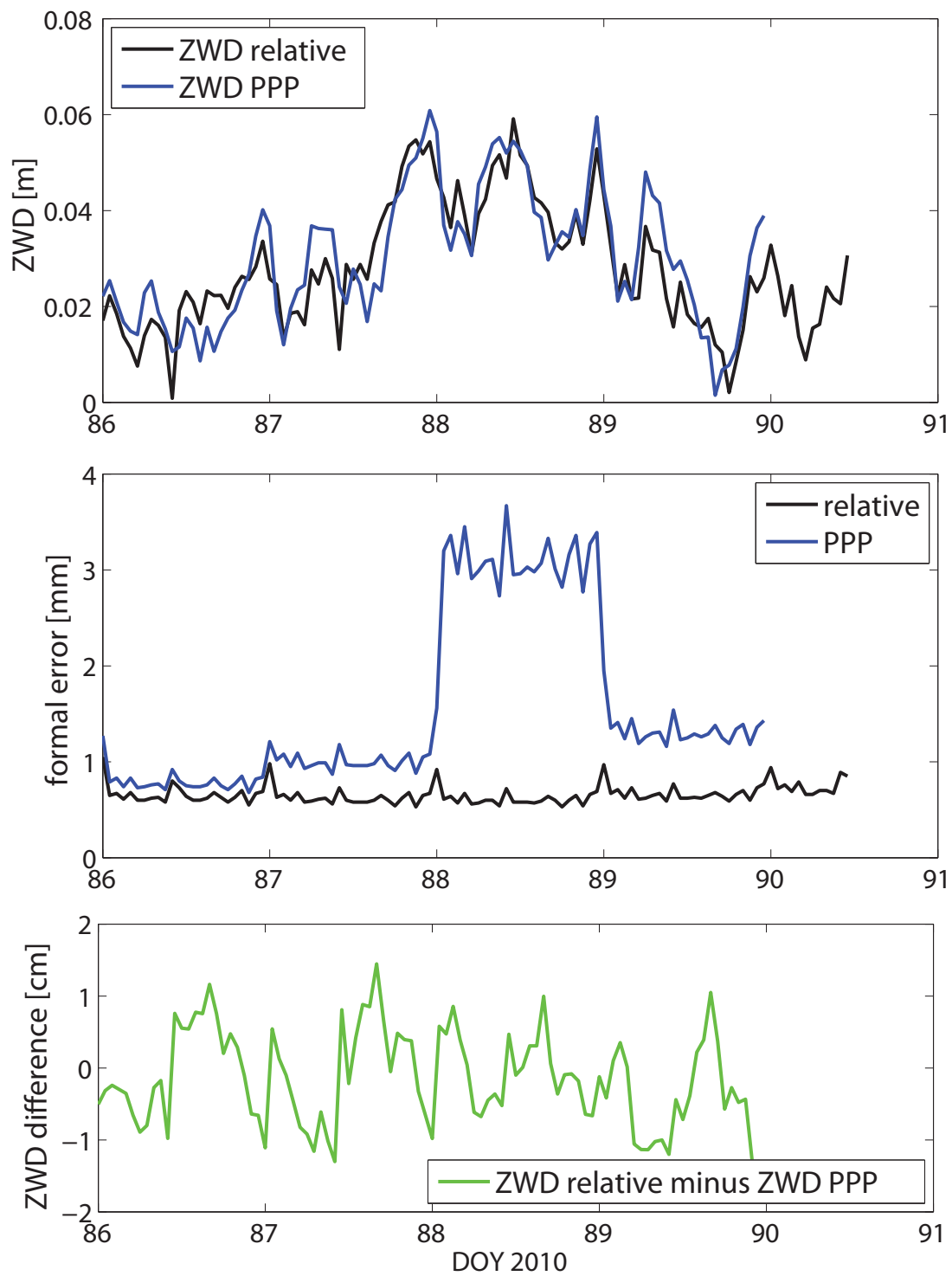


Figure C.7: Comparison of PPP and double-difference (relative) solution for station KOLM (March 27–April 16, 2010)

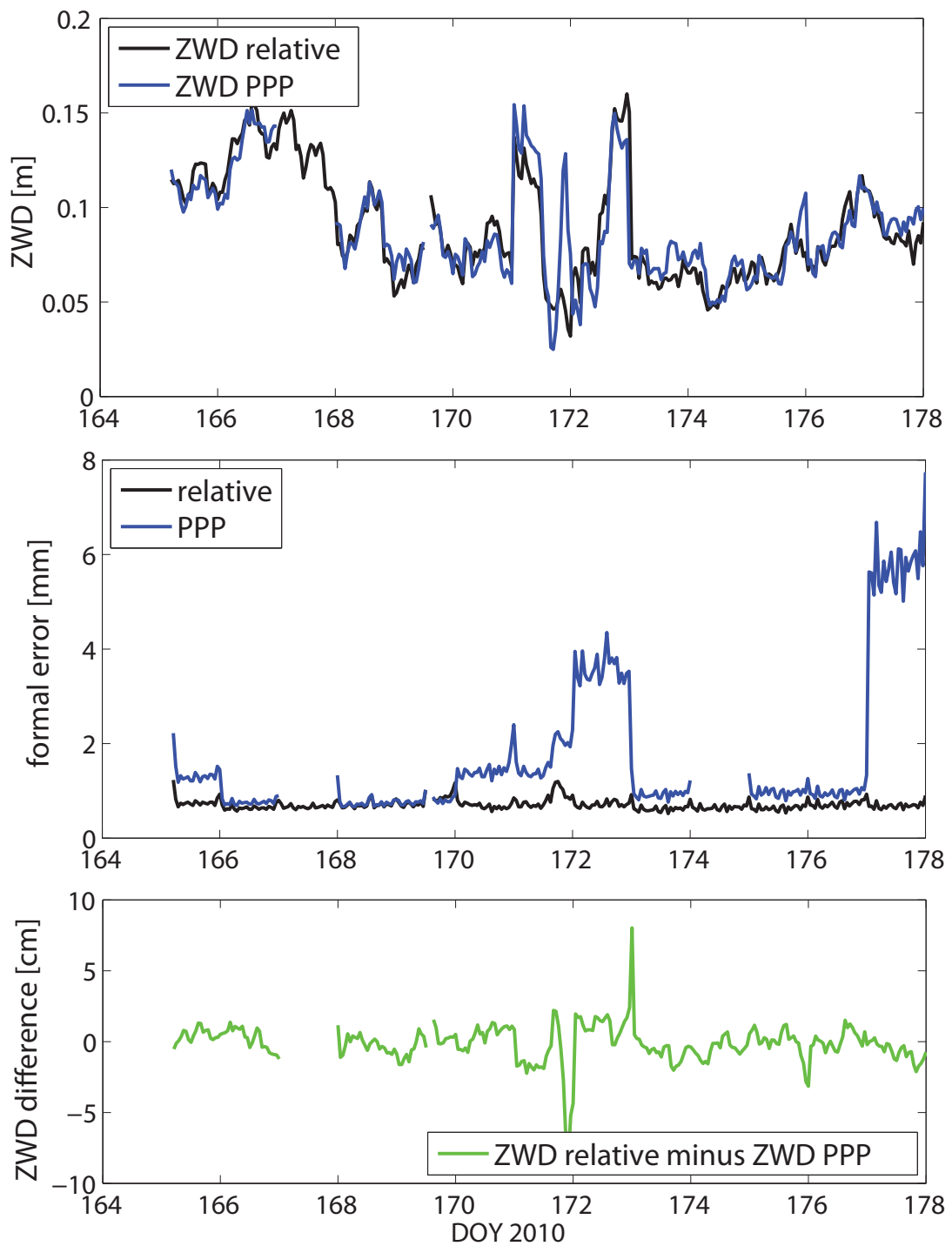


Figure C.8: Comparison of PPP and double-difference (relative) solution for station KOLM (June 13–26, 2010)

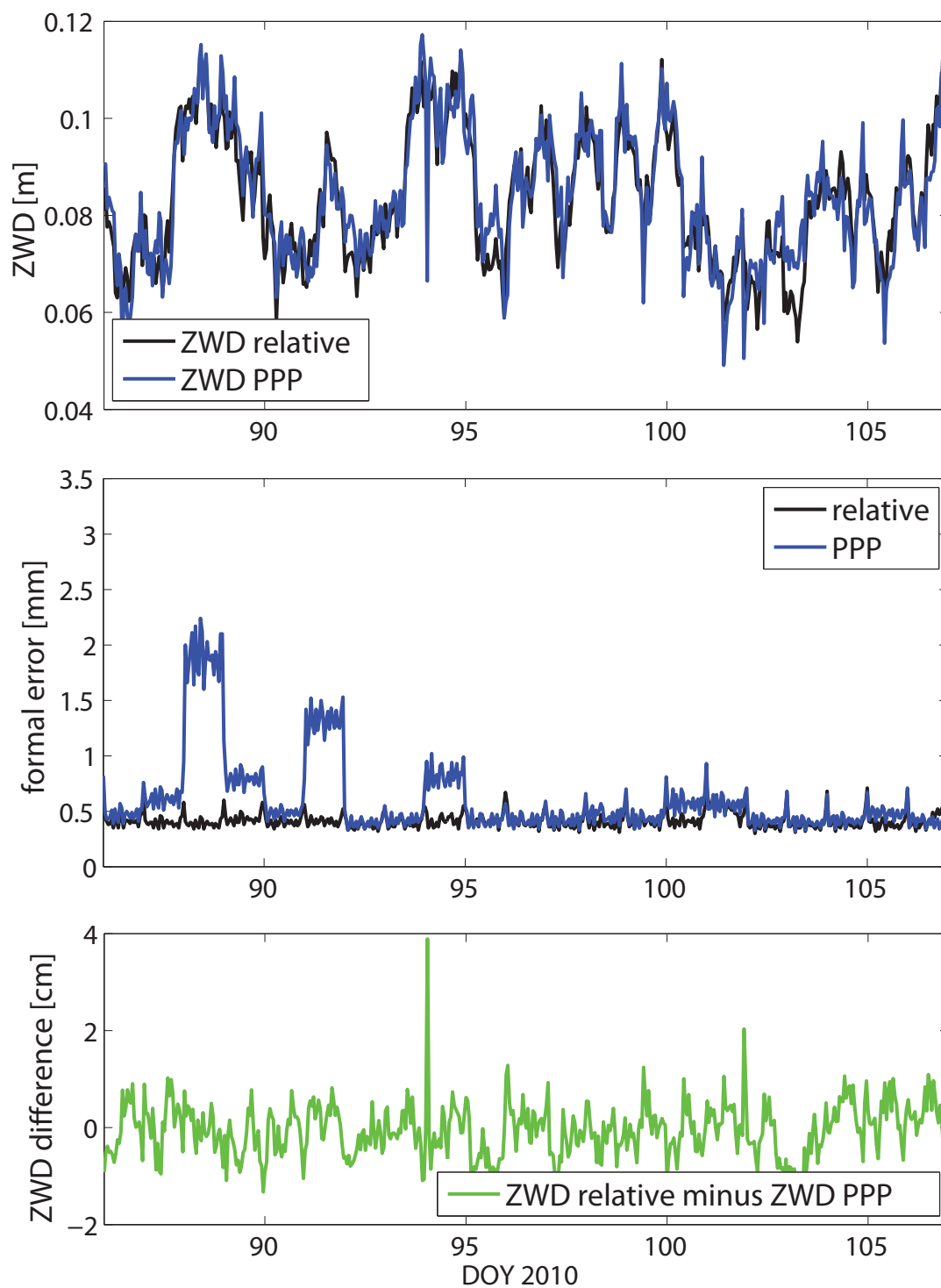


Figure C.9: Comparison of PPP and double-difference (relative) solution for station KOET (March 27–April 16, 2010)

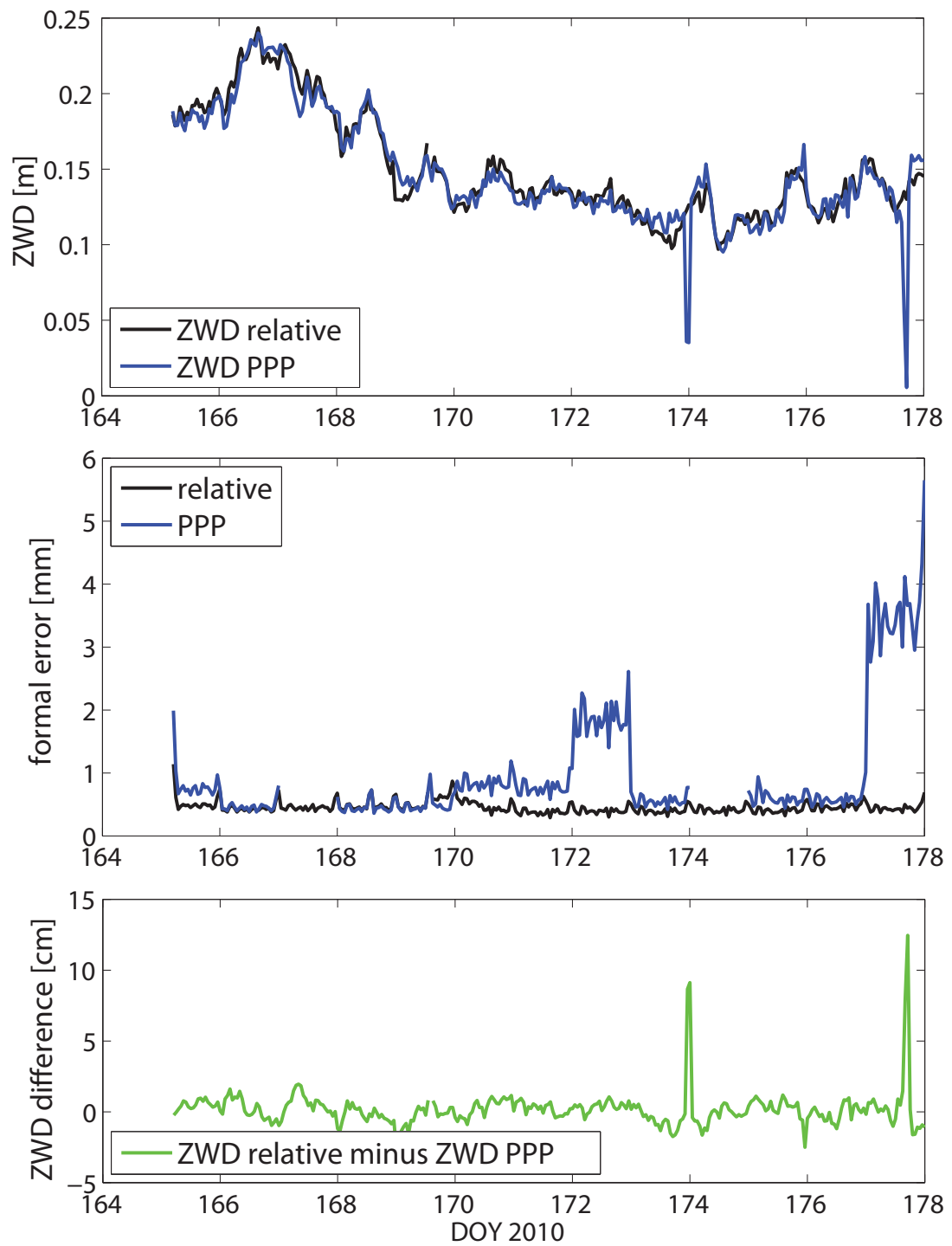


Figure C.10: Comparison of PPP and double-difference (relative) solution for station KOET (June 13–26, 2010)

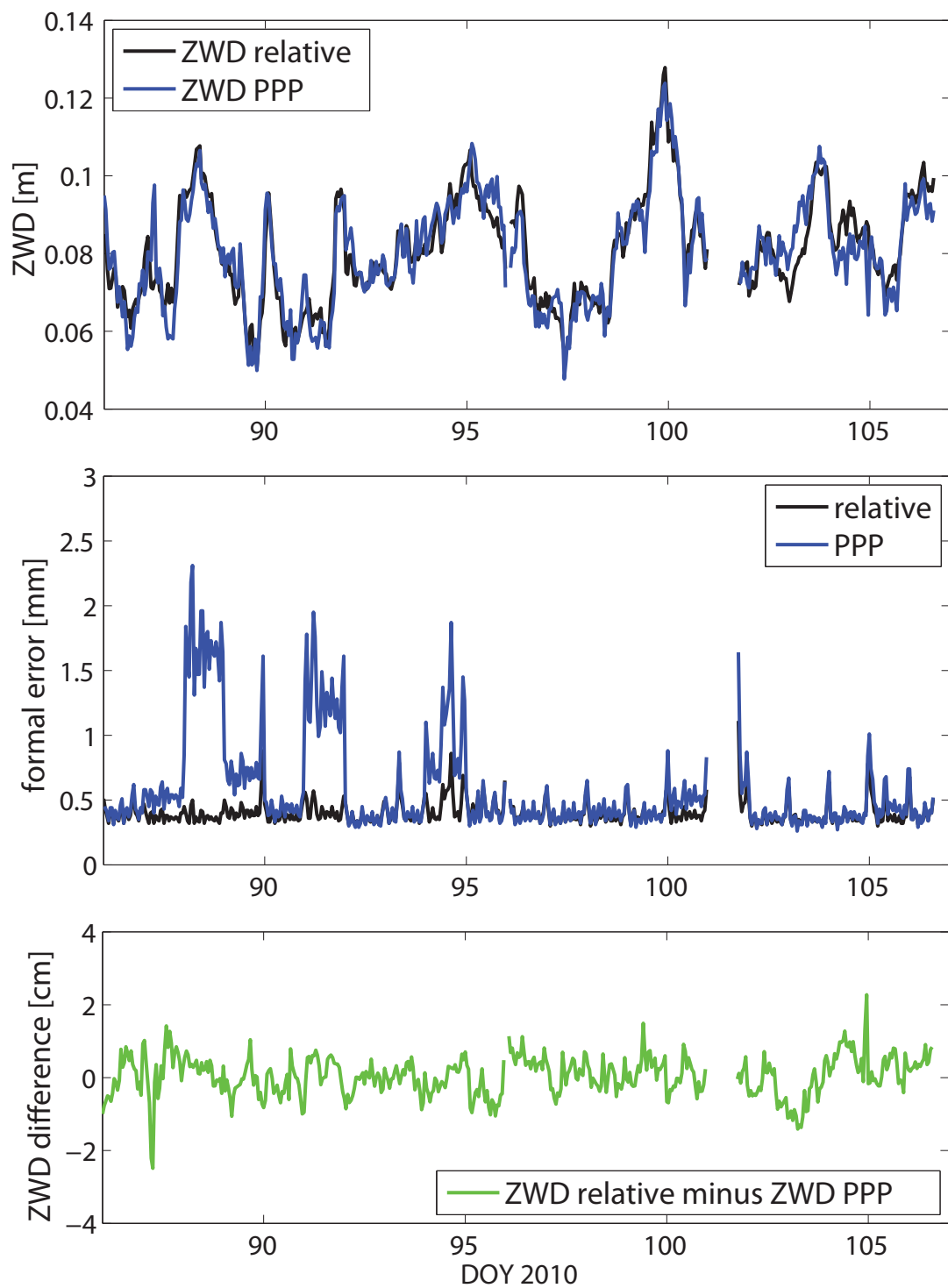


Figure C.11: Comparison of PPP and double-difference (relative) solution for station LEOB (March 27–April 16, 2010)

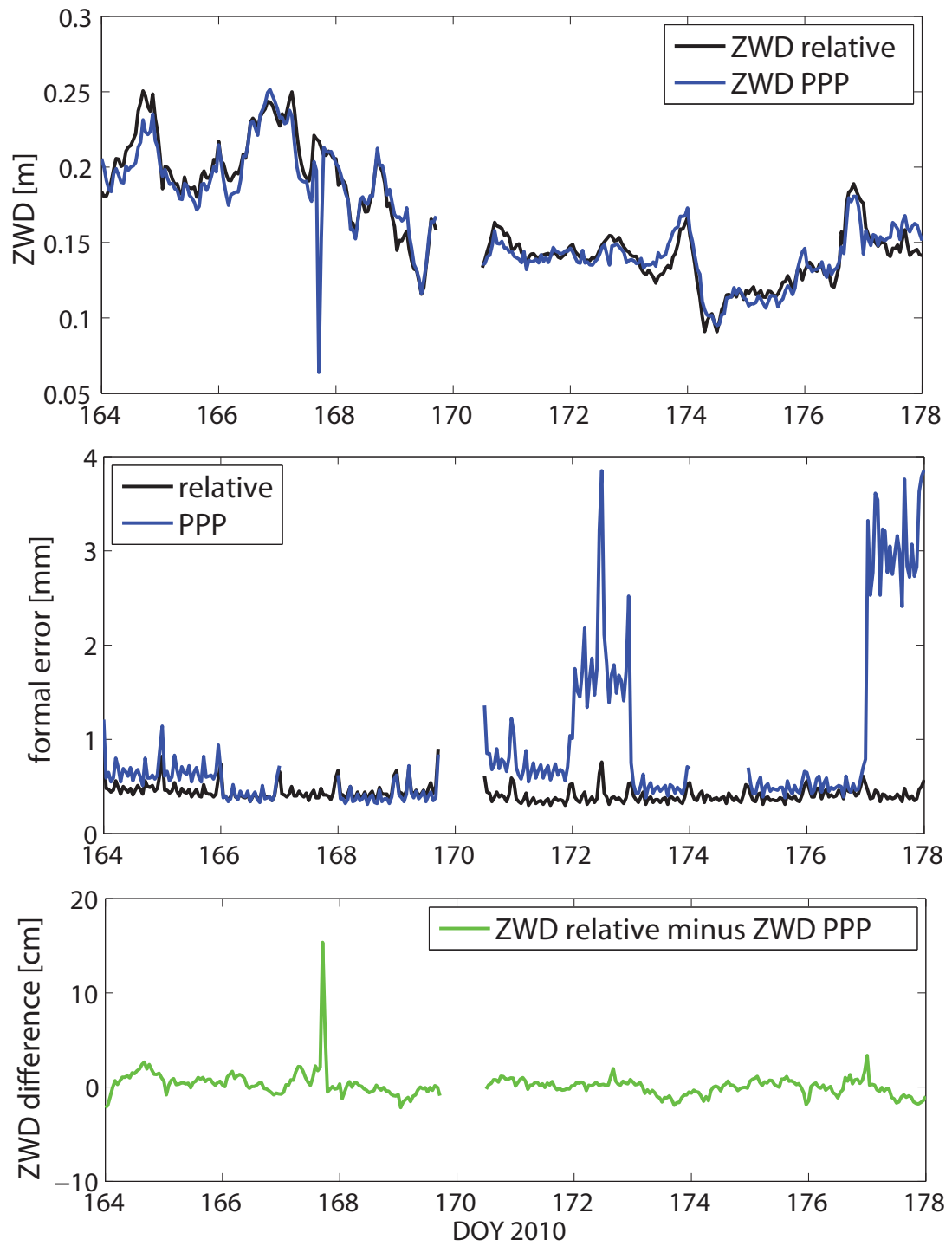


Figure C.12: Comparison of PPP and double-difference (relative) solution for station LEOB (June 13–26, 2010)

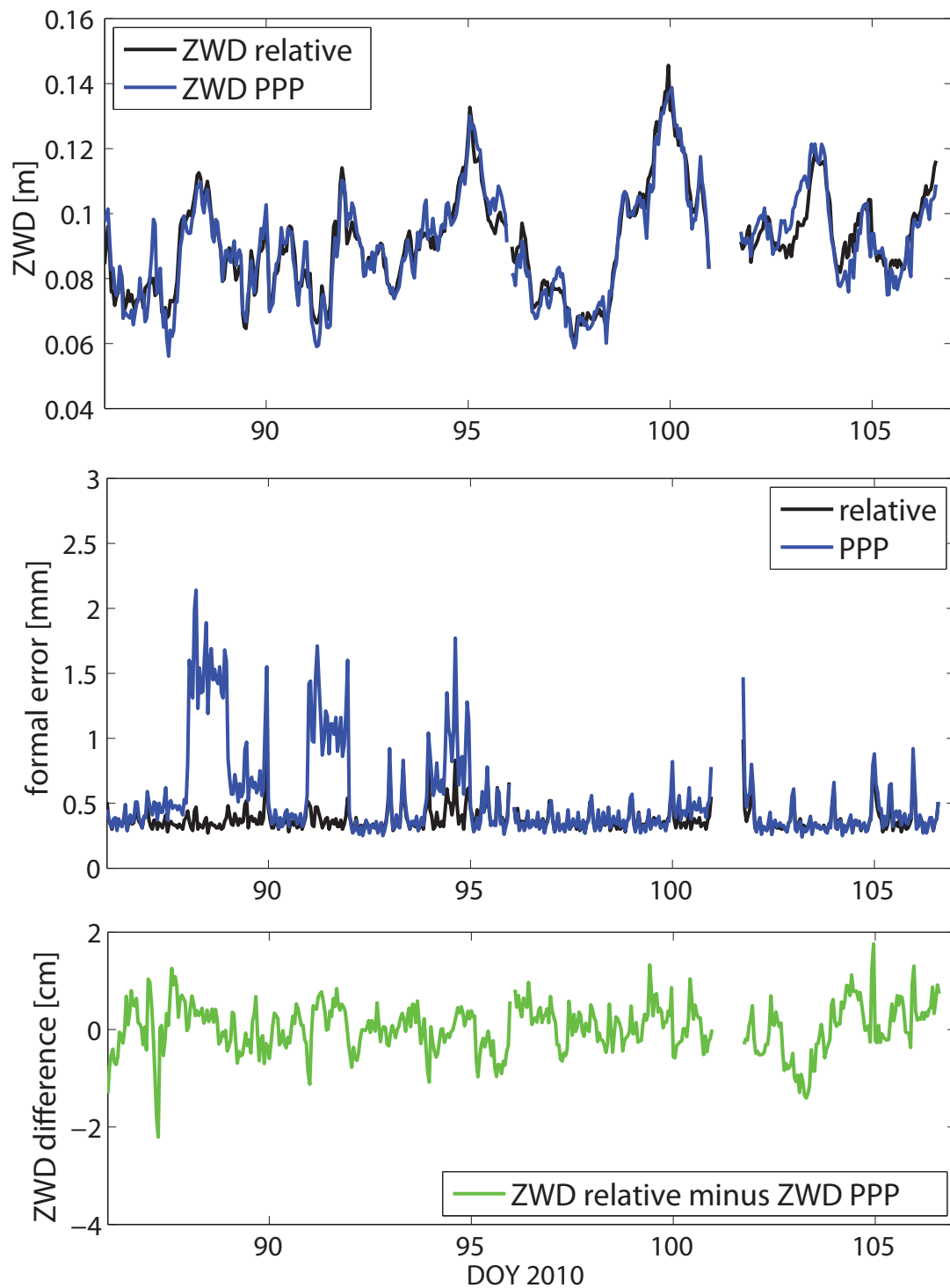


Figure C.13: Comparison of PPP and double-difference (relative) solution for station LEIB (March 27–April 16, 2010)

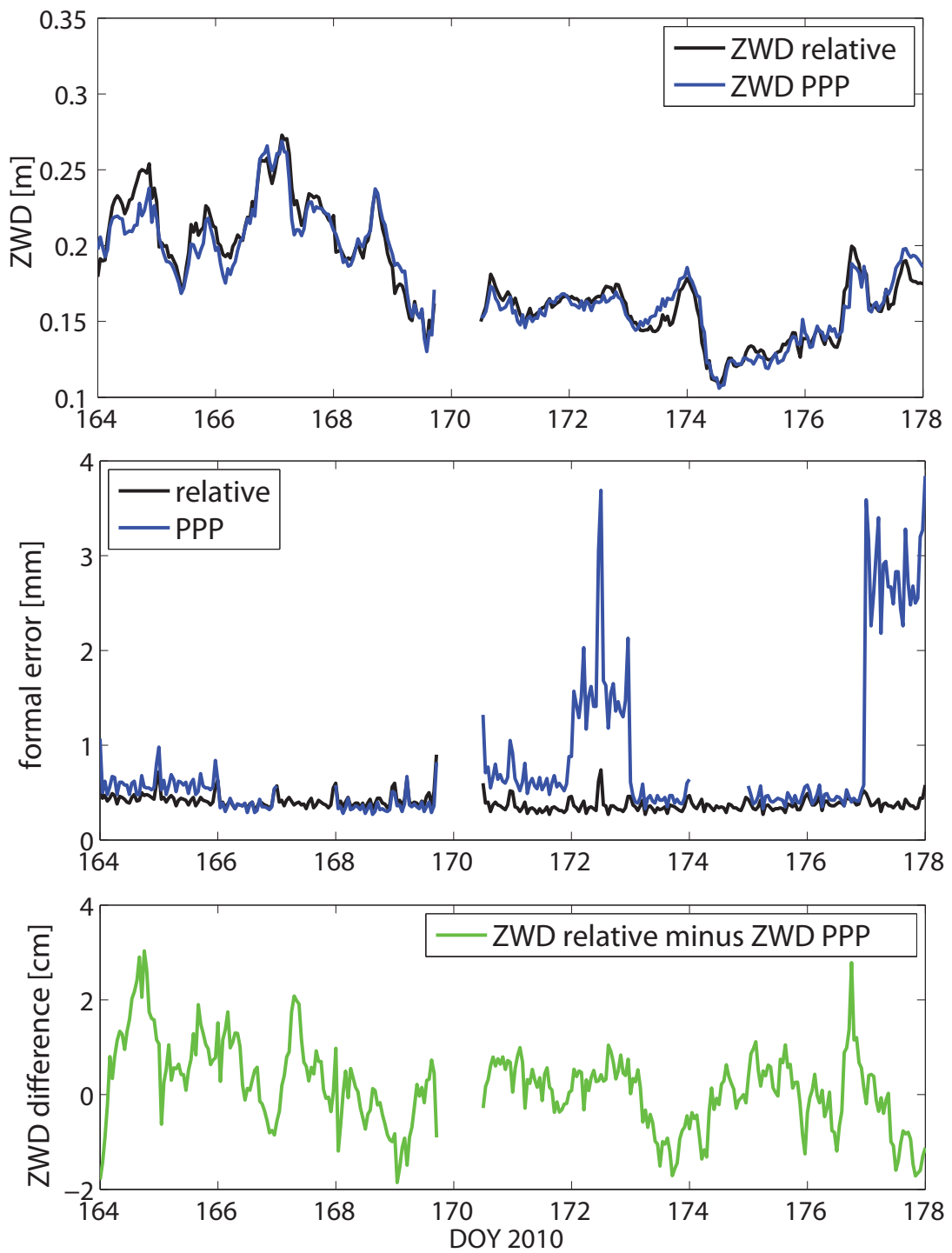


Figure C.14: Comparison of PPP and double-difference (relative) solution for station LEIB (June 13–26, 2010)

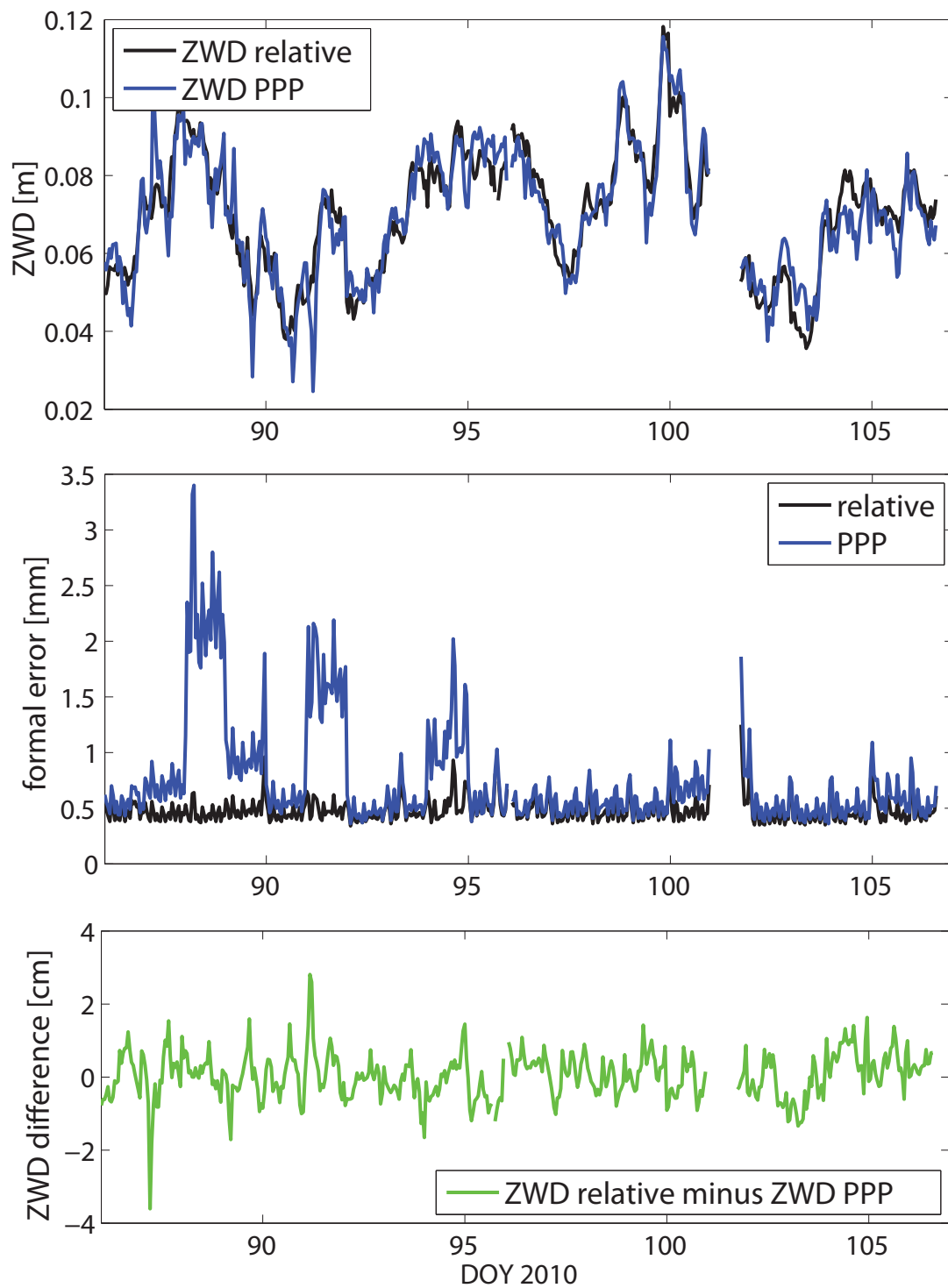


Figure C.15: Comparison of PPP and double-difference (relative) solution for station MATR (March 27–April 16, 2010)

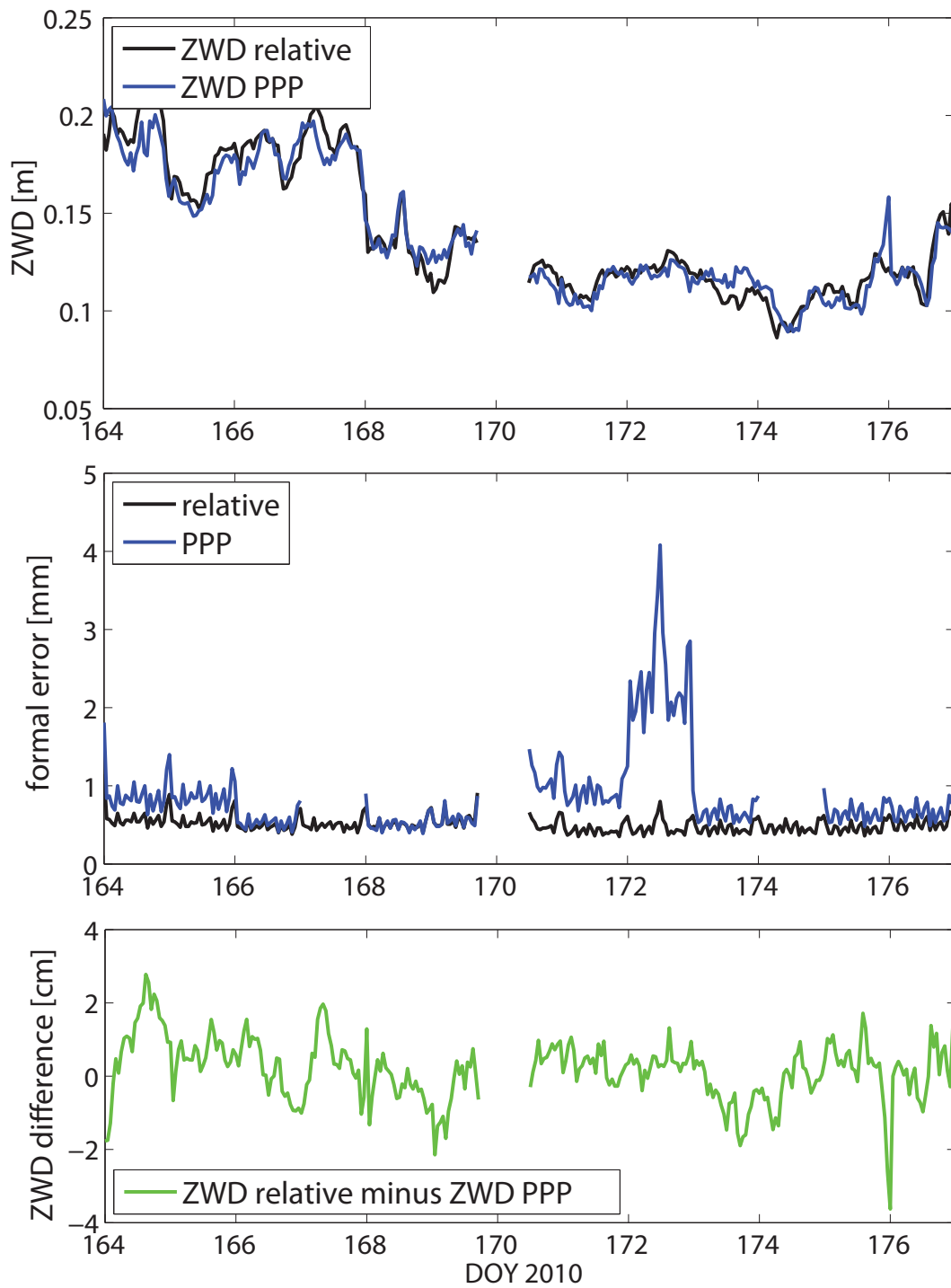


Figure C.16: Comparison of PPP and double-difference (relative) solution for station MATR (June 13–26, 2010)

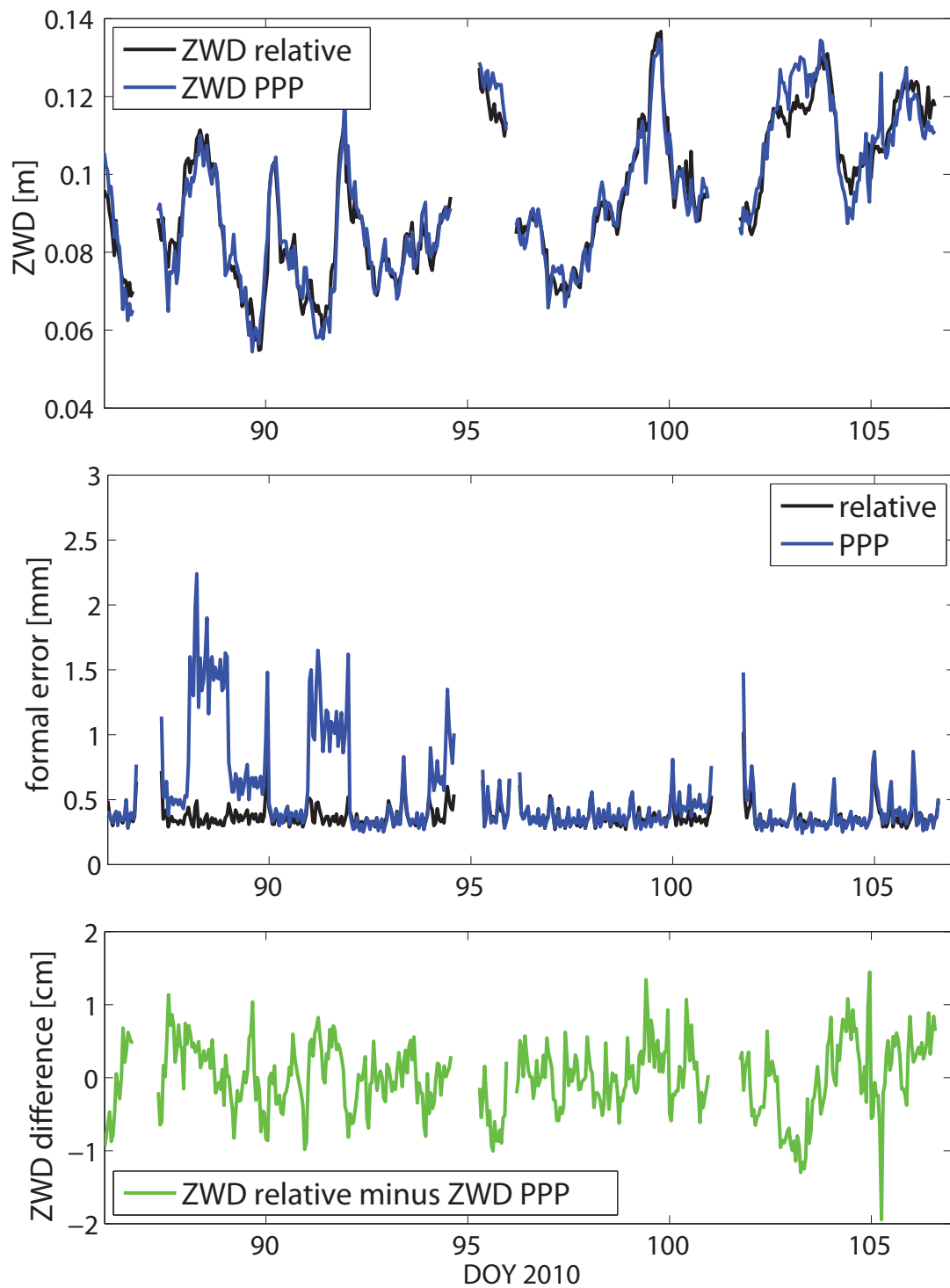


Figure C.17: Comparison of PPP and double-difference (relative) solution for station NEUS (March 27–April 16, 2010)

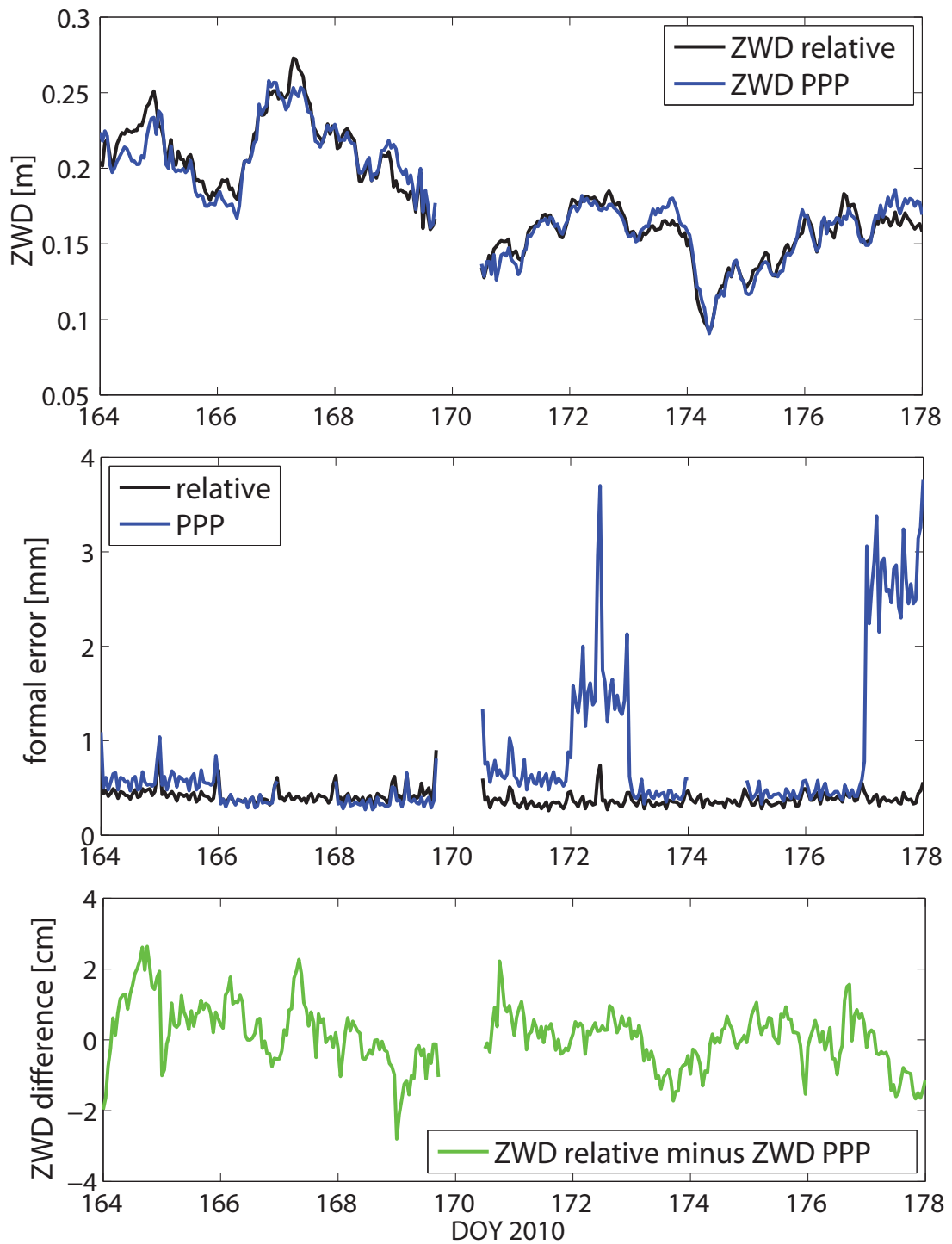


Figure C.18: Comparison of PPP and double-difference (relative) solution for station NEUS (June 13–26, 2010)

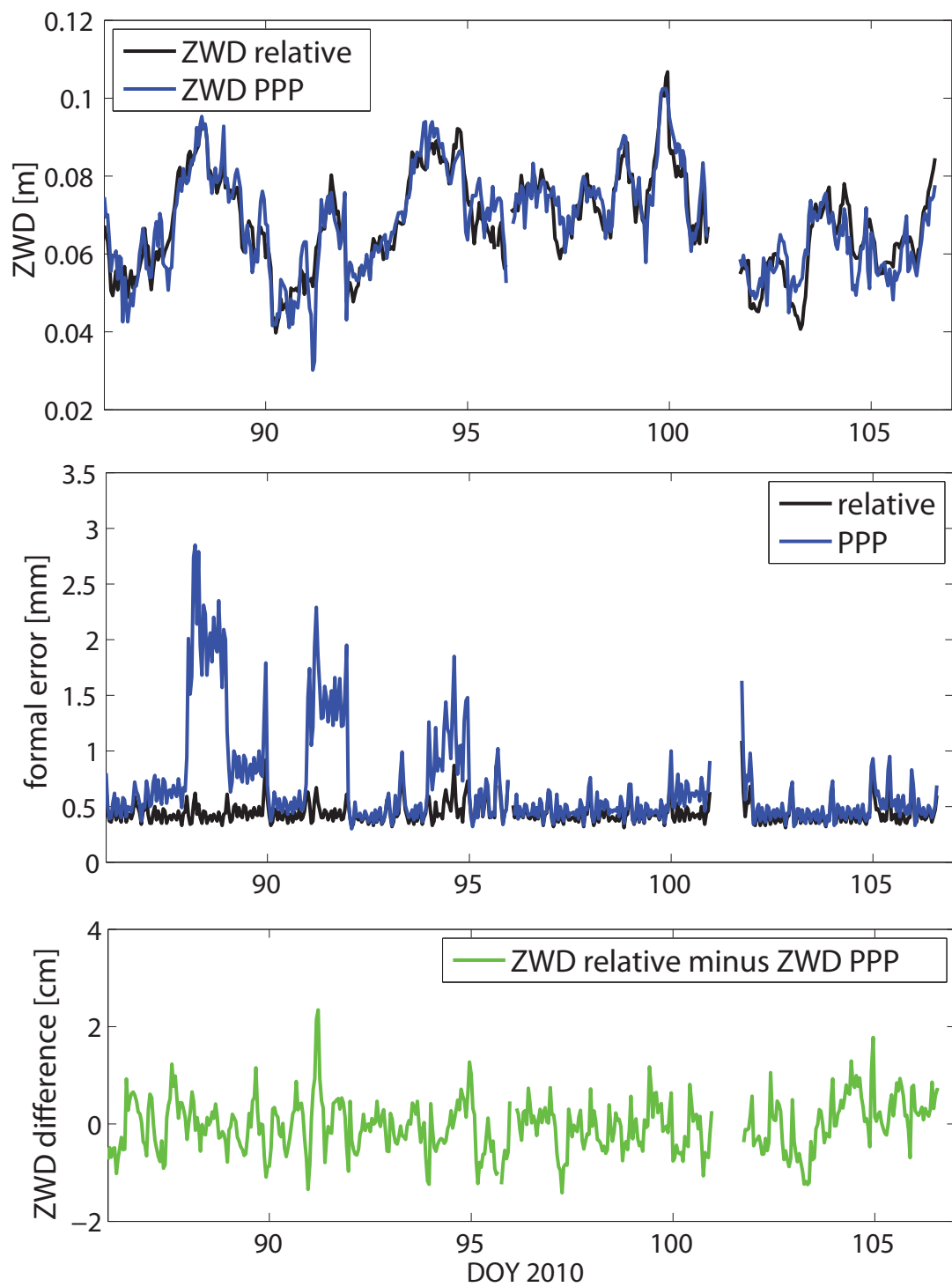


Figure C.19: Comparison of PPP and double-difference (relative) solution for station OCHS (March 27–April 16, 2010)

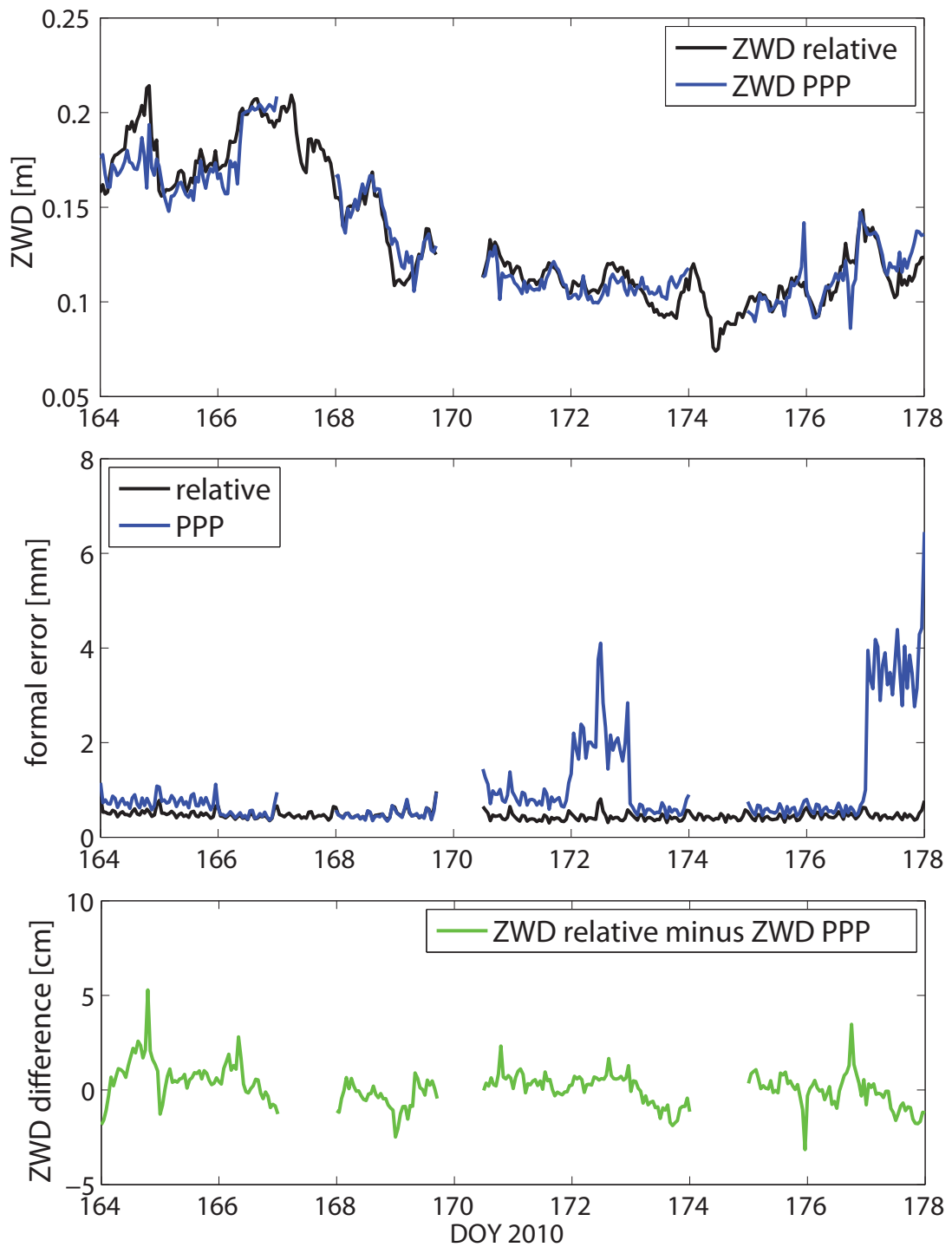


Figure C.20: Comparison of PPP and double-difference (relative) solution for station OCHS (June 13–26, 2010)

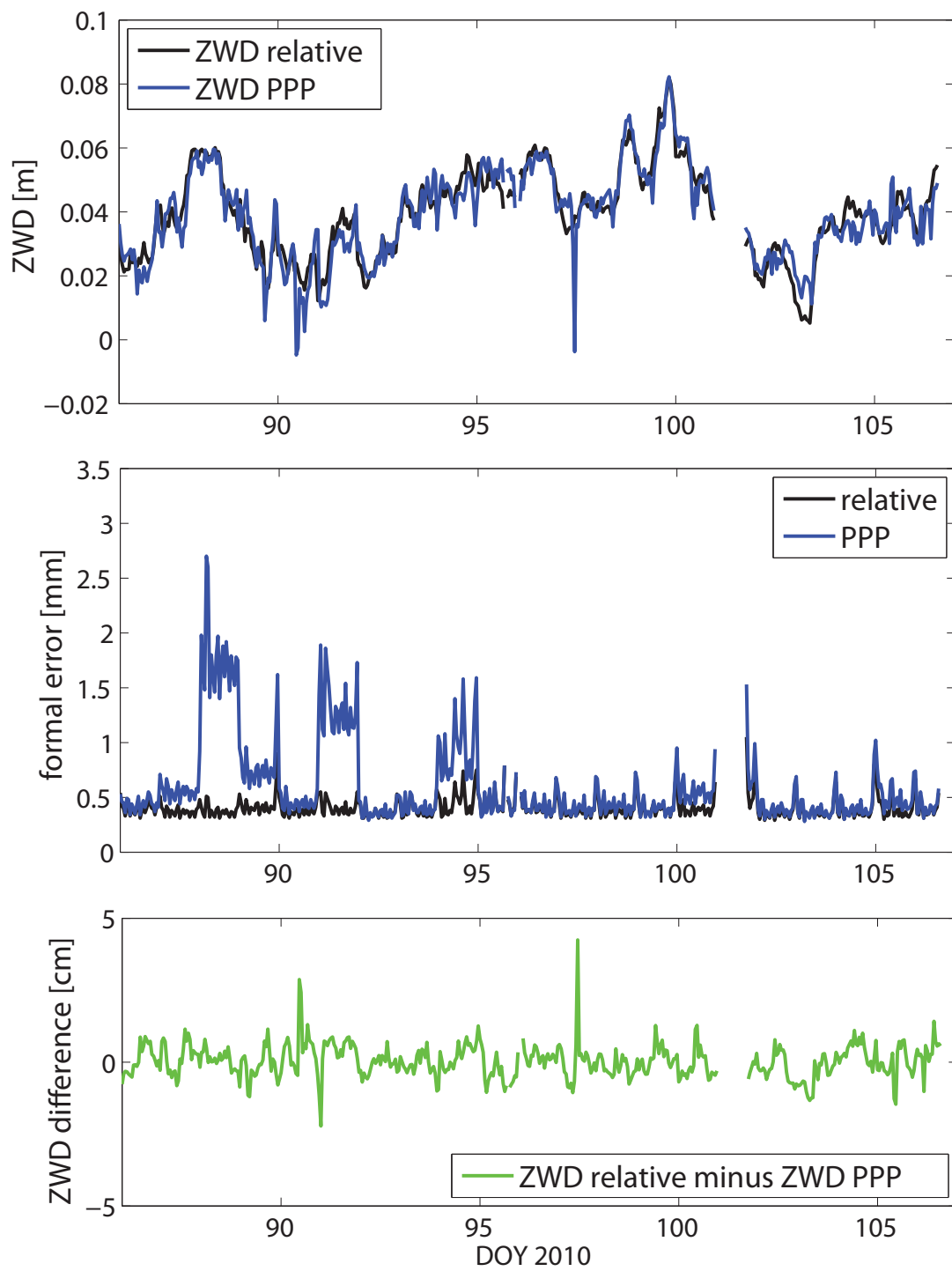


Figure C.21: Comparison of PPP and double-difference (relative) solution for station ROET (March 27–April 16, 2010)

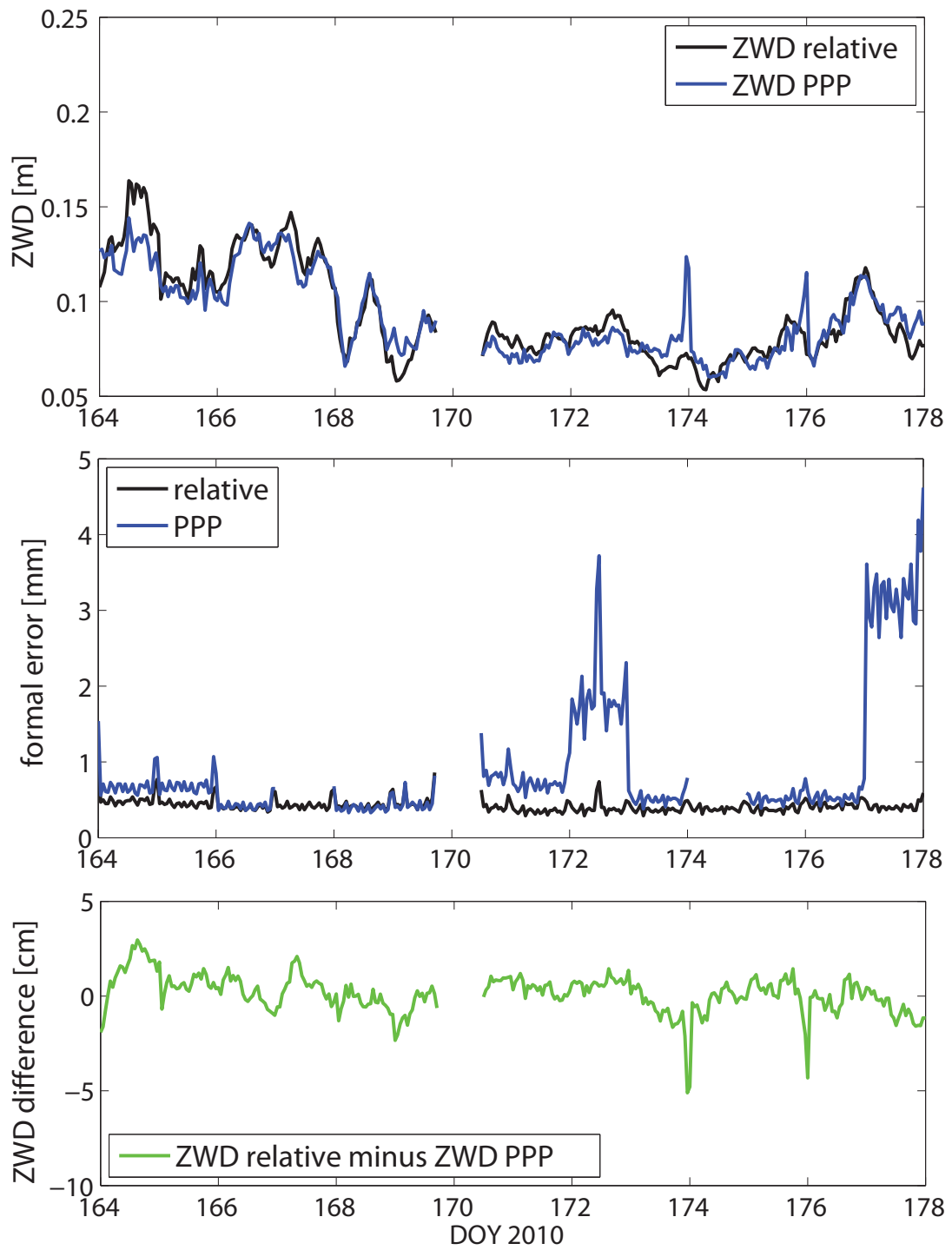


Figure C.22: Comparison of PPP and double-difference (relative) solution for station ROET (June 13–26, 2010)

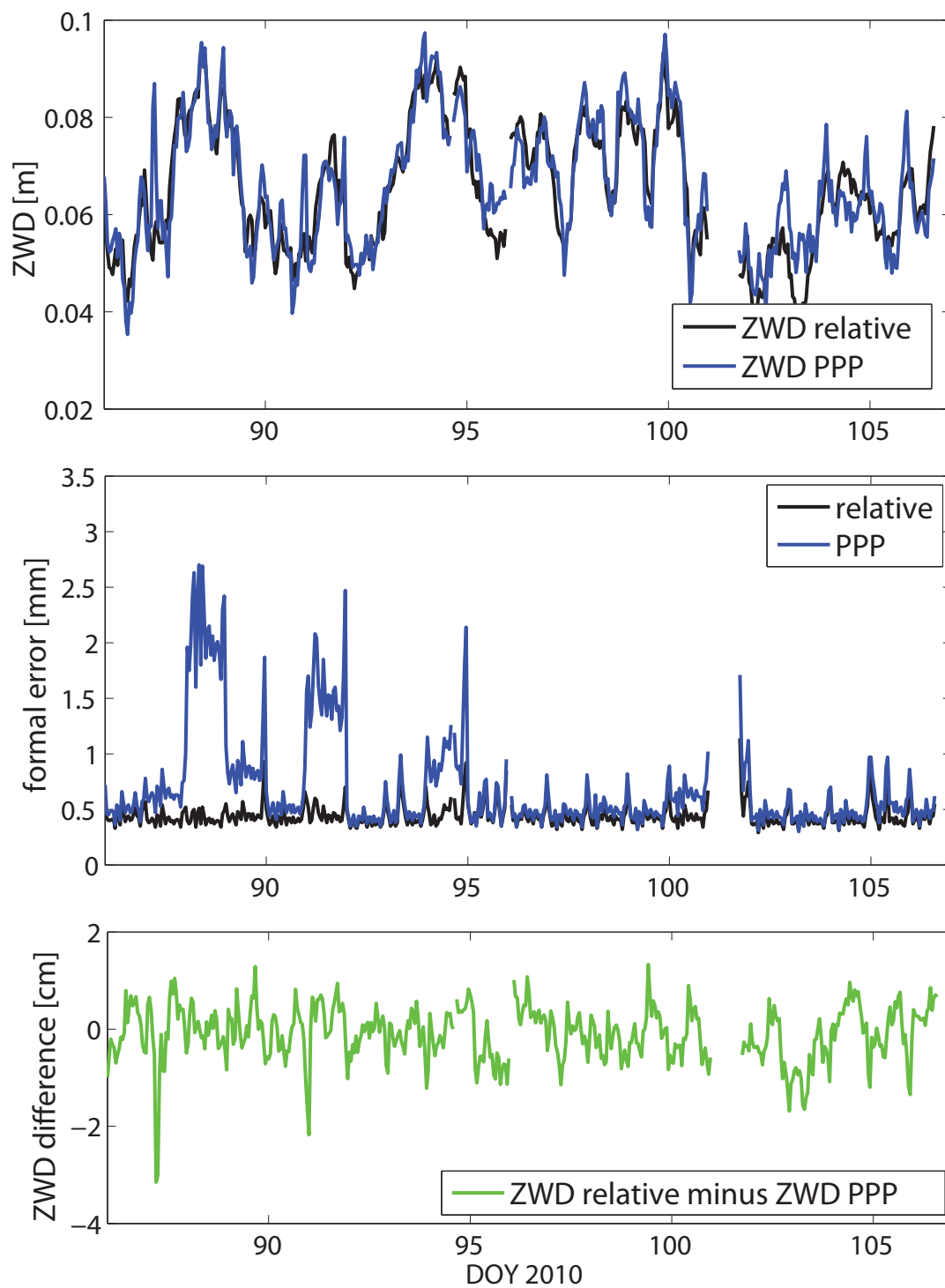


Figure C.23: Comparison of PPP and double-difference (relative) solution for station SILL (March 27–April 16, 2010)

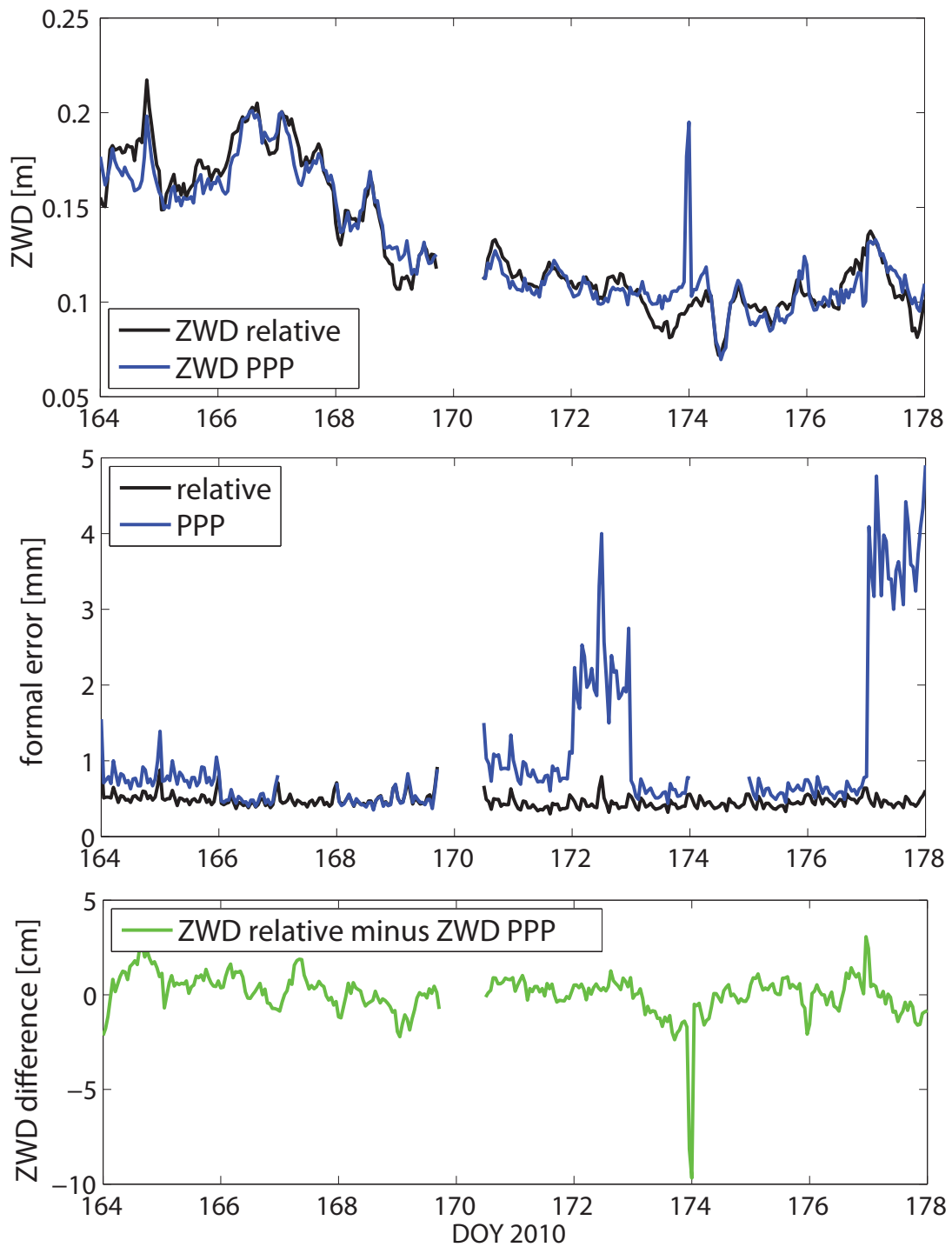


Figure C.24: Comparison of PPP and double-difference (relative) solution for station SILL (June 13–26, 2010)

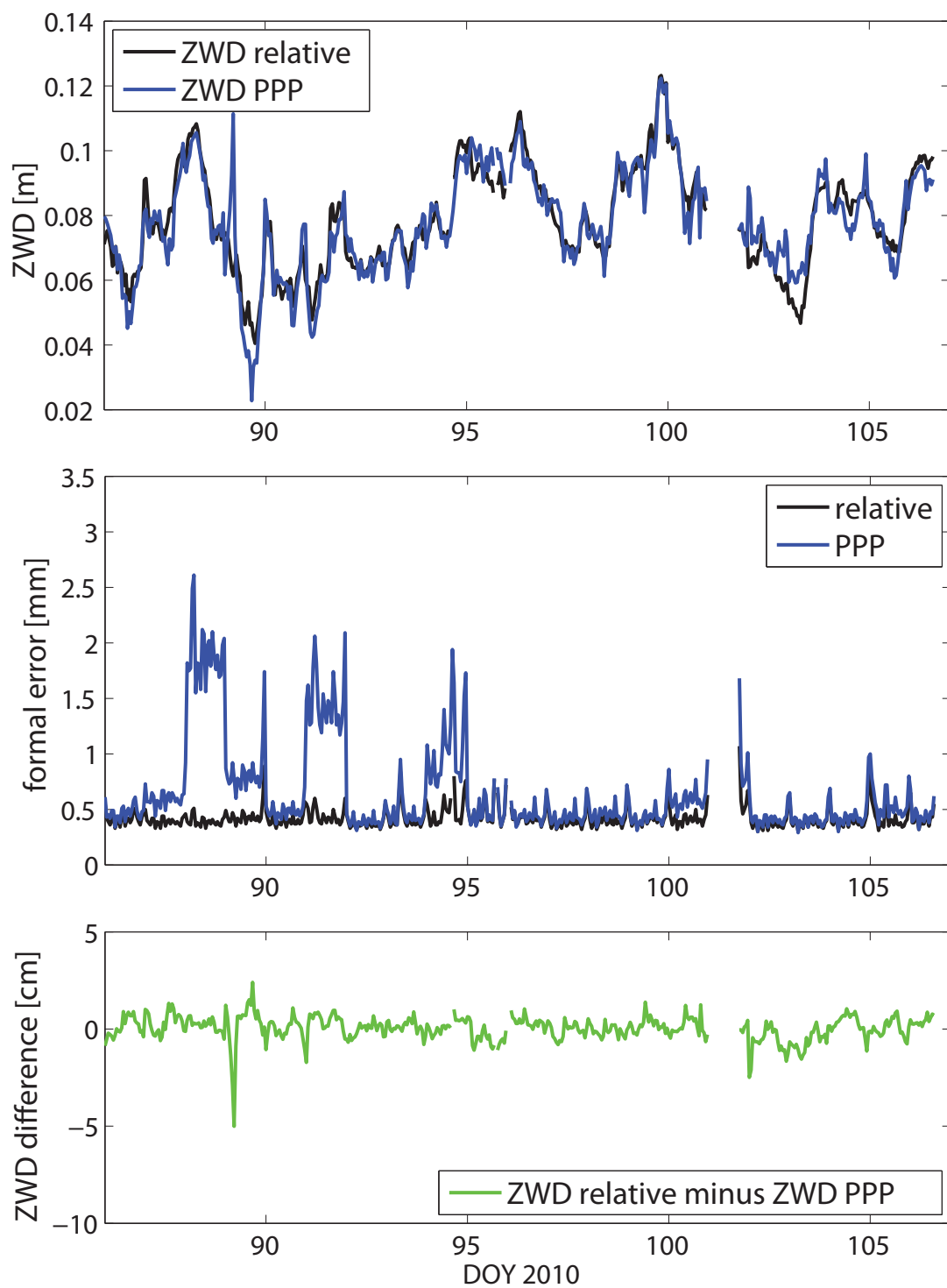


Figure C.25: Comparison of PPP and double-difference (relative) solution for station SHLA (March 27–April 16, 2010)

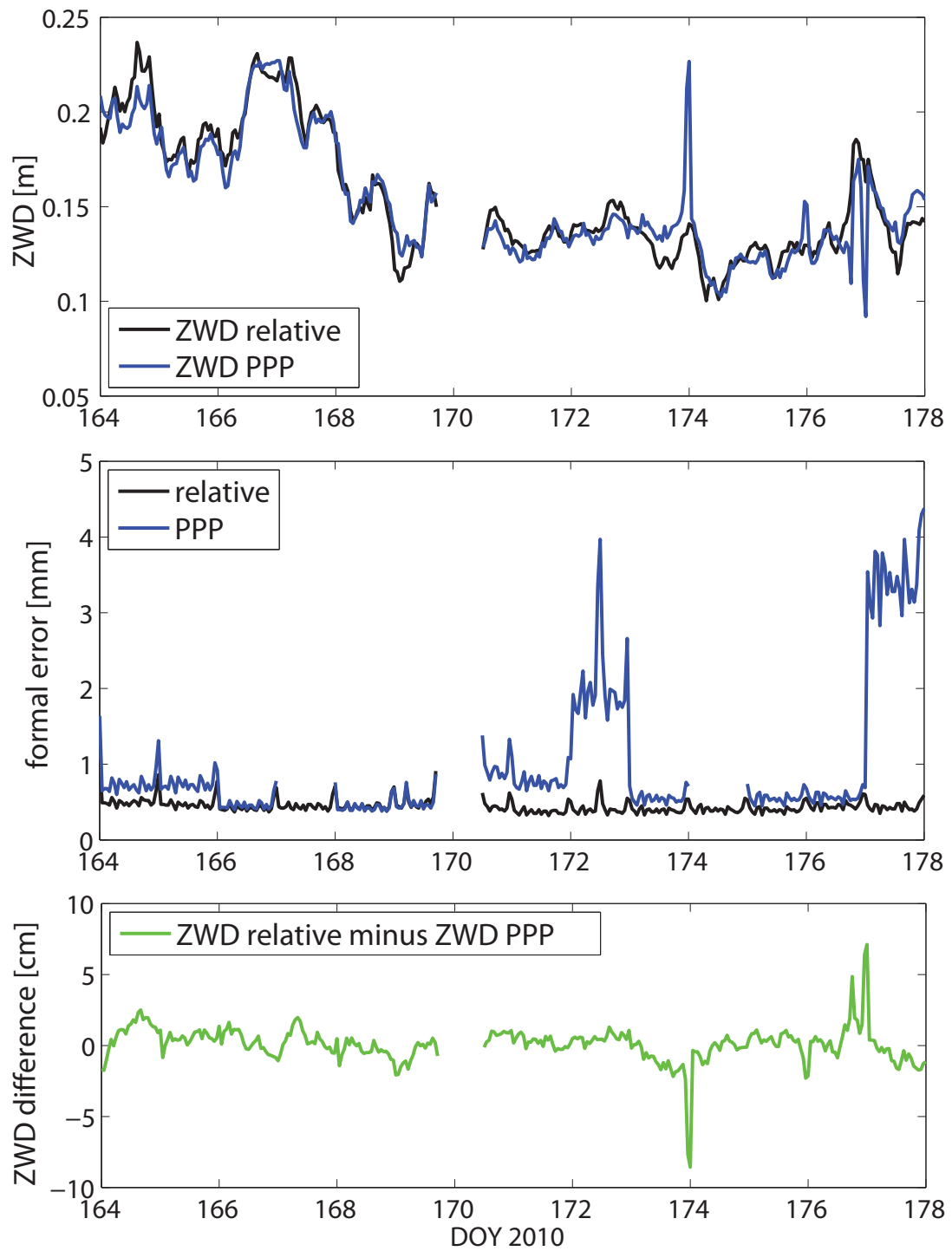


Figure C.26: Comparison of PPP and double-difference (relative) solution for station SHLA (June 13–26, 2010)

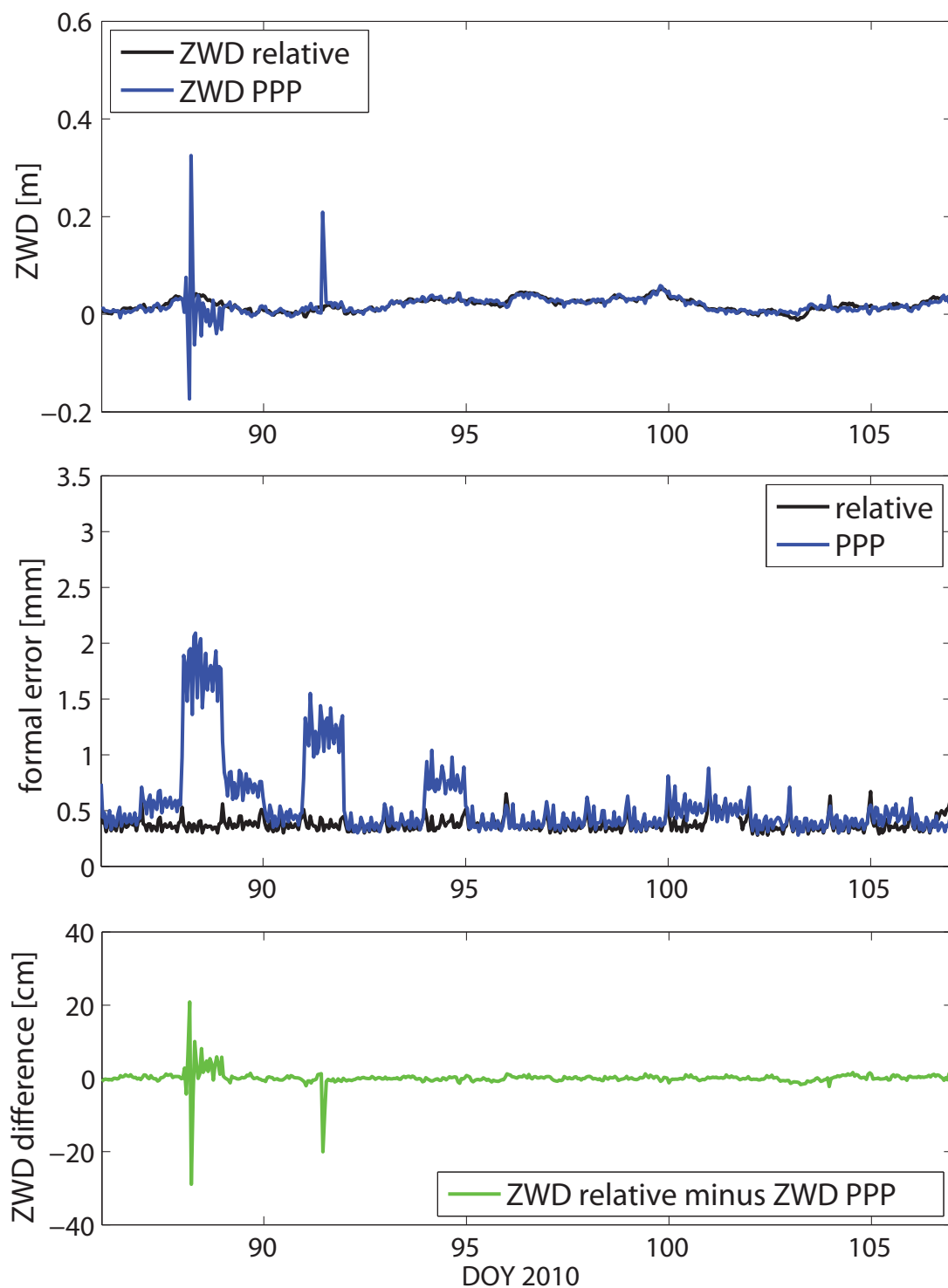


Figure C.27: Comparison of PPP and double-difference (relative) solution for station SONN (March 27–April 16, 2010)

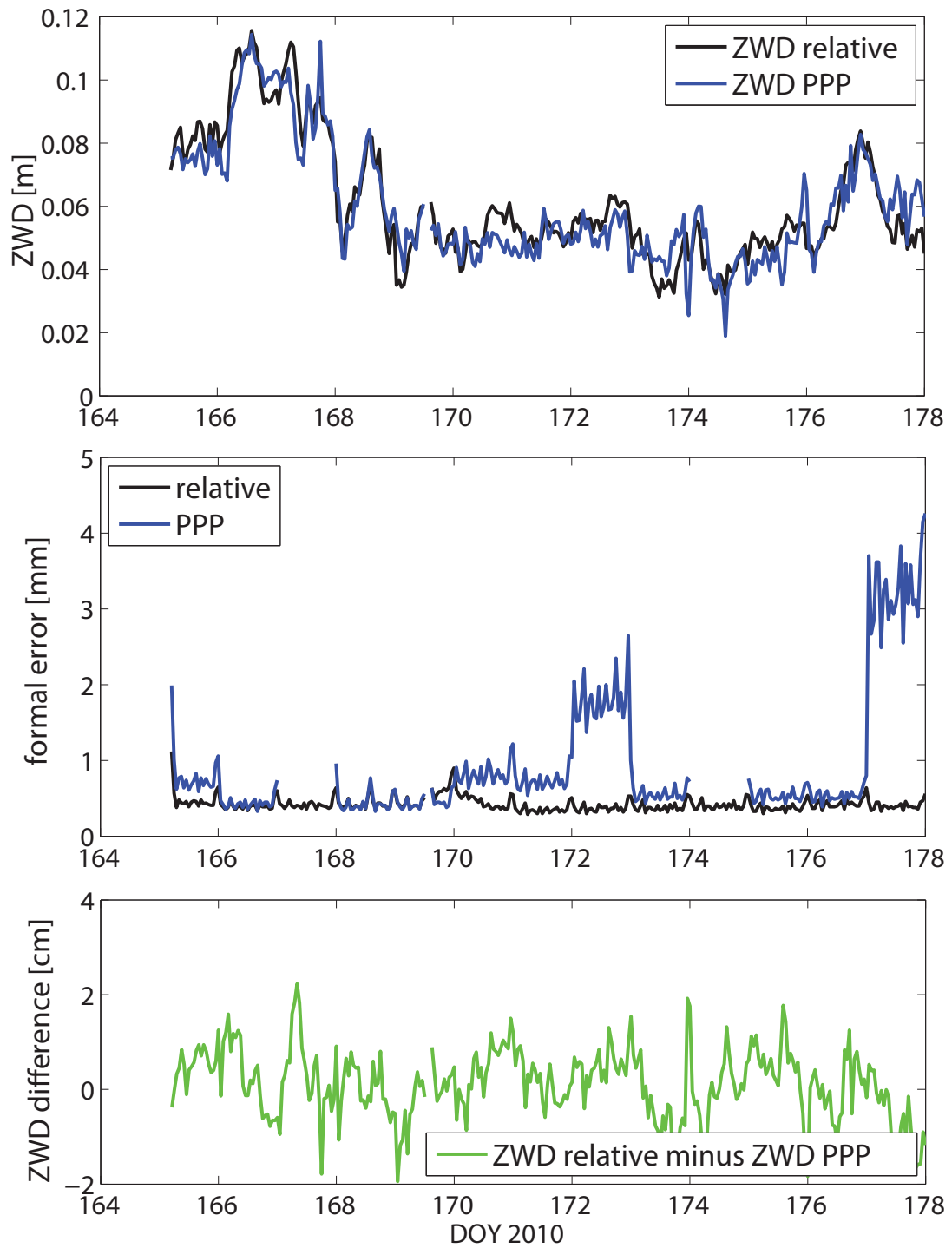


Figure C.28: Comparison of PPP and double-difference (relative) solution for station SONN (June 13–26, 2010)

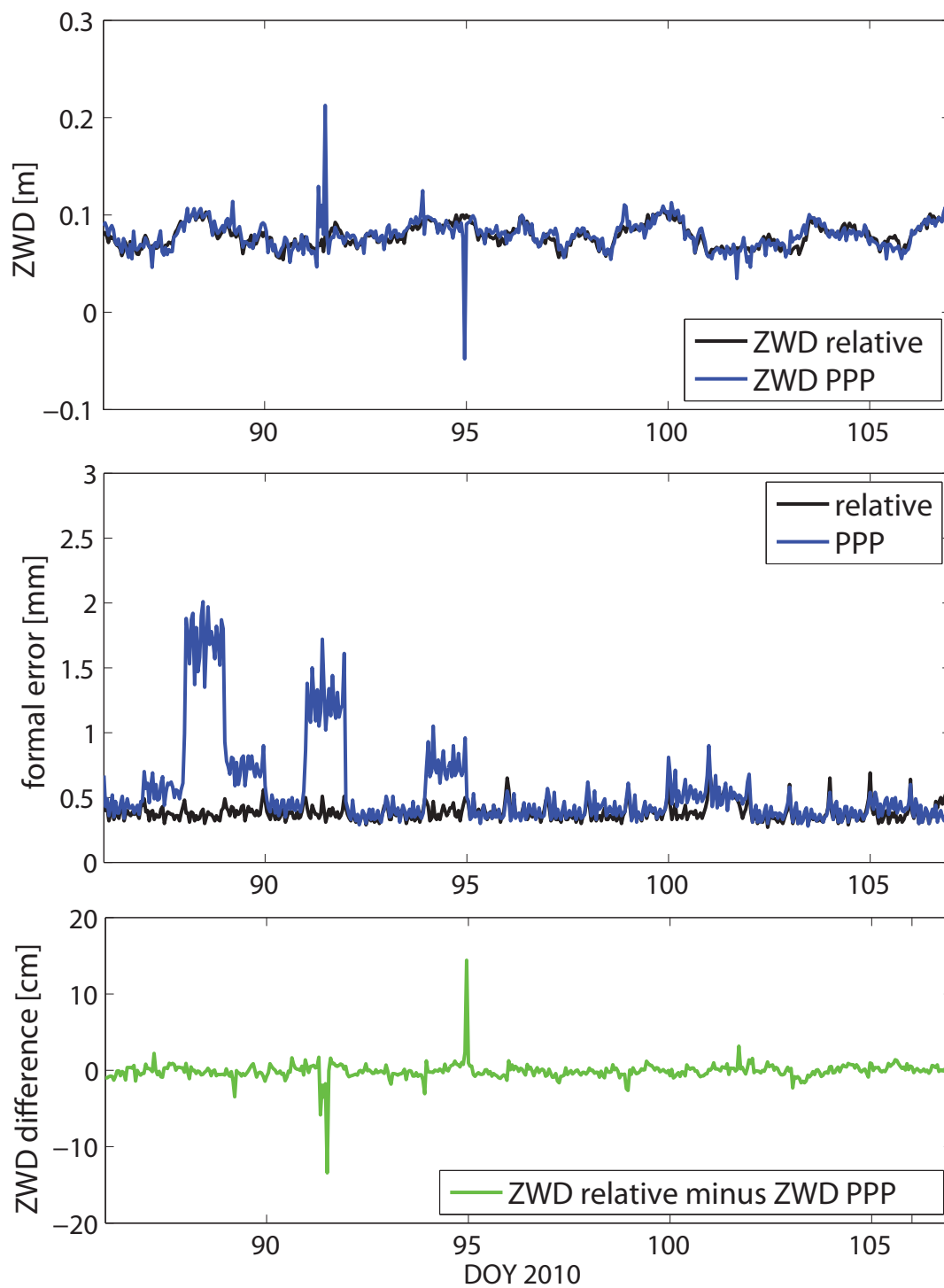


Figure C.29: Comparison of PPP and double-difference (relative) solution for station TREI (March 27–April 16, 2010)

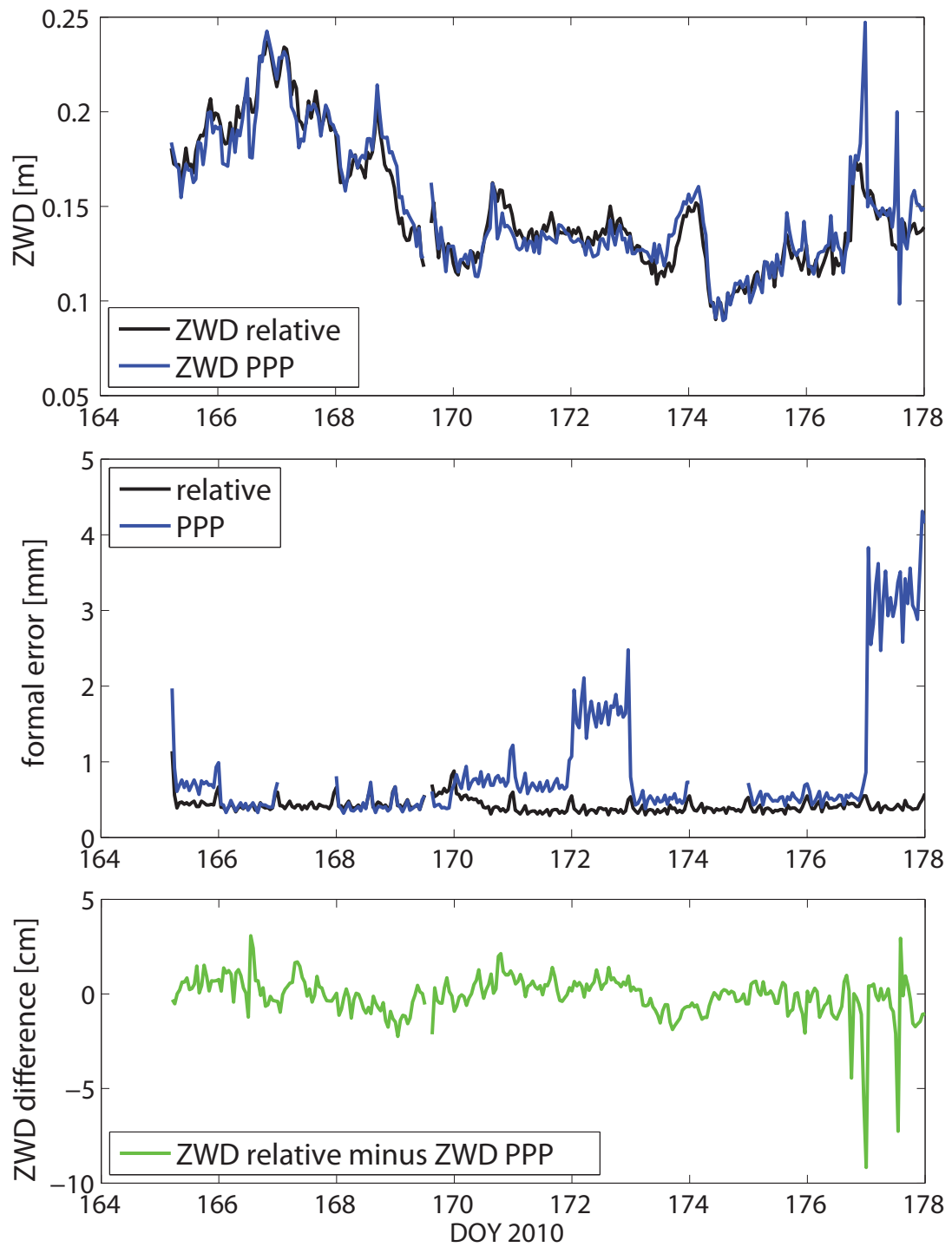


Figure C.30: Comparison of PPP and double-difference (relative) solution for station TREI (June 13–26, 2010)

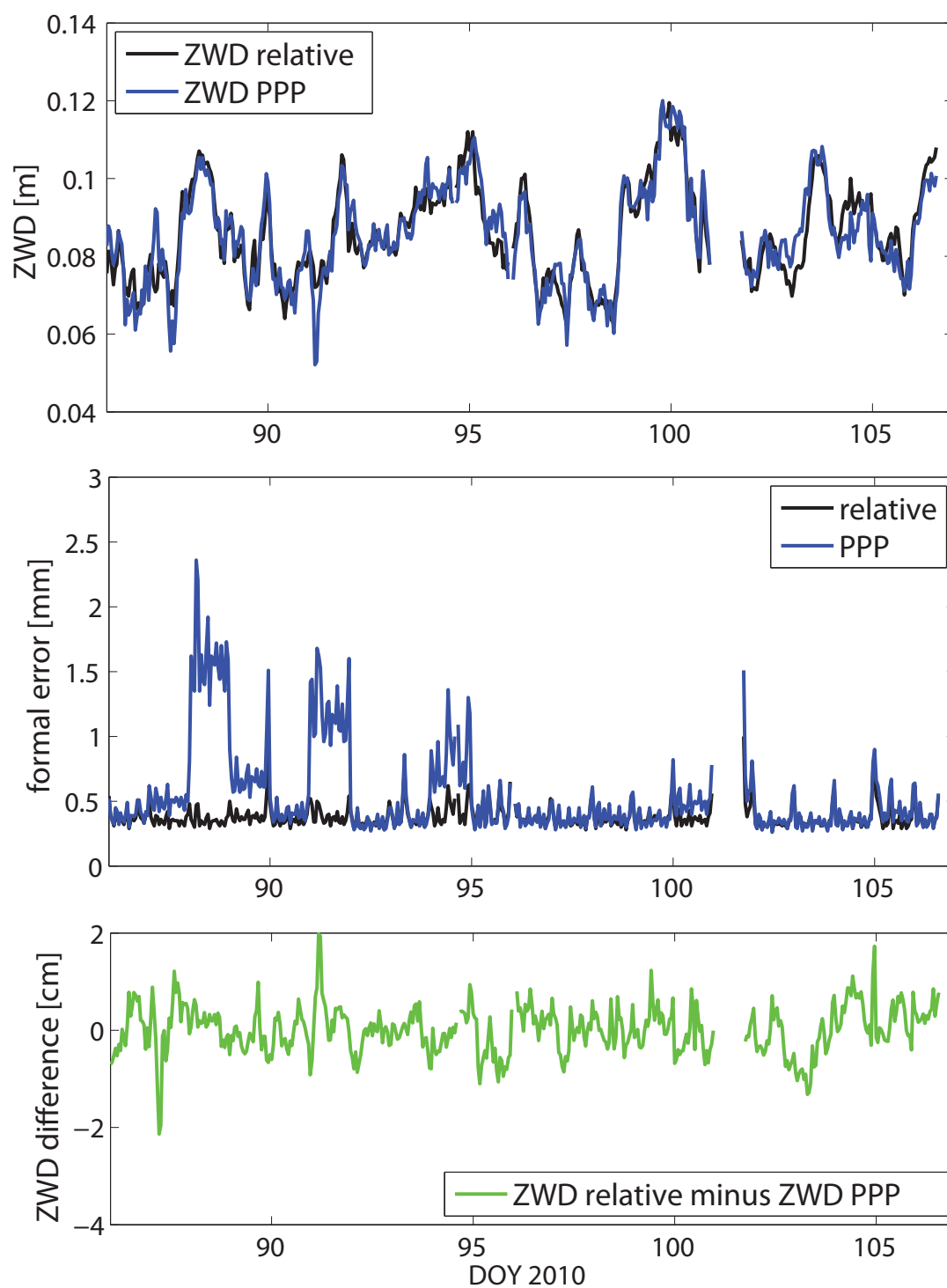


Figure C.31: Comparison of PPP and double-difference (relative) solution for station WOBG (March 27–April 16, 2010)

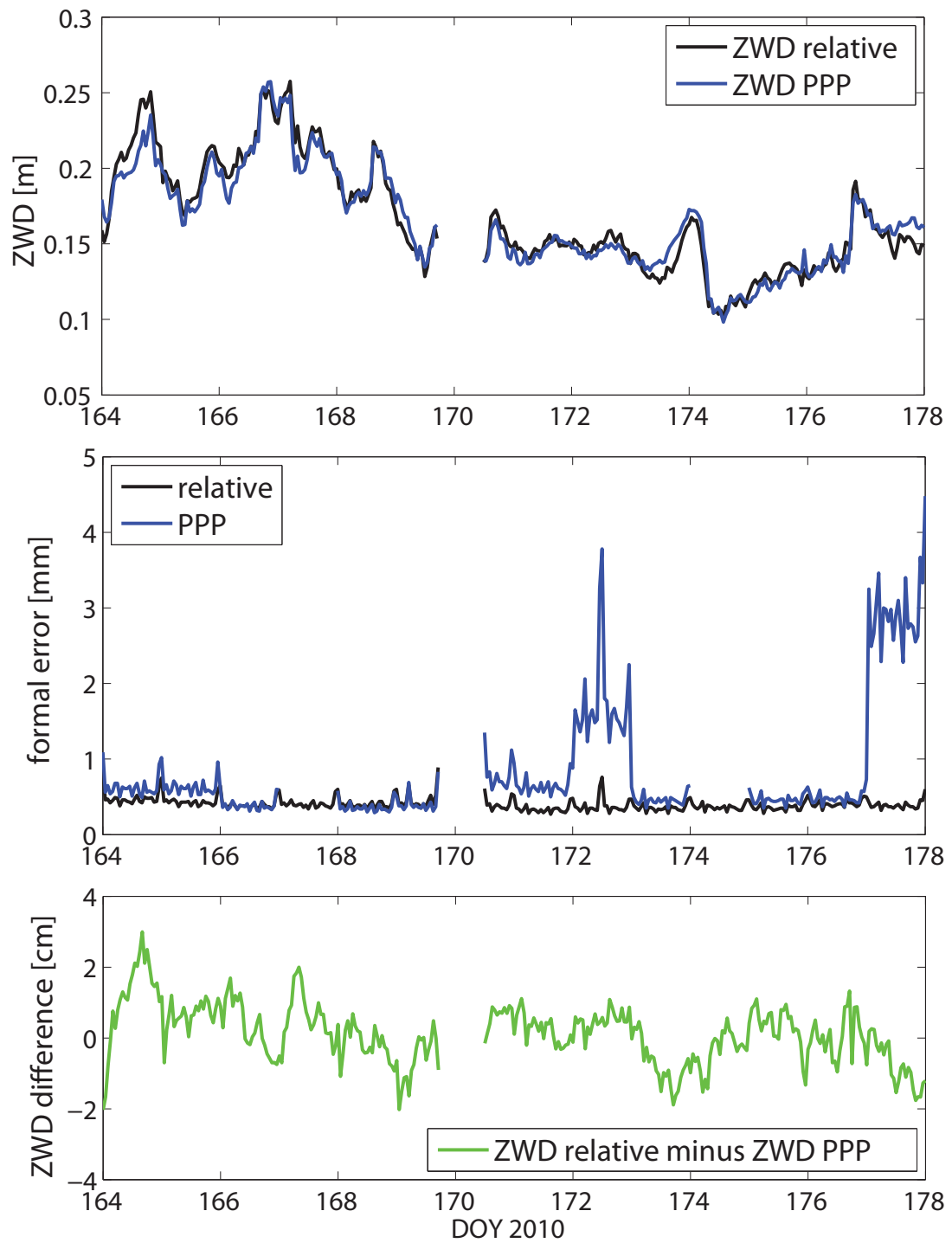


Figure C.32: Comparison of PPP and double-difference (relative) solution for station WOBG (June 13–26, 2010)

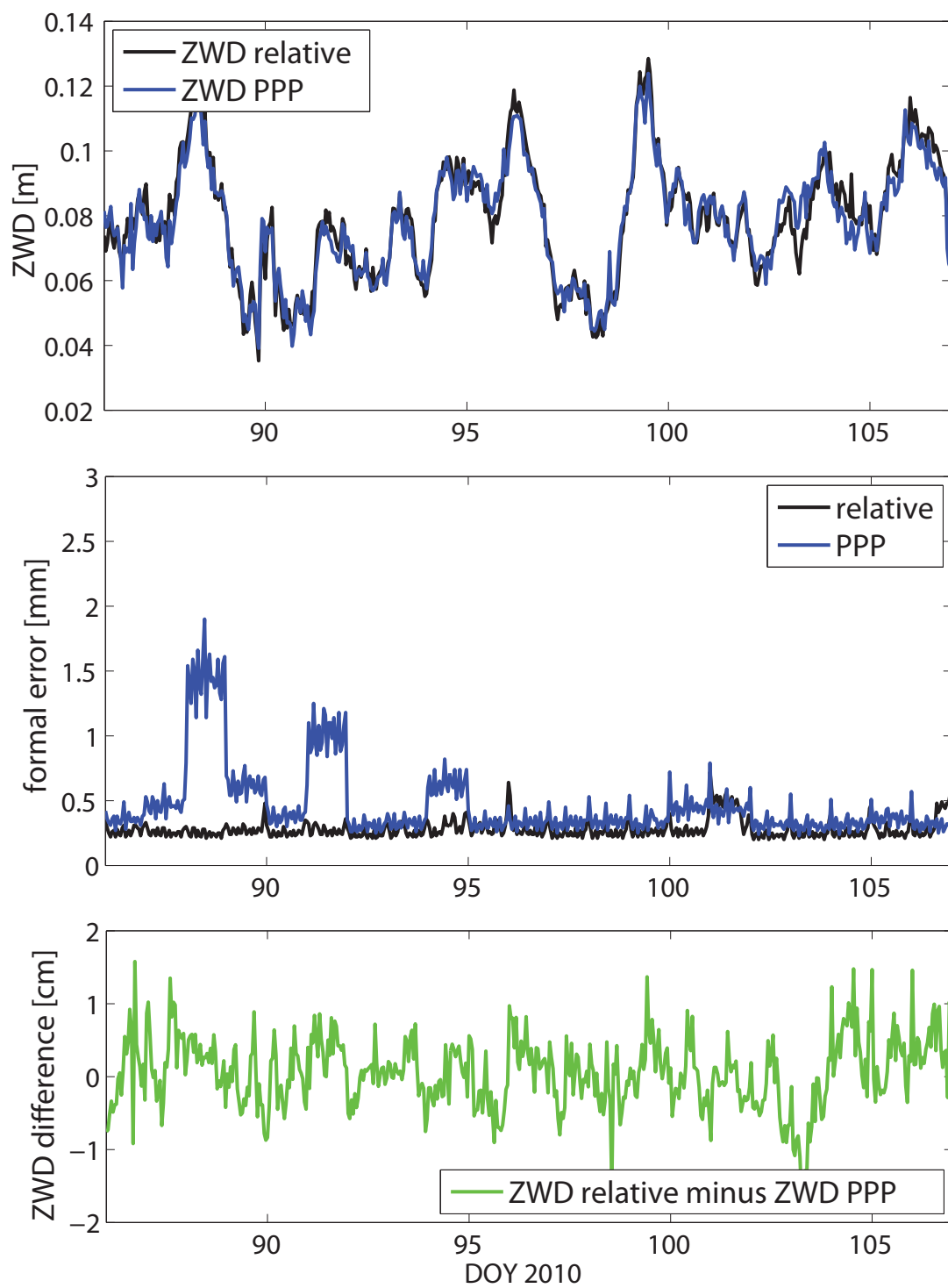


Figure C.33: Comparison of PPP and double-difference (relative) solution for station WTZR (March 27–April 16, 2010)

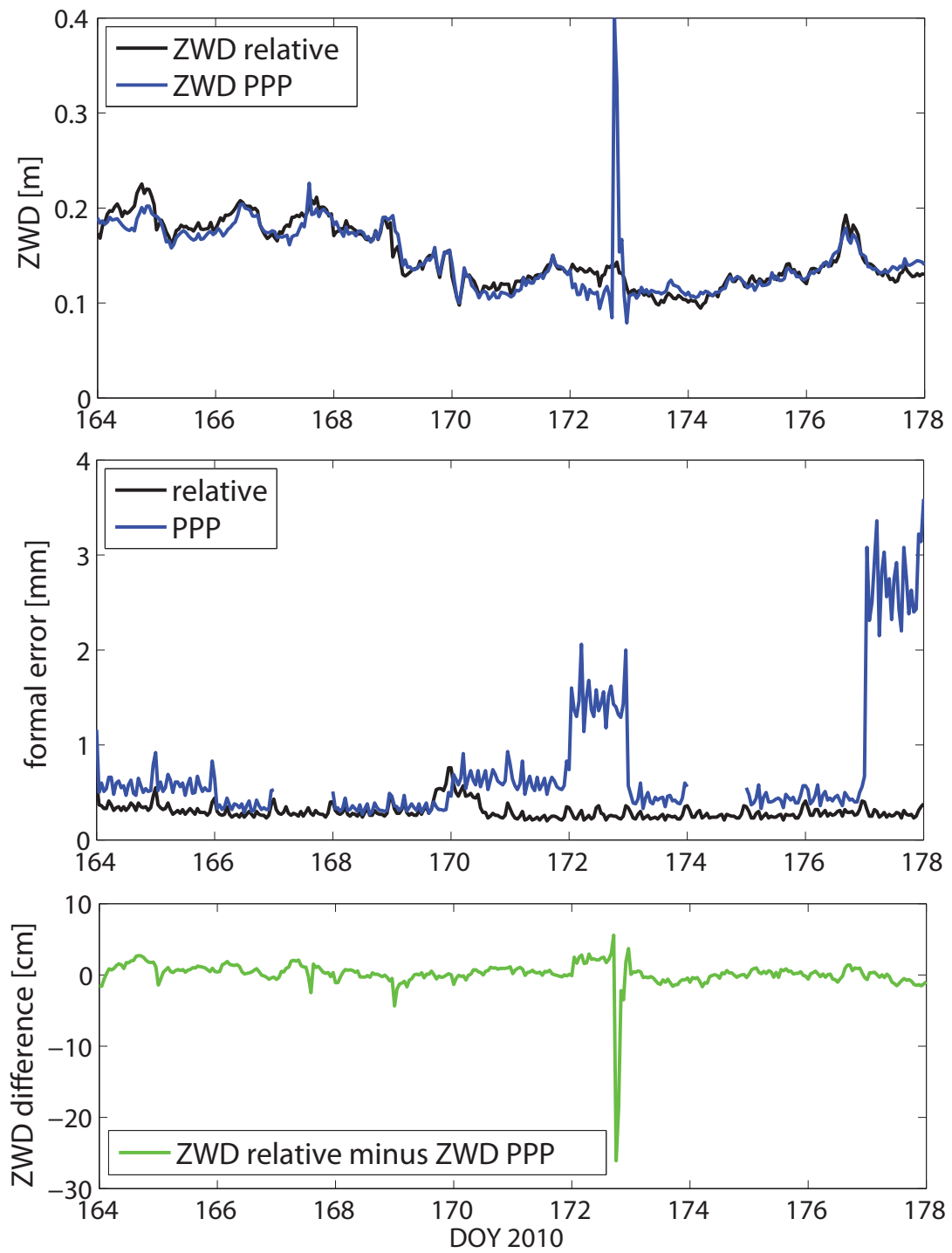


Figure C.34: Comparison of PPP and double-difference (relative) solution for station WTZR (June 13–26, 2010)

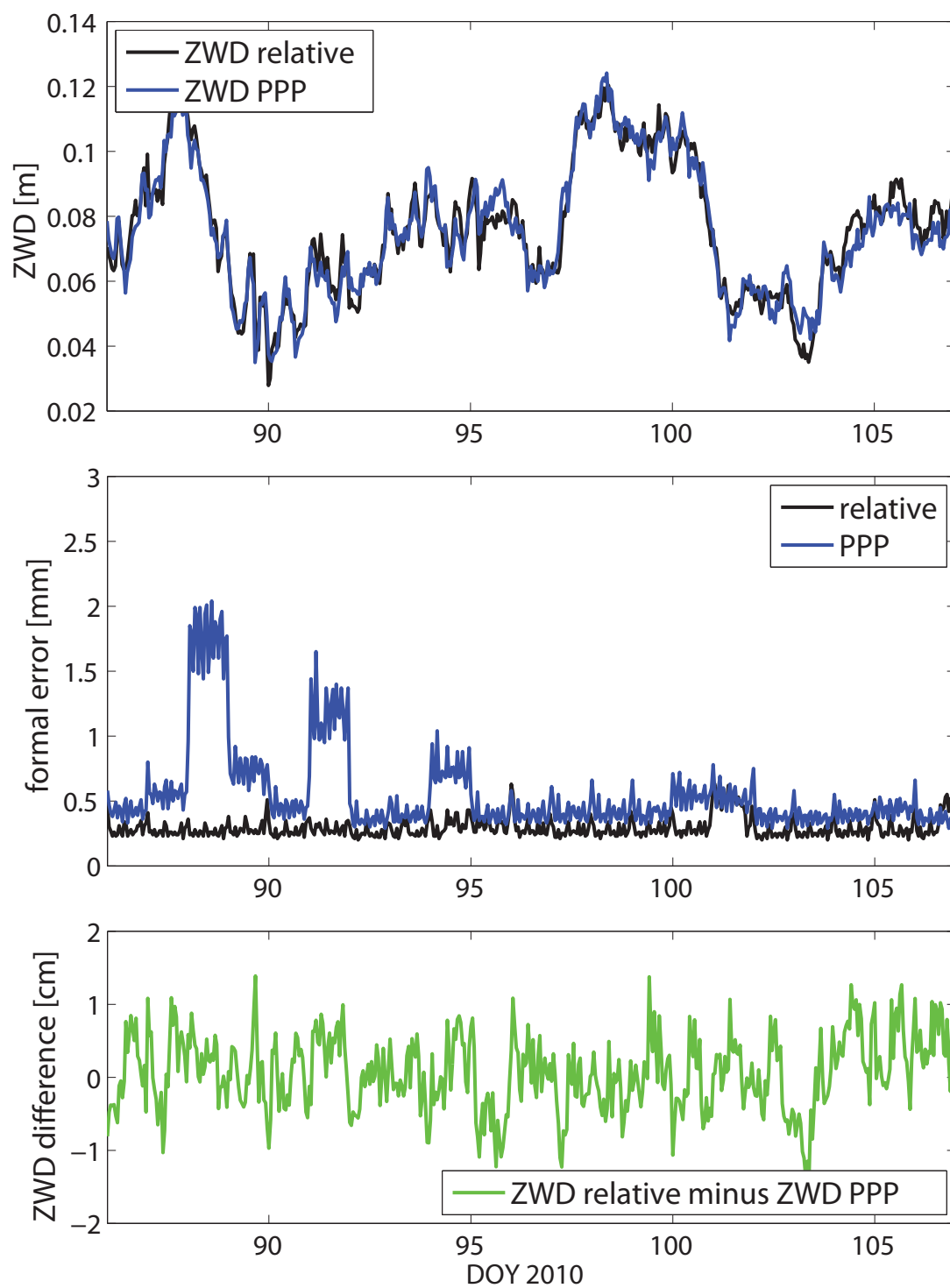


Figure C.35: Comparison of PPP and double-difference (relative) solution for station ZIMM (March 27–April 16, 2010)

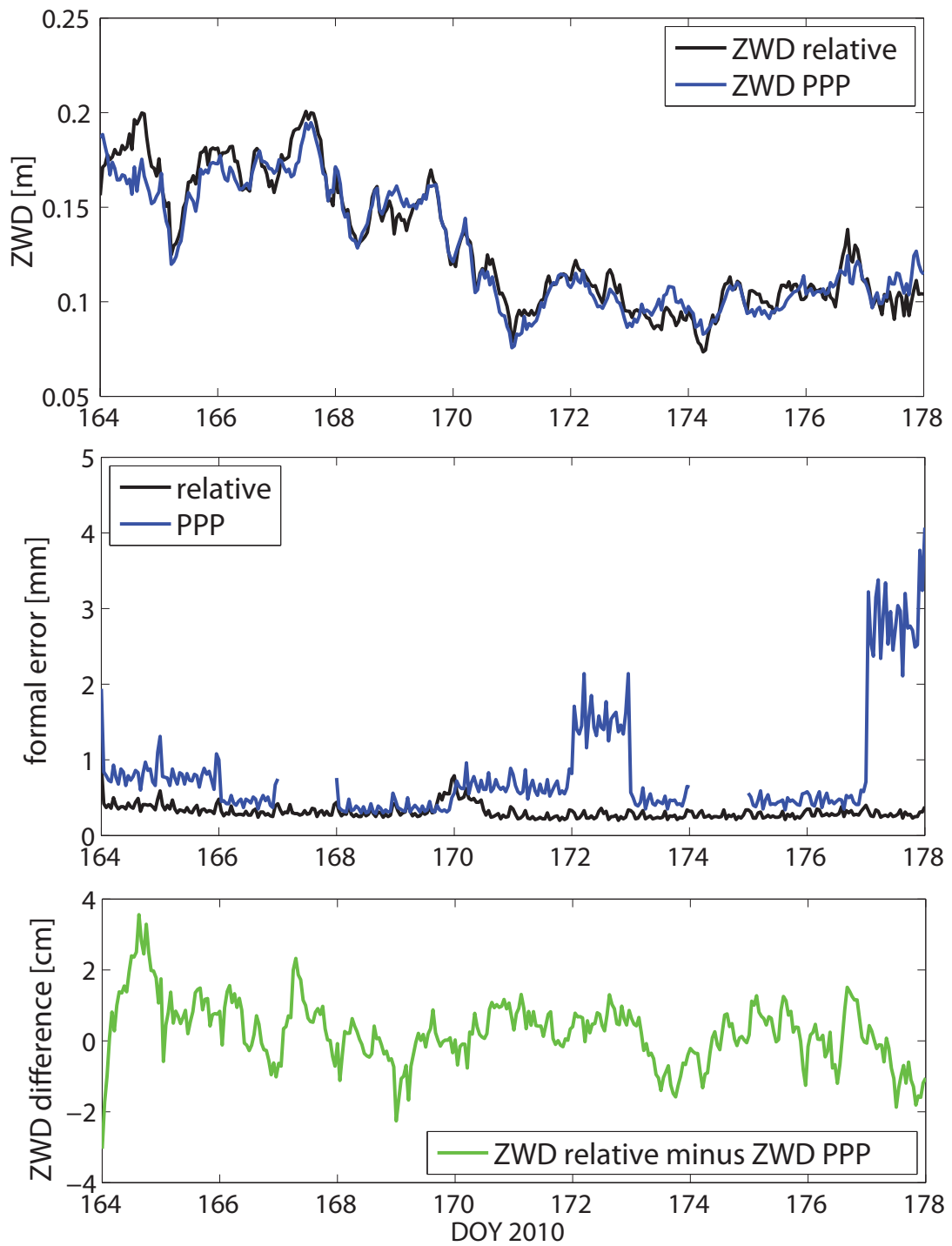


Figure C.36: Comparison of PPP and double-difference (relative) solution for station ZIMM (June 13–26, 2010)

Bibliography

- ASHBY, N. (2003). Relativity in the Global Positioning System. *Living Reviews in Relativity*, Vol. 6, <http://www.livingreviews.org/lrr-2003-1>. 23
- BABY, H., GOLÉ, P. & LAVERGNAT, J. (1988). A model for the tropospheric excess path length of radio waves from surface meteorological measurements. *Radio Science*, Vol. 23, pp. 1023–1038. 61
- BENDER, M. & RAABE, A. (2007). Preconditions to ground based GPS water vapour tomography. *Annales Geophysicae*, Vol. 25, pp. 1727–1734. 122
- BERG, H. (1948). *Allgemeine Meteorologie*. Dümmler. 57, 58
- BEVIS, M., BUSINGER, S. & CHISWELL, S. (1994). GPS Meteorology: Mapping zenith wet delays onto precipitable water. *Journal of Applied Meteorology*, Vol. 33, pp. 379–386. 52
- BILICH, A. & LARSON, K. (2007). Mapping the GPS Multipath Environment Using the Signal-to-Noise Ratio (SNR). *Radio Science*, Vol. 42. 30
- BISNATH, S. & GAO, Y. (2008). Current state of Precise Point Positioning and future prospects and limitations. In *Proceedings of IUGG 24th General Assembly*. 40
- BISNATH, S., PETOVELLO, M. & LACHAPELLE, G. (2007). What is carrier phase wind-up? What is its effect on GNSS performance/operation? *Inside GNSS*, July/August 2007, pp. 32–35. 28
- BÖHM, J. (2008). Atmospheric effects in geodesy. Lecture notes. xiv, 53
- BÖHM, J. & SCHUH, H. (2004). Vienna Mapping Functions in VLBI analyses. *Geophysical Research Letters*, Vol. 31. 63
- BÖHM, J., NIELL, A., TREGONING, P. & SCHUH, H. (2006a). Global Mapping Function (GMF): A new empirical mapping function based on numerical weather model data. *Geophysical Research Letters*, Vol. 33. 63

- BÖHM, J., WERL, B. & SCHUH, H. (2006b). Troposphere mapping functions for GPS and VLBI from ECMWF operational analysis data. *Journal of Geophysical Research*, Vol. 111. 64, 89
- BÖHM, J., HEINKELMANN, R. & SCHUH, H. (2007). Short Note: A global model of pressure and temperature for geodetic applications. *Journal of Geodesy*, Vol. 81, pp. 679–683. 57, 58, 64, 89
- BRUNNER, F.K. & GU, M. (1991). An improved model for the dual frequency ionospheric correction of GPS observations. *Manuscripta Geodaetica*, Vol. 16, pp. 205214. 46
- CHAO, C. (1974). The tropospheric calibration model for Mariner Mars 1971. Tech. Rep. 32-1587, Jet Propulsion Laboratory, California Institute of Technology, Pasadena, CA. 61
- CHEN, G. & HERRING, T. (1997). Effects of atmospheric azimuthal asymmetry on the analysis from space geodetic data. *Journal of Geophysical Research*, Vol. 102, pp. 20489–20502. 64
- DACH, R., HUGENTOBLE, U., FRIDEZ, P. & MEINDL, M. (2007). *User Manual of the Bernese GPS Software Version 5.0*. Astronomical Institute, University of Bern, Bern, Switzerland. 27, 29, 47, 70, 71, 87, 88, 129
- DAVIS, J., HERRING, T., SHAPIRO, I., ROGERS, A. & ELGERED, G. (1985). Geodesy by radio interferometry: effects of atmospheric modeling errors on estimates of baseline length. *Radio Science*, Vol. 20, pp. 1593–1607. 52, 54, 56, 57, 58, 60, 61
- DAVIS, K. (1990). *Ionospheric Radio*. IEE Electromagnetic Waves Series 31, Peter Pergrinus Ltd., London. 44, 45, 46
- DOW, J., NEILAN, R. & RIZOS, C. (2009). The International GNSS Service in a changing landscape of Global Navigation Satellite Systems. *Journal of Geodesy*, Vol. 83, pp. 191–198. 38
- EISSFELLER, B., IRSIGLER, M., AVILA-RODRIGUEZ, J.A. & SCHÜLER, T. (2007). Das Europäische Satellitennavigationssystem Galileo - Entwicklungsstand. *Allgemeine Vermessungsnachrichten AVN*, pp. 42–55. 120
- ENGELSBERG, V., BABAKOV, V. & PETROVSKI, I. (2008). Expert Advice - GLONASS Business Prospects. *GPS World*, Online article. 15

- GIBBONS, G. (2008). Russia Approves CDMA Signals for GLONASS, Discussing Common Signal Design. *Inside GNSS*, March/April 2008, online edition, <http://www.insidegnss.com/node/648>. 14
- HAIDEN, T., KANN, A., STADLBACHER, K., STEINHEIMER, M. & WITTMANN, C. (2007). Integrated Nowcasting through Comprehensive Analysis (INCA) - System overview. Tech. rep., Austrian Meteorological Agency (ZAMG). 68
- HAIMBERGER, L., TAVOLATO, C. & SPERKA, S. (2008). Toward elimination of the warm bias in historic radiosonde temperature records - Some new results from a comprehensive intercomparison of upper-air data. *Journal of Climate*, Vol. 21, pp. 4587–4606. 79
- HERNÁNDEZ-PAJARES, M., JUAN, J. & SANZ, J. (2000). Application of ionospheric tomography to real-time GPS carrier-phase ambiguities resolution, at scales of 400–1000 km and with high geomagnetic activity. *Geophysical Research Letters*, Vol. 27, pp. 2009–2012. 48
- HERRING, T. (1992). A modified Hopfield tropospheric refraction correction model. In *Proceedings of Symposium on Refraction of Transatmospheric Signals in Geodesy, Delft, The Netherlands, 19-22 May, Netherlands geodetic Commission, Publication on Geodesy*, No. 36, pp. 157–164. 61, 62
- HITSCH, U. (2004). *Comparison of GPS and radiosonde derived humidity values*. Master's thesis, Institute of Meteorology, University of Vienna. 71
- HOFMANN-WELLENHOF, B., LICHTENEGGER, H. & WASLE, E. (2008). *GNSS - Global Navigation Satellite System. GPS, GLONASS, Galileo, and more..* SpringerWien-NewYork, 1st edn. 8, 9, 11, 14, 27, 70
- HOPFIELD, H. (1969). Two-quartic tropospheric refractivity profile for correcting satellite data. *Journal of Geophysical Research*, Vol. 74, pp. 4487–4499. 58, 59, 61
- ICD-GPS-200C (2006). Interface control document, navigation user interfaces. Tech. rep., NAVSTAR GPS Space Segment, Fountain Valley, CA. 29
- IFADIS, I. (1986). The atmospheric delay of radio waves: Modeling the elevation dependence on a global scale. Tech. Rep. 38L, School of Electrical and Computer Engineering, Chalmers University of Technology, Göteborg. 59, 61, 62

- KARABATIĆ, A., WEBER, R. & HAIDEN, T. (2010). Near real-time estimation of tropospheric water vapour content from ground based GNSS data and its potential contribution to weather now-casting in Austria. *Advances in Space Research*, in press. 68
- KOUBA, J. (2004). Improved relativistic transformations in GPS. *GPS Solutions*, Vol. 8, pp. 170–180. 22
- KOUBA, J. (2008). Implementation and testing of the gridded Vienna Mapping Function 1 (VMF1). *Journal of Geodesy*, Vol. 82, pp. 193–205. 63
- KOUBA, J. (2009). A guide to using International GNSS Service (IGS) products. *IGS Online article*: <http://igsceb.jpl.nasa.gov/overview/pubs.html>. 107
- KOUBA, J. & HÉROUX, P. (2001). Precise Point Positioning using IGS orbit and clock products. *GPS Solutions*, Vol. 5, pp. 12–28. 19
- LANGLEY, R. (1998). Propagation of the GPS Signals. In P. Teunissen & A. Kleusberg, eds., *GPS for Geodesy*, pp. 111–149, Springer, 2nd edn. 30, 52
- LANYI, G. (1984). Tropospheric delay effects in radio interferometry. The telecommunications and data acquisition progress report 42-78, Jet Propulsion Laboratory, California Institute of Technology, Pasadena, CA. 63
- LE, A. & TIBERIUS, C. (2007). Phase wind-up effects in precise point positioning with dynamic platforms. In *Proceedings of the 3rd ESA Workshop on Satellite Navigation User Equipment Technologies, NAVTEQ 2006, 11-13 December 2006*, ESA publications, Noordwijk, The Netherlands. 27
- LEANDRO, R. (2009). *Precise Point Positioning with GPS: A New Approach for Positioning, Atmospheric Studies, and Signal Analysis*. Ph.D. thesis, Department of Geodesy and Geomatics Engineering, University of New Brunswick, Fredericton, New Brunswick, Canada. 57
- LEANDRO, R., LANGLEY, R. & SANTOS, M. (2007). Estimation of P2-C2 biases by means of Precise Point Positioning. In *Proceedings of ION Annual Meeting 2007*. 28, 29
- LUTZ, S., TROLLER, M., PERLER, D., GEIGER, A. & KAHLE, H.G. (2010). Better weather prediction using GPS. *GPS World*, Vol. 21, pp. 40–47. 122, 123
- MACMILLAN, D. (1995). Atmospheric gradients from very long baseline interferometry observations. *Geophysical Research Letters*, Vol. 22, pp. 1041–1044. 64, 65

- MACMILLAN, D. & MA, C. (1994). Evaluation of Very Long Baseline Interferometry atmospheric modeling improvements. *Journal of Geophysical Research*, Vol. 99, pp. 637–651. 64
- MARINI, J. (1972). Correction of satellite tracking data for an arbitrary tropospheric profile. *Radio Science*, Vol. 7, pp. 223–231. 61
- MARINI, J. & MURRAY, C. (1973). Correction of laser range tracking data for atmospheric refraction at elevation above 10 degrees. In *NASA-TM-X-70555, Goddard Space Flight Center, Greenbelt, Md.* 61
- MCCARTHY, D. & PÉTIT, G. (2004). IERS conventions (2003). IERS Technical Note No. 32, International Earth Rotation and Reference Systems Service. 8, 31, 33, 55
- MEINDL, M., SCHAER, S., HUGENTOBLE, U. & BEUTLER, G. (2004). Troposphere gradient estimation at CODE: results from global solutions. In R. Anthes, ed., *Applications of GPS remote sensing to meteorology and related fields*, vol. Vol. 82 of *Journal of the Meteorological Society of Japan*, pp. 331–386, Meteorological Society of Japan. 64
- MENDES, V. (1999). *Modeling the neutral atmosphere propagation delay in radiometric space techniques*. Ph.D. thesis, Department of Geodesy and Geomatics, University of New Brunswick, Fredericton, New Brunswick, Canada. 56, 59, 61
- MENDES, V. & LANGLEY, R. (1998). Tropospheric zenith delay prediction accuracy for airborne GPS high-precision positioning. In *Proceedings of the institute of Navigation 54th annual meeting, June 1-3, 1998, Denver, USA*, pp. 337–347. 59
- NIELL, A. (1991). Vertical change and atmosphere correction in VLBI. In *In proceedings of AGU Chapman Conference on Geodetic VLBI: Monitoring Global Change, NOAA Tech. Rep. NOS 137 NGS 49*, pp. 147–158. 64
- NIELL, A. (1996). Global mapping functions for the atmosphere delay at radio wavelengths. *Journal of Geophysical Research*, Vol. 101, pp. 3227–3246. 57, 60, 61, 62
- NIELL, A. (2001). Preliminary evaluation of atmospheric mapping functions based on numerical weather models. *Phys. Chem. Earth*, Vol. 26, pp. 475–480. 63
- NIELL, A., COSTER, A., SOLHEIM, F., MENDES, V., TOOR, P., LANGLEY, R. & UPHAM, C. (2001). Comparison of atmosphere wet delay by radiosonde, water vapor radiometer, GPS and VLBI. *Journal of Atmospheric and Oceanic Technology*, Vol. 18, pp. 830–850. 79

- NILSSON, T. (2008). *Measuring and modelling variations in the distribution of atmospheric water vapour using GPS*. Ph.D. thesis, Department of Radio and Space Science, Chalmers University of Technology, Göteborg, Sweden. 122
- OWENS, J. (1967). Optical refractive index of air: dependence on pressure, temperature and composition. *Applied Optics*, Vol. 6, pp. 51–59. 52
- PÉTIT, G. & LUZUM, B. (2010). IERS conventions (2010). IERS Technical Note No. 36, International Earth Rotation and Reference Systems Service. 34, 46
- PETROV, L. & BOY, J. (2004). Study of the atmospheric pressure loading signal in very long baseline interferometry observations. *Journal of Geophysical Research*, Vol. 109, pp. B03405.1–B03405.14. 33
- SAASTAMOINEN, J. (1972). Atmospheric correction for the troposphere and stratosphere in radio ranging of satellites. In *The use of artificial satellites for Geodesy*, vol. Vol. 15 of *Geophys. Monogr. Series*, pp. 247–251, AGU. 56, 57, 58, 59, 60, 61
- SCHAER, S., BEUTLER, G. & ROTACHER, M. (1998). Mapping and predictiong the ionosphere. In *Proceedings of the IGS AC Workshop, February 9-11, 1998, Darmstadt, Germany*. 45
- SCHUH, H., ESTERMANN, G., CRÉTAUX, J., BERGU-NGUYEN, M. & VAN DAM, T. (2003). Investigation of atmospheric and hydrological loading by space geodetic techniques. In *Satellite Altimetry for Geodesy, Geophysics and Oceanography*, Proceedings of the International Workshop on Satellite Altimetry, September 8-13, 2002, Wuhan, China, Springer. 33
- SEEBER, G. (2003). *Satellite Geodesy*. Walter de Gruyter, 2nd edn. 8, 49
- SIMSKY, A., MERTENS, D., SLEEWAGEN, J.M., DE WILDE, W., HOLLREISER, M. & CRISCI, M. (2008). Multipath and tracking performances of Galileo ranging signals transmitted by GIOVE-B. In *Proceedings of ION GNSS 2008, 21st International Technical Meeting of the Satellite Division, September 16-19 2008, Savannah, USA*. 120
- SMITH, E. & WEINTRAUB, S. (1953). The constants in the equation of atmospheric refractive index at radio frequencies. In *Proceedings of the Institute of Radio Engineers*, vol. Vol. 41, No. 8, pp. 1035–1037. 52
- THAYER, G. (1974). An improved equation for the radio refractive index of air. *Radio Science*, Vol. 9, pp. 211–222. 52

- VAN DAM, T. & WAHR, J. (1998). Modeling environment loading effects: a review. *Phys. Chem. Earth*, Vol. 23, pp. 1077–1087. 32
- VAN DAM, T., BLEWITT, G. & HEFLIN, M. (1994). Atmospheric pressure loading effects on Global Positioning System coordinate determinations. *Journal of Geophysical Research*, Vol. 99, pp. 23939–23950. 33
- VEY, S., CALAIS, E., LLUBES, M., FLORSCH, N., WOPPELMANN, G., HINDERER, J., AMALVICT, M., LALANCETTE, M., SIMON, B., DUQUENNE, F. & HAASE, J. (2002). GPS measurements of ocean loading and its impact on zenith tropospheric delay estimates: a case study in Brittany, France. *Journal of Geodesy*, Vol. 76, pp. 419–427. 33
- WANG, J. & ZHANG, L. (2008). Systematic errors in global radiosonde precipitable water data from comparisons with ground-based GPS measurements. *Journal of Climate*, Vol. 21, pp. 2218–2238. 79
- WEBER, R. & KARABATIĆ, A. (2009). Potential Improvements in GNSS-based Troposphere Monitoring by use of upcoming GALILEO-signals. In *Proceedings of 2nd Colloquium - Scientific and Fundamental Aspects of the Galileo Program, October 14-16 2009, Padua, Italy*. 119
- WEBER, R., ENGLISH, S. & TODOROVA, S. (2008a). Scientific applications in geodesy and geodynamics - Innovations offered by the new Galileo signals. In *Proceedings of 1st Colloquium on Scientific and Fundamental Aspects of the Galileo Programme, October 1-4 2007, Toulouse, France*. 117
- WEBER, R., KARABATIĆ, A., LEROCH, S. & HAIDEN, T. (2008b). Final report of project GNSS-MET. Tech. rep., Austrian Research Promotion Agency (FFG). 68
- WOLFE, D. & GUTMAN, S. (2000). Developing an Operational, Surface-Based, GPS, Water Vapor Observing System for NOAA: Network Design and Results. *Journal of Atmospheric and Oceanic Technology*, Vol. 17, pp. 426–440. 67
- WOODEN, W. (1984). NAVSTAR Global Positioning System overview. In *Proceedings of the pacific congress on marine technology, Honolulu, Hawaii, April 24-27, 1984*. 9
- WU, J., WU, S., HAJJ, G., BERTIGER, W. & LICHTEN, S. (1993). Effects of antenna orientation on GPS carrier phase. *Manuscripta Geodaetica*, Vol. 18, pp. 91–98. 28

- XU, G. (2003). *GPS: Theory, Algorithms and Applications*. Springer-Verlag Berlin Heidelberg New York. 8, 24
- ZUMBERGE, J., HEFLIN, M., JEFFERSON, D., WATKINS, M. & WEBB, F. (1997). Precise point positioning for the efficient and robust analysis of GPS data from large networks. *Journal of Geophysical Research*, Vol. 102, pp. 5005–5017. 19